UNIVERSIDAD DE GRANADA

Facultad de Ciencias

Departamento de Física Aplicada

Programa de Doctorado en Física y Ciencias del Espacio

Tesis doctoral

Non-linear Magnetorheology:

multibody and multipole effects on the Yield Stress

Autor: José Rafael Morillas Medina

Director: Juan de Vicente Álvarez-Manzaneda

2019

Editor: Universidad de Granada. Tesis Doctorales
Autor: José Rafael Morillas Medina
ISBN: 978-84-1306-366-9
URI: http://hdl.handle.net/10481/58100

Agradecimientos

Cuando empecé el doctorado, en las típicas charlas de bienvenida, nos dijeron que la investigación es un camino duro en el que continuamente aparecen nuevos e inesperados escollos pero que, una vez superados, es tremendamente gratificante. Ahora que han pasado cuatro años de aquello, puedo atestiguarlo. Es más, me atrevería a decir que dicho camino tiene más partes duras que gratificantes. Esta página quiero dedicarla a todos aquellos que, de una manera u otra, me han ayudado a seguir en esta primera etapa del recorrido. Espero contar con vuestro ánimo y confianza en lo que resta.

En primer lugar y como era de esperar, dar las gracias a mi director Juan. Gracias por tu apoyo y positivismo, incluso en esas reuniones que se resumen en "esto no sale", por quitar dramatismo al asunto y por toda la ayuda que me has prestado tanto en lo científico como en lo académico y burocrático. Confío en que un día la tasa de cerrar frentes supere a la de abrirlos y reduzcamos el taco de informes sobre la mesa.

Quisiera continuar con todos los integrantes, antiguos y actuales, de la Sala π^f y alrededores: Keshvad, Elisa, Guille, Pablo, Aixa, Irene, Nico, Leo, Luis, Alicia, Matt, Óscar, Yan, Yang, José Alberto, José Antonio, Migue y Ana. Formáis un grupo de amigos excepcional, sano, familiar y donde da gusto trabajar.

Extiendo mi agradecimiento también al Grupo de Física de Fluidos y Biocoloides, por acogerme y permitir, no solo desarrollar esta tesis, sino también iniciarme en labores docentes. En estas últimas quiero nombrar especialmente a Fernando, Paco, Antonio y José Antonio por vuestros consejos y confianza mostrada.

No puedo olvidar tampoco a Antonio Bombard y Elizabeth Carreón quienes también me guiaron en mis primeros pasos en el laboratorio de reología. Gracias por vuestra paciencia, por compartir vuestras ideas y nuevos puntos de vista. Aprovecho estas líneas para agradecer también a Claas Bierwisch y su grupo la grata acogida que me brindaron en Alemania durante mi estancia así como su continua disposición y ánimo a discutir los resultados incluso por correo electrónico.

Fuera de la facultad también me han acompañado amigos cuya forma de ser ha contribuido a elaborar esta tesis. Mil gracias a los miembros de Physical Action (y los impuestos que pagan) y de Vuelta a los orígenes (al único que no está incluido en los grupos anteriores) por todas esas charlas en las que arreglamos el mundo. Cómo no, gracias a todos los bosones y fermionas por agitarme, literalmente, las ideas. No sé si favoreceremos aquello de mente sana en cuerpo sano, pero le ponemos empeño.

Mención especial requieren los bendecidos por el pollo. Sin duda, sois amigos de corazón que me habéis prestado vuestra ayuda, consejo y tiempo, no solo a lo largo de la tesis sino desde que tengo uso de memoria. Por todo ello y por lo que vendrá, gracias.

Por último y no menos importante, dar las gracias a mis padres y a mi tía. Puesto que saben cómo soy, basta con mencionarles para indicar lo que significan para mí.

Contents

Abstract

Magnetorheological fluids (MRFs) are suspensions consisting of ferromagnetic microparticles that are usually dispersed in a Newtonian liquid. Under the presence of an external magnetic field, the dispersed particles self-assemble through magnetostatic interactions giving rise to anisotropic structures oriented in the field direction. The strength of these structures depends on the particle concentration and on the applied field strength.

As a result of the field-induced structuration (at the microscopic level), the viscosity of the MRF (at the macroscopic level) increases several orders of magnitude and, when the viscosity becomes infinite, the system can even bear an applied stresses. In this latter case it is necessary to exert a minimum force level (i.e. the so-called yield stress) in order to make the suspension flow. The ability to induce such a liquid to solid transition in a controlled manner only by changing the particle concentration and the magnetic field has been used to implement MRFs as smart electromechanical interfaces in several torque-transfer devices. Typically, these kind of applications deal with large concentrations and strong responsive magnetic particles in order to cover the widest possible range of required mechanical properties with only one sample and at moderate applied fields.

Under these operational conditions, the mean distance between particle surfaces is exceedingly small (smaller than particle diameter) promoting the appearance of non-negligible magnetic multipoles and the necessity of considering multibody interactions as non-pairwise ones. This, together with the non-linear ferromagnetic behavior, triggers non-linear effects also in the magnetostatic force and, thus, in the material yield stress. Despite of this, traditional models in magnetorheology frequently neglect multipoles, and when they are considered, forces in the large particle collectivity are simplified. As a result, the calculated yield stresses systematically underestimate experimental measurements.

To overcome these shortcomings, a Finite Element Method simulation based on periodic boundary conditions and a reduced formulation is proposed here to model field induced structures as periodic arrays of magnetic particles. The model includes all multipoles, multibody effects and non-linear magnetic behavior in the solution and is applicable regardless the particle concentration and field strength. In addition, as it is only restricted to periodic arrangements, it properly simulates any strain in the structure whenever the shear affine motion is accepted. Predicted yield stress values show a good agreement with experimental ones for all investigated fields (from linear to saturation regime) and concentrations (evaluated up to 50 vol%).

The comparison between traditional models and the proposed one highlights that the former are useful only at small strains, small concentrations and small field strengths (i.e. when the dispersed particles behave as linear magnetic materials). The proposed model is also verified in the saturated regime (high fields, at any concentration) when the magnetostatic force is truly dipolar. To do so, a simple numerical computation (based again in periodic arrangements) is proposed. This dipolar computation shows a perfect agreement with the new model and points that long-range multibody effects, introduced analytically, have to been maintained in this regime as well.

The experimental validation is carried out in a conventional magnetorheometer with texturized/sandblasted plates to avoid wall-slip phenomena. However, in order to apply

sufficiently strong magnetic fields needed to reach the saturation regime, a novel magnetorheometer (double-gap) cell was designed, tested and used. This new design keeps the main advantages of commercial ones (high shear rate operational range and the elimination of normal forces) but also allows applying larger magnetic fields guaranteeing a high field homogeneity to measure the yield stress properly.

The aforementioned yield stress computations and measurements are performed on model MRFs in order to keep the systems as simple as possible while still including the key ingredients to capture the Physics behind. However, for instance, these kind of samples show a very poor stability against sedimentation what does not make them directly suitable for applications. In this sense, a novel route to minimize a severe kinetic destabilization is described using a second population of magnetic particles. Different from traditional methods, where the second population consists of only single or multidomain particles, here it is shown that the use of particles with sizes in the limit between single and multidomain regimes can enhance the yield stress and the long-term stability.

Resumen

Los fluidos magnetorreológicos (FMR) son suspensiones basadas en microparticulas ferromagnéticas usualmente dispersadas en un líquido newtoniano. Bajo la presencia de un campo magnético externo, las partículas interaccionan magnetoestáticamente autoensamblándose y dando lugar a estructuras anisótropas en la dirección del campo. La resistencia de dichas estructuras depende de la concentración de partículas y de la intensidad del campo magnético aplicado.

Como resultado de la estructuración inducida por el campo (a nivel microscópico), la viscosidad del FMR (a nivel macroscópico) aumenta varios ordenes de magnitud y, cuando se hace infinita, el sistema incluso puede soportar un esfuerzo aplicado sin deformarse. En tal caso, es necesario aplicar una fuerza mínima (el llamado esfuerzo umbral) para hacer fluir a la suspensión. La habilidad para inducir esta transición de líquido a sólido de forma controlada simplemente cambiando la concentración de partículas y el campo magnético ha sido usada para implementar los FMR como interfaces electromecánicas en diversos aparatos de trasmisión de torque/esfuerzo. Normalmente, los FMR utilizados en este tipo de aplicaciones constan de partículas con una fuerte respuesta magnética y en altas concentraciones con el objetivo de cubrir el intervalo más amplio posible de propiedades mecánicas con solo una muestra y aplicando campos moderados.

Bajos estas condiciones de operación, la distancia media entre superficies de partículas es extremadamente pequeña (menor que el diámetro de la partícula) favoreciendo la aparición de multipolos magnéticos no despreciables y la necesidad de considerar interacciones multicuerpo en lugar de interacciones entre parejas. Esto, unido al comportamiento ferromagnético no lineal de las partículas, hace que la fuerza magnetoestática entre las mismas no sea lineal, y en consecuencia, tampoco lo sea el esfuerzo umbral. A pesar de esta fenomenología, los modelos tradicionales en magnetorreología generalmente no tienen en cuenta multipolos magnéticos y, cuando lo hacen, es a costa de simplificar las fuerzas entre la colectividad de partículas. Como resultado, el esfuerzo umbral calculado subestima sistemáticamente las medidas experimentales.

Para superar estas limitaciones, en esta tesis se propone modelar las estructuras inducidas por el campo magnético como redes periódicas de partículas magnéticas usando un método de elementos finitos basado en condiciones periódicas y formulación reducida. El modelo incorpora todos los efectos magnéticos multipolares, multicuerpo y no lineales en la solución y es aplicable independientemente de la concentración o el campo aplicado. Además, como únicamente está limitado a estructuras periódicas, puede simular cualquier grado de deformación en la estructura siempre que se admita como válida la deformación afín. Los valores de esfuerzo umbral predichos muestran un buen acuerdo con los experimentales para todos los campos (desde régimen lineal hasta saturación) y concentraciones (evaluadas hasta el 50 vol%) investigados.

La comparación entre los modelos tradicionales y el propuesto resaltan que los primeros son útiles solo a pequeñas deformaciones, bajas concentraciones y campos de poca intensidad (cuando las partículas se comportan como materiales lineales). El modelo propuesto también se verifica en el régimen de saturación (campos aplicados altos a cualquier concentración) cuando la interacción magnética es solamente dipolar. Para ello, se propone un cálculo numérico sencillo (de nuevo sobre estructuras periódicas). Este

cálculo con fuerzas dipolares coincide perfectamente con el modelo de elementos finitos e indica que las interacciones multicuerpo de largo alcance, introducidas analíticamente, también deben considerarse en el régimen de saturación.

Para llevar a cabo la validación experimental se utilizó un magnetorreómetro convencional equipado con platos texturizados y rugosos evitando así fenómenos asociados a deslizamiento en paredes. Sin embargo, para aplicar los campos necesarios para alcanzar el régimen de saturación se diseñó, validó y utilizó una celda magnetorreológica nueva ("double-gap"). Este nuevo diseño mantiene las principales ventajas de los diseños comerciales (capacidad de aplicar velocidades de deformación elevadas y eliminación de fuerzas normales) a la vez que puede aplicar campos elevados garantizando una gran homogeneidad y permitiendo la medida correcta del esfuerzo umbral.

Tanto el modelado como las medidas experimentales anteriores de esfuerzo umbral fueron realizadas en FMR modelo con el objetivo de mantener el sistema tan sencillo como fuese posible pero incluyendo los elementos clave para observar la física subyacente. Sin embargo, este tipo de FMR muestran, por ejemplo, muy poca estabilidad contra la sedimentación lo que hace difícil su aplicación comercial directa. En este sentido, se describe la adición de una segunda población de partículas magnéticas como una nueva ruta para minimizar tal inestabilidad cinética. A diferencia de los métodos tradicionales, donde la segunda población de partículas magnéticas consiste exclusivamente en partículas mono- o multidominio, aquí se muestra que la utilización de partículas con un tamaño en el límite entre ambos regímenes puede mejorar el esfuerzo umbral y mantener al sistema estable durante más tiempo.

Chapter 1. Magnetic Suspensions

1.1 Introduction: simple magnetic suspensions, applications and related problems

Over time, Science and Technology, and in particular Material Science, have addressed the synthesis and development of diverse systems with specific characteristics. These systems are designed in order to be applied in particular processes that require the aforementioned characteristics to perform optimally. Unfortunately, this route allows the synthesis of particular materials for very particular problems. Thus, it would be desirable to develop materials that are capable to adapt to more than one specific case. With this target, a new kind of adaptative material has been created, the so-called smart materials [1].

Interestingly, the properties of these (smart) materials (permeabilities, conductivities, stiffness, viscosity, shape, size, etc.) can be tuned by external stimuli such as temperature, magnetic and electric fields, strain, electric current, pH or light exposure among others. In this context, smart materials open a new and broad spectrum of applications thanks to their ability to be controlled *ad hoc*. Among the different smart materials available today, magnetic suspensions and especially magnetorheological fluids (MRFs) have attracted a lot of attention due to their multiple applications in research and industry fields (see below).

Generally speaking, magnetic suspension are multiphase systems where, at least, one of the phases responds to an applied magnetic field. In the simplest cases, there are only two phases. The magnetizable one is constituted by spherical particles, usually made of ferro- or ferrimagnetic materials due to their stronger magnetic response, while the second phase is a non-field responsive Newtonian liquid that serves as a carrier. Depending on the dispersed particle size, two main groups can be distinguished: ferrofluids (FFs) and conventional magnetorheological fluids (CMRFs) [2]. In this dissertation, we will focus only in the (magneto) rheological response of magnetic suspensions, i.e., how they react to an imposed stress/strain when they are under the presence of a magnetic field. Indeed, this macroscopic behavior strongly depends on the particle size in the magnetic suspension.

In FFs, the particulate phase has a typical size below 10 nm. Because of this, particles continuously suffer from Brownian motion (they are truly colloids) both in the absence and presence of magnetic fields. As a result, under an external field, the system gets magnetized (i.e. the particle magnetic moment orients according to the external field) but remains itself in the fluid state (i.e. the Brownian motion is still capable to keep the particles properly dispersed). In this way, FFs can be seen as continuous media with homogeneous properties (magnetization and viscosity) only dependent, in many circumstances, on the applied magnetic field and temperature [3]. The first feature (FF magnetization) allows the FF to be dragged and located in the desired region using magnetic field gradients while the second feature (FF remains as a fluid) allows the FF to adapt to the surrounding geometry. In this context, major applications consist in using FFs as lubricants and sealings of rotating shafts [4-6], cooling systems [7] and contrast agents for magnetic resonance image [8] among many others [9].

In CMRFs, the particulate phase has a typical size above 1 μm. These systems exhibit a strong response to magnetic fields (much more intense than in FFs) that prevails over Brownian motion giving rise to phase separation phenomena (particle structuration), extrinsic and/or non-material properties (dependent on the sample size, sample shape, experimental conditions, etc.).

Upon the application of a magnetic field, the particles dispersed in a CMRF become magnetized and start to interact through magnetic forces. In only a few milliseconds, these interactions lead to the arrangement of the particles in structures that offer some resistance to be deformed under flow. As a consequence, the viscosity of a CMRF increases several orders of magnitude (so-called MR effect). What is more, if the structures are strong and large enough to percolate the sample, the application of the magnetic field can induce a yield stress. In other words, it is necessary to macroscopically apply a minimum force to make the sample flow. Below this threshold, the suspension behaves as a viscoelastic material [10-12].

Such a strong, reversible and fast change in the rheological behavior has motivated the use of CMRFs in torque transfer application with electronic control. Typical examples are clutches, brakes or dampers included in diverse engineering branches: civil, automotive, military equipment, prosthetic, robotic, haptic, etc. [13,14]. Furthermore, CMRFs can also be seen in chemical sensors [15] and in biomedical applications [16].

Unfortunately, so simple magnetic suspensions only consisting of particles dispersed in a liquid, as described so far, do not fulfill the stringent requisites of current commercial applications. On the one hand, due to their high surface to volume ratio, FF nanoparticles tend to irreversibly aggregate [2]. On the other hand, CMRF microparticles are prone to aggregate as well, in this case, due to the magnetic remanence still present in the particles when the external field is switched off. But, undoubtedly, the most important problem towards real life applications of CMRFs is their tendency to settle down because of the absence of Brownian motion and the large density mismatch between the particles and the carrier fluid [12]. In addition, depending on the continuous phase, the surface of the bare ferromagnetic particles can be oxidized or degraded over time reducing their magnetic response [17]. In the case of CMRFs, this also supposes a limit in their lifetime since an oxidized surface is weaker than the particle body what leads to more and more severe particle wear. As a result, CMRFs become a cake that is impossible to be redispersed [18,19].

1.2 Partial solutions: sophisticated magnetic suspensions

Common approaches to avoid interparticle aggregation in the absence of magnetic fields are based on the use of surfactants to cover the particles surfaces through a steric stabilization mechanism. Once adsorbed at the surfaces, the surfactant tails provide a layer (of a few nm) that acts as an elastic spring preventing direct contacts between the particles, increasing the typical interparticle distance and with this, reducing the effects of dispersion, surface and/or remanence interactions. Obviously, the choice of the surfactant must be done according to the nature of the particulate and continuous phases so that surfactant molecules are tightly adsorbed onto particles but their tails are fully stretched into the carrier liquid [2,3].

Steric stabilization together with other well-known techniques in Colloid Science (for example, interparticle repulsion due to electric double layers) have shown to be effective against particle agglomeration and favor sample redispersibility both in FFs [2,3,20] and

CMRFs [21-23]. However, they are not effective in preventing particle sedimentation in CMRFs.

With this in mind, several modifications of the traditional formulation of CMRFs have led to a steady growth of the family of magnetic suspensions today. In this sense, it has been proposed the substitution of the Newtonian carrier fluids by yield stress fluids such as thixotropic media (e.g. MR greases, MRGs, and gels) to reduce the sedimentation rate [24-26]. Particles can be trapped in a thixotropic network when the latter exhibits a sufficiently large yield stress in comparison to the gravitational stress. However, if the yield stress is too large the MR effect can be reduced. Typically, redispersion is hindered when using thixotropic carriers. An extreme case corresponds to magnetorheological elastomers (MREs) where the carrier liquid is substituted by an elastic matrix (for a recent review on this topic see Ref. [27]). More frequently, the matrix gelation occurs in the presence of the magnetic particles and under the presence of an external field. In this way, the particle structuration occurs at the initial stage of the curing process and the field-directed structures are frozen in the matrix (so-called anisotropic or aligned elastomers). Due to their (visco) elastic nature, both MRGs and MREs are commonly used in applications that do not require the sample to flow but in passive apparatuses (where changes in the elastic modulus via magnetic fields are useful) such as dampers or piezoresistive sensors.

Other alternatives to improve particle stability against sedimentation, keeping the continuous phase as a liquid, have been mainly directed towards changes in the particulate phase. Probably the simplest modification is given by bimodal MRFs. These suspensions use a Newtonian liquid as a carrier but consist of, at least, two particle populations with different size. One of them belongs to the typical size scale of CMRFs, around 1 μm, to guarantee a noticeable MR effect. The other one with diameters one order of magnitude higher (around 10 μm) [28-30] or in the nanometric scale [31,32]. The incorporation of another population in the micronsized range cannot mitigate sedimentation problems as neither of these particles suffer from Brownian motion, however these mixtures show a smaller viscosity in the absence of a magnetic field than the corresponding monomodal CMRF with the same solids concentration. This enhances the MR effect and sample handling. On the other hand, bimodal suspensions containing nanoparticles can reduce sedimentation rate probably due to the collisions (driven by Brownian motion) between both particle populations but, at the same time, they increase the viscosity in the absence of a field and reduce the MR effect because of the smaller magnetic properties of the nanoparticles.

Changes in the particle shape have been also investigated. In this sense, it has been shown that the use of magnetic fibers, instead of spheres, in MRFs can enhance the MR effect for the same solids concentration. In addition, fiber suspensions do not settle down so easily because fibers, randomly oriented in the absence of field, entangle themselves resulting in a yield stress bearing structure. Unfortunately, this fact also restricts their use to dilute systems since highly concentrated samples already have a non-negligible yield stress that precludes sample flow or handling in the absence of magnetic fields [33,34].

Several steps have been done also in reducing particle density. An example is the case of tailor-made core-shell particles (typically a magnetic core surrounded by a non-magnetic shell). The shell is usually made of a softer material, e.g. a polymer, so that effective density of the core-shell structure is smaller than the original particle [35]. In addition, these shells would act as a protection layer against chemical corrosion improving the MRF lifetime [36,37]. Other examples are hollow particles (shells of magnetic material)

[38] and magnetic latexes (latex particles doped with magnetic nanoparticles) [39,40]. In all these synthesis routes, a compromise must be reached always since magnetic response of the new particles is weakened by the relative magnetic content reduction.

In another approximation, magnetic particles are mixed with non-magnetic ones. When the latter particles are abrasive, these MRFs can be used in polishing applications since the places where abrasion takes place can be located using an external field [41-43]. Also, non-magnetic particles (without any other especial property) mixed with magnetic ones have shown to be useful since they can enhance or maintain the MR effect of CMRFs for the same solids concentration. As a result, one obtains MRFs with the same performance but being lighter and cheaper [44].

Nevertheless, the most characteristic magnetic suspension using non-magnetic particles are the so-called inverse ferrofluids (IFFs) [45,46] where non-magnetic particles are suspended in a FF. As a first approximation, IFFs can be regarded as magnetic analogues of CMRFs (that is, the magnetization mechanism of the sample does not depend on which phase, particulate or continuous, is magnetic). Moreover, from the point of view of the synthesis, IFFs exhibit some advantages basically because there exist multiple, simple and well-known methods to synthesize non-magnetic microparticles with tailored properties [12]. In this sense, particles can be produced with a strict control of their size (monodisperse suspensions), made of materials with densities that match those of the FFs (so that sedimentation is avoided), they can be surface activated (to eliminate aggregation) or fluorescently labeled (to track their movement).

These features allows a wide control over IFFs what makes them a model system useful for academia. In contrast, the yield stress developed in IFFs is significantly smaller in comparison to CMRFs and hence their use in commercial applications is very limited. Of course, magnetic particles can be dispersed also in a FF to recover usual values of the MR effect. In addition, certain control is gained over the carrier fluid in comparison to CMRFs. However, since both phases are magnetic, this control is not decoupled from the particle behavior what can lead to different particle structures and interactions [47-49].

Further progress in material engineering can be achieved by introducing in the formulation other constituents that are dependent on other external variables. In this sense, in the previous literature it has been proposed the synthesis of particles with an anisotropic magnetic content or particles that are responsive to both magnetic and electric fields so that particle orientation can be tuned *ad hoc* giving rise to more complex structures with anisotropic yielding behaviors [50]. Similarly, carrier fluids experiencing a liquid to solid transition upon temperature change have also been studied as a bridge between MRFs and MREs [51] and thus sharing the major advantages of both families.

Finally, more sophisticated formulations concern magnetic suspensions where magnetic and non-magnetic liquid phases coexist. In this case, in addition to the stabilization step to get appropriate FFs, it is necessary to choose a carrier fluid that is immiscible with the FF and an additional stability agent to avoid phase separation due to coalescence. A classic example are magnetic emulsions (FF drops in a non-magnetic carrier fluid) commonly used as model systems for magnetic suspensions with deformable constituents [52,53] but also applied in optics as filters [54]. Furthermore, magnetic emulsions have been also used as carriers (so-called ternary systems) to enhance sedimentation stability and MR effect [55]. Of course, if a magnetic particulate phase is already present, neither of two liquids have to be magnetic to get a MR effect as in the case of capillary MRFs. For these systems, the secondary fluid phase shows a surface activity completely opposed

to the main carrier fluid, therefore it prefers to be adsorbed on the particle surfaces connecting or bridging them. As a result, magnetic particles also form a structure in the absence of magnetic field avoiding sedimentation but making sample flow more difficult [56].

1.3 Dissertation scope and structure

As shown in Sec. 1.1, MRFs are currently present in multiple and different day to day applications. Therefore, the deepest knowledge possible about these systems is necessary in order to correctly predict their behavior and optimize their performance. However, due to the inherent complexity of MRFs, most of the current analytical and simulation methods are based on assumptions that are hardly reachable in real systems, namely: low concentrations, low particle magnetic response and low applied field strengths [57].

The two first assumptions allows regarding MRF particles as a group of interacting dipoles while the last one allows treating them as a linear material. On the contrary, common MRF applications typically use highly concentrated systems (above 30 vol%) [58], particles have a strong magnetic response (magnetic multipoles are present) and are ferromagnetic (inherently non-linear when interrogated along typical applicable magnetic fields).

Due to the high concentration and strong magnetic response, the small interparticle distance favors the appearance of induced multipoles above the dipolar one. In addition, the magnetic interaction related to these multipoles is not additive. This stage involves accounting for multipolar and multibody effects what, together with the ferromagnetic behavior of the particles, results in a highly non-linear MR response [59]. As a consequence, current methods in the literature commonly underestimated the main rheological properties (viscosity, yield stress, viscoelactic moduli) of MRFs. In this dissertation a numerical method is proposed to take into account these multibody, multipole and non-linear effects on the yield stress of periodic particle arrangements.

Regarding MRF colloidal instability, Sec. 1.2 points that current solutions are only partial and, although they can slow down sedimentation and aggregation rates, they also entail some undesired effects such as reduction of the MR effect or more sophisticated and delicated synthesis routes. In the second part of this dissertation, we explore the use, for first time, of particles with sizes in the limit between single and multidomain regimes as a secondary particle population of bimodal MRFs showing better stability and MR effect.

The dissertation is organized as follows: first, specific objectives are itemized in Chapter 2. Next, current available methods reported in the literature together with the theoretical basis to understand the rheological behavior of CMRFs are summarized in Chapter 3. In addition, particular experimental and numerical techniques employed in the dissertation are explained in Chapter 4.

From Chapter 5 to Chapter 8 we propose the aforementioned numerical method (based on the Finite Element Method) to compute the yield stress in CMRF including all multipoles, multibody and non-linear effects. Throughout these chapters, the proposed model is validated experimentally, compared to traditional numerical methods (to see its advantages/shortcomings) and verified analytically in the saturated regime, where only dipolar contribution remains. In order to reach that regime and properly carry out the rheological measurements, a new magnetorheometer double gap cell, Chapter 9, was developed.

In the last chapters the novel bimodal MRFs are investigated. To do so, first the rheological behavior of MRFs, exclusively based on those particles in the frontier between single and multidomain regimes, is evaluated in Chapter 10. Then, these particles are used as a secondary population of bimodal MRFs (Chapter 11 and Chapter 12). Basing on experiments and simulations, it is shown how the performance of the bimodal MRFs can be optimized depending on the particle material.

Finally, the dissertation ends with the main conclusions.

References

[1] Schwartz, M. (Ed.) Smart materials (CRC Press, Boca Raton, 2008).

[2] Vékás, L. (2008). Ferrofluids and magnetorheological fluids. Advances in Science and Technology, 54, 127-136.

[3] Rosensweig, R. E. Ferrohydrodynamics (Dover Publications, Mineola, 2014).

[4] Walker, J. S., and Buckmaster, J. D. (1979). Ferrohydrodynamic thrust bearings. International Journal of Engineering Science, 17(11), 1171-1182.

[5] Kuzhir, P. (2008). Free boundary of lubricant film in ferrofluid journal bearings. Tribology International, 41(4), 256-268.

[6] Shahrivar, K., and de Vicente, J. (2014). Ferrofluid lubrication of compliant polymeric contacts: effect of non-homogeneous magnetic fields. Tribology Letters, 56(2), 281-292.

[7] Odenbach, S. (2003). Ferrofluids—magnetically controlled suspensions. Colloids and Surfaces A: Physicochemical and Engineering Aspects, 217(1-3), 171-178.

[8] Kim, E. H., Lee, H. S., Kwak, B. K., and Kim, B. K. (2005). Synthesis of ferrofluid with magnetic nanoparticles by sonochemical method for MRI contrast agent. Journal of Magnetism and Magnetic Materials, 289, 328-330.

[9] Felicia, L. J., Vinod, S., and Philip, J. (2016). Recent advances in magnetorheology of ferrofluids (magnetic nanofluids)—a critical review. Journal of Nanofluids, 5(1), 1-22.

[10] Ginder, J. M. (1998). Behavior of magnetorheological fluids. MRS Bulletin, 23(8), 26-29.

[11] Bossis, G., Volkova, O., Lacis, S., and Meunier, A. (2002). Magnetorheology: fluids, structures and rheology. In: Odenbach, S. (Ed.) Ferrofluids. Lecture Notes in Physics (Vol. 594) (Springer, Berlin).

[12] de Vicente, J., Klingenberg, D. J., and Hidalgo-Álvarez, R. (2011). Magnetorheological fluids: a review. Soft Matter, 7(8), 3701-3710.

[13] Bica, I., Liu, Y. D., and Choi, H. J. (2013). Physical characteristics of magnetorheological suspensions and their applications. Journal of Industrial and Engineering Chemistry, 19(2), 394-406.

[14] Ahamed, R., Choi, S. B., and Ferdaus, M. M. (2018). A state of art on magneto-rheological materials and their potential applications. Journal of Intelligent Material Systems and Structures, 29(10), 2051-2095.

[15] Read, D. H., and Martin, J. E. (2010). Field-Structured Chemiresistors. Advanced Functional Materials, 20(10), 1577-1584.

[16] Liu, J., Flores, G. A., and Sheng, R. (2001). In-vitro investigation of blood embolization in cancer treatment using magnetorheological fluids. Journal of Magnetism and Magnetic Materials, 225(1-2), 209-217.

[17] Liu, Y. D., Fang, F. F., and Choi, H. J. (2011). Core–shell-structured silica-coated magnetic carbonyl iron microbead and its magnetorheology with anti-acidic characteristics. Colloid and Polymer Science, 289(11), 1295-1298.

[18] Carlson, J. D. (2001). What makes a good MR fluid? In: Proceedings of 8th International Conference on Electrorheological Fluids and Magnetorheological Suspensions (World Scientific, Singapore).

[19] Jang, I. B., Kim, H. B., Lee, J. Y., You, J. L., Choi, H. J., and Jhon, M. S. (2005). Role of organic coating on carbonyl iron suspended particles in magnetorheological fluids. Journal of Applied Physics, 97(10), 10Q912.

[20] Odenbach, S. (Ed.) Ferrofluids: magnetically controllable fluids and their applications. Lecture Notes in Physics (Vol. 594) (Springer, Berlin, 2008).

[21] Viota, J. L., de Vicente, J., Duran, J. D. G., and Delgado, A. V. (2005). Stabilization of magnetorheological suspensions by polyacrylic acid polymers. Journal of Colloid and Interface Science, 284(2), 527-541.

[22] Rabbani, Y., Ashtiani, M., and Hashemabadi, S. H. (2015). An experimental study on the effects of temperature and magnetic field strength on the magnetorheological fluid stability and MR effect. Soft Matter, 11(22), 4453-4460.

[23] Morillas, J. R., Bombard, A. J., and de Vicente, J. (2015). Preparation and characterization of magnetorheological fluids by dispersion of carbonyl iron microparticles in PAO/1-octanol. Smart Materials and Structures, 25(1), 015023.

[24] Rankin, P. J., Horvath, A. T., and Klingenberg, D. J. (1999). Magnetorheology in viscoplastic media. Rheologica Acta, 38(5), 471-477.

[25] de Vicente, J., López-López, M. T., González-Caballero, F., and Durán, J. D. G. (2003). Rheological study of the stabilization of magnetizable colloidal suspensions by addition of silica nanoparticles. Journal of Rheology, 47(5), 1093-1109.

[26] Lim, S. T., Cho, M. S., Jang, I. B., and Choi, H. J. (2004). Magnetorheological characterization of carbonyl iron based suspension stabilized by fumed silica. Journal of Magnetism and Magnetic Materials, 282, 170-173.

[27] Cantera, M. A., Behrooz, M., Gibson, R. F., and Gordaninejad, F. (2017). Modeling of magneto-mechanical response of magnetorheological elastomers (MRE) and MRE-based systems: a review. Smart Materials and Structures, 26(2), 023001.

[28] Foister, R. T. (1997). U.S. Patent No. 5667715. Washington, DC: U.S. Patent and Trademark Office.

[29] Trendler, A. M., and Böse, H. (2005). Influence of particle size on the rheological properties of magnetorheological suspensions. International Journal of Modern Physics B, 19(07n09), 1416-1422.

[30] Li, W. H., and Zhang, X. Z. (2010). A study of the magnetorheological effect of bimodal particle based magnetorheological elastomers. Smart Materials and Structures, 19(3), 035002.

[31] Rosenfeld, N., Wereley, N. M., Radakrishnan, R., and Sudarshan, T. S. (2002). Behavior of magnetorheological fluids utilizing nanopowder iron. International Journal of Modern Physics B, 16(17n18), 2392-2398.

[32] Chaudhuri, A., Wang, G., Wereley, N. M., Tasovksi, V., and Radhakrishnan, R. (2005). Substitution of micron by nanometer scale powders in magnetorheological fluids. International Journal of Modern Physics B, 19(07n09), 1374-1380.

[33] Bell, R. C., Karli, J. O., Vavreck, A. N., Zimmerman, D. T., Ngatu, G. T., and Wereley, N. M. (2008). Magnetorheology of submicron diameter iron microwires dispersed in silicone oil. Smart Materials and Structures, 17(1), 015028.

[34] Morillas, J. R., Carreón-González, E., and de Vicente, J. (2015). Effect of particle aspect ratio in magnetorheology. Smart Materials and Structures, 24(12), 125005.

[35] Seo, Y. P., Han, S., Choi, J., Takahara, A., Choi, H. J., and Seo, Y. (2018). Searching for a stable high-performance magnetorheological suspension. Advanced Materials, 30(42), 1704769.

[36] Cvek, M., Mrlik, M., Ilcikova, M., Plachy, T., Sedlacik, M., Mosnacek, J., and Pavlínek, V. (2015). A facile controllable coating of carbonyl iron particles with poly (glycidyl methacrylate): a tool for adjusting MR response and stability properties. Journal of Materials Chemistry C, 3(18), 4646-4656.

[37] Cvek, M., Mrlík, M., Mosnáček, J., Babayan, V., Kuceková, Z., Humpolíček, P., and Pavlínek, V. (2015). The chemical stability and cytotoxicity of carbonyl iron particles grafted with poly (glycidyl methacrylate) and the magnetorheological activity of their suspensions. RSC Advances, 5(89), 72816-72824.

[38] Jiang, W., Cao, Z., Gu, R., Ye, X., Jiang, C., and Gong, X. (2009). A simple route to synthesize ZnFe2O4 hollow spheres and their magnetorheological characteristics. Smart Materials and Structures, 18(12), 125013.

[39] Liu, Y. D., Hong, C. H., and Choi, H. J. (2012). Polymeric colloidal magnetic composite microspheres and their magneto-responsive characteristics. Macromolecular Research, 20(12), 1211-1218.

[40] Shahrivar, K., Carreón-González, E., Morillas, J. R., and de Vicente, J. (2017). Aggregation kinetics of carbonyl iron based magnetic suspensions in 2D. Soft Matter, 13(14), 2677-2685.

[41] Kordonsky, W. I., Prokhorov, I. V., Gorodkin, G., Jacobs, S. D., Puchebner, B., and Pietrowski, D. (1993). Magnetorheological finishing. Optics and Photonics News, 4(12), 16-17.

[42] Jha, S., and Jain, V. K. (2004). Design and development of the magnetorheological abrasive flow finishing (MRAFF) process. International Journal of Machine Tools and Manufacture, 44(10), 1019-1029.

[43] Kordonsky, W. I., and Shorey, A. (2007). Magnetorheological (MR) Jet Finishing Technology. Journal of Intelligent Material Systems and Structures, 18, 1127-1130.

[44] Wilson, B. T., and Klingenberg, D. J. (2017). A jamming-like mechanism of yield-stress increase caused by addition of nonmagnetizable particles to magnetorheological suspensions. Journal of Rheology, 61(4), 601-611.

[45] Skjeltorp, A. T. (1983). One-and two-dimensional crystallization of magnetic holes. Physical Review Letters, 51(25), 2306.

[46] Ramos, J., Klingenberg, D. J., Hidalgo-Álvarez, R., and de Vicente, J. (2011). Steady shear magnetorheology of inverse ferrofluids. Journal of Rheology, 55(1), 127-152.

[47] Erb, R. M., Son, H. S., Samanta, B., Rotello, V. M., and Yellen, B. B. (2009). Magnetic assembly of colloidal superstructures with multipole symmetry. Nature, 457(7232), 999.

[48] López-López, M. T., Zubarev, A. Y., and Bossis, G. (2010). Repulsive force between two attractive dipoles, mediated by nanoparticles inside a ferrofluid. Soft Matter, 6(18), 4346-4349.

[49] Susan-Resiga, D., and Vékás, L. (2017). Ferrofluid based composite fluids: Magnetorheological properties correlated by Mason and Casson numbers. Journal of Rheology, 61(3), 401-408.

[50] Bharti, B., and Velev, O. D. (2015). Assembly of reconfigurable colloidal structures by multidirectional field-induced interactions. Langmuir, 31(29), 7897-7908.

[51] Shahrivar, K., and de Vicente, J. (2013). Thermogelling magnetorheological fluids. Smart Materials and Structures, 23(2), 025012.

[52] Bibette, J. (1993). Monodisperse ferrofluid emulsions. Journal of Magnetism and Magnetic Materials, 122(1-3), 37-41.

[53] Cunha, L. H., Siqueira, I. R., Oliveira, T. F., and Ceniceros, H. D. (2018). Field-induced control of ferrofluid emulsion rheology and droplet break-up in shear flows. Physics of Fluids, 30(12), 122110.

[54] Philip, J., Jaykumar, T., Kalyanasundaram, P., and Raj, B. (2003). A tunable optical filter. Measurement Science and Technology, 14(8), 1289.

[55] Yang, J., Vereda, F., Morillas, J. R., and de Vicente, J. (2018). Ternary solid-ferrofluid-liquid magnetorheological fluids. Smart Materials and Structures, 27(7), 075017.

[56] Yang, J., Hu, Z., Yan, H., and Niu, F. (2019). Magnetorheological suspension with capillary network. Journal of Intelligent Material Systems and Structures, 30(12), 1850-1857.

[57] Ghaffari, A., Hashemabadi, S. H., and Ashtiani, M. (2015). A review on the simulation and modeling of magnetorheological fluids. Journal of Intelligent Material Systems and Structures, 26(8), 881-904.

[58] Rankin, P. J., Ginder, J. M., and Klingenberg, D. J. (1998). Electro-and magneto-rheology. Current Opinion in Colloid & Interface Science, 3(4), 373-381.

[59] Jones, T. B., and Saha, B. (1990). Nonlinear interactions of particles in chains. Journal of Applied Physics, 68(2), 404-410.

Chapter 2. Objectives

There are two major objectives behind this dissertation. First, to conceive a numerical method to reproduce the yield stress of real CMRFs. Second, to come up with a novel route to synthesize MRFs of larger yield stress and colloidal stability using bimodal suspensions.

Other specific objectives read as follow:

- To present a numerical method that is capable of predicting the yield stress of CMRFs when these are regarded as periodic arrangements of particles. The model has to take into account multibody, multipole and non-linear effects. Thus, it should be applicable regardless the particle concentration, the applied magnetic field strength or the magnetic constitutive behavior of the particles.
- To study how the particular particle arrangement influences the yield stress.
- To study how interparticle gaps, typically present due to particle roughness and oxidized layers, affect the yield stress.
- To explore the predictive behavior of the proposed model in the post-yield regime.
- To identify the shortcomings of the traditional methodologies in view of the present model.
- To validate the proposed method using experiments in the dilute and concentrated regimes as well as over linear and saturating field regimes.
- To validate the proposed method using a theoretical analysis on unbounded lattices of dipoles in the saturation regime.
- To develop a micromechanical model to compute shear and normal stresses in isolated chains of dipoles.
- To design, construct and validate (using experiments and numerical simulations) an improved magnetocell device capable to generate homogeneous and saturating fields.
- To measure the rheological properties of CMRFs in the saturation regime.
- To study (using experiments and numerical simulations) how particle coercivity affects the rheological behavior of MRFs based on particles in the single-multidomain limit.
- To measure the yielding behavior and kinetic stability of bimodal MRFs with a secondary particle population based on particles in the single-multidomain limit.
- To extend the proposed numerical method to these novel bimodal MRFs giving an explanation to their yielding behavior.
- To compare the performance (MR effect and long-time stability) of these novel bimodal MRFs with CMRFs and classic bimodal MRFs.

Chapter 3. Theoretical Overview

As it happens to any other kind of suspension, the macroscopic behavior of MRFs is intimately connected to the phenomena that take place at the microscale. In this chapter, the theoretical basis necessary to describe and understand the particle micro-configuration, its dynamics and how these two are related to the MRF collective response are summarized. In the following, MRFs will be treated as suspensions of N magnetic monodisperse spherical particles (diameter d) in a continuous phase occupying a total volume V.

The chapter is mainly focused on CMRFs. In these particular MRFs Brownian motion can be neglected. However, at the end of the chapter some comments about FFs are given. Brownian motion plays a key role in FFs.

3.1 Microscopic description of the dynamics

For any colloid or suspension (i.e. it does not have to be magnetic), the size of the dispersed particles is large enough to consider the carrying continuous phase as a fluid with a well-defined viscosity η_c. When a dispersed particle moves within the continuous viscous phase, for example under the action of an external force, it will distort the fluid velocity and pressure fields. Thus, the new velocity and pressure fields will drag neighboring particles hence changing their positions. With this in mind, any particle acts over its neighbors through a fluid-mediated force, the hydrodynamic one $\vec{F}_h$, that would not exist if the particles were in vacuum.

Generally speaking, hydrodynamic forces are not pairwise analytical interactions and hence they cannot be written solely in terms of the relative positions or dynamic state (i.e. velocity and/or acceleration) of the particles. Instead, since they are fluid-mediated forces, they depend on the dynamics of the surrounding fluid. Consequently, the fluid flow problem must be solved first.

In most cases, the carrier fluid is found to be incompressible (i.e. it is a liquid). Thus, the mass-balance (continuity) equation reduces to:

$$\nabla \cdot \vec{v} = 0 \tag{3.1}$$

where $\vec{v}$ is the fluid velocity field. In addition, if the fluid satisfies the Newton's viscosity law (i.e. the fluid is Newtonian), the hydrodynamic pressure p and velocity fields are coupled by the momentum-balance (Navier-Stokes) equation:

$$\frac{\partial \vec{v}}{\partial t} + (\vec{v} \cdot \nabla)\vec{v} = \frac{1}{\rho_c}\left(-\nabla p + \eta_c \nabla^2 \vec{v} + \vec{f}_{ext}\right) \tag{3.2}$$

where ρ_c is the fluid density and $\vec{f}_{ext}$ is the body force (per unit volume) exerted by any external agent. Furthermore, if the flow is not isothermal an additional energy-balance differential equation must be solved. However, for incompressible fluids this equation is uncoupled (i.e. it does not depend on velocity or pressure fields) and can be solved *a posteriori*. Nevertheless, through this dissertation temperature dependencies and heat transfer phenomena are not considered. As a result, the energy equation does not need to be solved.

In order for the problem to be well-posed, Eqs. (3.1) and (3.2) must be completed with boundary conditions. These strongly depend on the specific geometry under study. However, they typically consist in imposing uniform velocity fields as far-field conditions or periodicity (for unbounded media), a prescribed fluid velocity (the so-called no-slip condition) or a pressure on the confining walls (for bounded media).

Finally, the coupling between the carrier fluid and the particle movement is accounted for by imposing no-slip conditions in all particle surfaces, that is, $\vec{v}$ must meet the particle velocity on its surface:

$$\vec{v} = \vec{u} + \vec{\omega} \times \vec{r}_S \tag{3.3}$$

here $\vec{u}$ is the translational velocity of the particle, $\vec{\omega}$ is its angular velocity and $\vec{r}_S$ is a vector joining each point of the particle surface (where $\vec{v}$ is evaluated) with the particle center.

The particle velocity is given by Newton's second law:

$$m\frac{d\vec{u}}{dt} = \vec{F} = \vec{F}_h + \vec{F}_{nh} \tag{3.4}$$

$$\tilde{I}\frac{d\vec{\omega}}{dt} = \vec{T} = \vec{T}_h + \vec{T}_{nh} \tag{3.5}$$

where m is the particle mass, $\tilde{I}$ is its inertia tensor and $\vec{F}$ $(\vec{T})$ is the total force (torque) acting over the particle. This force (torque) can be split into the hydrodynamic force (torque) $\vec{F}_h$ $(\vec{T}_h)$ plus contributions coming from non-hydrodynamic effects $\vec{F}_{nh}$ $(\vec{T}_{nh})$, that is, all those forces (torques) that the particles would experience if they were not immersed in a fluid.

Regarding the hydrodynamic interaction, the total force exerted by the fluid over the particle is given by the integral, over the particle surface S_p, of the fluid total stress tensor $\tilde{t}$:

$$\tilde{t} = -p\tilde{\delta} + \eta_c 2\tilde{E} \tag{3.6}$$

where $\tilde{\delta}$ is the second-order identity tensor and $\tilde{E}$ is the strain rate tensor which can be written in terms of the flow kinematics (velocity field) as $\tilde{E} = [\nabla\vec{v} + (\nabla\vec{v})^T]/2$. Therefore:

$$\vec{F}_h = \int_{S_p} \vec{t}_n ds \equiv \int_{S_p} \tilde{t} \cdot \hat{n} ds \tag{3.7}$$

here $\hat{n}$ is the surface normal vector pointing to the fluid. Due to the continuous nature of the fluid, this does not only exert a punctual force over the particle but a continuous distribution over its surface. As a consequence, the hydrodynamic interaction is not reduced only to a total force; the fluid also exerts a moment. In its more general form, the first moment of the hydrodynamic force can be written as follows:

$$\widetilde{M} = \int_{S_p} \widetilde{t_n r_S} ds \tag{3.8}$$

where the symbol $\widetilde{t_n r_S}$ is understood as the dyadic product of the vectors $\vec{t}_n$ and $\vec{r}_S$ (note that given two vectors $\vec{a}$ and $\vec{b}$, the second-order tensor $\widetilde{ab}$ would read in index notation $a_i b_j$). However, in fluid dynamics it is more useful to split $\widetilde{M}$ in its symmetric and antisymmetric parts. The former part is called the stresslet:

$$\tilde{S} = \frac{1}{2}\left(\widetilde{M} + \widetilde{M}^T\right) \tag{3.9}$$

and it does not have any effect on the dynamics of rigid particles (see below). On the contrary, it can be shown that the antisymmetric part $\tilde{A} = \left(\widetilde{M} - \widetilde{M}^T\right)/2$ is just the torque due to $\vec{F}_h$ [1]:

$$\vec{T}_h = \int_{S_p} \vec{r}_S \times \vec{t}_n ds \tag{3.10}$$

and thus, responsible for the particle rotation.

As it can be seen, the coupling between particle and fluid motion is done in both directions. The velocity of the fluid $\vec{v}$ depends on the particle translational $\vec{u}$ and angular $\vec{\omega}$ velocities through the no-slip condition (Eq. (3.3)) and the particle velocities depend on the fluid velocity through the hydrodynamic force and torque (Eqs. (3.7) and (3.10)) that accelerates/decelerates the particles.

Equations (3.1)-(3.10) govern the dynamics of the (Newtonian) continuous and (solid) dispersed phases using first principles. However the resultant differential equation system is extremely complicated to solve. Firstly, just regarding the fluid dynamics, Navier-Stokes equation is a nonlinear partial differential equation and approximations are needed to be solved. Secondly, a many-body problem with nonlinear and irreversible features results when a dispersed phase is incorporated to the fluid. In addition, due to the absence of Brownian motion, the problem becomes deterministic what requires tracking the explicit movement of a vast number of particles precluding any analytical treatment.

Tackling the problem from a numerical point of view is neither easy. Most common Computational Fluid Dynamics (CFD) simulations are mesh-based techniques where the fluid domain has to be discretized (in mesh elements). In this way, the governing partial differential equations (Eqs. (3.1) and (3.2)) can be transformed in algebraic ones to be solved by a computer. However, in MRFs problems, the fluid domain continuously evolves when the particles change their position. Consequently, at every time step both the computational domain and the mesh should adapt to the new particle configuration. Furthermore, in order to evaluate the time derivative in Eq. (3.2) at the present time step, the velocity field in the previous time step has to be projected onto the new mesh (by interpolating the velocity field) [2].

Taking this into consideration together with the fact that: (i) the mesh has to be dense enough around every particle (to properly compute the force and torque acting on them), (ii) the great difference between the involved lengths scales (in a CMRF, the typical particle diameter is around 1 μm but the sample size is usually around 0.3-1 mm) and (iii) the large number of unknowns (pressure plus three velocity components) one can see that solving Eqs. (3.1)-(3.10) is not straight forward and some approximations are required.

3.1.1 Stokes approximation

In many cases, the study of MRFs is done under conditions where both fluid and particle inertia is negligible in comparison to the viscous dissipation at both sample and particle length scales. Therefore, Navier-Stokes equation is reduced to the Stokes equation:

$$\nabla p = \eta_c \nabla^2 \vec{v} \tag{3.11}$$

In this expression, external body forces are assumed to be conservative and therefore can be included in the pressure term (LHS). Consequently, p will not stand for the absolute pressure and derived forces exerted by the fluid (see Eqs. (3.6) and (3.7)) will not account for the effects of that body forces. As it can be seen, Stokes equation is linear and it does not contain any explicit dependence on the time. Consequently, although a new mesh would be required at each time step, the flow field in the previous steps is not needed. It only depends on the current particle configuration and particle velocities (that are introduced as boundary conditions, that is, known values from previous step).

Although the use of Eq. (3.11) instead of Eq. (3.2) allows to get rid of projecting and time deriving the flow field, solving the MRF dynamics by mesh-based CFD techniques still implies a large computational effort due to the large number of nodes present in the meshes. During the evolution of the system the highest velocity gradients, and with them the highest forces (see Eqs. (3.6) and (3.7)), are localized in the gaps between solid surfaces and confining walls (if apply). In order to accurately resolve the velocity gradients, these gaps should be densely meshed increasing the computational cost. The situation is aggravated with the number of particles and geometry complexity restricting mesh-based CFD simulations to very simple systems with a small number (tens) of particles and/or 2D domains [3-5].

This problem can be partially overcome using techniques that do not require adaptive meshes such as the Lattice Boltzmann Method (LBM) [6,7] where an initial mesh can be defined without further rearrangement because the flow field is only solved on those nodes that are not occupied by the particles. Notwithstanding, a dense mesh is still needed to solve plausible field gradients. Finally, mesh-free methods such as Smooth Particle Hydrodynamics (SPH) [8,9] or Dissipative Particle Dynamics (DPD) [10,11] have also been used to study MRFs. The basic difference with respect to mesh-based CFD methods lies on regarding the continuous phase not as a continuum but as an ensemble of discrete 'fluid elements' at the mesoscale. These interact with each other in a way that, once time- and space-averaged, are able to reproduce the fluid macroscopic behavior. Nevertheless, these mesh-free methods base their accuracy on the 'fluid element' size, that is, the smaller the 'fluid element' the greater the resolution of the flow field around the particles. Thus, although they are more versatile and some computational effort can be saved, the necessity of a very fine discretization (of the continuous phase instead of the computational domain) to resolve the flow problem does not make them the best choice to deal with MRFs neither.

From the previous discussion it seems that solving explicitly the flow field around the particulate phase is an unaffordable task from a computational point of view. To circumvent this problem, other methods have been proposed taking advantage of the linear properties of Stokes equation. As a first approximation, any flow field, regardless of its complexity, can be expressed around a given point $\vec{r}_0$ by its Taylor series:

$$\vec{v}(\vec{r}) = \vec{V}_0 + \tilde{E}_0 \cdot (\vec{r} - \vec{r}_0) + \vec{\Omega}_0 \times (\vec{r} - \vec{r}_0) \tag{3.12}$$

where $\vec{\Omega} = (\nabla \times \vec{v})/2$ and it should be understood that the velocity $\vec{V}_0$, the shear rate tensor $\tilde{E}_0$ and the vorticity $\vec{\Omega}_0$ are evaluated on $\vec{r}_0$. As it can be seen, according to Eq. (3.12) any flow can be approximated, till first order, as the sum of simpler flow fields (Fig. 3.1): a homogeneous flow field $\vec{V}_0$, a pure straining flow field $\tilde{E}_0 \cdot (\vec{r} - \vec{r}_0)$ and a pure rotational flow field $\vec{\Omega}_0 \times (\vec{r} - \vec{r}_0)$.

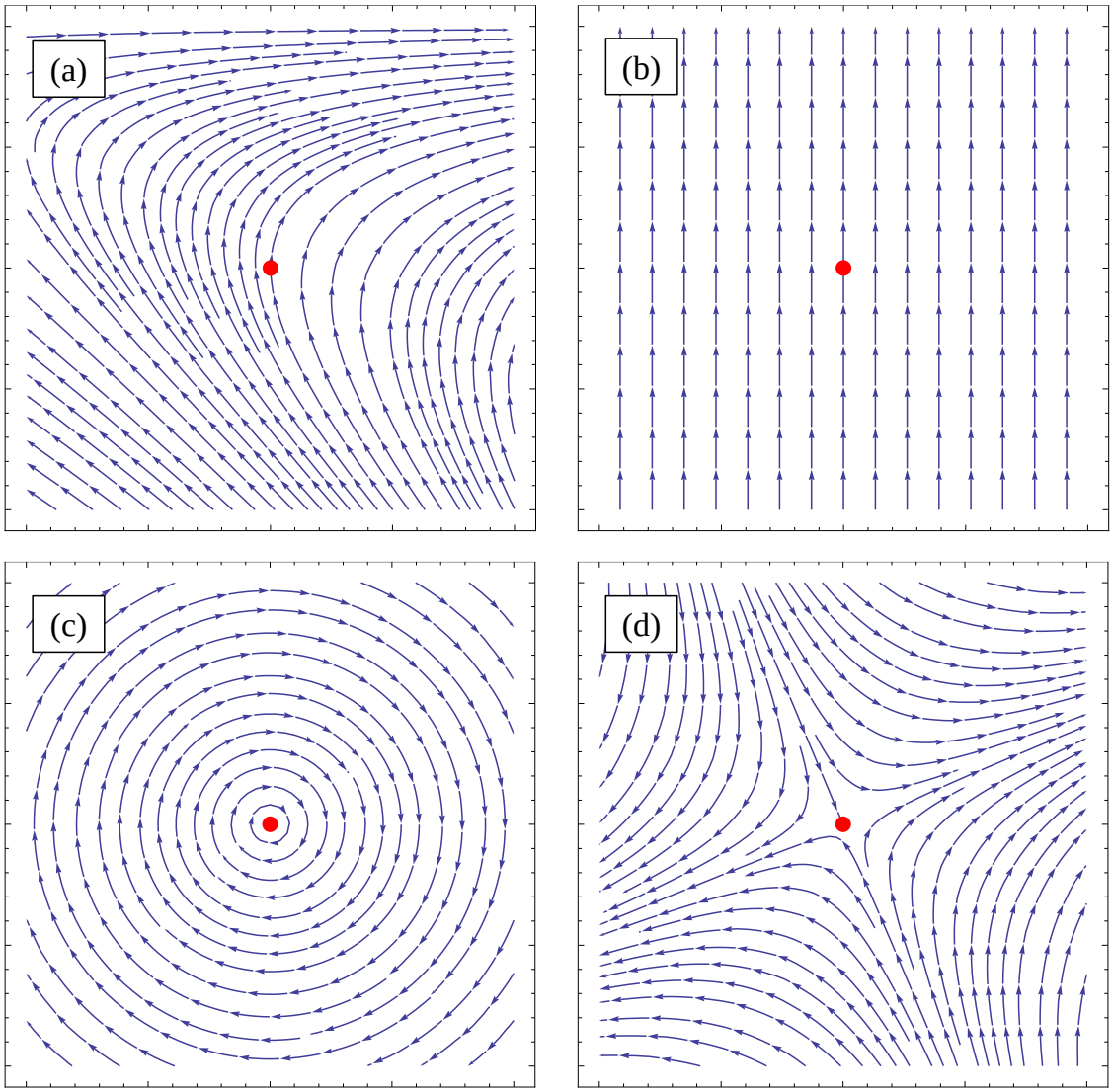

Figure 3.1: Any flow field (a) around a given point (red dot) can be decomposed in three simpler flows: a homogeneous component (b), a pure rotational component (c) and a pure straining component (d).

Linearity implies that the effect of the total flow field over the immersed particles can be also split in the individual effects that each of the previous simpler flow fields have on the particles separately. In this way, for any flow field, one can evaluate the associated total hydrodynamic force/torque over a particle by addition of the corresponding force/torque suffered by the particle under a homogeneous, pure rotational and pure straining flow.

With this, the problem reduces to solve the total flow field (Eqs. (3.1) and (3.11) together with the boundary condition (3.3)) around a spherical particle under these three simpler flows. It can be shown that, applying Eqs. (3.7) and (3.10) at the particles surface,

hydrodynamic force and torque over the particle, till first order, can be written as follows [1]:

$$\vec{F}_h = 3\pi\eta_c d\left(\vec{\mathrm{V}} - \vec{u}\right) \tag{3.13}$$

$$\vec{T}_h = \pi\eta_c d^3\left(\vec{\Omega} - \vec{\omega}\right) \tag{3.14}$$

Equation (3.13) is commonly also known as Stokes' drag law. Several points can be highlighted from Eqs. (3.13) and (3.14):

1. The hydrodynamic force (torque) comes only from the homogeneous (pure rotational) flow field, that is, a spherical particle immersed in a homogeneous (pure rotational) flow does not experience any hydrodynamic torque (force).
2. The pure straining flow does not exert any force or torque over the particle.
3. The flow field and particle movement are supposed to be non-inertial. Thus both force and torque can be expressed as a function of the relative velocity, that is, it is always possible to find a reference frame where the particle or the fluid are quiescent.
4. A linear dependence exists between the force (torque) and the translational (rotational) velocity because Stokes equation is linear.

From the previous discussion, it could be inferred that the pure straining flow is not affected by the presence of the particles as no net force or torque are developed. However, this result arises from the spatial symmetry of the straining flow field around a spherical particle. Actually, particles are really under a stresslet only due to the pure straining flow component:

$$\tilde{S} = \frac{5}{6}\pi\eta_c d^3\tilde{E} \tag{3.15}$$

but, as solid bodies, they can bear any stresslet without straining ($\tilde{E} = 0$ inside the particles), and consequently $\tilde{S}$ does not play any role in their movement. Note also that, because of this, the stresslet in Eq. (3.15) is not expressed in terms of the relative strain field as it happens for the force and the torque (Eqs. (3.13) and (3.14)).

Till now, it has only been considered that the continuous phase has a negligible inertia. Taking into consideration the small size of the particles it can also be supposed that the particles are inertialess, and hence, the total force, $\vec{F}$, and torque, $\vec{T}$, acting on them must be zero. According to Eqs. (3.4) and (3.5), this implies that the hydrodynamic force/torque is always balanced by the non-hydrodynamic forces/torques: $\vec{F}_h = -\vec{F}_{nh}$ and $\vec{T}_h = -\vec{T}_{nh}$. Introducing these conditions in Eqs. (3.13)-(3.15) yields:

$$\vec{F}_{nh} = 3\pi\eta_c d\left(\vec{u} - \vec{\mathrm{V}}\right) \tag{3.16}$$

$$\vec{T}_{nh} = \pi\eta_c d^3\left(\vec{\omega} - \vec{\Omega}\right) \tag{3.17}$$

$$\tilde{S} = \frac{5}{6}\pi\eta_c d^3\tilde{E} \tag{3.18}$$

Note that in this new set of Eqs. (3.16)-(3.18), force and torque values do not depend on the kinematic state of the continuous phase as it happens in Eqs. (3.13)-(3.15). Now the forces and torques are the non-hydrodynamic ones that usually depend on the particles positions.

Equations (3.16)-(3.18) govern the particle dynamics in the suspension (whenever inertia is neglected) but it should be born in mind that, in these expressions, the quantities $\vec{\mathrm{V}}$, $\vec{\Omega}$ and $\tilde{E}$ are not simply constants. They contain the homogeneous, pure rotational and pure straining parts of the total flow at the particle position, that is, the flow externally imposed $\left(\vec{\mathrm{V}}_\infty, \vec{\Omega}_\infty, \tilde{E}_\infty\right)$ plus the perturbation flow field created by each dispersed particle $\left(\vec{\mathrm{V}}_\alpha, \vec{\Omega}_\alpha, \tilde{E}_\alpha\right)$ at that position. Focusing only in the translational motion, it is clear that the homogeneous part of the flow field created by particle α, $\vec{\mathrm{V}}_\alpha$, will depend on its translational velocity and non-hydrodynamic force, $\vec{\mathrm{V}}_\alpha = \vec{f}_\alpha\left(\vec{u}_\alpha, \vec{F}_{nh,\alpha}, \cdots\right)$.

However, if particle α is also rotating at $\vec{\omega}_\alpha$ and suffering a non-hydrodynamic torque $\vec{T}_{nh,\alpha}$, it will create another flow field that will have homogeneous, pure rotation and pure straining components, all of them dependent on $\vec{\omega}_\alpha$ and $\vec{T}_{nh,\alpha}$. In the same sense, if the particle α is under a straining flow, it will create another flow field with its corresponding components that depends, in this case, on the stresslet $\tilde{S}_\alpha$.

Therefore, when all homogeneous components are joined together, it yields $\vec{\mathrm{V}}_\alpha = \vec{f}_\alpha\left(\vec{u}_\alpha, \vec{F}_{nh,\alpha}, \vec{\omega}_\alpha, \vec{T}_{nh,\alpha}, \tilde{S}_\alpha\right)$ with the main advantage that the previous dependence is linear in all variables due to Stokes flow properties. Now extending the previous reasoning to rotational and straining components induced by the rest of the particles we arrive to:

$$\vec{\mathrm{V}} = \vec{\mathrm{V}}_\infty + \sum_\alpha \vec{f}_\alpha \tag{3.19a}$$

$$\vec{\Omega} = \vec{\Omega}_\infty + \sum_\alpha \vec{g}_\alpha \tag{3.19b}$$

$$\tilde{E} = \tilde{E}_\infty + \sum_\alpha \tilde{h}_\alpha \tag{3.19c}$$

Since each function $\left(\vec{f}_\alpha, \vec{g}_\alpha, \tilde{h}_\alpha\right)$ is linear in its variables, when they are introduced in Eqs. (3.16)-(3.18) they can be rearranged so that the particle dynamics governing equations can be written as a matrix equation:

$$\begin{pmatrix} \vec{\boldsymbol{F}}_{nh} \\ \vec{\boldsymbol{T}}_{nh} \\ \tilde{\boldsymbol{S}} \end{pmatrix} = \begin{pmatrix} \mathcal{R}_{Fu} & \mathcal{R}_{F\omega} & \mathcal{R}_{FE} \\ \mathcal{R}_{Tu} & \mathcal{R}_{T\omega} & \mathcal{R}_{TE} \\ \mathcal{R}_{Su} & \mathcal{R}_{S\omega} & \mathcal{R}_{SE} \end{pmatrix} \cdot \begin{pmatrix} \vec{\boldsymbol{u}} - \vec{\mathbf{V}}_\infty \\ \vec{\boldsymbol{\omega}} - \vec{\boldsymbol{\Omega}}_\infty \\ \tilde{\boldsymbol{E}}_\infty \end{pmatrix} = \widetilde{\boldsymbol{\mathcal{R}}} \cdot \begin{pmatrix} \vec{\boldsymbol{u}} - \vec{\mathbf{V}}_\infty \\ \vec{\boldsymbol{\omega}} - \vec{\boldsymbol{\Omega}}_\infty \\ \tilde{\boldsymbol{E}}_\infty \end{pmatrix} \tag{3.20}$$

where the bold symbols consist of the corresponding magnitude of each particle appended one after another, that is, $\vec{\boldsymbol{F}}_{nh} = \left(\vec{F}_{nh1}, \vec{F}_{nh2}, \cdots, \vec{F}_{nhN}\right)$. Note that with this notation, each element of $\widetilde{\boldsymbol{\mathcal{R}}}$ is not a scalar but a tensor of the proper order to satisfy the linear relationship between the dynamic and kinematic variables. The terms $\vec{\mathrm{V}}_\infty$, $\vec{\Omega}_\infty$ and $\tilde{E}_\infty$ are usually known because they are imposed macroscopically, hence the solution is expressed in terms of the relative velocities.

$\widetilde{\boldsymbol{\mathcal{R}}}$ is known as the grand resistance matrix. It consists of the proper combination of the $\vec{f}_\alpha$, $\vec{g}_\alpha$ and $\tilde{h}_\alpha$ functions to relate the particles kinematics (translational and rotational velocities) and fluid strain to the dynamics acting over a given particle. Importantly, both $\widetilde{\boldsymbol{\mathcal{R}}}$ [12] and the LHS of Eq. (3.20) only depend on the relative position of the particles,

therefore the kinematics of each particle can be obtained just evaluating both terms in the current position of the particles and computing $\widetilde{\boldsymbol{\mathcal{R}}}^{-1}$. Once the velocities are solved, the next particle configuration can be obtained by integration over time. This scheme constitutes the basis of the Stokesian Dynamics (SD) technique [13].

As it can be seen, Stokes flow linearity allowed the construction of a matrix system to solve the particle dynamics but nothing has been said about how to compute the elements within $\widetilde{\boldsymbol{\mathcal{R}}}$. Frequently, these are obtained by computing the flow field around a pair of particles that is subjected to the three aforementioned components of a general flow: homogeneous, pure rotational and pure straining. Depending on the interparticle distance this total flow field is solved using a reflection/perturbation method (large distances above $2d$), the lubrication approximation (short distances, from $1d$ to $1.01d$) or tabulated values coming from simple CFD simulations for intermediate interparticle distances [14,15]. Note that according to these methods, the elements within $\widetilde{\boldsymbol{\mathcal{R}}}$ are really accounting for two-particle interactions only. Nevertheless, it is stated that during $\widetilde{\boldsymbol{\mathcal{R}}}^{-1}$ computation, these elements are combined and thus many-body interactions are finally considered [13].

It is not the scope of this dissertation to find the particular expressions for the elements within $\widetilde{\boldsymbol{\mathcal{R}}}$. Nevertheless, it is worth mentioning two of their basic features. On the one hand, at long interparticle distances $R_{\alpha\beta}$, the flow field and, with it, the hydrodynamic force induced by particle β at the position of particle α scales as $\propto R_{\alpha\beta}^{-1}$. Clearly, this is a long ranged force that obliges to consider force contributions even from particles that are widely separated [16].

On the other hand, at short $R_{\alpha\beta}$, the main hydrodynamic force is due to the lubrication. For the case of two particles, approaching at a constant velocity U along their common axis, this force is repulsive and scales as $\propto U/\left(R_{\alpha\beta}-d\right)$. As it can be seen, the lubrication force diverges with the surface-to-surface distance meaning that particle contacts take an infinite time to happen. Actually, contacts may occur in real systems because of surface roughness and the existence of non-hydrodynamic interactions.

The computation of $\widetilde{\boldsymbol{\mathcal{R}}}$ is a tedious process. However, it can be implemented numerically without a high computational cost since it starts from already known/tabulated functions. Moreover, the resolution of particle dynamics using SD does not imply any approximations (whenever inertia can be neglected) regarding hydrodynamic interactions but, at the same time, does not require explicitly solving the continuous phase dynamics. As a result, it becomes a molecular-like treatment of the problem where only particle-particle interactions (dependent only on the relative positions) are considered.

Although molecular-like SD simulations require a smaller computational effort in comparison to mesh-based CFD ones, they are still computationally expensive as a dense matrix (remember that hydrodynamic interactions are long-ranged and thus couple the motion of all dispersed particles regardless their separation) inversion is needed for each time step. Looking at Eq. (3.20), it can be seen that in order to follow the system evolution with time, it is necessary to solve only the two first rows concerning translational and rotational velocities of the particles. Therefore, from a computational point of view, the more expensive required step is to invert a matrix of dimension $6N \times 6N$, where N is the number of simulated particles and 6 refers to the total number of components of the force and torque together. Note that the last row in Eq. (3.20) concerning stresslets is not needed if only the particle configuration is pursued. However, it will be shown in Sec. 3.4 that

stresslets are fundamental to understand sample rheology. Nevertheless, their computation can be seen as a separated problem once particle velocities are solved.

Dense matrix inversion constitutes a strong limitation to the implementation of SD simulations to study MRF systems with only hundreds of particles, usually in 2D [17,18]. If SD are applied outside these borders, some kind of approximations in the hydrodynamics interactions, neglecting their short or long range effects, for example, are needed [19-22].

As commented above, available methodologies described so far to solve hydrodynamics (based on Stokes or Navier-Stokes equations) are too expensive from a computational point of view to model MRFs. This is essentially because the number of particles explicitly simulated to properly resemble real systems and do averages is typically above 1000. Thus, most frequently used approaches aim to solve particle and fluid dynamics separately, designing (or not) a coupling scheme to obtain consistent solutions for the whole system. In these approximations, particles move in the same spatial domain occupied by the fluid, that is, there is not a volume exclusion and particles do not displace the surrounding fluid during their motion.

Particle dynamics are governed again by Newton's second law (Eq. (3.4)), usually neglecting rotational degrees of freedom. Although different expressions can be taken in order to consider neighboring particles, inertial flow and other effects on the hydrodynamic force [23,24], the latter is typically given by the Stokes' drag law:

$$\vec{F}_S = 3\pi\eta_c d(\vec{u} - \vec{v}) \tag{3.21}$$

where $\vec{v}$ is the fluid velocity at the particle position. This velocity together with the pressure fields are computed by solving continuity equation (Eq. (3.1)) and a modified Navier-Stokes as follows:

$$\frac{\partial \vec{v}}{\partial t} + (\vec{v} \cdot \nabla)\vec{v} = \frac{1}{\rho_c}\left(-\nabla p + \eta_c \nabla^2 \vec{v} + \vec{f}_{ext} + \vec{f}_c\right) \tag{3.22}$$

Equation (3.22) differs from Eq. (3.2) in the term $\vec{f}_c$. It stands for the force exerted by all the immersed particles over the fluid and is the responsible for the coupling between particle dynamics and fluid flow problems [25]. In order to satisfy Newton's third law we have:

$$\vec{f}_c = -\frac{1}{V_c}\sum_{\alpha} \vec{F}_{S,\alpha} \tag{3.23}$$

where V_c is the fluid unit volume and the summation on α runs over those particles inside V_c. This scheme (usually known as two-way coupling) roughly considers the effect of a particle on the fluid that surrounds it reducing/increasing the fluid velocity to adjust it to the particle one. The many-body problem of particle dynamics is usually solved through molecular-like simulations (such as Molecular Dynamics or Discrete Element Method, see Chapter 4) while the flow problem is addressed again using FEM (in this case, V_c in Eq. (3.23) is the mesh element volume) or SPH (V_c would be the cutoff distance related to each 'fluid particle'), for example.

The two-way coupling scheme is capable to deal with 3D systems containing a large number of particles ($N \sim 1000$), but it can take a considerable computation time. In addition, through this section it has not been addressed other factors that could influence

the particle dynamics and that may increase the required computational effort. Examples of these factors can be confining wall effects [26,27], complex flow geometries [28], non-spherical particles [29-31], rotational degrees of freedom [32,33], polydispersity [34-36] or complex non-hydrodynamic interactions that do not have to be pairwise [37-39]. Thus, in order to include and study these new features but still keeping a reasonable computational time and cost, a final approximation is commonly used. It is the one-way coupling, where $\vec{f}_c = 0$. This scheme completely disconnects particle and fluid dynamics. Both problems are solved independently: the flow field is solved first without any immersed particle and then it is introduced in the particle dynamics problem through Stokes drag law.

3.2 Magnetic interactions

In Sec. 3.1 it has been shown that, at least theoretically, it is possible to compute particle trajectories in a CMRF as long as the non-hydrodynamic forces acting over all dispersed particles are known at each time step. In this section only magnetostatic forces are addressed because they are the most relevant ones in magnetorheology. It will be seen that, in order to exactly compute the magnetostatic forces, it is not only needed the particle spatial configuration but also how the total magnetic field, flux and magnetization distribute in the whole system.

Ultimately, these distributions will depend on the magnetic behavior of the dispersed particles, and therefore on the particle material and size. Magnetic particles used in the formulation of CMRFs are usually made of (soft) ferro- or ferri-magnetic materials such as iron (and its oxidized derivatives: magnetite and maghemite), nickel, cobalt or their alloys. The reason for this is that these materials exhibit a reasonably large magnetization under moderate magnetic fields (e.g. for a field strength of ∼100 kA/m, magnetization reaches values of the order of 1000 kA/m (iron), 300 kA/m (nickel) and 100 kA/m (cobalt) [40]).

Regarding their size, particles within a CMRF have a typical diameter of the order of microns (above 1 μm). From an atomistic perspective, these can be seen as multidomain magnetic bodies: each particle can be divided in regions (domains), separated by Bloch walls, where the atomic spins are strongly coupled, all pointing in the same direction. As a consequence, in every domain there is a net magnetization. In the absence of an external magnetic field, the direction related to each domain within the particle is randomly distributed yielding a null particle magnetization.

When an external magnetic field $\vec{H}_{ext}$ is applied (acting as a homogenous background field), domains initially aligned, or almost aligned, with the field start to grow at the expense of misaligned domains. As a result, the net particle magnetization becomes non-zero. Then, as $\vec{H}_{ext}$ is further increased, favorable domains grow larger and magnetization increases till all atomic spins are aligned with $\vec{H}_{ext}$. At this moment the particle is fully saturated, that is, increasing $\vec{H}_{ext}$ does not result in a higher magnetization level [41].

The atomistic description of the particle magnetization mechanism is an extraordinarily complex task that is out the scope this dissertation. Fortunately, this is not necessary as all these microscopic events involved can be accounted for working with ‘macroscopic’ magnitudes (understood at the particle scale). In this sense, the previous discussion can be simplified defining the particle magnetization as a function of the total magnetic field

evaluated inside the particle (the so-called internal field $\vec{H}_{int}$) with some phenomenological features [42]: (i) it should saturate to a constant value M_S at high magnetic field, (ii) it should increase linearly (slope of $\mu_i - 1$) at low magnetic fields, (iii) it should be zero in the absence of the field and (iv) it should be collinear with the magnetic field. Note that previous description captures a non-linear response and assumes the absence of coercivity or anisotropy.

There are several models for the magnetization-field constitutive equation. Through this dissertation, the Fröhlich-Kennelly model was chosen as it is commonly done in the literature:

$$\vec{M} = (\mu_r(H_{int}) - 1)\vec{H}_{int} = \frac{(\mu_i - 1)M_S}{M_S + (\mu_i - 1)H_{int}}\vec{H}_{int} \tag{3.24}$$

where $\mu_r(H_{int})$ is the scalar and field-dependent relative permeability while M_S and μ_i (saturation magnetization and initial magnetic permeability, respectively) are the two parameters of the model. It must be noted again that $\vec{H}_{int}$ stands for the total magnetic field inside the particle and this one does not meet with $\vec{H}_{ext}$.

Generally speaking, if a finite magnetic body is magnetized, its induced magnetization will act as a source of a secondary magnetic field $\vec{H}_{sec}$ defined over the whole space, inside and outside the body [41]:

$$\vec{H}_{sec} = \frac{1}{4\pi}\int_{V_p} \rho_M \frac{\vec{R}}{R^3} dv + \frac{1}{4\pi}\int_{S_p} \varrho_M \frac{\vec{R}}{R^3} ds \tag{3.25}$$

where the first (second) integral is done over the body volume (surface), $\vec{R}$ is position vector of the point where $\vec{H}_{sec}$ is computed, relative to the considered differential element of the magnetic body during integration; $\rho_M = \nabla \cdot \vec{M}$ is the magnetization charge density, $\varrho_M = \hat{n} \cdot \vec{M}$ is the magnetization charge surface density and $\hat{n}$ is the normal vector of the body surface (pointing outwards).

Clearly, $\vec{H}_{sec}$ depends on its source magnetization (how it is distributed in the magnetic body), on the body shape as well as on the evaluation point (it is not homogeneous). Traditionally, when $\vec{H}_{sec}$ is evaluated inside its own source body it becomes to be known as the demagnetization field $\vec{H}_{de}$ since it has opposite direction to its source magnetization. In the following we will keep this convention, saving the name $\vec{H}_{sec}$ only for the secondary field created by the body outside it.

Thus, for the case of an isolated body, it is easy to identify the only two contributions to the internal field as $\vec{H}_{int} = \vec{H}_{ext} + \vec{H}_{de}$. In Fig. 3.2, the relative permeability for an isolated magnetizable spherical particle $(\vec{H}_{de} = -\vec{M}/3)$ is shown as a function of H_{int} and H_{ext}. As it can be seen, it undergoes three differentiated regimes (the boundaries indicated by illustrative vertical lines): a linear regime at low fields where $\mu_r(H_{int}) \to \mu_i$, a saturation regime at high magnetic fields where $\mu_r(H_{int}) \to 1$ and a transition regime connecting previous values, which is responsible for the non-linear behavior. These three regimes will appear throughout this dissertation as the magnetic response of the dispersed particles is intimately connected to the rheological response of the CMRFs.

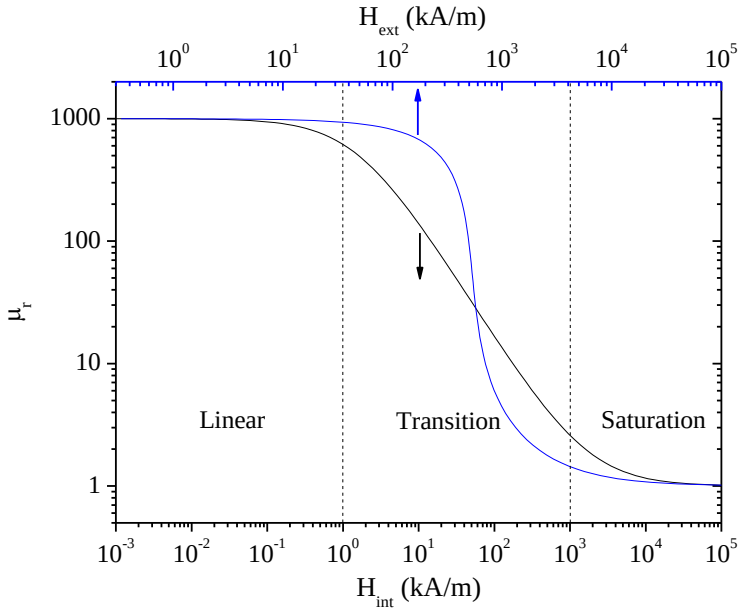

Figure 3.2: Relative permeability for an isolated magnetizable spherical particle as a function of the internal field H_{int} and the external one H_{ext}. The Fröhlich-Kennelly model is assumed with $\mu_i = 1000$ and $M_S = 1600$ kA/m. These parameters correspond to the carbonyl iron typically used in magnetorheology [43].

Results shown in Fig. 3.2 can be computed easily because only an isolated particle has been regarded. On its part, CMRFs are constituted by a large number of magnetized particles therefore, a particle β in a given CMRF will be exposed to a local field that is the sum of $\vec{H}_{ext}$ plus all the non-homogenous secondary fields created by the rest of the magnetized particles $\vec{H}_{sec,\alpha}$: $\vec{H}_{loc} = \vec{H}_{ext} + \sum_\alpha \vec{H}_{sec,\alpha}$. Bearing this in mind, the internal field of particle β is given now, as a function of the local field instead of the external one, by $\vec{H}_{int,\beta} = \vec{H}_{loc} + \vec{H}_{de,\beta}$ with $\vec{H}_{loc}$ evaluated at the particle β position. At this point two main problems appear. Firstly, the calculation of $\vec{H}_{sec,\alpha}$ due to the rest of dispersed particles is a hard task as it depends on the corresponding $\vec{H}_{int,\alpha}$ that, at the same time, depends on $\vec{H}_{loc}$ but now evaluated on the rest of α particle positions and thus, containing the initially pursued $\vec{H}_{int,\beta}$. Secondly and more severe, as any of the CMRF particles are not under a homogeneous field, their demagnetization fields will not fulfill $\vec{H}_{de} = -\vec{M}/3$ as in the case of an isolated particle. Indeed, the only thing that can be said is that relationship between both magnitudes has to fulfill Eq. (3.25) when it is evaluated inside each particle.

As it can be seen, the computation of the magnetic field inside a CMRF is not trivial and requires a self-consistent approach. Nevertheless, from first principles, the total field $\vec{H}$ at any point can be obtained from Maxwell equations [44]:

$$\nabla \cdot \vec{D} = \rho \tag{3.26}$$

$$\nabla \times \vec{E} = -\frac{\partial \vec{B}}{\partial t} \tag{3.27}$$

$$\nabla \cdot \vec{B} = 0 \tag{3.28}$$

$$\nabla \times \vec{H} = \vec{j} + \frac{\partial \vec{D}}{\partial t} \tag{3.29}$$

where $\vec{D}$ and $\vec{B}$ are the electric and magnetic field flux densities respectively, $\vec{E}$ is the electric field, ρ is the free charge density and $\vec{j}$ is the free current density. As it is known, fields and flux densities are not independent from each other but they are related through the constitutive equations:

$$\vec{D} = \varepsilon_0 \vec{E} + \vec{P} \tag{3.30}$$

$$\vec{B} = \mu_0 (\vec{H} + \vec{M}) \tag{3.31}$$

being ε_0 and μ_0 the vacuum permittivity and permeability respectively, $\vec{P}$ the material polarization and $\vec{M}$ the previously introduced material magnetization (for example, given by Eq. (3.24)). Typically, in CMRFs, the field changes in time are very slow allowing a quasi-static study. In addition, there are not free charges nor currents thus, Eqs. (3.26)-(3.29) are reduced to:

$$\nabla \cdot (\varepsilon_0 \vec{E} + \vec{P}) = 0 \tag{3.32}$$

$$\vec{E} = -\nabla V_e \tag{3.33}$$

$$\nabla \cdot (\vec{H} + \vec{M}) = 0 \tag{3.34}$$

$$\vec{H} = -\nabla V_m \tag{3.35}$$

where V_e and V_m are scalar electric and magnetic potentials. As it can be seen $\vec{E}$ is fully decoupled from $\vec{H}$, and, since the former does not play any relevant role, it will not be regarded in the following discussion. However, before discarding it, it is worth noticing the total analogy between $\vec{E}$ and $\vec{H}$, pointing that phenomena observed in a magnetic suspension must have an electric counterpart based on polarizable particles. Effectively those systems exist and are known electrorheological fluids (ERFs). Although, from an experimental of view, ERFs entail some crucial differences with respect to CMRFs (which made them not so useful from an application point of view), ERFs can be theoretically seen as electric analogues when CMRFs are interrogated in their linear magnetic regime [45]. This will allow us to extract some results from ERF references in Sec. 3.4.

Equations (3.32) and (3.35) are applicable in the whole CMRF, that is, inside each dispersed particle and in the continuous phase. Just at the interphase between the two media, continuity equations apply:

$$\hat{n} \cdot (\vec{B}_p - \vec{B}_c) = 0 \tag{3.36}$$

$$\hat{n} \times (\vec{H}_p - \vec{H}_c) = 0 \tag{3.37}$$

where $\hat{n}$ is the normal vector of the interphase and the subscripts p and c denote field/flux density in the particulate and continuous phase, respectively. Equations (3.30)-(3.37) together with an appropriate boundary condition (for example, $\vec{H} = \vec{H}_{ext}$ far away from the CMRF if the CMRF is of finite size) are a closed system that allows us to solve the magnetostatic problem yielding magnetic field, magnetic field flux density and magnetization.

Once the field variables are known, the magnetic interaction, i.e. the force acting between magnetized particles, can be calculated. This is of fundamental interest because, as it will be shown in Sec. 3.4, the interparticle force determines the rheological behavior of the CMRF. To compute the force, one can use the well-known expression from Lorentz or, in a more treatable way, that proposed by Kelvin [46]. However, these expressions require as input the magnetization of the particle (which is known) and the local field at its position, that is, they do not require the total field (local plus demagnetization one). This can be a shortcoming since, typical methods used to solve the magnetostatic problem in CMRFs (see below) yield the total fields, without splitting them in external, local nor demagnetization fields.

At this point, it is more advantageous to compute the force following the Maxwell's stress tensor formulation. This approach directly comes from the Lorentz force approach and expresses the force in terms of the total magnetic field and flux density that are the most easily accessible quantities. In addition, it reduces the complexity of the computation since it is based on the integration of the proper tensor components over an arbitrary surface that must encompass the body over which force is to be computed. This approach is different from the Lorentz force because the latter requires a volume integration.

Surface arbitrariness can be leveraged to choose a simple one, for example, lying completely in the continuous phase (which is a linear material without magnetic response). Following the Maxwell's stress tensor formulation, the magnetic force acting on the body $\vec{F}_m$ is given by:

$$\vec{F}_m \cdot \hat{e} = \int_S \hat{e}^T \cdot \tilde{T} \cdot \hat{n} ds \tag{3.38}$$

where $\hat{e}$ denotes the direction of the force component that is to be computed, S is the arbitrary surface encompassing the body, $\hat{n}$ is its normal vector and $\tilde{T}$ is the Maxwell's stress tensor (do not confuse this second-order tensor with the torque vector $\vec{T}$):

$$\tilde{T} = \widetilde{BH} - \tilde{\delta}\frac{BH}{2} \tag{3.39}$$

where B and H are the modulus of magnetic field flux density and magnetic field respectively. The use of this definition for $\tilde{T}$ implies that surface integration must be done in a linear medium [47]. In addition, that surface must not cross an interphase between media with different constitutive equations.

Finally, in some particular cases, it could be also useful to compute the energy of the CMRF as a whole in a volume V. In this case, the magnetostatic energy is defined as [48]:

$$W_V = -\int_V \left(\int_0^{\vec{H}} \vec{B} d\vec{H}' \right) dv \tag{3.40}$$

The previous expression depends on the constitutive equation and therefore the integrand changes depending on whether dv is placed in the continuous phase or in the particulate one. If both phases are isotropic (that is $\vec{B}$ and $\vec{H}$ are collinear) the constitutive equations can be expressed as $\vec{B} = \mu_0 \mu_r(H)\vec{H}$ and therefore, Eq. (3.40) is rewritten as:

$$W_V = -\mu_0 \int_V \left(\int_0^H \mu_r(H') H' dH' \right) dv \tag{3.41}$$

In the case of a linear media, $\mu_r(H)$ is constant and therefore the magnetostatic energy is reduced to $W_V = \mu_0 \mu_r H^2/2 = BH/2$. For non-linear materials a more complex dependency $W_V(H)$ is expected (see Chapter 5 for example).

The energy computation has interest by itself because it allows comparing different particle configurations within the CMRF, discerning which is the most favorable (i.e. minimum energy state) and, hence, the most probable state at equilibrium. In addition, for conservative systems (note that according to Eq. (3.35) this is the case), it also offers another way to compute forces by properly changing the configuration of the system:

$$\vec{F}_m \cdot \hat{e} = -\frac{\partial W_V}{\partial e} \tag{3.42}$$

being e the generalized coordinate related to the desired force component. At a first glance, it could seem that the force computation from energy arguments has not any advantage over the force computation from the Maxwell's stress tensor as the former implies a volume integral and an additional derivation operation. However, as it was pointed out previously, the Maxwell's stress tensor related surface S must lie in a linear material, and this is a condition that cannot be always fulfilled (think for example in a magnetic particle dispersed in a non-linear magnetic continuous phase as it happens in IFFs). In this particular case, the energetic approach is of more interest because it can circumvent non-linearities in both media (as it explicitly accounts for the constitutive equation, see Eq. (3.41)) yielding the force related to the generalized coordinate e.

As it can be seen, once the magnetostatic problem is solved, magnetic field and flux density are known in each point of the space and forces and/or energy can be calculated. Unfortunately, the necessity of applying Eqs. (3.36) and (3.37) at each interphase restricts the analytical solution to very simple problems consisting of two or three particles in high symmetry configurations. In cases where a large number of particles is intended to be taken into consideration, methods based on capacitance matrices [49], multipole expansion [50] or boundary elements [38] have been applied in the literature. Nevertheless, the aforementioned solutions are restricted to linear materials (that is, not applicable to ferro- or ferri-magnetic materials of interest in magnetorheology) and besides, they do not yield a complete solution as this is given in terms of a finite number of multipoles or approximate particle positions at large interparticle distances.

When the materials involved are magnetically non-linear, numerical methods are practically mandatory. Clearly, the Finite Element Method (FEM) is the preferred choice in magnetorheology [43,51-54]. This kind of numerical simulations aim to solve Eqs. (3.34)-(3.37) directly including all multipoles, so, they can be seen as virtually exact. The basis of FEM techniques are given in Chapter 4 to highlight their performance. At this moment, it is enough to point out that FEM is a mesh-based method and therefore it can become computationally expensive for systems involving very different length scales (since it was noted when flow field problem was regarded). Due to this fact, FEM is not the definitive method to solve magnetostatic problems related to CMRFs.

3.2.1 Mean Magnetization Approximation (MMA)

Alternatively, one can decide to solve Eqs. (3.34)-(3.37) till a first order approximation using the so-called 'Mean Magnetization Approximation' (MMA). This is based on a

well-known magnetostatic problem: an isolated spherical particle in a homogeneous external field $\vec{H}_{ext}$ is magnetized homogeneously (i.e. its magnetization is constant through the particle volume) and creates, outside the particle, the field corresponding to a point dipole placed at the particle center [55]:

$$\vec{H}_d = \frac{1}{4\pi}\frac{3\vec{R}\left(\vec{m}\cdot\vec{R}\right) - R^2\vec{m}}{R^5} \tag{3.43}$$

where $\vec{R}$ is the vector joining the particle center with the field point (i.e. the place where the magnetic field is evaluated) and $\vec{m}$ is the dipole moment. Since the particle is homogeneously magnetized, this is simply given by $\vec{m} = V_p\vec{M}$ being $V_p = \pi d^3/6$ the particle volume and $\vec{M}$ the magnetization:

$$\vec{M} = 3\beta(H_{int})\vec{H}_{ext} = 3\,\frac{\mu_{r,p}(H_{int}) - \mu_{r,c}}{\mu_{r,p}(H_{int}) + 2\mu_{r,c}}\,\vec{H}_{ext} \tag{3.44}$$

where $\beta(H_{int})$ is the contrast factor, $\mu_{r,c}$ is the relative permeability of the continuous phase (required to be linear) and $\mu_{r,p}$ is the relative permeability of the particulate phase (linear or not). Taking this into consideration, MMA states that, although any particle is surrounded by many others in a CMRF, they magnetize following Eq. (3.44) but evaluated at the local magnetic field $\vec{H}_{ext} \to \vec{H}_{loc}$. Note that this approximation tries to incorporate multibody effects but, at the end of the day, it is equivalent to suppose that the particles are still isolated, not under $\vec{H}_{ext}$ but under another homogeneous field with value $\vec{H}_{loc}$. In addition, Eq. (3.44) shows that magnetization mechanism comes from the permeability difference between particulate and continuous phases. In particular, it demonstrates that non-magnetic particles dispersed in a linear magnetic media also interact, at least, through dipoles. This allows to consider IFFs (where $\beta < 0$) as analogues of CMRFs ($\beta > 0$) whenever the used FF is linear.

The main advantage of the MMA is that it allows computing local field easily at any point in the CMRF because the secondary field due to every dispersed particles is just $\vec{H}_{sec,\alpha} = \vec{H}_{d,\alpha}$ (that now is analytically known from Eq. (3.43)):

$$\vec{H}_{loc} = \vec{H}_{ext} + \sum_{\alpha=1}^{N}\vec{H}_{d,\alpha} \tag{3.45}$$

The summation in Eq. (3.45) should run over all particles in the CMRF, however, since the magnetic field decreases with the distance, a cutoff distance is commonly used to save computational cost. With this, only neighboring particles are considered.

Again, once the magnetic field is known in every point, the interparticle force $\vec{F}_d$ can be computed using the Maxwell's stress tensor, Lorentz or Kelvin law. However, the force on a (field) point dipole $\vec{m}_\alpha$ due to a magnetic field is also known analytically. What is more, as the particles are replaced by point dipoles, any of them will suffer a magnetic torque $\vec{T}_m$ under the presence of the field that tries to align with it. Both magnitudes read as follows:

$$\vec{F}_d = \mu_0\mu_{r,c}\nabla\left(\vec{m}_\alpha\cdot\vec{H}_{loc}\right) \tag{3.46}$$

$$\vec{T}_m = \mu_0 \mu_{r,c} \vec{m}_\alpha \times \vec{H}_{loc} \tag{3.47}$$

Nevertheless, as noted at the beginning of this section, the particle magnetization is supposed to be collinear with the field and thus, CMRF particles are not expected to suffer this torque. Regarding the force, Eq. (3.46) shows that it is zero unless the magnetic field changes in the space. Ideally, CMRFs are subjected to external homogeneous fields and thus, the only magnetic force their particles experience should be due to the secondary field created by another (source) dipole $\vec{m}_\beta$. In that case, the force can be written as:

$$\begin{aligned} &\vec{F}_d \\ &= \frac{3\mu_0 \mu_{r,c}}{4\pi} \left[\frac{(\vec{m}_\alpha \cdot \vec{m}_\beta)\vec{R}_{\alpha\beta} + (\vec{m}_\beta \cdot \vec{R}_{\alpha\beta})\vec{m}_\alpha + (\vec{m}_\alpha \cdot \vec{R}_{\alpha\beta})\vec{m}_\beta}{R_{\alpha\beta}^5} \right. \\ &\left. - 5\frac{(\vec{m}_\alpha \cdot \vec{R}_{\alpha\beta})(\vec{m}_\beta \cdot \vec{R}_{\alpha\beta})\vec{R}_{\alpha\beta}}{R_{\alpha\beta}^7} \right] \end{aligned} \tag{3.48}$$

where $\vec{R}_{\alpha\beta}$ is the vector joining the dipole $\vec{m}_\beta$ with the dipole $\vec{m}_\alpha$. Note that, in general, $\vec{m}_\alpha$ and $\vec{m}_\beta$ do not have to be the same in magnitude and/or direction. These will depend on the local field at the respective positions of both dipoles.

To get a deeper insight into the interparticle dipolar interaction, it is worthwhile to particularize Eq. (3.48) for the case of two identical dipoles $\vec{m}_\alpha = \vec{m}_\beta = \vec{m}$. Writing Eq. (3.48) in spherical coordinates (centered in the source dipole and supposed to be directed in the z direction):

$$\begin{aligned} \vec{F}_d &= -\frac{3\mu_0 \mu_{r,c} m^2}{4\pi R^4} \left[(3\cos^2\theta - 1)\hat{R} + \sin(2\theta)\,\hat{\theta} \right] \\ &= -F_{mag} \left(\frac{d}{R} \right)^4 \left[(3\cos^2\theta - 1)\hat{R} + \sin(2\theta)\,\hat{\theta} \right] \end{aligned} \tag{3.49}$$

Clearly, it can be seen that the dipolar force is not central. It does not depend on the azimuthal coordinate but it is anisotropic; repulsive for $55^o \leq \theta \leq 125^o$ and attractive in other case. Regarding the polar component, it is negative for $\theta \leq 90^o$ (thus, it tries to move the field dipole over the source one) and positive for $90^o \leq \theta$ (in this case, it moves the field dipole under the source one). Just at $\theta = 90^o$ the polar component is null but unstable, that is, any small perturbation that pushes apart the field particle from $\theta = 90^o$ will provoke that the field dipole aligns with the source one. At $\theta = 0^o$ and $\theta = 180^o$, the polar coordinate is also zero, however, in these cases, the position is stable: any perturbation at these positions will be balanced by a restoring-like force that will place the field dipole aligned with the source one. In addition, for a chosen interparticle distance R, it can be seen that the force in the dipole orientation direction, $\vec{F}_d(\theta = 0^o)$ and $\vec{F}_d(\theta = 180^o)$ is typically two times larger than in the normal direction, $\vec{F}_d(\theta = 90^o)$. Thus, when the particles are freely suspended in the continuous phase, this behavior is translated in the formation of chain-like structures directed along the dipole (field) direction.

Finally, it is worthwhile to remark that the MMA predicts a magnetic force scale as

$$F_{mag} = \frac{\mu_0 \mu_{r,c} \pi}{48} d^2 M^2 = \frac{3\mu_0 \mu_{r,c} \pi}{16} d^2 \beta^2 H_{ext}^2 \tag{3.50}$$

Looking at Fig. 3.2 and Eq. (3.44), it can be inferred that, at low magnetic fields when the material behaves linearly with β constant, this force will be proportional to H_{ext}^2. On

the contrary, at high magnetic fields when the material saturates and M^2 tends to M_S^2, the force becomes independent on the external field. As it will be seen in Sec. 3.4, this is roughly the same trend observed macroscopically in CMRFs, pointing that basic polarization phenomena under the MR effect is properly accounted for by regarding only dipoles.

Although the MMA offers a simple solution to the magnetostatic problem, it should be remembered that, strictly speaking, it is only valid in two limiting cases: (i) when the particles are far enough from each other to feel only an homogeneous field or (ii) when particles are fully saturated so that their magnetization is uniform through the particle volume and really act as point dipoles. However, the case (i) is impossible to fulfill in CMRFs; as it is pointed in Eq. (3.49), dipolar forces can be attractive and therefore, even at very low concentrations, they will tend to form particles aggregates where interparticles distances are small. As a consequence, particles will not feel a homogeneous field and the MMA would not be valid. For its part, the saturation regime in case (ii) is hard to be reached experimentally in a controlled way, i.e. guaranteeing that all particles experience the same high external field and thus all of them are magnetized at the same (saturation) level. In Chapter 9, a device that is capable to apply homogeneous saturating fields is presented while the rheological behavior in this regime is evaluated theoretically and experimentally in Chapter 8.

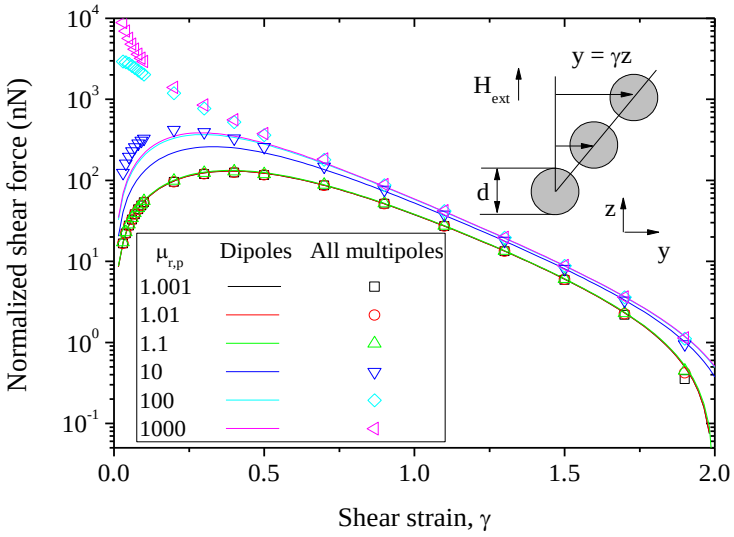

Figure 3.3: Shear magnetic force (normalized by β^2) in an infinite chain of linear particles with relative permeability $\mu_{r,p}$ as a function of the shear strain. Results considering only dipolar interaction or all multipoles are plotted with lines and points, respectively. Particle diameter $d = 1$ μm, $H_{ext} = 400$ kA/m, $\mu_{r,c} = 1$.

Undoubtedly, the main drawback of the use of MMA as a first order solution, is that it does not take into consideration magnetization non-uniformity in the particle volume. Importantly, this is, ultimately, the responsible for the multipolar magnetic interactions. These multipoles enhance the magnetic field level in small regions between particles what leads to greater induced magnetization levels. Consequently, when the interparticle distance is small, multipoles play a critical role in the magnetic force computation. As an example, in Fig. 3.3 the magnetostatic force in an infinitely long isolated chain of particles is plotted as a function of the chain shear strain in affine deformation for a range of $\mu_{r,p}$. Lines stand for the MMA solution including only dipoles and points stand for the

complete solution, all multipoles included, computed by FEM. It can be seen that, only when the magnetic particles are separated enough (high strains) or $\mu_{r,p}$ is small [56] (as in IFFs and magnetic latexes), the MMA can reproduce the complete solution. In other case, the true magnetic interaction will be strongly underestimated (till four orders of magnitude for the worst case in Fig. 3.3). In Sec. 3.4, it will be shown that this underestimation can lead to a non-negligible error in the rheological material functions of CMRFs.

3.3 Other non-hydrodynamic interactions

As in any suspension, particles in a CMRF experience other non-hydrodynamic forces besides magnetostatic ones. Most of them are classic interactions in Colloid Science, so we refer to well-known treatises in this field for further details [57,58]. In this section we only summarize them to see whether they have or not an effect on the particle dynamics when compared to magnetostatic forces.

Regardless of the kind of particulate or continuous phase, any pair of dispersed particles will interact through the London-van der Waals or dispersion forces. These are attractive interactions coming from the polarization of one particle atoms induced by the atoms of the second particle. For the case of two perfect spherical particles, this attractive interaction diverges as the surface-to-surface distance goes to zero pointing to an irreversible aggregation (similar to what happened with lubrication forces –see Sec. 3.1.1–). Again, particle roughness poses a limit to the attractive force. For the case of CMRFs where $d > 1$ μm and supposing a typical roughness of the order of nanometers, the ratio van der Waals to magnetostatic forces takes values of 10^{-5} or smaller [59]. As a result, van der Waals forces can be safely neglected when accounting for other non-hydrodynamic forces.

The fact that van der Waals forces favor particle aggregation should not be a problem in the presence of a magnetic field since this is precisely the purpose of applying it; to promote the directed self-assembly with the difference that van der Waals forces do not yield anisotropic structures. However, as it was commented in Chapter 1 , in the absence of a magnetic field it is desired that the CMRFs keep kinetically stable and with this aim in mind several routes are followed in the literature: core-shell structures, surfactant addition and surface charges, among others. These elements introduce other interactions between the particles (electric double-layer, osmotic and elastic potentials, depletion, etc.) that need to be considered when studying the rheological behavior of the system. Their effects depend on a large number of factors (continuous phase permeability, electrolyte concentration, surfactant type and concentration, hydrophobicity of the continuous phase, particle size, etc.), and hence it is not easy to summarize their final role on the rheology of the MRFs.

Here, we will limit to say that, because the main objective of these approaches is to counteract van der Waals forces, it is expected that an optimal route gives rise to a stabilization force (regardless of its origin) whose order of magnitude is similar to the van der Waals one. Thus, as a first approximation, its effects can be also neglected in the presence of a field.

Classical colloidal forces are due to particle-particle interactions but in a CMRF particles are subjected to body forces as well. The main one is the gravitational force that, including buoyancy effects, can be written as $\vec{F}_g = \vec{g}(\rho_p - \rho_c)V_p$ where ρ_p is the particle density.

The magnetostatic force is typically three orders of magnitude larger than the gravitational one so, *a priori*, the latter could be neglected. In the case that the height of the macroscopic sample is above a critical size $\sim 2dF_{mag}/F_g$, experimental and simulation studies have shown that gravity can collapse the field induced structures [60]. However, in the worst scenario explored throughout this dissertation (i.e. the smallest applied field) the largest gap confining the sample is below this critical height. Thus, gravitational forces will not be considered in the analysis.

In addition to previously discussed forces, any particle dispersed in a continuous phase will experience the well-known Brownian motion. This is a diffusive movement due to the continuous and random collisions between the dispersed particles and the continuous phase molecules. In order to see its importance in comparison to other forces, a typical force scale related to the Brownian motion can be defined $F_B \sim k_B T/d$ where k_B is the Boltzmann's constant ($1.381 \cdot 10^{-23}$ J/K) and T is the absolute temperature (do not confuse with the vector torque $\vec{T}$ nor the Maxwell's stress tensor $\tilde{T}$). Taking this into consideration, the specialized literature defines the so-called λ ratio (or coupling factor) to measure the relative importance of magnetostatics over thermal forces:

$$\lambda = \frac{F_{mag}}{F_B} = \frac{\mu_0 \mu_{r,c} \pi d^3 M^2}{96 k_B T} \tag{3.51}$$

In CMRFs this ratio is very large, above 100, even for low external fields what leads to discard Brownian motion in these systems.

As it can be inferred from the previous discussion, with the exception of hydrodynamic forces, any classical colloidal forces can be safely neglected in the study of CMRFs because the large particle size (above 1 μm) favors magnetostatic interactions. Indeed, strictly speaking, CMRFs are not true colloidal systems due to the absence of Brownian motion; they seem to share more features with granular suspensions, especially when high concentrations are considered (above volume fractions of 0.4). In the concentrated regime, particles suffer repeated collisions with each other and this makes contact forces (repulsive and frictional ones) to become a critical agent, even more important than long-ranged hydrodynamics, in the macroscopic sample behavior [61].

Different expressions have been proposed in the literature to model both contact interactions although current works in granular rheology usually choose Hertzian repulsion (see Chapter 4) and Coulomb-like friction forces for repulsion and frictional forces, respectively. Instead of particularizing then here, it is only said that they do not introduce a new force scale in the problem to compete against magnetic or hydrodynamic forces. On the contrary, they are conceived to model a hard sphere potential and thus, they should be able to bear any applied load [61,62]. Ascertaining the actual role of friction in rheology is nowadays an open field of research, even in non-magnetic suspensions, due to the entailed complexity from all experimental, simulation and theoretical points of view. Nevertheless, the parallelism between these granular suspensions and CMRFs would suggest that contact forces are also an ingredient to be taken into account in the complete description of CMRFs.

3.4 Rheology

Sections 3.1 and 3.2 deal with CMRFs from a microscopic point of view. By solving the governing equations, under a given macroscopic constraint (particle concentration,

applied flow field, external magnetic field) and initial conditions, it is possible to precisely know the dynamic state of the system: particle positions, velocities and fluid flow field at any time.

Although complete and detailed, this microscopic description does not inform, by itself, about the collective behavior of the system, that is, about its macroscopic state where the CMRF is not seen as a suspension of magnetizable solid particles in a Newtonian fluid but as continuous medium with macroscopic physical properties. To get these macroscopic properties and to relate them to the aforementioned constraints it is necessary a further step to link both micro- and macro- descriptions.

Similar to other suspensions and colloids, CMRFs are constituted by an extraordinarily large number of interacting particles. As a result, the link between both kinds of descriptions must be done following the Statistical Physics formalism. According to this, for each set of macroscopic constraints there is a group, called ensemble, of compatible microscopic states each of them having a different probability to really happen.

Eventually, any physical observable x depends on its micro-configuration, however, the macroscopically accessible value is given by its ensemble average $\langle x \rangle$: the sum of its value at each microscopic state of the ensemble weighted by the probability of the corresponding microscopic state. This average would imply to know all compatible microscopic states together with their probability, and this is extremely complex. Hence, what is actually done is to average the pursued physical observable spatially over the system [1]:

$$\langle x \rangle = \frac{1}{V} \int_V x \, dv \tag{3.52}$$

This procedure is valid whenever all particles in the system are statistically equivalent, that is, each particle is surrounded by a configuration with the same macroscopic properties. In this way, each particle can be regarded as placed in a different microscopic state, but compatible with the imposed macroscopic one, what allows identifying volume average with the ensemble average.

The major goal in this dissertation is to elucidate how a CMRF of a given concentration responds to a mechanical stimulus (deformation or stress) under the presence of an external magnetic field $\vec{H}_{ext}$; this is the so-called magnetorheological response. Since the mechanical state of a material is determined by its total stress tensor $\langle \tilde{t} \rangle$, this tensor together with $\langle \tilde{E} \rangle$ will be the physical observables that will be ascertained macroscopically [1]:

$$\begin{aligned} \langle \tilde{t} \rangle &= \frac{1}{V} \int_{V_f} \tilde{t} \, dv + \frac{1}{V} \sum_{\alpha=1}^{N} \int_{V_p} \tilde{t} \, dv \\ &= \frac{1}{V} \int_{V_f} \left(-p\tilde{\delta} + \eta_c 2\tilde{E} \right) dv + \frac{1}{V} \sum_{\alpha=1}^{N} \int_{V_p} \tilde{t} \, dv \end{aligned} \tag{3.53}$$

In Eq. (3.53) it has been taken into account that the total volume occupied by the CMRF can be split in the volume occupied by the fluid V_f and the volume of each immersed particle V_p. In addition, since the carrier fluid is a Newtonian liquid, the total stress tensor within the first integral has been substituted by Newton's viscosity law (Eq. (3.6)). Extending the first integral to the whole volume V, remembering that particles are rigid

(i.e. $\tilde{E} = 0$ in V_p) and bearing in mind that $\langle \tilde{E} \rangle = \tilde{E}_\infty$ (the macroscopically imposed flow field) we arrive to:

$$\langle \tilde{t} \rangle = \frac{1}{V} \int_V \left(-p\tilde{\delta} + \eta_c 2\tilde{E} \right) dv + \frac{1}{V} \sum_{\alpha=1}^{N} \int_{V_p} \left(\tilde{t} + p\tilde{\delta} \right) dv$$
$$= -\langle p \rangle \tilde{\delta} + \eta_c 2\tilde{E}_\infty + \frac{1}{V} \sum_{\alpha=1}^{N} \int_{V_p} \left(\tilde{t} + p\tilde{\delta} \right) dv \qquad (3.54)$$

The stress tensor $\tilde{t} + p\tilde{\delta}$ inside the rigid particles is undetermined. However, supposing that there is not any non-hydrodynamic torque acting over the particles (what is fulfilled in CMRFs if magnetization is assumed to be collinear to the field), it can be written using the stresslet $\tilde{S}$ (Eqs. (3.8) and (3.9)) over the particles as [17,63]:

$$\frac{1}{V} \sum_{\alpha=1}^{N} \int_{V_p} \left(\tilde{t} + p\tilde{\delta} \right) dv = \frac{1}{V} \sum_{\alpha=1}^{N} \left(\tilde{S}_\alpha - \frac{1}{3} \tilde{\delta} \int_{S_p} \vec{r}_S \cdot \tilde{t} \cdot \hat{n} ds \right)$$
$$= \frac{1}{V} \sum_{\alpha=1}^{N} \left(\tilde{S}_\alpha - \tilde{\delta}^*_\alpha \right) = \frac{6\phi}{\pi d^3} \left(\langle \tilde{S} \rangle - \langle \tilde{\delta}^* \rangle \right) \qquad (3.55)$$

where S_p is the particle surface and $\phi = NV_p/V$ is the particle volume fraction. Equation (3.55) is general, providing that Stokes flow without non-hydrodynamic torques are accepted, because no assumption has been done regarding the volume fraction. It indicates that the particle contribution to the macroscopic stress is just the sum, per unit volume, of the stresslets of all particles plus an isotropic term $\propto \langle \tilde{\delta}^* \rangle$. The later can be merged with the also isotropic mean pressure $-\langle p \rangle \tilde{\delta}$ of Eq. (3.54) since they do not play any role in the rheology of incompressible magnetic colloids.

The value of $\tilde{S}_\alpha$ can be computed just from its definition (Eqs. (3.8) and (3.9)) once the flow field around each particle is known. However, remembering the theoretical development of Sec. 3.1.1, stresslets can be directly solved from the linear system presented in Eq. (3.20). In particular, we get:

$$\tilde{\boldsymbol{S}} = \tilde{\boldsymbol{R}}_{Su} \left(\vec{\boldsymbol{u}} - \vec{\mathbf{V}}_\infty \right) + \tilde{\boldsymbol{R}}_{SE} \tilde{\boldsymbol{E}}_\infty$$
$$= \tilde{\boldsymbol{R}}_{Su} \tilde{\boldsymbol{R}}_{Fu}^{-1} \left(\vec{\boldsymbol{F}}_{nh} - \tilde{\boldsymbol{R}}_{FE} \tilde{\boldsymbol{E}}_\infty \right) + \tilde{\boldsymbol{R}}_{SE} \tilde{\boldsymbol{E}}_\infty$$
$$= \left(\tilde{\boldsymbol{R}}_{SE} - \tilde{\boldsymbol{R}}_{Su} \tilde{\boldsymbol{R}}_{Fu}^{-1} \tilde{\boldsymbol{R}}_{FE} \right) \tilde{\boldsymbol{E}}_\infty + \tilde{\boldsymbol{R}}_{Su} \tilde{\boldsymbol{R}}_{Fu}^{-1} \vec{\boldsymbol{F}}_{nh}$$
$$= \tilde{\boldsymbol{S}}_h + \tilde{\boldsymbol{S}}_p \qquad (3.56)$$

Remember that bold symbols (in the following omitted) stand for the stresslet associated to all suspended particles. It can be seen that the total stresslet has two contributions, the so-called hydrodynamic stresslet $\tilde{S}_h$ (all those terms accompanying $\tilde{E}_\infty$) and particle interaction stresslet $\tilde{S}_p$ (proportional to F_{nh}). It is important to notice here that, in order to avoid a long expression, rotation contributions in Eq. (3.56) have been omitted. However, since in CMRFs non-hydrodynamic torques are absent, full expression (i.e. containing also the rotation contribution) will be still separable only in terms that exclusively accompany $\tilde{E}_\infty$ or $\vec{F}_{nh}$. At this point, some issues can be highlighted.

Firstly, the hydrodynamic stresslet $\tilde{S}_h$ is not null even when $\vec{F}_{nh} = 0$ (i.e. particles do not interact through non-hydrodynamic forces). The origin of this contribution lies on the infinite resistance of rigid particles to be strained, thus the only presence of rigid particles

in the straining flow field contributes to $\tilde{S}_h$. It will be later shown that this stresslet is the responsible for the viscosity increase seen in any particle suspension (Sec. 3.4.3).

Secondly, the particle interaction stresslet $\tilde{S}_p$ (in the following only particle stresslet, although both $\tilde{S}_h$ and $\tilde{S}_p$ comes from the dispersed particles) clearly comes from non-hydrodynamic forces $\vec{F}_{nh}$ experienced by the particles. However, it should be born in mind that the origin of any stresslet is the distribution of the traction force $\tilde{t} \cdot d\vec{S}$ over the particle surface. This indicates that $\tilde{S}_p$ exits not only because there exists non-hydrodynamic forces but also because there is a continuous phase able to mediate the non-hydrodynamic interactions and transmit their effects. In other words, $\tilde{S}_p$ would be zero even though $\vec{F}_{nh} \neq 0$ in a static ensemble of particles (fixed in the space) able to interact through long-range forces (for example, magnetic ones) but not dispersed in a fluid. Furthermore, if we suppose the same ensemble but now dispersed in a quiescent fluid (for example, a MRF under an external magnetic field without a flow field), since $\vec{u} - \vec{\mathrm{V}}_\infty$ and $\tilde{E}_\infty$ are both zero, there would not be any stresslet neither.

The two previous comments demonstrate that $\tilde{S}_p$ cannot be the only contribution coming from non-hydrodynamic forces to the total stress tensor $\langle \tilde{t} \rangle$. By definition, $\langle \tilde{t} \rangle \cdot d\vec{S}$ must account for the total force acting across $d\vec{S}$. If we suppose an imaginary surface halving the ensemble in the previous example consisting of long-range interacting particles not immersed in a fluid, all particles in one halve would act over the other halve with a net force, but this would not be taken into account since $\tilde{S}_p = 0$. To account properly for the total non-hydrodynamic force experienced by the particle in the total stress tensor, the so-called $\widetilde{xF}$ term [64] or thermodynamic stress must be included in the computation of $\langle \tilde{t} \rangle$:

$$\langle \widetilde{xF} \rangle = -\frac{1}{V} \sum_{\alpha=1}^{N} r_\alpha \widetilde{F}_\alpha \tag{3.57}$$

where $\vec{r}_\alpha$ is the position vector of particle α and $\vec{F}_\alpha$ is the total non-hydrodynamic force acting over it. Although the example proposed here only considers long-ranged non-hydrodynamic forces, Eq. (3.57) is also valid for hard-sphere interactions (and, for example, contact forces).

Putting together all previous contributions, the rheological constitutive equation of the suspension can be written as follows:

$$\langle \tilde{t} \rangle = -\langle p \rangle \tilde{\delta} + \eta_c 2\tilde{E}_\infty + \langle \widetilde{xF} \rangle + \frac{6\phi}{\pi d^3} \left(\langle \tilde{S}_h \rangle + \langle \tilde{S}_p \rangle \right) \tag{3.58}$$

Here $\langle p \rangle \tilde{\delta}$ is the mean pressure corrected by the isotropic term $\langle \tilde{\delta}^* \rangle$ derived during the stresslet computation (see Eq. (3.55)). At first sight, Eq. (3.58) already shows some characteristics that differentiate $\langle \tilde{t} \rangle$ from the Newtonian constitutive relationship:

1. Under Stokes flow approximation, all contributions to $\langle \tilde{t} \rangle$ depend on the particle positions. Thus, in addition to interparticle forces, their structure also plays a role in the rheological behavior.
2. In the absence of flow and depending on the particle positions, due to the $\langle \widetilde{xF} \rangle$ term, the system can develop shear stresses (non-diagonal elements). Thus, when an external stress is imposed trying to move the system from its equilibrium state,

an internal restoring stress appears to keep particles in their original configuration, i.e., there is a yield stress below that the system does not flow.

3. Not all terms are directly proportional to $\tilde{E}_\infty$. On the contrary, some of them are proportional to $\tilde{E}_\infty$ while others are scalable by F_{nh}. These two sources of stress imply different stress regimes depending on which source is prevailing. As a main result, CMRFs show a marked shear-thinning behavior.
4. Terms coming from particles and their interactions, $\langle \widetilde{xF} \rangle$, $\langle \tilde{S}_h \rangle$ and $\langle \tilde{S}_p \rangle$, are not isotropic and consequently normal stress differences can appear at rest or in simple shear flow.

In Secs. 3.4.1-3.4.4, these topics are reviewed from theoretical, experimental and numerical points of view. When the system is strained, the discussion will be mainly focused in simple shear as it is the most studied flow mode in the MRF research. In this case, the flow direction is supposed to be $\hat{y}$, the vorticity direction $\hat{x}$ and the gradient direction, together with the external field direction, is $\hat{z}$ (see Fig. 3.4). With this choice, the flow field is $\vec{v}_\infty = \dot{\gamma} z \hat{y}$, the strain rate tensor is

$$\tilde{E}_\infty = \frac{1}{2}\begin{pmatrix} 0 & 0 & 0 \\ 0 & 0 & \dot{\gamma} \\ 0 & \dot{\gamma} & 0 \end{pmatrix} \tag{3.59}$$

and $\dot{\gamma}$ is the shear rate. Also, to simplify notation, the stress in the shear direction will be denoted as $\langle t \rangle_{zy} = \tau$ while deviatoric normal stresses (components of total stress tensor in the diagonal excluding the isotropic pressure contribution) will be denoted as σ_{xx}, σ_{yy} and σ_{zz}.

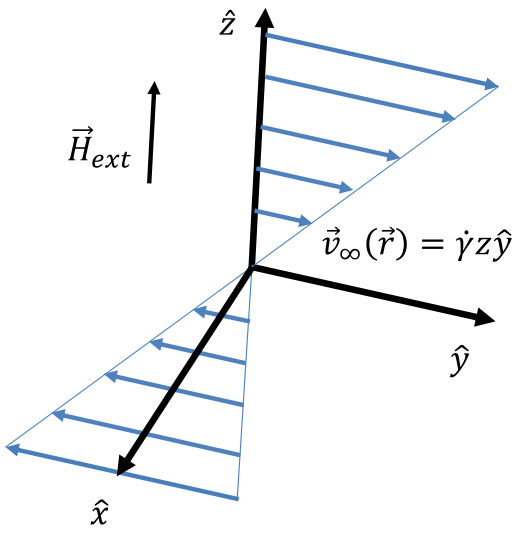

Figure 3.4: Linear shear flow $\vec{v}$ macroscopically imposed and external magnetic field $\vec{H}_{ext}$ together with flow ($\hat{y}$), gradient ($\hat{z}$) and vorticity directions ($\hat{x}$).

3.4.1 Structure

As it was indicated in Sec. 3.2.1, the magnetostatic interaction is anisotropic and contributes to the particle aggregation in the same direction that the applied magnetic field. Traditionally, the field-induced structuration of a MRF is studied under no flow conditions in connection to the onset of a yield stress and with emphasis in determining the time scale for structure formation and associated order parameters.

In view of the theoretical analysis in Secs. 3.1 and 3.2, imposing that the background flow $\left(\vec{V}_\infty, \vec{\Omega}_\infty, \tilde{E}_\infty\right)$ is zero, the particles positions can be tracked just solving Eq. (3.20). Since there is not flow and particle inertia is neglected, there is only one time scale in the structuration problem. As a first approximation, this time scale can be obtained as the time needed by a particle to displace a length equal to its diameter under the action of dipolar magnetostatic interaction (Eq. (3.50)) and Stokes' drag force (Eq. (3.21)):

$$t_a = \frac{d}{u} = \frac{144\eta_c}{\mu_0 \mu_{r,c} M^2} \tag{3.60}$$

As observed in Eq. (3.60), the time scale depends on the applied magnetic field strength (contained in the magnetization) and the carrier fluid viscosity. In view of this analysis, the final structure morphology of an MRF is independent on these magnitudes; t_a simply determines how quickly the structuration process occurs [65].

Numerical studies (using magnetic dipolar forces, Stokes' drag approximation and one-way coupling scheme without a background fluid velocity) [66,67] together with experiments (based on optical microscopy observations for 2D systems [68-70] or light scattering [71-73] and computerized tomography for 3D systems [74]) show that the final structure morphology and inner particle arrangement strongly depend on the volume fraction, sample confinement and way of applying the magnetic field.

When a uniaxial DC magnetic field is suddenly applied and then kept constant, particles reorganize and start to form doublets that quickly merge into short chains along the field direction. The onset of this doublet formation also depends on the particle concentration: the larger concentration the smaller initial interparticle distance and thus the smaller onset time. For the particular example of dilute 2D suspensions, the onset time is found to be $\sim t_a/\left(100\phi_{2D}^{2.5} h^{0.22}\right)$ and hence also (slightly) dependent on the sample height in the field direction h [75].

In a second stage, these chains start to aggregate in more complex structures depending on the volume fraction and the confinement h. Nevertheless, as the chain length increases, the aggregation rate is reduced due to the higher hydrodynamic resistance (the longer the chains the larger the resistance) and also the nature of the magnetic interaction between chains. The magnetic interaction between chains can be repulsive or attractive depending on chain length (which is determined by the confinement) and the mean interchain distance (which is controlled by the volume fraction). Generally speaking, low volume fractions favors isolated chains that repel each other giving rise to a final structure consisting of simple chains of one particle width. As volume fraction increases (above 0.05), initial chains have a richer configuration spectrum (off-/ registered chains, different lengths) that leads to the formation of thick interconnected columns/fibers.

The aggregation process described in the paragraph above takes a very short time; of the order of milliseconds for the chain formation and of the order of minutes for the subsequent fibers formation. However, these final aggregates are not equilibrium structures (in the case of interacting dipoles, the expected equilibrium structure is a tetragonal body centered lattice BCT [76-79]). Instead, the particles are kinetically arrested in open elongated flocs with a large number of defects. There are several possibilities to avoid the formation of kinetically arrested states. The simplest approach consists in slowly increasing the magnetic field (instead of suddenly applying it). This results in the formation of well separated columns [80]. Another possibility is to use toggled fields. This allows the structure to accommodate by diffusion during the short

period when external field is absent. This approach results in the formation of disperse 'drops' consisting of particles that are arranged in a BCT lattice [81,82].

3.4.2 Pre-yield regime. Static yield stress

Undoubtedly, the yield stress τ_0 is the most relevant figure of merit in a MRF [83]. Theoretically, it is defined as the critical stress below which a material does not flow but behaves as an elastic solid. Thus, if the applied stress is lower than τ_0, the sample will undergo a strain but once the applied stress is removed the sample will recover its initial state. On the contrary, if the applied stress is larger than τ_0, it is said that the sample leaves the elastic or pre-yield regime, breaks (also called sample failure) and starts to flow or to strain continuously [84].

However, the previous definition together with its related phenomenology is hardly seen experimentally (e.g. Ref. [85]). In terms of the measured shear rate versus the applied stress, it is found that samples experience a drastic change in the shear rate (usually several orders of magnitude) when the applied stress is varied through a narrow interval (smaller than one order of magnitude) around τ_0. This narrow interval of stress is called apparent yield stress. Generally speaking, for stresses outside this interval (above or below), the sample shows a nearly Newtonian behavior with the shear rate proportional to the applied stress [86]. As it can be seen, the behavior at stresses above the aforementioned interval perfectly agree with the definition of τ_0. On the contrary, the appearance of the Newtonian behavior below τ_0 is controversial as the MRF is not perfectly elastic.

This discussion and related controversy around τ_0 measurement or existence are well-known from long time ago and highlight the paradox about what flows or not: to properly demonstrate that a material is elastic for any stress below τ_0, it would be necessary experiments of infinite duration to see that the shear rate is effectively null in this regime [87,88]. Actually, what can be stated is that an apparent yield stress exists (in the sense of a dramatic change in the rheological properties) while the related τ_0 is subjected to a time scale that has been previously chosen, typically the time scale of the experiment or problem under study. In this way, below the apparent yield stress the sample can be seen as a solid albeit it creeps at very slow rate, i.e. very slow in comparison to the experimental time scale. Therefore, τ_0 is a magnitude that depends on the measurement conditions. Nevertheless, its circumspect use, at least, as engineering concept has been undoubtedly useful in material characterization [89].

Yield stress ambiguity has given rise to several yield stress definitions. In this dissertation, we will deal only with two of them: the so-called static and dynamic yield stresses. Static yield stress will be discussed in this section and is identified with τ_0, that is, the lowest stress required for the onset of irreversible flow [89]. On the other hand, the dynamic yield stress (τ_y) will be introduced in Sec. 3.4.3 (see pag. 57).

Motivated by torque-transfer applications in electro-mechanical systems, experimental studies on the yielding behavior of CMRFs have mainly focused on the dependence of the yield stress with the applied magnetic field strength. This dependence has been usually parameterized as a power law $\tau_0 \propto H_{ext}^m$ where the exponent m is not constant but changes with the field strength. At low fields (linear regime) some authors obtain $m = 2$ [90-94]. Increasing the magnetic field strength, the exponent spans from 1.4 to 1.7 [94,95-103] while further increasing the field strength leads to a (saturation) regime where the field dependence disappears, $m = 0$ [98,104-106]. Note that these three intervals

correspond to the same ones observed in the magnetic permeability (and thus magnetization) of a particle (Fig. 3.2) in Sec. 3.2. This observation highlights the close relationship between yield stress, interparticle force and particle magnetization.

Apart from the magnetic field strength, the yield stress is also strongly dependent on the particle concentration. However, very few systematic works exist describing this dependence probably because of the complexity involved when dealing with a many-body problem both from an experimental and theoretical point of view [107,108]. Generally speaking, for CMRFs at low-moderate fields, the yield stress increases linearly at low volume fractions (below $\phi = 0.1$) and at a slightly faster rate for intermediate volume fractions ($\phi > 0.1$).

Previous experimental trends have been investigated from both analytical and simulation points of view as well. Theoretically, hydrodynamics can be neglected in the pre-yield regime (i.e. absence of flow), and therefore, the strain suffered by the sample takes a very long time to relax, so that the only non-isotropic contribution to the total stress tensor is given by Eq. (3.57). This, of course, depends on the non-hydrodynamic forces exerted over the particles and their positions, i.e., their microstructure. Hence, the goal is to find the rheological constitutive equation that relates the shear stress generated by the structure (restoring stress based only in the non-hydrodynamic forces) when it is shear strained an amount γ, $\tau = f(\gamma)$. Note that according to this, any MR system with the same microstructure than a CMRF (for example, anisotropic MREs) will share theoretically the same rheological constitutive equation.

A typical example of this kind of curve is plotted in Fig. 3.5a where different regimes can be delineated. Starting from the left, at sufficiently low strains, particle positions are little distorted and consequently the interparticle force change is linear. This results in an elastic behavior where the dependence between the restoring stress and the applied strain is also linear (its slope is defined as the shear modulus G): as the structure is strained from the (meta)stable state, $\gamma = 0$, to $\gamma > 0$, a larger restoring stress appears trying to turn the structure back to the original state. Then, the stress stops being linear, reaches a maximum $\tau_0 = f(\gamma_0)$ and starts to decrease: in this second stage, greater strains find smaller and smaller restoring stresses, this implies that the structure cannot remain stable and breaks. In this context, it is easy to identify the aforementioned maximum τ_0 with our definition of static yield stress understood as the onset of flow. The related strain γ_0 will be called here yield strain despite the fact that some references save this name for the limit of the linear elastic behavior [109]. Analogously to the yield stress, the yield strain denotes the limit where the structure can recover its original shape once the applied stress has been removed.

As it was said in Sec. 3.3, in CMRFs non-hydrodynamics forces are completely dominated by magnetostatic ones. Thus, the restoring stress will be given by the magnetic field distribution inside the CMRF (Sec. 3.2). However, as described in that section, the complexity of the field-induced structure together with the length scale mismatch between the structure (sample length scale around 1 mm) and its constitutive elements (particles length scale around 1 μm) prevent us from fully solving the magnetic field distribution, and with it the magnetostatic forces, neither theoretical nor computationally. Because of this, two main approximations are assumed in the literature to get some insight on the yield stress. On the one hand, magnetic interactions are supposed to be known, while the structuration under shear is computed. On the other hand, particles positions are imposed and both magnetostatic forces and the total stress are solved.

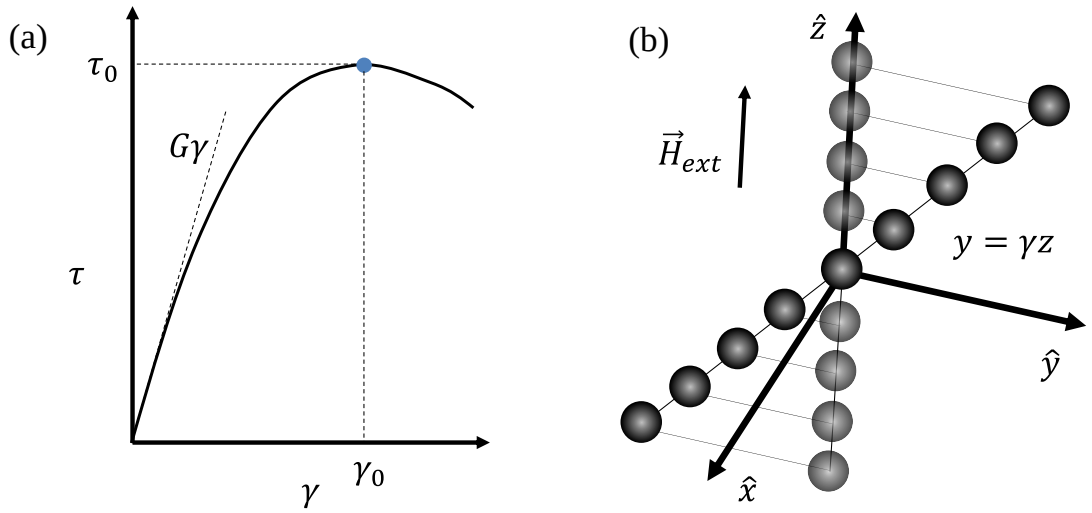

Figure 3.5: (a) Restoring shear stress as a function of the microstructure strain. (b) Under an affine shear strain the particles are displaced along the shear direction a quantity that is proportional to their height z.

The first approximation is just the one-way coupling scheme referred in Sec. 3.1: magnetic forces are supposed to be dipolar (Eq. (3.48)) while hydrodynamic forces are reduced to Stokes' law (Eq. (3.21)). From the total force acting over each particle, their positions can be tracked by solving Newton second law (Eq. (3.4)). Different from structuration studies in the quiescent state, now it is necessary to move the particles in order to evaluate how the stress changes with the sample shear strain. To do this, exceedingly small shear rates are applied to drag the particles and the strain is computed as $\gamma = \dot{\gamma} t$ (where t is the simulated time). Obviously, this contradicts our definition of pre-yield regime (where there is not flow or any dependence on time), however if the drag force coming from the imposed shear rate is small enough in comparison to the magnetostatic force (ratio of 10^{-3} or smaller [36,110]), the computed shear stress versus γ still shows the expected behavior consisting of a linearly increase followed by a maximum, that is identified with the static yield stress.

Generally speaking, although this approximation is capable to mimic the structures experimentally seen in CMRFs, it underestimates the experimental yield stress values (multipoles are not included in the computation, remember Sec. 3.2) and it is not computationally efficient neither because it needs very small simulation time steps in order not to suffer convergence problems (see Sec. 4.2.1).

In the second approximation, the MRF structure is imposed and the force/stress computed from magnetostatic theory (Sec. 3.2). Traditionally, methods within this group can be classified in micro- and macroscopic depending on whether they account for particle positions inside the field induced aggregates or not. In Secs. 3.4.2.1 and 3.4.2.2, main features behind both models are discussed.

3.4.2.1 *Macroscopic methods*

In the macroscopic approaches the particles are supposed to arrange following the applied field direction in fusiform (cylinders or ellipsoids) or sheet-like aggregates whose internal structure (precise position of the constituent particles) is unknown but described by the aggregate internal volume fraction ϕ_a (commonly approximated by the randomly closed packing for spheres $\phi_a = 0.64$). In this case, the stress curve $\tau = f(\gamma)$ is calculated

starting from the magnetostatic energy (Eq. (3.40)) that for linear materials can be rewritten as (see pages 95-98 from Ref. [111]):

$$\tau = -\frac{1}{V}\frac{\partial W_V}{\partial \gamma} = \frac{1}{2V}\mu_0 H_{ext}\frac{\partial m_z}{\partial \gamma} \tag{3.61}$$

where $m_z = V(1-\mu_{zz}^{-1})H_{ext}$ is the dipole component in the field direction written in terms of the permeability tensor μ_{zz} of the suspension. This depends on the aggregate shape and strain. In the case of sheet like aggregates and cylinders, it can be written as follows [112,113]:

$$\mu_{zz} = \mu_{\parallel}\frac{1}{1+\gamma^2} + \mu_{\perp}\frac{\gamma^2}{1+\gamma^2} \tag{3.62}$$

Here $\mu_{\parallel}$ and $\mu_{\perp}$ are the permeability components in the parallel and perpendicular directions to the aggregate axis respectively. Both are independent on the field (linear material) and the strain but they depend on the aggregate shape, contrast factor β and sample volume fraction. Rather than focusing in deriving these dependencies (the full expression computed according to the Maxwell-Garnett theory can be found in Ref. [112]) here we will merge them in a general function g to directly study τ. Supposing isolated aggregates that do not interact with each other:

$$\tau = \mu_0\mu_c\frac{2\gamma}{(1+\gamma^2)^2}\frac{\phi}{\phi_a}\left(1-\frac{\phi}{\phi_a}\right)H_{ext}^2 g(\gamma,\phi,\phi_a,\beta) \tag{3.63}$$

where the dependence of g on the aggregate shape is captured through β and the dependence on γ must be included again to cover the case of ellipsoidal aggregates. Nevertheless, it has to be said that dependences on γ and ϕ are weak. Consequently, the yield stress will happen at the maximum of the function $2\gamma/(1+\gamma^2)^2$ that is around 0.58.

Two main factors control the (yield) stress. In first place, it is proportional to the external magnetic field squared due to the linear magnetic behavior previously assumed. In second place, despite the fact that aggregates are supposed not to interact with each other, the stress is not a linear function of the volume fraction. The explanation for this is that as ϕ gets closer to ϕ_a, the aggregates tend to fill the whole sample volume. Consequently, at $\phi = \phi_a$ the whole sample is a gap-spanning homogeneous aggregate (since internal structure is not taken into account) that do not change its energy under the external field as it is strained (i.e. there is not any difference between an unbounded homogeneous body that is strained or not).

The comparison between the macroscopic models and experimental data on the yield stress of CMRFs is not satisfactory [112]. Similar to what happened with the first approximation using the one-way coupling scheme, the theoretical predictions are below the experimental data. Clearly, a good match was not expected at intermediate-high fields when particles are partially or fully saturated as the model was thought for linear media. However, the agreement is not good neither at low fields when the particles fulfill this requisite. The main problem is the absence of interactions between neighbor aggregates and of multipolar contributions in the model. The latter will enhance the local field in the particle poles and gaps hence increasing the magnetic field in these regions. On the contrary, the model assumes that the field inside of the sample is homogeneous and determined by μ_{zz} what cannot approximate the real field distribution of the field in the aggregates. Despite this finding, macroscopic models do agree very well when compared with experiments on IFFs [107,112]. The fact that FFs have a much smaller permeability

than ferromagnetic particles used in CMRFs allows neglecting multipoles (see Fig. 3.3) and therefore the macroscopic model properly works because it is not crucial to know the exact position of every particle. The agreement with IFFs is good not only regarding the field dependence but also regarding the volume fraction dependence. It can also be seen an experimental maximum in the yield stress with the volume fraction that is also anticipated theoretically by Eq. (3.63) [107]. Besides, it must be said that these macroscopic models have been also derived for the case of non-linear materials (thus involving a numerical resolution) and grounding the computation of the force on the Maxwell's stress tensor [114]. In this case, the agreement with experiments on CMRFs is comparable with that provided by microscopic methods exposed in Sec. 3.4.2.2.

Finally, it is also worth mentioning a last approximation for the pre-yield behavior based on the continuum theory at small strains. In this context, the CMRF is seen as a homogeneous body with a field-independent anisotropic permeability tensor but now independent of the aggregate shape. In fact, the model does not assume the existence of aggregates but anisotropy in the magnetic permeability [115]. Of course, the preferred direction is that along the field-induced aggregates that changes when the body is sheared. By computing how the permeability tensor changes with the strain (something that is accessible experimentally), it is possible to compute the rheological constitutive equation of the material. Although the model is limited to linear materials and small strains, the major advantage behind this formalism is that it does not require a microscopic description of the sample, that is, it does not depend on the particle shape/size neither magnetization mechanism (dipolar o multipolar terms) or plausible forces between particles (non-/hydrodynamics ones) that played a role in the eventual particle structure.

3.4.2.2 *Microscopic models*

In the microscopic approaches the position of each particle is imposed for every applied strain. This allows computing the magnetic field distribution from Maxwell equations, (Eqs. (3.34) and (3.35)), from this the magnetic force between particles (Eq. (3.38)) for each strain and finally the constitutive relationship $\tau = f(\gamma)$ to identify the yield stress from the maximum of the curve. *A priori*, any particle configuration could be solved, however this is a hard task, even for a few particles, due to the necessity of imposing boundary conditions (Eqs. (3.36) and (3.37)). Only in the case of linear materials, methods based on multipolar expansions that always include a finite number of multipoles L (L-th order solution) have been implemented [49,50].

In the case of non-linear materials such as CMRFs, the most frequent choice is to use FEM to numerically solve Maxwell equations without any further approximation [54,116-120]. However, the high computational cost associated to FEM has restricted the study to strong symmetric systems; in particular, periodic arrangements. Their main advantage is that they can approximate the CMRF only computing the magnetic field distribution around one or two particles in a unit cell whose dimensions are chosen according to the volume fraction.

Due to the small number of explicitly simulated particles, the effects of neighbors (rest of dispersed particles in the CMRF) can be accounted for using the appropriate boundary conditions. These must be fulfilled regardless the strain in the particle arrangement, thus when boundary conditions are imposed, it must be taken into consideration what kind of particle arrangement they are giving rise to and whether it resembles the experimental one or not. This requirement usually limits the type of shear strain to the very simple

affine shear mode where particles maintain constant their positions in the z and x directions while the y component is changed as $y = \gamma z$ (see Fig. 3.5b).

In view of the structures experimentally reported (see Sec. 3.4.1), the natural choice for the periodic arrangement would be the 3D tetragonal lattice with body centered basis that evolves to a monoclinic one when it is sheared. However, only a few works really simulate a 3D lattice [121-123]. Furthermore, these works deal with linear materials. Undoubtedly, the preferred geometry is the axisymmetric model originally proposed by Ginder and Davis [43], which later has been extensively used or adapted by many other authors [116,117,119,124,125].

Once the cylindrical symmetry is applied, Ginder and Davis' model approximates the 3D tetragonal lattice by an infinite chain of particles aligned with the external field and centered in a cylindrical computational domain. As boundary conditions, they impose mirror symmetries on the lateral wall of the cylinder, i.e. the total field normal to this wall is zero. This cylindrical geometry and mirror boundary conditions are kept for any strain because affine shear strain is modeled with a two-step process: first the chain is elongated at constant volume fraction and then the stress along the chain axis is projected analytically in the shear direction (chain rotation) to compute τ.

In this dissertation, from Chapter 5 to Chapter 8, we propose an improved method over this classical work, thus it is worthwhile to pause here in order to see the main approximations and related shortcomings of the classical approach. The first one clearly is that a 3D tetragonal or monoclinic lattice is not axisymmetric. Supposing this symmetry together with mirror boundary conditions forces the chain axis and particle magnetization to be parallel. This picture could resemble, to some extent, the real structure only in the non-strained state (tetragonal lattice). However, at strains different from zero it is not possible to know, *a priori*, the total field direction at the boundaries due to the lack of symmetry in the real system (the applied field is pointing in the z direction but the chain axis is not). Therefore, supposing that in a strained lattice mirror symmetries are still valid can lead to interchain interactions quite different from those that truly occur.

With respect to chain rotation, two major approximations are done in Ginder and Davis' work. The first one is the aforementioned two-step process to model the affine motion. This is a geometrical approximation to keep the model axisymmetric but it only works at small strains. Hence, its extension to large strains, as it is done in Ginder and Davis' work, is questionable. The second approximation is related to the anisotropic behavior of magnetic interaction. Due to the axial symmetry, in classical simulations the applied magnetic field, the chain axis and the particle magnetization are all aligned for any strain. As a consequence, the simulated interaction between particles placed in the same chain is always attractive and aligned with the chain axis, that is, the force acts through the line which connects the particles as if it were a central force. However, the magnetic interaction is not central (see Sec. 3.2.1, Eq. (3.49)) and magnetization direction is not given by the chain axis but by the total magnetic field inside the particle (unknown *a priori*). Thus, computing the shear force simply projecting in this direction as it is done in the classical model does not seem to be a good method neither.

In Chapter 5, a new 3D method based on periodic boundary conditions and a background field formulation is introduced to overcome these shortcomings. In addition, in Chapter 7 it is investigated the physical meaning of assuming as right the Ginder and Davis' model assumptions.

Despite the previously noted deficiencies, the classical work of Ginder and Davis was capable to address (probably, for the first time) the effects of the non-linear magnetic properties of the particles on the CMRF yield stress: due to the presence of multipoles, the magnetic field is enhanced in the gaps present between the particles. As a consequence, the particle polar regions start to saturate so they cannot increase more their magnetization level. This eventually explains why the interparticle force saturates as well.

In striking contrast to the macroscopic models, the microscopic ones (solved using FEM) can reproduce the experimental dependence of the yield stress on the external magnetic field. This is basically because they can take into consideration the non-linear magnetization of the particles. Regarding the quantitative comparison to experiments, a good agreement, at least in the order of magnitude, can be seen in Figure 1b of Ref. [126] for several works of the specialized literature. However, some care should be taken in these comparisons since FEM simulations are not typically carried out using representative values of the particle permeability. For example, in the aforementioned Ref. [126], $\mu_i = 71$ although the use of this particular value requires including an interparticle gap (i.e. a non-magnetic shell [51]), to reproduce experimental measured permeabilities (which are much more smaller, around 10, see Fig. 4.1 for instance). However such an interparticle gap is not included in the simulations. The situation is aggravated in many other works where this gap is neither considered and $\mu_i = 1000$ is taken. Thus, the good agreement between classical FEM simulations and experiments could be based on the fact that classical FEM approximations are balanced by a non-realistic permeability choice. In Chapter 6, the effect of the interparticle gap on the yield stress is evaluated when the particle permeability is imposed to be $\mu_i = 1000$ and $\mu_i \sim 10$.

Experimental and numerical trends of the yield stress against the external field strength have been also corroborated from an analytical point of view. These theoretical analyses have been applied to a simple system consisting of one isolated chain but introducing the non-linear magnetic behavior of the particles. In summary, three regions are identified:

$$\tau_0 = \begin{cases} c_1 \mu_0 H_{ext}^2 \phi & \text{Low fields} \\ c_2 \mu_0 M_S^{1/2} H_{ext}^{3/2} \phi & \text{Intermediate fields} \\ 0.086 \mu_0 M_S^2 \phi & \text{High fields [127]} \end{cases} \tag{3.64}$$

where M_S is the saturation magnetization of the particles and the proportional constants depend upon the reference [116,127].

As it can be seen, the three reminiscent regimes of the particle magnetization behavior (see Fig. 3.2) appear also theoretically. The frontiers between linear, sub-quadratic (transition) and saturated regimes are difficult to be established. Indeed, they depend on the constitutive equation and preassembled structure of the particles among others. Actually, the sub-quadratic dependence is only a particular case because the exponent of H_{ext} continuously changes from 2 to 0 as the particles saturate from their poles till their center [128]. Note that, in any regime, the yield stress is always proportional to the volume fraction. This comes from initially supposing isolated non-interacting chains. Assuming a homogeneous distribution of chains, it can be shown that the area per chain w^2 goes as $w^2 \propto \phi^{-1}$, thus $\tau_0 = F_m / w^2 \propto \phi$ [129].

Finally, with the same goal than in the previous analytical derivation, some models based on the MMA (usually neglecting local field computation) for the yield stress of an isolated chain have been proposed as well. In general, the yield stress can be written as:

$$\tau_0 = c_3 \mu_0 M^2 \phi \tag{3.65}$$

where $M = 3\beta H_{ext}$ in the linear regime (see Eq. (3.44)) or $M = M_S$ in the saturation regime. c_3 is a proportionality constant that depends on the particular assumptions made: $c_3 = 0.086$ for the axisymmetric model [127], $c_3 = 0.114$ for a pair or particles [130], $c_3 = 0.123$ for a semi-infinite chain [131]) or $c_3 = 0.274$ for the force experienced by one particle in the chain [132]. In Chapter 8, a similar method to the one used in the previous references is used to compute the yield stress of an isolated chain of saturated particles under a true shear strain motion. More complex models can be also found, for example in Ref. [133], where the yield stress considering multipoles is computed for a pair of linear particles, or in Ref. [131], where a 'bead-rod' model is regarded resulting in a yield stress that is dependent on the size of the sample.

3.4.3 Post-yield regime. Shear thinning behavior

When the applied shear stress overcomes the static yield stress, the structure cannot bear it and consequently breaks. At this stage, the sample starts to flow and the shear stress consists of the last four terms in Eq. (3.58). This equation can be rearranged as follows:

$$\tau = \left(\eta_c + \frac{6\phi}{\pi d^3}\frac{\langle \tilde{S}_h \rangle_{zy}}{\dot{\gamma}}\right)\dot{\gamma} + \left(\langle \widetilde{xF} \rangle_{zy} + \frac{6\phi}{\pi d^3}\langle \tilde{S}_p \rangle_{zy}\right) = \eta_h \dot{\gamma} + \tau_p \tag{3.66}$$

where the different terms have been grouped depending on whether they are proportional to $\dot{\gamma}$ (first bracket that we will call 'hydrodynamic' contribution η_h) or proportional to the non-hydrodynamic forces $F_{nh} = F_d$ (second bracket or 'particle' contribution τ_p).

According to the definitions of the stresslets $\langle \tilde{S}_h \rangle$ and $\langle \tilde{S}_p \rangle$ (Eq. (3.56)) and the $\langle \widetilde{xF} \rangle$ term (Eq. (3.57)), it can be seen that neither η_h nor τ_p depends explicitly on $\dot{\gamma}$. However, it should be born in mind that all those terms do depend on the particle microstructure and this one is eventually affected by $\dot{\gamma}$, thus it should be written $\eta_h = \eta_h(\phi, \dot{\gamma})$ and $\tau_p = \tau_p(\phi, \dot{\gamma})$. What is more, taking into account that τ_p is proportional to F_d and this is, at the same time, proportional to M^2 (see Eqs. (3.48)-(3.50)), it can be further written $\tau_p = f(\phi, \dot{\gamma})M^2$. Note that, if the dependence on $\dot{\gamma}$ through the microstructure is neglected, CMRFs would follow a plastic Bingham model.

It is well known in the Rheology community that the use of material functions (such as the shear viscosity in a simple shear flow) is more convenient than the use of the stress itself. Simply dividing Eq. (3.66) by $\dot{\gamma}$ and bearing in mind the aforementioned dependencies on ϕ, $\dot{\gamma}$ and M^2 we arrive to:

$$\eta = \frac{\tau}{\dot{\gamma}} = \eta_h(\phi, \dot{\gamma}) + f(\phi, \dot{\gamma})\frac{M^2}{\dot{\gamma}} \tag{3.67}$$

The ratio $M^2/\dot{\gamma}$ is traditionally introduced through dimensional analysis. It is the so-called Mason number Mn and can be conceived as the ratio between hydrodynamic (drag) and magnetostatic force scales, advection and magnetic-controlled velocity/ times scales, etc. In this dissertation, the first option is chosen and therefore:

$$\mathrm{Mn} = \frac{72\eta_c \dot{\gamma}}{\mu_0 \mu_{cr} M^2} \tag{3.68}$$

With this and calling $\eta_\infty(\phi)$ the limiting behavior of $\eta_h(\phi, \dot{\gamma})$ at large Mn (see below) the CMRF viscosity can be made dimensionless:

$$\frac{\eta}{\eta_\infty(\phi)} = \frac{\eta_h(\phi,\dot{\gamma})}{\eta_\infty(\phi)} + \frac{\mathrm{Mn}^*(\phi,\dot{\gamma})}{\mathrm{Mn}} \tag{3.69}$$

where a critical Mason number has been introduced to bring the different constants together:

$$\mathrm{Mn}^*(\phi,\dot{\gamma}) = \frac{72\eta_c\tau_p(\phi,\dot{\gamma})}{\mu_0\mu_{cr}M^2\eta_\infty(\phi)} \tag{3.70}$$

In Fig. 3.6, the dimensionless viscosity η/η_∞ for a given ϕ is sketched together with the contributions from the functions $\eta_h(\phi,\dot{\gamma})$ and $\tau_p(\phi,\dot{\gamma})$. This figure must be regarded as a qualitative description to roughly catch the viscosity behavior since it is only adapted from SD results given in Ref. [17] for a monolayer of particles with linear polarization behavior. Till three regions are usually differentiated. By analyzing them, it is possible to give the proper physical meaning to the previously introduced functions $\tau_p(\phi,\dot{\gamma})$ and $\eta_h(\phi,\dot{\gamma})$.

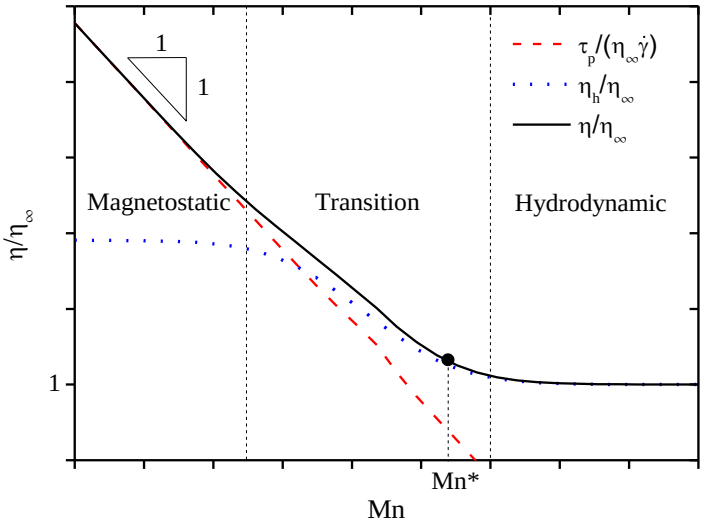

Figure 3.6: Sketch adapted from numerical results in Ref. [17] showing the behavior of the dimensionless viscosity, hydrodynamic and particle contributions as a function of Mn. Logarithmic scale is used in both axes.

At low Mn (the borderline being dependent on ϕ), particle motion is expected to be fully governed by the magnetostatic forces since they are much greater than the drag created by $\dot{\gamma}$. Thus, when the CMRF starts to flow, the initial aggregates induced by the magnetic field will start to rupture and reattach in more relaxed configurations. However, this re-configuration of the particles takes place almost instantaneously, or in other words, at a time scale that is much smaller than the time scale related to $\dot{\gamma}$. Consequently the microstructure, and with it $\tau_p(\phi,\dot{\gamma})$, are both independent on $\dot{\gamma}$ [110]. In addition, according to Fig. 3.6, the contribution from $\eta_h(\phi,\dot{\gamma})$ (blue dotted line) is several orders of magnitude smaller than the $\tau_p(\phi,\dot{\gamma})$ contribution and then negligible [8,17]. These two facts imply that, at low Mn, the CMRF stress level is only given by $\tau_p(\phi,\dot{\gamma}) = \tau_y(\phi)$, that is, in the magnetostatic regime, the function $\tau_y(\phi)$ truly stands for a dynamic yield stress generated by the continuously (and almost instantaneously) rearrangement of the particles [89]. From here and remembering that $\tau_p(\phi,\dot{\gamma})$ is proportional to M^2, it is

straightforward to see that the viscosity will diverge as Mn decreases in the magnetostatic regime: $\eta = \tau/\dot{\gamma} \sim \tau_y(\phi)/\dot{\gamma} = f(\phi)M^2/\dot{\gamma} \propto f(\phi)/\mathrm{Mn}$.

On the contrary, in the hydrodynamic regime at large Mn, particles are dragged by the fluid flow without any significant influence from magnetostatics: $F_{mag}/\dot{\gamma} \propto 1/\mathrm{Mn} \sim 0$ (see Eq. (3.50) for the definition of F_{mag}). Hence, the suspension behaves as it would consist of non-interacting spheres. This makes $\tau_p(\phi,\dot{\gamma})/\dot{\gamma} \sim 0$ but also establishes $\dot{\gamma}$ as the only driving parameter in the CMRF dynamics. Bearing in mind that Stokes flow is linear in its driving parameters, it is expected that $\langle \tilde{S}_h \rangle \propto \dot{\gamma}$ (regardless the particle microstructure or ϕ). Introducing this in the first bracket of Eq. (3.66), it is seen that η_h does not depend on $\dot{\gamma}$ in the hydrodynamic regime, thus: $\eta_h(\phi,\dot{\gamma}) = \eta_\infty(\phi)$ as it was previously anticipated. Because of the fact large Mn values are usually reached by applying large shear rates, $\eta_\infty(\phi)$ is known as the high shear rate viscosity.

Finally, increasing Mn over the transition regime is expected to trigger particles separation from aggregates. As the aggregate size is reduced, they offer less resistance to the flow and thus viscosity decreases as well. Ideally, the typical size of the aggregates continuously goes down until $\mathrm{Mn} = \mathrm{Mn}^*$ when it can be considered that pair of particles are forming and breaking continuously in the CMRF [134]. Note that in this regime, due to the interplay between the particle microstructure and the different stresslets of Eq. (3.66), it is not easy to extract any information about $\eta_h(\phi,\dot{\gamma})$ or $\tau_p(\phi,\dot{\gamma})$.

To do so, it is necessary to turn to numerical studies that are capable to discern the different contributions to the shear stress (or viscosity) such as SD [17] or two-way coupling schemes [8]. Results from this kind of studies were sketched in Fig. 3.6. As it can be seen in the transition regime, the particle contribution $\tau_p/(\eta_\infty\dot{\gamma})$ (red dashed line) is roughly proportional to $1/\mathrm{Mn}$. This means, that its behavior in the magnetostatic regime (that can be predicted analytically) is applicable also at intermediate Mn.

Regarding the hydrodynamic contribution, a more complicated behavior is observable due to the destruction of the field-induced structure. However, the high computational cost required to study this regime (that is, modeling a large number of particles with a complete description of hydrodynamic and magnetostatic interactions) has precluded a deeper and more detailed understanding of it. Currently, what is done in the literature is to extrapolate the behavior of the hydrodynamic contribution away from the hydrodynamic regime, i.e., to assume that $\eta_h(\phi,\dot{\gamma}) = \eta_\infty(\phi)$ for any Mn. Obviously, this approximation is appropriate in the magnetostatic regime. However, it may not be valid in the transition regime unless $\eta_h(\phi,\dot{\gamma}) \ll \tau_p/(\eta_\infty\dot{\gamma})$ [8].

Under this scenario, Eqs. (3.69) and (3.70) are strongly simplified since now, only dependencies on ϕ are kept:

$$\frac{\eta}{\eta_\infty(\phi)} = 1 + \frac{\mathrm{Mn}^*(\phi)}{\mathrm{Mn}} \tag{3.71}$$

$$\mathrm{Mn}^*(\phi) = \frac{72\eta_c\tau_y(\phi)}{\mu_0\mu_{cr}M^2\eta_\infty(\phi)} \tag{3.72}$$

Equations (3.71) and (3.72) show that, under conditions referred in the previous paragraph, the flow behavior of CMRFs follows the Bingham model and depends only on Mn and ϕ. Furthermore, this last dependence is solely contained in Mn^*. According to this, the flow curve of any CMRF has the same shape than the one plotted in Fig. 3.6.

The only effect of ϕ is to shift the curve (and the frontiers between the three regimes) in the x-axis according to the value of Mn^* (see point in Fig. 3.6).

Numerous experimental works in magnetic colloids [107,119,131,135-141] and, in minor extent, simulation ones [19,27,33,142] works have tried to collapse viscosity data in a master curve following Eq. (3.71). In general, the data do not exactly follow that trend; instead, they can be better fitted as $\eta/\eta_\infty = 1 + (\mathrm{Mn}^*/\mathrm{Mn})^\Delta$ with Δ ranging from 2/3 to 1. The origin of this expression is not physical but just a relaxed version of Eq. (3.71) to get a better fit. Actually, a perfect agreement is not expected neither since the Bingham model arose from the supposition that both η_∞ and τ_y do not depend on $\dot{\gamma}$ and hence involves a certain grade of approximation, especially in the transition regime.

Other experimental sources of error can appear as well. For example, it is impossible to guarantee that non-hydrodynamic forces will be exclusively the magnetostatic ones in any CMRFs. This fact can introduce new factors not accounted for in this section that probably will have a deeper effect in the transition regime (when neither magnetostatics nor hydrodynamics dominate) [17]. To enhance the fitting in this regime, other macroscopic models such as the Casson one or the microstructural viscosity model proposed in [143] have been used.

3.4.3.1 *Critical Mason number*

Equation (3.71) offers a route to test experimental and simulation data on any MRF subjected to (steady simple shear) flow. However, until now, it has a very limited predictive utility because nothing has been said about the functional form of $\mathrm{Mn}^*(\phi)$. Looking at Eq. (3.72) it can be seen that, indeed, both $\eta_\infty(\phi)$ and $\tau_y(\phi)$ dependences are needed separately.

The determination of $\eta_\infty(\phi)$ has been extensively addressed in the literature under the context of the calculation of the high shear viscosity of non-Brownian Hard Sphere suspensions. The solution was provided by Einstein [1] for low volume fractions ($\phi < 0.05$). In this concentration regime the particles do not interact, even hydrodynamically, and the stresslet $\langle \tilde{S}_h \rangle$ in Eq. (3.66) can be identified with the stresslet of an isolated particle (Eq. (3.18)), hence:

$$\eta_\infty(\phi) = \eta_c + \frac{6\phi}{\pi d^3}\frac{\langle \tilde{S}_h \rangle_{zy}}{\dot{\gamma}} = \eta_c + \frac{6\phi}{\pi d^3 \dot{\gamma}}\frac{5}{6}\pi\eta_c d^3 \langle \tilde{E} \rangle_{zy}$$
$$= \eta_c\left(1 + \frac{5}{2}\phi\right) \tag{3.73}$$

Here it has been taken into consideration that $\langle \tilde{E} \rangle = \tilde{E}_\infty$ (the imposed macroscopic shear rate) and $\tilde{E}_\infty$ is given by Eq. (3.59). The calculation of $\eta_\infty(\phi)$ for larger concentrations is more complicated. It involves non-negligible hydrodynamic interactions that require simulation techniques to be solved. As it has already been pointed out, these simulations are highly time/computational consuming and not always offer results comparable to experimental data due to the further required simplifications needed to implement them numerically. Alternatively, several phenomenological expressions have been proposed in the literature coming from mean field theories. In this dissertation, the so-called Quemada expression is used [144]:

$$\eta_\infty(\phi) = \eta_c\left(1 - \frac{\phi}{\phi_a}\right)^{-2} \tag{3.74}$$

where $\phi_a = 0.64$ is the randomly closed packing for spheres where viscosity diverges.

Regarding $\tau_y(\phi)$, two main approaches have been followed in the literature: (i) microscopic models and (ii) one-way coupling scheme simulations. In both cases, magnetostatic interactions are supposed to be dipolar while Stokes' drag law is used to model particle-fluid interaction.

Similar to those summarized in Sec. 3.4.2, microscopic models are limited to isolated chains but now subjected to simple shear flows; the application of these models is constrained to the dilute regime. Instead of looking for the maximum of the shear stress as a function of the strain (static yield stress), dipolar and drag forces are balanced in the chain to obtain the dynamic yield stress. Similar to what happened with the static yield stress, working with an isolated chain implies $\tau_y \propto \phi$ whereas the high shear rate is simply $\eta_\infty(\phi) = \eta_c$. Consequently $\mathrm{Mn}^*(\phi) = c_4\phi$ where c_4 is a constant that depends on the particular forces and the specific mechanical stability condition: $c_4 = 5.25$ [131], $c_4 = 8.49$ [137] or $c_4 = 8.82$ [145].

Of course, increasing the particle volume fraction needs the use of numerical simulations. Current work has been done with one-way coupling schemes, accounting for magnetostatic and hydrodynamic interactions only through dipolar (Eq. (3.48)) and Stokes' drag (Eq. (3.21)) forces [129,142,146]. Results from these simulations yield $c_4 = 0.24$.

At this point, it should be questioned whether this kind of simulations, without coupling between particles and fluid, provide a good estimation. *A priori*, only simulations capable to assess the three stresslets $\langle\tilde{S}_h\rangle$, $\langle\tilde{S}_p\rangle$ and $\langle\widetilde{xF}\rangle$, forming part of the total viscosity, should be used. However, as it was previously mentioned, $\langle\tilde{S}_h\rangle$ (through η_∞) is the main contribution to the viscosity only at large Mn [17], when it only depends on the volume fraction and therefore it can be computed analytically from Eqs. (3.73) or (3.74) depending on the concentration. With regards to $\langle\widetilde{xF}\rangle$, it is properly computed in one-way schemes as non-hydrodynamic forces are properly taken into account as well. Main claims could arise from $\langle\tilde{S}_p\rangle$ that requires the use of two-way methods at the expense of higher computational effort and smaller simulated systems.

From an experimental point of view, MRF dominated by magnetostatic dipolar forces (e.g. IFFs), regardless of the volume fraction, and CMRFs in the dilute regime ($\phi \leq 0.05$) show an excellent agreement with previous one-way coupling results. On the contrary, CMRFs at higher concentrations, show that $\mathrm{Mn}^*(\phi)$ is not linear and almost two order of magnitude higher than simulations [129,142,146]. In these references, the disagreement was explained in terms of other non-hydrodynamic colloidal forces present in the experimental samples but not included in the simulations. In Chapter 6, a new explanation will be proposed: only when magnetic multipole and multibody effects are accounted for the static yield stress, this one shows a very good agreement with the experimental dynamic yield stress (i.e., according to Eq. (3.72), with Mn^*). Of course, this does not mean that both yield stresses are interchangeable but could be another evidence that multipole and multibody effects play a crucial role in the rheology of concentrated CMRFs.

As it can be seen, once the dependence $\mathrm{Mn}^*(\phi)$ is known, it is possible to predict the steady shear flow behavior of any CMRF (regardless its volume fraction, the applied shear rate and the applied magnetic field) from Eq. (3.71), that is, it is a master curve. As a consequence, it could be considered that we have a general constitutive rheological

equation for any CMRF. However, it must be taken into consideration that this section is only focused in steady simple shear flows and therefore shear stresses. A true constitutive equation should also describe the rest of the components of the stress tensor (e.g. normal stresses).

3.4.4 Normal stresses

The appearance of non-isotropic normal stresses, as well as normal stress differences, in simple shear flow together with the shear rate-dependent viscosity and the yield stress are classical signatures of non-Newtonian flow behavior. From Eq. (3.58) and taking into account the field-induced anisotropic structures devised in Sec. 3.4.1, it is easy to deduce that MR fluids will have also anisotropic normal stress components in the field/gradient σ_{zz}, shear σ_{yy}, and vorticity σ_{xx} directions (see Fig. 3.4).

These normal stresses play a very important role in MRF applications. They promote the appearance of macroscopic forces in the field direction acting over the walls confining the sample, an enhanced sample-geometry interaction to avoid wall slip, magnetostriction effects, etc. Unfortunately, the difficulties related to their precise measurement have hindered a substantial progress in their understanding and many previous publications in this topic give contradictory results.

To date, experimental work has focused in measuring the normal force (i.e. in the field direction) developed by the sample because it is a magnitude that can be easily accessed experimentally. In all reported cases, a positive normal force is found (i.e. the sample tries to elongate in the field direction) that approximately increases with H_{ext}^2. However, consensus does not seem to be reached regarding the strain/shear rate dependence of the normal force in the pre-/post- yield regime. In the pre-yield regime, some authors found that the normal force grows with the strain till a maximum associated to the yield stress [105,147]. On the contrary, it has also been reported that the normal force is initially maximum and decreases till a minimum when yield stress is reached [148].

From a theoretical/simulation point of view, any of the models presented in Sec. 3.4.2 can be extrapolated to compute the stress in the field direction as it only supposes to redo operations but working with the field-direction component of the force instead of the shear-direction one. Thus, results share the same properties, $\sigma_{zz} \propto \mu_0 M^2 \phi$, and would reproduce qualitatively the experimental trend with the field. On the contrary, the dependence on the volume fraction cannot even be tested as most of the works deal only with one concentration, which in addition is typically very high (0.3-0.5) questioning the subsequent comparison with these models as they were thought in the dilute limit.

Furthermore, any of the aforementioned models predict a negative normal force (i.e. the sample squeezes in the field direction) in the non-strained state since the magnetostatic force between particles in a chain aligned with the field is attractive. It seems that, in order to reproduce experimental trends, it is necessary to include effects related to the finite size of the sample (demagnetization fields [149] and Maxwell's stress jump at the boundaries [148]), plausible magnetic field gradients in the experimental setup and/or defects in the induced structure [52,150,151].

During flow, very different observations have been reported as well. While Refs. [105,152,153] report a monotonic decrease of the normal force with the shear rate, Ref. [148] describes also an initial decrease at low shear rates but followed by an increase that eventually leads to a plateau at high shear rates. Simulation studies of normal stresses under flow are scarce as well. Using SD simulations in a 2D system (areal fraction of 0.4)

Ref. [17] reports $(\sigma_{yy} - \sigma_{zz})/\dot{\gamma} < 0$ at any Mn. This quantity decreases, in absolute value, with Mn till it vanishes in the hydrodynamic regime.

3.5 Some comments on ferrofluids

From Chapter 10 to Chapter 12, a new route to enhance MRFs magnetic response and their stability is proposed based on the addition of another particle population with diameters in the nanometer scale. Thus, as indicated in Sec. 1.1, it could be expected that the resulting systems behave as a FF. In this section a brief overview of the basic FF phenomena in the dilute regime is given. For further details, the reader is referred to more comprehensive works on FFs. See for instance Refs. [111,154,155] and references therein.

The description of FFs can be made following an analogous approach to the one previously used for CMRFs just taking into consideration the new involved features due to the smaller diameter of the particles, namely: (i) single domain magnetic behavior and (ii) control of colloidal forces and Brownian motion over magnetostatic interactions. Next, it will be seen that both features are intimately coupled.

Despite having the same chemical composition, the nanoparticles in a FF exhibit a magnetic response to an external magnetic field that is very different from that of the microparticles in a CMRF. The reason for this is that in the case of FFs, the nanoparticles are so small that they only accommodate a single magnetic domain where all the spins are coupled and aligned in the same direction. Consequently, every particle is permanently magnetized even in the absence of a magnetic field. What is more, as all spins are perfectly aligned, the particle magnetization level does not depend on the total field inside the particle and all particles are fully saturated. As a first order approximation, the saturation value could be identified with the bulk one M_S. However, it is usually smaller due to size effects such as spin canting phenomena and/or the presence of absorbed layers at the atomistic scale [156].

As a result, every particle in a FF can be substituted by a point dipole; the MMA introduced in Sec. 3.2.1 fully applies. Hence, it would be expected that the nanoparticles within a FF experience interparticle dipolar forces, even in the absence of an external field, driving them to build chain-like structures in the direction of their dipole moment. This direction does not have to be the same in all dispersed nanoparticles. Before studying which is the direction of each nanoparticle dipole, it is worthwhile to check the magnitude of these interactions for comparison with the rest of colloidal forces.

This task was already accomplished for CMRFs in Sec. 3.3, however the different sizes of the dispersed particles in CMRFs and FFs introduce again severe changes with respect to the conclusions reached in that section. The main one is that, for FFs, the dominant force is not the magnetostatic one but the Brownian force. This can be easily seen just noting that the ratio between magnetostatic and Brownian forces (Eq. (3.51)) is proportional to volume of the particle, $\lambda \propto d^3$, and thus it falls quickly when the particle diameter is reduced. For typical FFs particle sizes are $d < 10$ nm and $\lambda \sim 0.01$. Thus, although dipolar forces are present in FFs, they are not strong enough to induce interparticle aggregation as any pair of coupled particles will be broken by the Brownian motion.

One can also compare gravity and Brownian forces in an analogous way as already done in Sec. 3.3 for CMRFs. Brownian forces clearly dominate in FFs, again because of the

small particle size. As a result, sedimentation is hindered. Although decreasing particle size improves stability against gravity, it enhances the surface to volume ratio and with this the surface energy.

Therefore, nanoparticles are prone to irreversibly aggregate in order to reduce this surface energy. Obviously, irreversible aggregation is not desirable and thus the synthesis of any FF always involves an additional stabilization step (electrostatic, steric or electrosteric) in order to prevent the particles from closely approaching [155,157]. In the following, it will be supposed that the FF is somehow properly stabilized and then dispersion or surface forces do not have to be considered in order to describe its rheological properties.

According to this discussion, the only non-hydrodynamic force to be taken into account in the motion of FF nanoparticles is the Brownian force. This yields a stochastic equation of motion called Langevin or 'overdamped' Langevin equation depending on whether it includes the inertia term or not [158]. Solving these equations is possible with methods analogous to those shown in Sec. 3.1, for instance, SD [159] or one-way scheme (i.e. Brownian Dynamics) [31].

In Sec. 3.1 it was shown that non-hydrodynamic torques are responsible for a flow distortion and, because of this, for a contribution to the suspension rheology as well. In the case of CMRFs, non-hydrodynamic torques were assumed to be zero since particle magnetization is collinear with the magnetic field. On the contrary, due to their single domain behavior, FF nanoparticles can experience a magnetic non-hydrodynamic torque depending on how its magnetization relaxes, that is, how the dipole direction changes in response to a change in the direction of the external field.

As noted before, reducing the size of a ferro/ferri- magnetic particle below a critical diameter makes the particles to accommodate only one single magnetic domain. As a consequence, all atoms in a particle have their spin pointing in the same direction, the so-called easy axis, even in the absence of an external magnetic field. The direction of this axis is fixed to the particle body by different anisotropy energies (crystalline, surface, etc.) that, in first approximation, can be written as $E = KV_p$ where K is the magnetic anisotropy energy density (for more details see Ref. [160]).

Interestingly, E is proportional to V_p and therefore, reducing the particle size will also reduce E till a point where it can be balanced by the thermal energy $k_B T$. In this case, the easy axis will be fully decoupled from the particle body being able to rotate freely. *A priori*, the critical size to get such a decoupling could be computed by equating $KV_p = k_B T$, however the stochastic nature of the thermal energy makes previous behavior time scale dependent, that is, easy axis fluctuations in the particle body take place within a typical period given by the so-called Néel time:

$$\Delta t_N = \Delta t_0 \exp\left(\frac{KV_p}{k_B T}\right) \tag{3.75}$$

where $\Delta t_0 \sim 10^{-9}$ s. In view of Eq. (3.75), it is important to emphasize the extraordinarily fast increase of Δt_N with V_p, even in the range of nanoparticle sizes. For example, the fluctuation time is around 1.6 μs for a cobalt nanoparticle ($K \sim 0.45$ MJ/m) of diameter 5 nm at $T = 293$ K. However, doubling the particle diameter (10 nm, still in the FF regime) the fluctuation time reaches $1.2 \cdot 10^9$ years.

Δt_N gives an estimation of how frequently the dipole rotates within the particle body. However it should be born in mind that FF nanoparticles are not pinned in the space but

dispersed in the continuous phase and constantly subjected to the Brownian motion. This introduces a second relaxation mechanism for the dipole where the change in its direction is due to the change in the particle orientation during the particle erratic motion. This second mechanism leads to the Brownian relaxation time:

$$\Delta t_B = \frac{3\eta_c V_p}{k_B T} \tag{3.76}$$

which is only linear on V_p. Common values of Δt_B for FFs are in the range of the μs although, as it can be seen in Eq. (3.76), they depend also on the continuous phase viscosity. For the cobalt nanoparticles used in the previous example, supposed to be dispersed in a given silicone oil of $\eta_c = 200$ mPa·s, $\Delta t_B = 18.75$ μs if $d = 5$ nm and $\Delta t_B = 0.15$ ms if $d = 10$ nm.

As both Néel and Brownian mechanisms coexist, after a given time t, the prevailing one will be that with a larger number of realizations, that is, the mechanism with the shorter typical time. In this way, because of the linear and exponential dependences on V_p, large (small) nanoparticles will relax with the time scale Δt_B (Δt_N).

Therefore, the question about whether FF nanoparticles suffer or not a magnetic torque depends on the interplay between Δt_N and Δt_B.Whenever $\Delta t_B < \Delta t_N$ each particle will have a dipole fixed to its body and consequently, under the presence of an external field both dipole and particle will suffer a magnetic torque given by Eq. (3.47). On the contrary, if $\Delta t_N < \Delta t_B$ the dipole will be continuously fluctuating within the particle body. Hence, although the dipole will feel the torque and will try to align accordingly, it will not be able to transmit the torque to the particle since both are uncoupled.

The rheology of FFs consisting of these two kinds of particles has been widely studied. In the case of $\Delta t_N < \Delta t_B$, since there is not a magnetic torque, the dipolar force is negligible and other attractive colloidal interactions are properly compensated via stabilization methods, it can be deduced that the system (a Brownian Hard Spheres suspension) is governed by the competition between Brownian and viscous forces. That is, the same behavior has to be obtained under the presence or absence of an external field. Similar to Mn in CMRFs, a dimensionless number can be defined to describe the system dynamics, namely the Peclet number: $\mathrm{Pe} = 3\eta_c \dot{\gamma} \pi d^3/(4k_B T)$. In short, at small Pe, Brownian motion promotes, by diffusion, an isotropic structure that shows some resistance to be moved from its equilibrium configuration. As Pe increases, the structure breaks and the FF exhibits a slight shear-thinning behavior [161].

When the magnetic torque has to be included (i.e. $\Delta t_B < \Delta t_N$) the rheology is affected by the external field what gives rise to the so-called magnetoviscous effect [162,163]. Qualitatively, if the external field is null, the imposed shear flow ($\hat{y}$ direction) will induce a rotational velocity to the particle in order to make the hydrodynamic torque (see Eq. (3.47)) zero: $\vec{\omega} = \vec{\Omega}_\infty = \hat{x}\,\dot{\gamma}/2$. Since the dipole is fixed, it will rotate solidary with the particle. As soon as the external field is applied in the $\hat{z}$ direction, it will exert a magnetic torque over the particle trying to align it also in the $\hat{z}$ direction. Consequently, the particle will not rotate freely any more inducing a perturbation in the imposed flow field. This perturbation will have a pure strain component, proportional to the magnetic torque, that will be reflected in an increase of the macroscopic viscosity.

Of course, the Brownian motion is also present in this process. On the one hand, when the external field is applied, not all particles will align with it but will be randomly

oriented. As a result, the viscosity will depend on the ratio between the magnetic and Brownian torques $\alpha = \mu_0 \pi d^3 M_S H_{ext}/(6k_B T)$. Note that, while $\lambda \propto M_S^2$ and thus it cannot be externally controlled in FFs, $\alpha \propto H_{ext}$ allowing to reach high values that overcome Brownian motion effects.

On the other hand, it will also play a role in the dipole relaxation. When thermal agitation is large in comparison to the applied shear rate, $\Delta t_B \dot{\gamma} < 1$, particle reorientation will be faster than the induced flow and, regardless the applied $\dot{\gamma}$, the number of dipoles pointing in the $\hat{z}$ direction will be given by α, that is, the magnetoviscous effect will result shear rate independent. To the contrary, if $\Delta t_B \dot{\gamma} \geq 1$ the particle rotational velocity $\vec{\omega}$ and sample viscosity will be determined by both α and $\dot{\gamma}$.

Finally, it is worthwhile to say that viscosity increments much larger than that predicted by the magnetoviscous effect have been reported experimentally, and in some cases a yield stress has also been observed. These phenomena seem to be related to systems poorly stabilized, which promote particle aggregation, or with a secondary particle population (polydisperse systems) with diameters that do not fulfill $\lambda < 1$.

References

[1] Guazzelli, É., and Morris, J. F. A physical introduction to suspension dynamics (Cambridge University Press, Cambridge, 2012).

[2] Hu, H. H., Joseph, D. D., and Crochet, M. J. (1992). Direct simulation of fluid particle motions. Theoretical and Computational Fluid Dynamics, 3(5), 285-306.

[3] Kang, T. G., Hulsen, M. A., den Toonder, J. M., Anderson, P. D., and Meijer, H. E. (2008). A direct simulation method for flows with suspended paramagnetic particles. Journal of Computational Physics, 227(9), 4441-4458.

[4] Kang, T. G., Gao, Y., Hulsen, M. A., den Toonder, J. M., and Anderson, P. D. (2013). Direct simulation of the dynamics of two spherical particles actuated magnetically in a viscous fluid. Computers & Fluids, 86, 569-581.

[5] Hashemi, M. R., Manzari, M. T., and Fatehi, R. (2017). Non-linear stress response of non-gap-spanning magnetic chains suspended in a Newtonian fluid under oscillatory shear test: A direct numerical simulation. Physics of Fluids, 29(10), 107106.

[6] Han, K., Feng, Y. T., and Owen, D. R. J. (2010). Three-dimensional modelling and simulation of magnetorheological fluids. International Journal for Numerical Methods in Engineering, 84(11), 1273-1302.

[7] Gusenbauer, M., and Schrefl, T. (2018). Simulation of magnetic particles in microfluidic channels. Journal of Magnetism and Magnetic Materials, 446, 185-191.

[8] Lagger, H. G., Breinlinger, T., Korvink, J. G., Moseler, M., Di Renzo, A., Di Maio, F., and Bierwisch, C. (2015). Influence of hydrodynamic drag model on shear stress in the simulation of magnetorheological fluids. Journal of Non-Newtonian Fluid Mechanics, 218, 16-26.

[9] Hashemi, M. R., Manzari, M. T., and Fatehi, R. (2016). A SPH solver for simulating paramagnetic solid fluid interaction in the presence of an external magnetic field. Applied Mathematical Modelling, 40(7-8), 4341-4369.

[10] Satoh, A., and Chantrell, R. W. (2006) Application of the dissipative particle dynamics method to magnetic colloidal dispersions. Molecular Physics, 104, 3287–3302.

[11] Gharibvand, A. J., Norouzi, M., and Shahmardan, M. M. (2019). Dissipative particle dynamics simulation of magnetorheological fluids in shear flow. Journal of the Brazilian Society of Mechanical Sciences and Engineering, 41(2), 103.

[12] Happel, J., and Brenner, H. Low Reynolds Number Hydrodynamics (Prentice-Hall. Inc., New Jersey, 1965).

[13] Bossis, G., and Brady, J. F. (1984). Dynamic simulation of sheared suspensions. I. General method. The Journal of Chemical Physics, 80(10), 5141-5154.

[14] Jeffrey, D. J., and Onishi, Y. (1984). Calculation of the resistance and mobility functions for two unequal rigid spheres in low-Reynolds-number flow. Journal of Fluid Mechanics, 139, 261-290.

[15] Brady, J. F., Phillips, R. J., Lester, J. C., and Bossis, G. (1988). Dynamic simulation of hydrodynamically interacting suspensions. Journal of Fluid Mechanics, 195, 257-280.

[16] Durlofsky, L., Brady, J. F., and Bossis, G. (1987). Dynamic simulation of hydrodynamically interacting particles. Journal of Fluid Mechanics, 180, 21-49.

[17] Bonnecaze, R. T., and Brady, J. F. (1992). Dynamic simulation of an electrorheological fluid. The Journal of Chemical Physics, 96(3), 2183-2202.

[18] Krishnamurthy, S., Yadav, A., Phelan, P. E., Calhoun, R., Vuppu, A. K., Garcia, A. A., and Hayes, M. A. (2008). Dynamics of rotating paramagnetic particle chains simulated by particle dynamics, Stokesian dynamics and lattice Boltzmann methods. Microfluidics and Nanofluidics, 5(1), 33-41.

[19] Melrose, J. R., Itoh, S., and Ball, R. C. (1996). Simulations of electrorheological fluids with hydrodynamic lubrication. International Journal of Modern Physics B, 10(23n24), 3211-3217.

[20] Satoh, A., Chantrell, R. W., Coverdale, G. N., and Kamiyama, S. I. (1998). Stokesian dynamics simulations of ferromagnetic colloidal dispersions in a simple shear flow. Journal of Colloid and Interface Science, 203(2), 233-248.

[21] Satoh, A. (2002). Development of effective Stokesian dynamics method for ferromagnetic colloidal dispersions (cluster-based Stokesian dynamics method). Journal of Colloid and Interface Science, 255(1), 98-106.

[22] Joung, C., and See, H. (2007). Simulation of magneto-rheological fluids incorporating hydrodynamic effects. Journal of Central South University of Technology, 14(1), 271-274.

[23] Li, S., Marshall, J. S., Liu, G., and Yao, Q. (2011). Adhesive particulate flow: The discrete-element method and its application in energy and environmental engineering. Progress in Energy and Combustion Science, 37(6), 633-668.

[24] Vågberg, D., and Tighe, B. P. (2017). On the apparent yield stress in non-Brownian magnetorheological fluids. Soft Matter, 13(39), 7207-7221.

[25] Pappas, Y., and Klingenberg, D. J. (2006). Simulations of magnetorheological suspensions in Poiseuille flow. Rheologica Acta, 45(5), 621-629.

[26] Lagger, H. G., Bierwisch, C., Korvink, J. G., and Moseler, M. (2014). Discrete element study of viscous flow in magnetorheological fluids. Rheologica Acta, 53(5-6), 417-443.

[27] Joung, C. G., and See, H. (2008). The influence of wall interaction on dynamic particle modelling of magneto-rheological suspensions between shearing plates. Rheologica Acta, 47(8), 917-927.

[28] Murariu, V. (2013). Simulating a low intensity magnetic separator model (LIMS) using DEM, CFD and FEM magnetic design software. In: Proceedings of 4th International Computational Modelling Symposium (Minerals Engineering International, Cornwall).

[29] Gŏsko D., and Lācis S. (2010). Magnetorheological suspension composed of fiber particles: numerical simulation of anisotropic behavior. In: Proceedings of the International Scientific Colloquium Modelling for Material Processing (University of Latvia, Riga).

[30] Kor, Y. K., and See, H. (2010). The electrorheological response of elongated particles. Rheologica Acta, 49(7), 741-756.

[31] Satoh, A. Modeling of magnetic particle suspensions for simulations (CRC Press, Boca Raton, 2017).

[32] Liu, T., Gu, R., Gong, X., Xuan, S., Wu, H., and Zhang, Z. (2010). Structural and rheological study of magnetic fluids using molecular dynamics. Magnetohydrodynamics, 46(3), 257-269.

[33] Kargulewicz, M., Iordanoff, I., Marrero, V., and Tichy, J. (2012). Modeling of magnetorheological fluids by the discrete element method. Journal of Tribology, 134(3), 031706.

[34] Kittipoomwong, D., Klingenberg, D. J., and Ulicny, J. C. (2005). Dynamic yield stress enhancement in bidisperse magnetorheological fluids. Journal of Rheology, 49(6), 1521-1538.

[35] Sherman, S. G., and Wereley, N. M. (2013). Effect of particle size distribution on chain structures in magnetorheological fluids. IEEE Transactions on Magnetics, 49(7), 3430-3433.

[36] Fernández-Toledano, J. C., Ruiz-López, J. A., Hidalgo-Álvarez, R., and de Vicente, J. (2015). Simulations of polydisperse magnetorheological fluids: A structural and kinetic investigation. Journal of Rheology, 59(2), 475-498.

[37] Klingenberg, D. J., van Swol, F., and Zukoski, C. F. (1991). The small shear rate response of electrorheological suspensions. II. Extension beyond the point–dipole limit. The Journal of Chemical Physics, 94(9), 6170-6178.

[38] Ly, H. V., Reitich, F., Jolly, M. R., Banks, H. T., and Ito, K. (1999). Simulations of particle dynamics in magnetorheological fluids. Journal of Computational Physics, 155(1), 160-177.

[39] Pei, L., Pang, H., Ruan, X., Gong, X., and Xuan, S. (2017). Magnetorheology of a magnetic fluid based on Fe_3O_4 immobilized SiO_2 core–shell nanospheres: experiments and molecular dynamics simulations. RSC Advances, 7, 8142-8150.

[40] Cullity, B. D., and Graham, C. D. Introduction to Magnetic Materials (John Wiley & Sons, Hoboken, 2009).

[41] Reitz, J. R., and Milford, F. J. Foundations of Electromagnetic Theory (Addison-Wesley, Reading, 1960).

[42] Lagger, H. G. PhD thesis. University of Freiburg, Freiburg, 2014.

[43] Ginder, J. M., and Davis, L. C. (1994). Shear stresses in magnetorheological fluids: role of magnetic saturation. Applied Physics Letters, 65(26), 3410-3412.

[44] Panofsky, W. K. H., and Phillips, M. Classical Electricity and Magnetism (Addison-Wesley, Reading, 1962).

[45] Rankin, P. J., Ginder, J. M., and Klingenberg, D. J. (1998). Electro-and magneto-rheology. Current Opinion in Colloid & Interface Science, 3(4), 373-381.

[46] Landau, L. D., and Lifshitz, E. M. Electrodynamics of Continuous Media (Pergamon Press, Elmsford, 1984).

[47] Franklin, J. Classical Electromagnetism (Pearson Addison Wesley, San Francisco, 2005).

[48] López-López, M. T., Kuzhir, P., Caballero-Hernandez, J., Rodríguez-Arco, L., Duran, J. D., and Bossis, G. (2012). Yield stress in magnetorheological suspensions near the limit of maximum-packing fraction. Journal of Rheology, 56(5), 1209.

[49] Bonnecaze, R. T., and Brady, J. F. (1990). A method for determining the effective conductivity of dispersions of particles. Proceedings of the Royal Society of London. Series A: Mathematical and Physical Sciences, 430(1879), 285-313.

[50] Clercx, H. J. H., and Bossis, G. (1993). Many-body electrostatic interactions in electrorheological fluids. Physical Review E, 48(4), 2721.

[51] de Vicente, J., Bossis, G., Lacis, S., and Guyot, M. (2002). Permeability measurements in cobalt ferrite and carbonyl iron powders and suspensions. Journal of Magnetism and Magnetic Materials, 251(1), 100-108.

[52] Han, Y., Hong, W., and Faidley, L. E. (2013). Field-stiffening effect of magneto-rheological elastomers. International Journal of Solids and Structures, 50(14-15), 2281-2288.

[53] Javili, A., Chatzigeorgiou, G., and Steinmann, P. (2013). Computational homogenization in magneto-mechanics. International Journal of Solids and Structures, 50(25-26), 4197-4216.

[54] Vereda, F., Segovia-Gutiérrez, J. P., de Vicente, J., and Hidalgo-Álvarez, R. (2014). Particle roughness in magnetorheology: effect on the strength of the field-induced structures. Journal of Physics D: Applied Physics, 48(1), 015309.

[55] Jones, T. B. Electromechanics of particles (Cambridge University Press, New York, 1995).

[56] Davis, L. C. (1992). Ground state of an electrorheological fluid. Physical Review A, 46(2), R719.

[57] Hunter, R. J. Foundations of colloid science (Oxford University Press, New York, 2001).

[58] Israelachvili, J. N. Intermolecular and surface forces. (Academic Press, San Diego, 2011).

[59] Klingenberg, D. J., Olk, C. H., Golden, M. A., and Ulicny, J. C. (2010). Effects of nonmagnetic interparticle forces on magnetorheological fluids. Journal of Physics: Condensed Matter, 22(32), 324101.

[60] Klingenberg, D. J., Ulicny, J. C., and Smith, A. L. (2007). Effects of body forces on the structure and rheology of ER and MR fluids. International Journal of Modern Physics B, 21(28n29), 4841-4848.

[61] Guazzelli, É., and Pouliquen, O. (2018). Rheology of dense granular suspensions. Journal of Fluid Mechanics, 852, P1.

[62] Mari, R., Seto, R., Morris, J. F., and Denn, M. M. (2014). Shear thickening, frictionless and frictional rheologies in non-Brownian suspensions. Journal of Rheology, 58(6), 1693-1724.

[63] Batchelor, G. K. (1970). The stress system in a suspension of force-free particles. Journal of Fluid Mechanics, 41(3), 545-570.

[64] Irving, J. H., and Kirkwood, J. G. (1950). The statistical mechanical theory of transport processes. IV. The equations of hydrodynamics. The Journal of Chemical Physics, 18(6), 817-829.

[65] Klingenberg, D. J., Van Swol, F., and Zukoski, C. F. (1989). Dynamic simulation of electrorheological suspensions. The Journal of Chemical Physics, 91(12), 7888-7895.

[66] Mohebi, M., Jamasbi, N., and Liu, J. (1996). Simulation of the formation of nonequilibrium structures in magnetorheological fluids subject to an external magnetic field. Physical Review E, 54(5), 5407.

[67] Ukai, T., and Maekawa, T. (2004). Patterns formed by paramagnetic particles in a horizontal layer of a magnetorheological fluid subjected to a dc magnetic field. Physical Review E, 69(3), 032501.

[68] Fraden, S., Hurd, A. J., and Meyer, R. B. (1989). Electric-field-induced association of colloidal particles. Physical Review Letters, 63(21), 2373.

[69] Fermigier, M., and Gast, A. P. (1992). Structure evolution in a paramagnetic latex suspension. Journal of Colloid and Interface Science, 154(2), 522-539.

[70] Shahrivar, K., Carreón-González, E., Morillas, J. R., and de Vicente, J. (2017). Aggregation kinetics of carbonyl iron based magnetic suspensions in 2D. Soft Matter, 13(14), 2677-2685.

[71] Liu, J., Lawrence, E. M., Wu, A., Ivey, M. L., Flores, G. A., Javier, K., Bibette, J., and Richard, J. (1995). Field-induced structures in ferrofluid emulsions. Physical Review Letters, 74(14), 2828.

[72] Martin, J. E., Odinek, J., and Halsey, T. C. (1992). Evolution of structure in a quiescent electrorheological fluid. Physical Review Letters, 69(10), 1524.

[73] Martin, J. E., Hill, K. M., and Tigges, C. P. (1999). Magnetic-field-induced optical transmittance in colloidal suspensions. Physical Review E, 59(5), 5676.

[74] Günther, D., Borin, D. Y., Günther, S., and Odenbach, S. (2011). X-ray micro-tomographic characterization of field-structured magnetorheological elastomers. Smart Materials and Structures, 21(1), 015005.

[75] Shahrivar, K., Carreón-González, E., and de Vicente, J. (2017). Effect of Confinement on the Aggregation Kinetics of Dilute Magnetorheological Fluids. Smart Materials and Structures, 26(10), 105031.

[76] Tao, R., and Sun, J. M. (1991). Three-dimensional structure of induced electrorheological solid. Physical Review Letters, 67(3), 398.

[77] Chen, T. J., Zitter, R. N., and Tao, R. (1992). Laser diffraction determination of the crystalline structure of an electrorheological fluid. Physical Review Letters, 68(16), 2555.

[78] Dassanayake, U., Fraden, S., and Van Blaaderen, A. (2000). Structure of electrorheological fluids. The Journal of Chemical Physics, 112(8), 3851-3858.

[79] Hynninen, A. P., and Dijkstra, M. (2005). Phase diagram of dipolar hard and soft spheres: Manipulation of colloidal crystal structures by an external field. Physical Review Letters, 94(13), 138303.

[80] Cutillas, S., Bossis, G., and Cebers, A. (1998). Flow-induced transition from cylindrical to layered patterns in magnetorheological suspensions. Physical Review E, 57(1), 804.

[81] Swan, J. W., Bauer, J. L., Liu, Y., and Furst, E. M. (2014). Directed colloidal self-assembly in toggled magnetic fields. Soft Matter, 10(8), 1102-1109.

[82] Bauer, J. L., Kurian, M. J., Stauffer, J., and Furst, E. M. (2016). Suppressing the Rayleigh–Plateau Instability in Field-Directed Colloidal Assembly. Langmuir, 32(26), 6618-6623.

[83] Bossis, G., Volkova, O., Lacis, S., and Meunier, A. (2002). Magnetorheology: fluids, structures and rheology. In: Odenbach, S. (Ed.) Ferrofluids. Lecture Notes in Physics (Vol. 594) (Springer, Berlin).

[84] Hackley, V. A., and Ferraris, C. F. Guide to rheological nomenclature: Measurements in ceramic particulate systems (National Institute of Standards and Technology, Gaithersburg, 2001).

[85] Wang, Z., Shahrivar, K., and de Vicente, J. (2014). Creep and recovery of magnetorheological fluids: Experiments and simulations. Journal of Rheology, 58(6), 1725-1750.

[86] Barnes, H. A., and Walters, K. (1985). The yield stress myth?. Rheologica Acta, 24(4), 323-326.

[87] Barnes, H. A. (1999). The yield stress—a review or ‘παντα ρει’—everything flows?. Journal of Non-Newtonian Fluid Mechanics, 81(1-2), 133-178.

[88] Møller, P. C., Mewis, J., and Bonn, D. (2006). Yield stress and thixotropy: on the difficulty of measuring yield stresses in practice. Soft Matter, 2(4), 274-283.

[89] Mewis, J., and Wagner, N. J. Colloidal suspension rheology (Cambridge University Press, New York, 2012).

[90] Laun, H. M., Kormann, C., and Willenbacher, N. (1996). Rheometry on magnetorheological (MR) fluids. Rheologica Acta, 35(5), 417-432.

[91] Laun, H. M., Gabriel, C., and Kieburg, C. (2010). Twin gap magnetorheometer using ferromagnetic steel plates - performance and validation. Journal of Rheology, 54(2), 327-354.

[92] Kim, M. S., Liu, Y. D., Park, B. J., You, C.-Y., and Choi, H. J. (2012). Carbonyl iron particles dispersed in a polymer solution and their rheological characteristics under applied magnetic field. Journal of Industrial and Engineering Chemistry, 18, 664–667.

[93] Bombard, A. J., Gonçalves, F. R., and de Vicente, J. (2015). Magnetorheology of carbonyl iron dispersions in 1-Alkyl-3-methylimidazolium ionic liquids. Industrial & Engineering Chemistry Research, 54, 9956-9963.

[94] Dong, Y. Z., Piao, S. H., Zhang, K., and Choi, H. J. (2018). Effect of CoFe2O4 nanoparticles on a carbonyl iron based magnetorheological suspension. Colloids and Surfaces A: Physicochemical and Engineering Aspects, 537, 102–108.

[95] Parziale, A. J., and Tilton, P. D. (1950). Characteristics of some magnetic-fluid clutch servomechanisms. Transactions of the American Institute of Electrical Engineers, 69(1), 150-157.

[96] Chin, B. D., Park, J. H., Kwon, M. H., and Park, O. O. (2001). Rheological properties and dispersion stability of magnetorheological (MR) suspensions. Rheologica Acta, 40(3), 211-219.

[97] Park, J. H., Chin, B. D., and Park, O. O. (2001). Rheological properties and stabilization of magnetorheological fluids in a water-in-oil emulsion. Journal of Colloid and Interface Science, 240(1), 349-354.

[98] Genç, S., and Phulé, P. P. (2002). Rheological properties of magnetorheological fluids. Smart Materials and Structures, 11(1), 140.

[99] See, H. (2003). Field dependence of the response of a magnetorheological suspension under steady shear flow and squeezing flow. Rheologica Acta, 42(1-2), 86-92.

[100] Deshmukh, S. S., and McKinley, G. H. (2004). Rheological behavior of magnetorheological suspensions under shear, creep and large amplitude oscillatory shear (LAOS) flow. In: Proceedings of XIVth International Congress on Rheology.

[101] Cheng, H. B., Wang, J. M., Zhang, Q. J., and Wereley, N. M. (2009). Preparation of composite magnetic particles and aqueous magnetorheological fluids. Smart Materials and Structures, 18, 085009.

[102] Esmaeilnezhad, E., Jin Choi, H., Schaffie, M., Gholizadeh, M., Ranjbar, M., and Hyuk Kwon, S. (2017). Rheological analysis of magnetite added carbonyl iron based magnetorheological fluid. Journal of Magnetism and Magnetic Materials, 444, 161–167.

[103] Plachy, T., Kutalkova, E., Sedlacik, M., Vesel, A., Masar, M., and Kuritka, I. (2018). Impact of corrosion process of carbonyl iron particles on magnetorheological behavior of their suspensions. Journal of Industrial and Engineering Chemistry, 66, 362–369.

[104] Burguera, E. F., Love, B. J., Sahul, R., Ngatu, G., and Wereley, N. M. (2008). A physical basis for stability in bimodal dispersions including micrometer-sized particles and nanoparticles using both linear and non-linear models to describe yield. Journal of Intelligent Material Systems and Structures, 19(11), 1361-1367.

[105] Laun, H. M., Gabriel, C., and Schmidt, G. (2008). Primary and secondary normal stress differences of a magnetorheological fluid (MRF) up to magnetic flux densities of 1 T. Journal of Non-Newtonian Fluid Mechanics, 148(1-3), 47-56.

[106] Han, Y. M., Kim, C. J., and Choi, S. B. (2009) A magnetorheological fluid-based multifunctional haptic device for vehicular instrument controls. Smart Materials and Structures, 18, 015002.

[107] Volkova, O., Bossis, G., Guyot, M., Bashtovoi, V., and Reks, A. (2000). Magnetorheology of magnetic holes compared to magnetic particles. Journal of Rheology, 44(1), 91-104.

[108] Segovia-Gutiérrez, J. P., Berli, C. L. A., and de Vicente, J. (2012). Nonlinear viscoelasticity and two-step yielding in magnetorheology: A colloidal gel approach to understand the effect of particle concentration. Journal of Rheology, 56(6), 1429-1448.

[109] Mewis, J., and Meire, C. (1984). Yielding in weakly flocculated systems. In: Mena, B., Garcia-Rejón, A., and Rangel-Nagaile, C. (Eds.) Advances in Rheology (Vol. 2) (National Autonomous University of Mexico, Mexico City).

[110] Klingenberg, D. J., Van Swol, F., and Zukoski, C. F. (1991). The small shear rate response of electrorheological suspensions. I. Simulation in the point–dipole limit. The Journal of Chemical Physics, 94(9), 6160-6169.

[111] Rosensweig, R. E. Ferrohydrodynamics (Dover Publications, Mineola, 2014).

[112] Bossis, G., Lemaire, E., Volkova, O., and Clercx, H. (1997). Yield stress in magnetorheological and electrorheological fluids: A comparison between microscopic and macroscopic structural models. Journal of Rheology, 41(3), 687-704.

[113] Kuzhir, P., López-López, M. T., and Bossis, G. (2009). Magnetorheology of fiber suspensions. II. Theory. Journal of Rheology, 53(1), 127-151.

[114] Tang, X., and Conrad, H. (2000). An analytical model for magnetorheological fluids. Journal of Physics D: Applied Physics, 33(23), 3026.

[115] Shkel, Y. M., and Klingenberg, D. J. (1999). A continuum approach to electrorheology. Journal of Rheology, 43(5), 1307-1322.

[116] Bossis, G., Lacis, S., Meunier, A., and Volkova, O. (2002). Magnetorheological fluids. Journal of Magnetism and Magnetic Materials, 252, 224-228.

[117] Lacis, S., Zavickis, E. and Bossis, G. (2002). Magnetic interactions of chains formed by ferromagnetic spheres. International Journal of Modern Physics B, 16(17–18), 2307-2313.

[118] Li, W. H., and Zhang, X. Z. (2010). A study of the magnetorheological effect of bimodal particle based magnetorheological elastomers. Smart Materials and Structures, 19(3), 035002.

[119] de Vicente, J., Vereda, F., Segovia-Gutiérrez, J. P., del Puerto Morales, M., and Hidalgo-Álvarez, R. (2010). Effect of particle shape in magnetorheology. Journal of Rheology, 54(6), 1337-1362.

[120] Vereda, F., de Vicente, J., and Hidalgo-Álvarez, R. (2017). Effect of surface roughness on the magnetic interaction between micron-sized ferromagnetic particles: Finite element method calculations. Journal of Intelligent Material Systems and Structures, 28(8), 992-998.

[121] Davis, L. C. (1992). Polarization forces and conductivity effects in electrorheological fluids. Journal of Applied physics, 72(4), 1334-1340.

[122] Davis, L. C. (1992). Finite-element analysis of particle-particle forces in electrorheological fluids. Applied Physics Letters, 60(3), 319-321.

[123] Clercx, H. J. H., and Bossis, G. (1995). Static yield stresses and shear moduli in electrorheological fluids. The Journal of Chemical Physics, 103(21), 9426-9437.

[124] Bossis, G., Khuzir, P., Lacis, S., and Volkova, O. (2003). Yield behavior of magnetorheological suspensions. Journal of Magnetism and Magnetic Materials, 258, 456-458.

[125] López-López, M. T., Kuzhir, P., Lacis, S., Bossis, G., González-Caballero, F., and Durán, J. D. (2006). Magnetorheology for suspensions of solid particles dispersed in ferrofluids. Journal of Physics: Condensed Matter, 18(38), S2803.

[126] Bossis, G., Grasselli, Y., and Ciffreo, A. (2019). The role of volume fraction and additives on the rheology of suspensions of micron sized iron particles. Frontiers in Materials, 6, 4.

[127] Ginder, J. M., Davis, L. C., and Elie, L. D. (1996). Rheology of magnetorheological fluids: Models and measurements. International Journal of Modern Physics B, 10(23n24), 3293-3303.

[128] Ocalan, M. PhD thesis. Massachusetts Institute of Technology, Cambridge, 2011.

[129] Ruiz-López, J. A., Fernández-Toledano, J. C., Hidalgo-Álvarez, R., and de Vicente, J. (2016). Testing the mean magnetization approximation, dimensionless and scaling numbers in magnetorheology. Soft Matter, 12(5), 1468-1476.

[130] Jolly, M. R., Carlson, J. D., and Muñoz, B. C. (1996). A model of the behaviour of magnetorheological materials. Smart Materials and Structures, 5(5), 607.

[131] de Gans, B. J. (1999). Non-linear magnetorheological behaviour of an inverse ferrofluid. Faraday Discussions, 112, 209-224.

[132] Shen, Y., Golnaraghi, M. F., and Heppler, G. R. (2004). Experimental research and modeling of magnetorheological elastomers. Journal of Intelligent Material Systems and Structures, 15(1), 27-35.

[133] Klingenberg, D. J., and Zukoski IV, C. F. (1990). Studies on the steady-shear behavior of electrorheological suspensions. Langmuir, 6(1), 15-24.

[134] Volkova, O., Cutillas, S., and Bossis, G. (1999). Shear banded flows and nematic-to-isotropic transition in ER and MR fluids. Physical Review Letters, 82(1), 233.

[135] Marshall, L., Zukoski, C. F., and Goodwin, J. W. (1989). Effects of electric fields on the rheology of non-aqueous concentrated suspensions. Journal of the Chemical Society, Faraday Transactions 1: Physical Chemistry in Condensed Phases, 85(9), 2785-2795.

[136] Felt, D. W., Hagenbuchle, M., Liu, J., and Richard, J. (1996). Rheology of a magnetorheological fluid. Journal of Intelligent Material Systems and Structures, 7(5), 589-593.

[137] de Vicente, J., López-López, M. T., Durán, J. D., and González-Caballero, F. (2004). Shear flow behavior of confined magnetorheological fluids at low magnetic field strengths. Rheologica Acta, 44(1), 94-103.

[138] Klingenberg, D. J., Ulicny, J. C., and Golden, M. A. (2007). Mason numbers for magnetorheology. Journal of Rheology, 51(5), 883-893.

[139] Ramos, J., Klingenberg, D. J., Hidalgo-Álvarez, R., and de Vicente, J. (2011). Steady shear magnetorheology of inverse ferrofluids. Journal of Rheology, 55(1), 127-152.

[140] Santiago-Quinones, D. I., Raj, K., and Rinaldi, C. (2013). A comparison of the magnetorheology of two ferrofluids with different magnetic field-dependent chaining behavior. Rheologica Acta, 52(8-9), 719-726.

[141] Sherman, S. G., Becnel, A. C., and Wereley, N. M. (2015). Relating Mason number to Bingham number in magnetorheological fluids. Journal of Magnetism and Magnetic Materials, 380, 98-104.

[142] Ruiz-López, J. A., Fernández-Toledano, J. C., Klingenberg, D. J., Hidalgo-Álvarez, R., and de Vicente, J. (2016). Model magnetorheology: A direct comparative study between theories, particle-level simulations and experiments, in steady and dynamic oscillatory shear. Journal of Rheology, 60(1), 61-74.

[143] Berli, C. L., and de Vicente, J. (2012). A structural viscosity model for magnetorheology. Applied Physics Letters, 101(2), 021903.

[144] Quémada, D. Modélisation rhéologique structurelle: dispersions concentrées et fluides complexes. (Editions TEC & DOC, Paris, 2006).

[145] Martin, J. E., and Anderson, R. A. (1996). Chain model of electrorheology. The Journal of Chemical Physics, 104(12), 4814-4827.

[146] Ruiz-López, J. A., Hidalgo-Álvarez, R., and de Vicente, J. (2017). Towards a universal master curve in magnetorheology. Smart Materials and Structures, 26(5), 054001.

[147] de Vicente, J., González-Caballero, F., Bossis, G., and Volkova, O. (2002). Normal force study in concentrated carbonyl iron magnetorheological suspensions. Journal of Rheology, 46(5), 1295-1303.

[148] López-López, M. T., Kuzhir, P., Durán, J. D., and Bossis, G. (2010). Normal stresses in a shear flow of magnetorheological suspensions: viscoelastic versus Maxwell stresses. Journal of Rheology, 54(5), 1119-1136.

[149] Ivaneyko, D., Toshchevikov, V., Saphiannikova, M., and Heinrich, G. (2014). Mechanical properties of magneto-sensitive elastomers: unification of the continuum-mechanics and microscopic theoretical approaches. Soft Matter, 10(13), 2213-2225.

[150] Guan, X., Dong, X., and Ou, J. (2008). Magnetostrictive effect of magnetorheological elastomer. Journal of Magnetism and Magnetic Materials, 320(3-4), 158-163.

[151] Stolbov, O. V., Raikher, Y. L., and Balasoiu, M. (2011). Modelling of magnetodipolar striction in soft magnetic elastomers. Soft Matter, 7(18), 8484-8487.

[152] See, H., and Tanner, R. (2003). Shear rate dependence of the normal force of a magnetorheological suspension. Rheologica Acta, 42(1-2), 166-170.

[153] Jiang, J., Tian, Y., Ren, D., and Meng, Y. (2011). An experimental study on the normal stress of magnetorheological fluids. Smart Materials and Structures, 20(8), 085012.

[154] Odenbach, S. (2004). Recent progress in magnetic fluid research. Journal of Physics: Condensed Matter, 16(32), R1135.

[155] Vékás, L. (2008). Ferrofluids and magnetorheological fluids. Advances in Science and Technology, 54, 127-136.

[156] Costo, R., Morales, M. P., and Veintemillas-Verdaguer, S. (2015). Improving magnetic properties of ultrasmall magnetic nanoparticles by biocompatible coatings. Journal of Applied Physics, 117(6), 064311.

[157] Chan, D. Y., Henderson, D., Barojas, J., and Homola, A. M. (1985). The stability of a colloidal suspension of coated magnetic particles in an aqueous solution. IBM Journal of Research and Development, 29(1), 11-17.

[158] Coffey, W., and Kalmykov, Y. P. The Langevin equation: with applications to stochastic problems in physics, chemistry and electrical engineering (World Scientific, New Jersey, 2012).

[159] Foss, D. R., and Brady, J. F. (2000). Structure, diffusion and rheology of Brownian suspensions by Stokesian dynamics simulation. Journal of Fluid Mechanics, 407, 167-200.

[160] Sorensen, C. M. (2009). Magnetism. In: Klabunde, K. J., and Richards, R. M. (Eds.) Nanoscale materials in chemistry (John Wiley & Sons, New York).

[161] Bergenholtz, J., Brady, J. F., and Vicic, M. (2002). The non-Newtonian rheology of dilute colloidal suspensions. Journal of Fluid Mechanics, 456, 239-275.

[162] Shliomis, M. I. (1971). Effective viscosity of magnetic suspensions. Zhurnal Eksperimentalnoi i Teoreticheskoi Fiziki, 61(2411), s1971d.

[163] Ilg, P., Kröger, M., and Hess, S. (2005). Magnetoviscosity of semidilute ferrofluids and the role of dipolar interactions: Comparison of molecular simulations and dynamical mean-field theory. Physical Review E, 71(3), 031205.

Chapter 4. Materials and Methods

4.1 Experimental

Most of the CMRFs investigated in this dissertation were formulated using carbonyl iron (CI) particles. These particles were kindly provided by BASF SE (Germany) as a powder. CI particles are synthesized by thermal decomposition of iron pentacarbonyl ($Fe(CO)_5$) and this is the reason for their name. This decomposition process yields polydisperse spherical particles in the range of microns with a very high purity of iron (around 97%). Undoubtedly, CI is the most frequently employed particulate material in the literature [1,2]. This is so because CI particles exhibit a high saturation magnetization and negligible hysteresis (see below). From the different available grades in the portfolio provided by BASF SE, HQ (mean diameter 1 μm) and EW (3 μm) grades were employed in this work. Their magnetization curves are shown in Fig. 4.1 together with the curve fit to the Fröhlich-Kennelly model (Eq. (3.24)). As expected, very small differences are observed between both grades. Only, a slightly larger saturation magnetization is observed for the largest particles that will be associated to a larger yield stress (see Sec. 3.4.2).

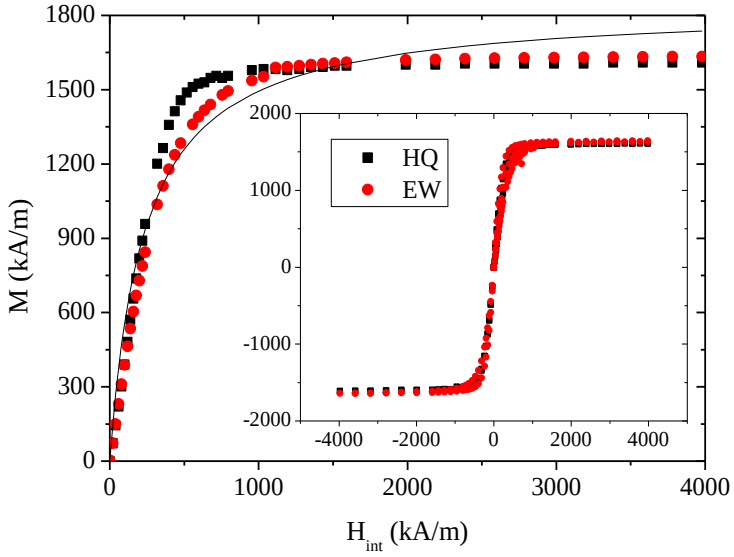

Figure 4.1: First magnetization curve of the CI particles used in this dissertation. The line corresponds to the best fit according to the Fröhlich-Kennelly model (Eq. (3.24)) with $\mu_i = 9.0 \pm 0.7$ and $M_s = 1840 \pm 40$ kA/m. Inset: Complete magnetic curves (i.e. up and down curves) where the absence of hysteresis, remanence and coercivity can be seen.

The CI powder was thoroughly dispersed in a carrier liquid to prepare a CMRF. In the case of low concentrations, the suspensions were prepared by manual dispersion with a spatula. However, in the case of high concentrations (above 20 vol%), the samples were dispersed through the use of a planetary mixer (Thinky ARE-310, USA) to guarantee homogeneity and the absence of air bubbles. The materials were used as received without further treatment and the suspensions were tested soon after their preparation because CI particles are prone to flocculate (especially in non-polar liquids) and settle down due to iron's hydrophilic character, interfacial activity and density mismatch between the carrier

(~ 1 g/cm^3) and the particles (~7.8 g/cm^3). Every experiment was repeated at least three times with a fresh new sample.

Several carrier fluids were used in this work depending on the specific requirements of the experiment to be carried out. From Chapter 5 to Chapter 8, the CMRF is investigated in the pre-yield regime and hence it was not expected that the fluid viscosity plays an important role. In this case, due to its hydrophilic character, glycerol 88 wt% (125 mPa·s, Scharlau) was used to favor particle stability against aggregation in the absence of the magnetic field.

Samples tested during the design and the evaluation of the double-gap device (Chapter 9) were formulated using silicone oils of viscosities 350 mPa·s and 500 mPa·s (Sigma Aldrich). These are nonpolar liquids with good chemical stability and very low surface tension what makes them useful to calibrate the new device. As a counterpart, a weak flocculation was seen in the absence of the magnetic field but without any measurable effect when the field was applied.

Finally, when dealing with MRFs containing nanoparticles, a careful choice of the carrier fluid was done to guarantee their kinetic stability. In this sense, milli-Q water was used in Chapter 10 due to the versatility of this carrier to stabilize colloids using a wide range of well-established mechanisms such as electrostatics and steric interactions. In its turn, mixtures of micro- and nanoparticles employed in Chapter 11 and Chapter 12 were dispersed in polyalphaolefin oil (6.4 mPa·s, Synfluid, Chevron-Philips) with 1-octanol (Sigma Aldrich) as a surfactant following a protocol previously described in the literature [3].

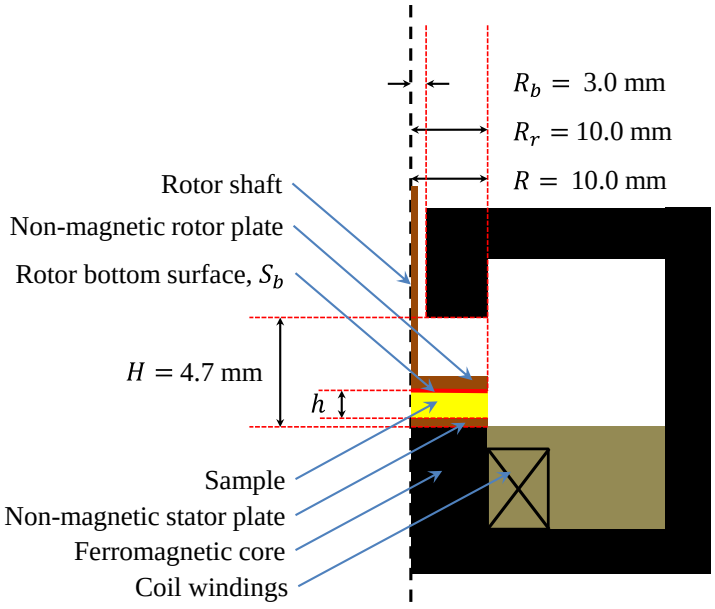

Figure 4.2: Schematics (not at scale) of the Anton Paar MRD 70/1T magnetocell. This includes the commercial ferromagnetic spacer ring of thickness 1.29 mm. R stands for the radius of the ferromagnetic yoke. This is exactly the same as the radius of the rotor in our particular setup R_r = 10.0 mm.

The rheological experiments were carried out in isothermal conditions (25 ºC) in a MCR 501 stress-controlled rheometer (Anton Paar, Austria) equipped with a rotational plate-plate geometry. Although different modifications were done in this geometry according to the experiment, in its more basic configuration, the plate radii were R_r = 10.0 mm

while the (single-)gap h between the plates was chosen in the range [0.3, 1] mm. Both shearing surfaces were sandblasted to avoid wall-slip (see at the end of this section). The rotor (upper plate) was made of titanium while the stator (bottom one) was made of brass and was 1.7 mm thick. The rheometer was equipped with the Anton Paar MRD 70/1T magnetocell in order to apply magnetic fields, parallel to the flow gradient direction, during the tests. A sketch of the Anton Paar MRD 70/1T magnetocell is plotted in Fig. 4.2. As shown, the magnetic circuit is axisymmetric and consists of a cylindrical ferromagnetic core with an air gap (thickness H) where the sample and the plates are placed. The upper yoke of the magnetic circuit is drilled (bore radius R_b) to accommodate the rotor plate shaft. Further details about the magnetic circuit geometry can be found in Ref. [4].

The electromagnetic circuit is fed with a current source generating magnetic fields up to a measured maximum of around 550 kA/m just on the top of the stator plate (see Fig. 4.3a). In Fig. 4.3b, the FEM simulated radial profile of the magnetic field at this height is plotted for different feeding currents. On the one hand, a positive field gradient is observed close to the center of the geometry ($r/R_r = 0$) due to the aforementioned bore through the upper yoke. This is more clearly observed at high fields (currents). On the other hand, a negative field gradient appears at the rim of the plate ($r/R_r = 1.0$) due to the yoke edge effects. The presence of any gradient is typically a shortcoming in rheology unless it would be carefully taken into account, what is not always simple. Otherwise, as the whole sample is not under the same macroscopic conditions, ensemble/volume averages are invalidated (see Sec. 3.4) and the rheological characterization cannot be done properly. In the case of magnetic suspensions, the presence of a magnetic field gradient is responsible for a gradient in the particle concentration as well. Indeed looking at Eq. (3.46), it can be deduced that non-homogeneous fields act over the particle dipole through so-called magnetophoretic forces. For fields with small gradients and linear materials they read as follows [5]:

$$\vec{F}_{MAP} = \frac{1}{4}\mu_0\mu_{r,c}\pi\beta d^3\nabla H_{ext}^2 \tag{4.1}$$

Note that the approximated expression for a non-linear material can be also found in Ref. [5] although it is not qualitative different. Equation (4.1) shows that magnetophoretic force drags the particles towards regions where the field intensity is maximum ($r/R_r \sim 0.7$ according to Fig. 4.3b) if $\beta > 0$ (i.e. CMRFs) or towards regions where it is minimum (geometry center and rim) if $\beta < 0$ (i.e. IFFs). Furthermore, this particle (field-gradient induced) migration is not instantaneous and therefore introduces transient effects in the measurement as well [4]. In view of Fig. 4.3b, an applied field strength of 265 kA/m was chosen as a safe value in order to sufficiently magnetize the samples still preventing the appearance of too large concentration gradients. Another route will be later explored to study the influence of higher (saturating) fields, minimizing the appearance of concentration gradients, in the rheological response of MRFs.

Of course, magnetic field gradients can be avoided substituting the magnetic circuit by a pair of Helmholtz coils. However, the field generated is of only tens of kA/m, they occupy a lot of space and are difficult to cool down. Alternatively, the magnetic circuit can be kept and make changes in the geometry of the cell. In this sense, a twin-gap device with ferromagnetic tools was proposed [6]. Among other advantages, this device can partially reduce the lack of homogeneity created by the upper bore. This concept has been generalized in Chapter 9 leading to a double-gap device. This device is more versatile as

well as capable to reduce even further the magnetic field gradient within the sample volume.

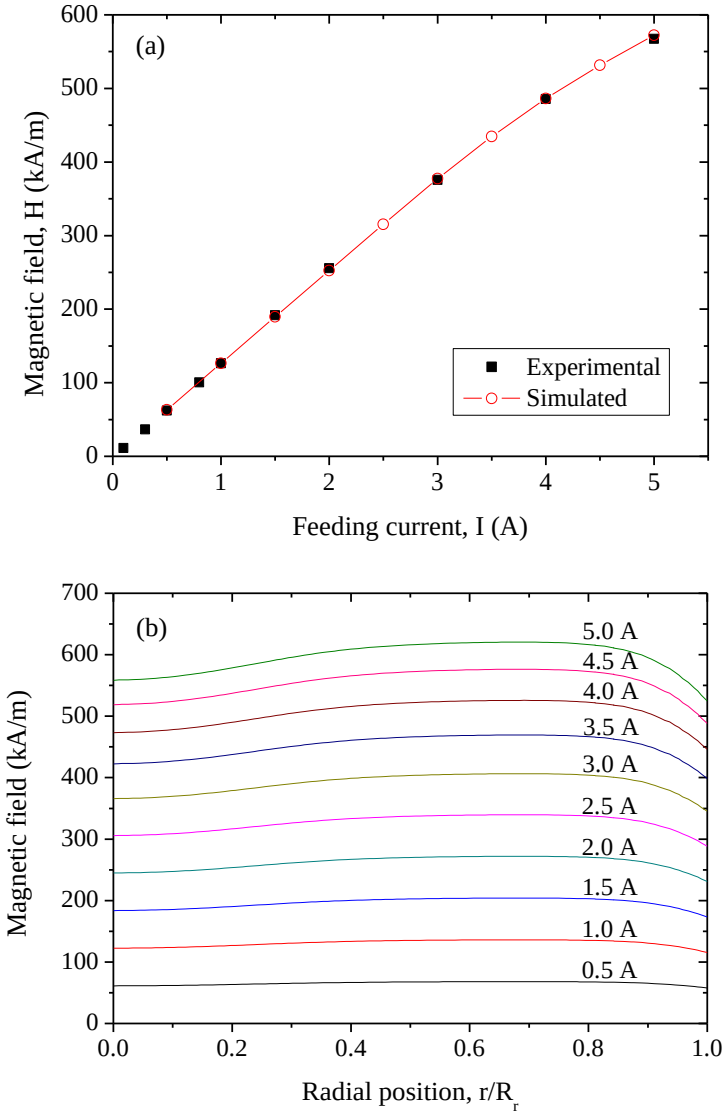

Figure 4.3: (a) Experimentally measured and FEM simulated magnetic field on the top of the rheometer stator plate as a function of the feeding current. (b) FEM simulated magnetic field (z-component) profile along the normalized cell radius at different feeding currents.

Three kinds of geometries; single-gap, double-gap and twin-gap devices have been used in this dissertation depending on the strength of the applied magnetic field. In this chapter we will focus our attention only in the single-gap device. The double-gap device will be extensively described in Chapter 9 and the twin-gap device is just a particular case of the double-gap device (when both gaps are the same).

With these geometries, the characterization of CMRFs was done through stress versus shear rate curves (i.e. the rheograms). To obtain the static yield stress, the rheograms were performed in stress-controlled mode (also called stress ramp experiment). The experiment was always preceded by other two intervals: pre-shear and structuration steps. In the pre-shear step, a large shear rate (usually 100 s^{-1} during 30-60 s) was imposed in the sample

to erase its previous mechanical history. After the pre-shear, the sample was let to structure at rest (in the absence of flow) under a magnetic field.

In most of the cases, at the beginning of the structuration step (i.e. the second interval) the magnetic field was suddenly applied (typically during 60 s) and then kept constant during the rheological experiment. As it was pointed in Sec. 3.4.1, imposing the magnetic field in this way leads to non-equilibrium structures: particles usually get kinetically arrested in metastable states consisting of fibrous and interconnected aggregates in the field direction (i.e. the total force acting over the particles is zero but they are not in the energetic ground state). In the case that the particles were required to aggregate in the minimum energy state configuration (i.e. the BCT equilibrium structure), the field was gradually increased in a stepwise way till the final desired field was reached [7]. The key behind this method is that each step is split in two parts: in the first one the field corresponding to the current step is applied to structure the sample while in the second one the field is switched off to allow particles to diffuse conforming to a more stable configuration. Once the final step has been reached, the field was maintained during the rest of the experiment.

As previously stated, the static yield stress was inferred from steady shear rheograms in stress controlled mode. However, bearing in mind the definition for the static yield stress provided in Sec. 3.4.2 it can be deduced that this is not the most suitable technique to measure it. Instead, creep-recovery tests should be used [8]. In these tests a constant shear stress $\tau_1 \neq 0$ is imposed during some time and then it is removed $\tau_1 = 0$ during another time interval. Throughout this two-step process the shear strain is recorded and according to its behavior once the stress is removed, in the second step, it can be said that: (i) $\tau_1 < \tau_0$ if the sample recovers its initial shape (the strain comes back to zero) or (ii) $\tau_1 > \tau_0$ if the sample strain keeps at a finite value corresponding to its plastic deformation or flow. By changing the value of τ_1, the rheological response of the material can be mapped and with a large enough number of measurements, it is possible to assess the frontier value between the pre-yield and post-yield regimes, i.e., the yield stress [9].

Unfortunately, creep-recovery tests are very time-consuming as they provide upper and bottom limits for the yield stress. In addition, a reasonably large amount of sample is needed because every test needs to be carried out with fresh new samples to avoid mechanical history effects. Alternatively to the creep-recovery tests, the yield stress can also be identified from critical points (maximum stress level) during sample flow. Examples of these methods are the stress growth test, evaluation of the stress during time while the sample is sheared at a given (small) shear rate, and amplitude sweeps in oscillatory tests. Although faster than creep-recovery tests, the other two methods are dependent on the particular imposed shear rate and frequency [10].

More frequently, the yield stress is evaluated from steady shear rheograms. With current rheometers, it is possible to perform such a rheogram in both strain (so called shear) or stress controlled modes. Undoubtedly, the shear mode is the more reproducible one but not the most suitable: in this test the shear rate is imposed, to increase linear or logarithmically, and the stress is evaluated for each shear rate. Typical curves show a stress plateau for small shear rates (usually below 10^{-2} s^{-1}) in log-log representation that is identified with the yield stress and usually evaluated by fitting the experimental curve to a plastic constitutive equation (e.g. Bingham, Casson or Herschel-Bulkley). At this point, nevertheless, it has to be taken into consideration that any stress measured during a shear controlled test does not correspond to a static yield stress since the sample is

always flowing. Thus, the obtained yield stress is usually identified with the dynamic yield stress as it is independent on the shear rate but implies flow.

On the other hand, in stress controlled mode, the stress is the imposed magnitude while the shear rate is the measured one. This is the most appropriate mode in the case of yield stress fluids. Again, the stress can be incremented linearly or logarithmically [11]. Only applied stresses above the yield stress should provoke non-zero shear rates. For materials with a high yield stress, as soon as the applied stress overcomes the yield point, the shear rate experiences a sudden jump, usually one or two orders of magnitude, indicating the onset of flow. In this dissertation, static yield stress was identified with the experimental point previous to the aforementioned jump. In those cases where the material exhibits a small yield stress, the breakage of the sample is more gradual. For that samples the yield stress was evaluated through the tangent method: fitting the pre- and post-yield regimes with two lines and finding the crossover point [12].

Clearly, the yield stress obtained from stress controlled tests depends on how small the steps in the stress are (i.e. the number of measured points per decade if a logarithmic ramp is used as in our case). The smaller the step size, the more accurate the measurement. However, this also results in longer tests that may be influenced by particle sedimentation and/or heating problems. In this dissertation, rheograms in the stress controlled mode were used by setting 15 points per decade and 5 s per point.

The description above has been done in terms of the shear stress/shear rate that the rheometer applies or measures. However, strictly speaking, a rheometer cannot directly impose or measure the stress/strain state of any material under any condition. Instead, the rheometer imposes/measures the total force (and/or the torque) and the velocity at the confining walls. From these quantities, the total stress $\tilde{t}$ and the velocity $\vec{v}$ fields in the bulk are obtained from continuity and Cauchy momentum equations for incompressible materials:

$$\nabla \cdot \vec{v} = 0 \tag{4.2}$$

$$\frac{\partial \vec{v}}{\partial t} + (\vec{v} \cdot \nabla)\vec{v} = \frac{1}{\rho}\left(\nabla \cdot \tilde{t} + \vec{f}_{ext}\right) \tag{4.3}$$

where ρ is the sample density. As it is known, Eqs. (4.2) and (4.3) need a constitutive relationship relating the stress and the (gradient of) velocity fields to be solved. However, both fields refer, in this case, to a sample whose constitutive expression is, *a priori*, totally or partially unknown (remember, for example, that theoretical results shown in Sec. 3.4 for CMRFs deal only with shear strain and were incomplete). To overcome this issue, rheometers are designed in such a way that their geometry and operation mode creates very simple velocity fields that can be solved without the necessity to tackle Eqs. (4.2) and (4.3) directly. These flows are known as viscometric ones and are developed under laminar and stationary conditions, negligible inertia and in the absence of secondary flows [13].

In the case of a rotational plate-plate rheometer, the kinematics are conventionally imposed by rotating the upper plate at a swirl velocity Ω (do not confuse Ω with the vorticity vector $\vec{\Omega}$ in Sec. 3.1.1) while the bottom plate remains at rest during the test. In addition, since the geometry is axisymmetric, the flow field is independent on the azimuthal coordinate φ. Hence, if the dimensions of the geometry (R_r, h) and the swirl velocity (Ω) are small enough so that viscometric conditions apply, the velocity field (in

cylindrical coordinates) of the fluid confined between the shearing plates is simply reduced to:

$$\vec{v}(r,z) = \frac{rz\Omega}{h}\hat{\varphi} \tag{4.4}$$

noting that the flow direction is $\hat{\varphi}$, the velocity gradient direction is $\hat{z}$ and the neutral direction is $\hat{r}$. With this, it can be seen that the shear rate is not homogeneous in the shearing gap. Instead, it linearly increases with the radius as follows:

$$\dot{\gamma}(r) = 2E_{\varphi z} = \frac{r\Omega}{h} \tag{4.5}$$

Introducing the flow field given by Eq. (4.4) in Eqs. (4.2) and (4.3), the continuity reduces to the identity while Cauchy equation simplifies to (by components):

$$0 = \frac{\partial t_{rr}}{\partial r} + \frac{t_{rr} - t_{\varphi\varphi}}{r} \tag{4.6}$$

$$0 = \frac{\partial t_{\varphi z}}{\partial z} \tag{4.7}$$

$$0 = \frac{\partial t_{zz}}{\partial z} \tag{4.8}$$

From Eq. (4.7) it can be deduced that $t_{\varphi z} = \tau(r)$ is just a function of the radial position. The torque M (do not confuse with the first moment $\widetilde{M}$ due to the hydrodynamic force of Sec. 3.1) experienced by the rheometer head consists of the torque exerted by the sample on each surface element of the rheometer plate (see red surface S_b in Fig. 4.2):

$$M = \hat{z} \cdot \int_{S_b} \vec{r} \times (\tilde{t} \cdot \hat{z}) ds = \int_{S_b} r\tau(r) ds = 2\pi \int_0^{R_r} r^2 \tau(r) dr \tag{4.9}$$

At this stage, it would seem that no further insight can be obtained as the function $\tau(r)$ is unknown and the constitutive $\tau(\dot{\gamma})$ equation is unknown as well. Nevertheless, this problem can be partially circumvented if the integral is written in terms of the shear rate instead of the radial position (Weissenberg-Rabinowitsch-Mooney, WRM, method) [14]. Taking into consideration Eq. (4.5), the torque can be expressed as:

$$M = 2\pi \int_0^{\dot{\gamma}_{R_r}} \left(\frac{h\dot{\gamma}}{\Omega}\right)^2 \tau(\dot{\gamma}) \frac{h}{\Omega} d\dot{\gamma} = 2\pi \frac{R_r^3}{\dot{\gamma}_{R_r}^3} \int_0^{\dot{\gamma}_{R_r}} \dot{\gamma}^2 \tau(\dot{\gamma}) d\dot{\gamma} \tag{4.10}$$

where $\dot{\gamma}_{R_r} = \dot{\gamma}(R_r) = R_r\Omega/h$ is the shear rate at the rim of the upper plate. The previous integral is a definite one and thus it does not depend on the functional form of $\tau(\dot{\gamma})$ but on the value of $\dot{\gamma}_{R_r}$. Passing the multiplicative factor to the LHS, deriving respect $\dot{\gamma}_{R_r}$ and applying the Leibnitz rule one arrives to:

$$\begin{aligned} \frac{d}{d\dot{\gamma}_{R_r}}\left(\frac{M\dot{\gamma}_{R_r}^3}{2\pi R_r^3}\right) &= \frac{1}{2\pi R_r^3}\left(\dot{\gamma}_{R_r}^3 \frac{dM}{d\dot{\gamma}_{R_r}} + 3M\dot{\gamma}_{R_r}^2\right) \\ &= \frac{d}{d\dot{\gamma}_{R_r}}\left(\int_0^{\dot{\gamma}_{R_r}} \dot{\gamma}^2 \tau(\dot{\gamma}) d\dot{\gamma}\right) = \dot{\gamma}_{R_r}^2 \tau\left(\dot{\gamma}_{R_r}\right) \end{aligned} \tag{4.11}$$

Finally, noting $\tau_{R_r} = \tau(\dot{\gamma}_{R_r})$ as the stress at the rim of the upper plate and bearing in mind that the relationship between $\dot{\gamma}_{R_r}$ and Ω is linear, thus $\log\Omega = \text{const.} + \log\dot{\gamma}_{R_r}$, the Eq. (4.11) can be rearranged as:

$$\tau_{R_r} = \frac{M}{2\pi R_r^3}\left(3 + \frac{\dot{\gamma}_{R_r}}{M}\frac{dM}{d\dot{\gamma}_{R_r}}\right) = \frac{M}{2\pi R_r^3}\left(3 + \frac{d\log M}{d\log\Omega}\right) \tag{4.12}$$

As it can be seen, Eq. (4.12) allows computing the shear stress at the rim, regardless of the functional form of $\tau(r)$ or $\tau(\dot{\gamma})$, just evaluating how the torque changes with the swirl velocity. Remember that the torque and swirl velocity are experimentally accessible magnitudes. Some comments on Eq. (4.12) are as follows:

- For Newtonian fluids, the resistance to flow is constant (i.e. independent on the shear rate), then a linear relationship holds between M and Ω. Therefore, the logarithmic derivative in Eq. (4.12) is 1 and the stress-torque conversion reduces to $\tau_{R_r} = 2M/(\pi R_r^3)$.
- For a yield stress fluid, just during yielding, the stress (torque) is constant, i.e. shows a plateau versus the shear rate (swirl velocity), thus the logarithmic derivative is 0 and therefore $\tau_{R_r} = 3M/(2\pi R_r^3)$.
- For a power law fluid, $\tau = m\dot{\gamma}^n$ (being m and n constants), the logarithmic derivative is just the flow index n, and thus $\tau_{R_r} = (3+n)M/(2\pi R_r^3)$.

The application of the WRM method has been possible thanks to the simplicity of the single-gap plate-plate geometry (integration only over S_b in Fig. 4.2) and the simple flow field (Eq. (4.4)). In other geometries, for example in the double-gap geometry, the resulting integrals cannot be solved so easily. In those cases, the stress-torque conversion can be approximated by supposing that the sample behaves, at least in a given shear rate range, as a power law fluid [15] and then identifying its flow index with the logarithmic derivative of the torque-swirl velocity curve at that shear rate range.

Of course, the WRM correction is not needed if the geometry is capable to create a homogeneous shear rate field within the sample volume. In this case, the shear stress would be constant and the integral relating the torque and the stress would be straightforward to solve. Examples of this kind of geometries are the concentric cylinders (with small gap) and the cone-plate device. However, only the parallel plate configuration is of interest in magnetorheology: (i) It is challenging to superimpose homogeneous magnetic fields in the gradient direction in concentric cylinders. (ii) It is challenging to interpret the stress data in a cone-plate geometry because the gap changes in the radial direction.

In addition to the torque, modern rheometers can also measure the normal force exerted by the sample on the upper tool in the z direction (i.e. the thrust). This force is related to the total stress over S_b (Fig. 4.2) as follows:

$$\begin{aligned} F_z = -\hat{z}\cdot\int_{S_b}\tilde{t}\cdot\hat{z}ds &= -\int_{S_b} t_{zz}(r)ds \\ &= -2\pi\int_0^{R_r}[-p(r)+\sigma_{zz}(r)]rdr \end{aligned} \tag{4.13}$$

Here, the dependence $t_{zz}(r)$ has been deduced from Eq. (4.8) and the total stress tensor has been split in the isotropic pressure p and its deviatoric part $\tilde{\sigma}$. The main problem with

the previous expression is that it depends on the pressure, which does not play any role in the rheology of incompressible materials. Because of this, it is convenient to define the first N_1 and second N_2 normal stress differences:

$$N_1 = t_{\varphi\varphi} - t_{zz} = \sigma_{\varphi\varphi} - \sigma_{zz} \tag{4.14}$$

$$N_2 = t_{zz} - t_{rr} = \sigma_{zz} - \sigma_{rr} \tag{4.15}$$

With this, $t_{zz}(r)$ can be written as a function of only N_1 and N_2. Combining Eq. (4.15) and Eq. (4.6) to eliminate t_{rr} we arrive to [14]:

$$\frac{dt_{zz}}{dr} = \frac{dt_{rr}}{dr} + \frac{dN_2}{dr} = \frac{N_1 + N_2}{r} + \frac{dN_2}{dr} \tag{4.16}$$

Equation (4.16) can be integrated to recover t_{zz} (but as a function of N_1 and N_2, or equivalently, as a function of the diagonal deviatoric stress components according to Eqs. (4.14) and (4.15)):

$$\begin{aligned} t_{zz}(R_r) - t_{zz}(r) &= \int_r^{R_r} dt_{zz} = \int_r^{R_r} \frac{N_1 + N_2}{\varsigma} d\varsigma + \int_r^{R_r} dN_2 \\ &= N_2(R_r) - N_2(r) + \int_r^{R_r} \frac{N_1 + N_2}{\varsigma} d\varsigma \\ &= t_{zz}(R_r) - t_{rr}(R_r) - N_2(r) + \int_r^{R_r} \frac{N_1 + N_2}{\varsigma} d\varsigma \end{aligned} \tag{4.17}$$

If the surface tension is negligible and the velocity profile (Eq. (4.4)) is not distorted at the free surface (no edge effects), the shape of the sample between the parallel plates is cylindrical. This implies $t_{rr}(R_r) = 0$ as the ambient pressure balances the deviatoric normal stress σ_{rr} at that boundary. Thus, solving for $t_{zz}(r)$:

$$t_{zz}(r) = N_2(r) - \int_r^{R_r} \frac{N_1 + N_2}{\varsigma} d\varsigma = N_2(r) - u(r) \tag{4.18}$$

Next, this expression has to be substituted into Eq. (4.13). If we focus first in the latter term $u(r)$ and integrating by parts:

$$\begin{aligned} 2\pi \int_0^{R_r} \left(\int_r^{R_r} \frac{N_1 + N_2}{\varsigma} d\varsigma \right) r dr &= 2\pi \int_0^{R_r} u(r) r dr \\ &= 2\pi \left[\frac{r^2}{2} u(r) \right]_0^{R_r} + 2\pi \int_0^{R_r} \frac{r^2}{2} \frac{N_1 + N_2}{r} dr \end{aligned} \tag{4.19}$$

Bearing in mind that $u(R_r) = 0$ due to its definition and knowing that a square bracket $[f(x)]_a^b$ stands for $f(b) - f(a)$, it can be seen that this square bracket is zero. Therefore, substituting Eq. (4.18) in Eq. (4.13) we obtain:

$$\begin{aligned} F_z = -2\pi \int_0^{R_r} t_{zz}(r) r dr &= -2\pi \int_0^{R_r} \left(N_2 - \frac{N_1 + N_2}{2} \right) r dr \\ &= \pi \int_0^{R_r} \frac{N_1 - N_2}{2} r dr \end{aligned} \tag{4.20}$$

Again, the dependence of $N_1(r) - N_2(r)$ is not known, but changing the variable from r to $\dot{\gamma}(r)$ (Eq. (4.5)), as it was done in the WRM method during the calculation of τ_{R_r}, we arrive to:

$$N_1(R_r) - N_2(R_r) = \frac{F_z}{\pi R_r^2}\left(2 + \frac{d\log F_z}{d\log \Omega}\right) \tag{4.21}$$

Equations (4.5), (4.12) and (4.21) constitute the basis to obtain the material functions of any sample using a rotational rheometer with parallel plates. These equations relate the stress and strain states of the sample (just in a point, in particular, the rim of the upper plate) to three experimentally accessible magnitudes: the torque, the swirl velocity and the normal force. In addition, Eqs. (4.5), (4.12) and (4.21) show how the geometrical dimensions (R_r, h) can be modified in order to expand the range of measurable stresses and shear rates as any rheometer is always limited by minimum detectable values. In the rheometer used in this dissertation: $M_{min} = 1$ nN·m, $\Omega_{min} = 1.7{\cdot}10^{-7}$ s^{-1} and $F_{z,min} =$ 0.01 N.

It is worth to remark that Eqs. (4.5), (4.12) and (4.21) are strictly valid only under viscometric flow conditions. Otherwise corrections have to be taken into account [14,16]. Deviations from viscometric flows typically come from secondary flows or instrument inertia (negligible in this dissertation as the system is usually interrogated near to the yield point) and surface tension effects (also negligible in comparison to the magnetostatic contribution for MRFs). Next, only the slip phenomena will be revisited as it is expected to strongly affect yield stress measurements.

In the previous analyses, it has been supposed that the shearing walls are in full contact with a homogeneous sample whose material functions are well defined. Thus, by continuity of the total stress and the no-slip condition, the shear stress and the shear rate in the sample are unambiguously linked to the rheometer's applied/measured torque and swirl velocity through Eqs. (4.5) and (4.12). However, due to the discrete nature of any particle-based suspension, the initial supposition does not have to be fulfilled. Actually, a particle-depleted region appears close to the shearing surfaces [17]; i.e. the rheometer walls are not in contact to a homogeneous sample but to a (carrier) liquid layer whose viscosity is (infinitely) smaller than the (yield stress) suspension. Consequently, the stress applied/measured by the rheometer is translated to/comes from only the strain within the depletion layer while the bulk suspension barely suffers any deformation; it just slips over the rheometer walls.

This introduces a mismatch between the shear rate field presumably imposed/measured by the rheometer walls (which is given by Eq. (4.5)) and the one that really occurs within the sample. Artifacts derived from this mismatch are known as 'wall-slip effects' and are not negligible especially when determining the yield stress. Wall-slip effects are typically manifested by gap-dependent rheograms and/or a quasi-Newtonian behavior in the pre-yield regime (i.e. the apparent absence of a yield stress).

There are several explanations for the appearance of a depletion layer and it is not clear which one plays the major role. Some examples are steric repulsion, shear gradients, competition between particle-particle and particle-wall interactions, etc. [18]. Nevertheless, several methods have been proposed to prevent or correct wall-slip phenomena. More traditional ones, e.g. the classical work from Yoshimura and Prud'homme [19] or using a vane geometry, do not seem to be the more appropriate ones

in magnetorheology due to the involved changes in the geometry that make more difficult to properly control/apply the magnetic field [20].

Alternatively, the use of texturized/rough plates (to trap particles and aggregates at the asperities of the plates) and/or ferromagnetic ones (to enhance particle-wall interactions) have shown to be very effective against wall-slip [20-23]. In this dissertation, all experiments were done in the absence of wall-slip using ferromagnetic plates or brass texturized ones (containing a pattern with 16 radial grooves of 250 μm depth and 250 μm width). If none of the previous geometries are specified, then, the experiment was carried out, by default, with sandblasted plates with a mean roughness of $R_a = 0.323 \pm 0.012$ μm (measured with white light confocal microscopy).

4.2 Simulations

As it was seen in Chapter 3, any time that a multibody system is to be studied, the use of simulations is practically mandatory. In this dissertation, MRFs were simulated by means of two well-known numerical methods. On the one hand, one-way Discrete Element Method (DEM) simulations were performed in the SimPARTIX® software package (https://www.simpartix.com) to study the flow behavior of dilute MRFs. On the other hand, MRFs in the pre-yield regime were modeled as a periodic 3D lattice with the Finite Element Method implemented by COMSOL Multiphysics® software (https://www.comsol.com). In addition, the latter was also used to solve magnetic and flow field distributions created in the rheometer.

In this section an overview of DEM and FEM simulations is given. For further details about the specific simulation parameter choice, boundary conditions, mesh size, etc. we refer to the corresponding dissertation chapters.

4.2.1 Discrete Element Method

The one-way coupling scheme was already introduced in Sec. 3.1. In short, this considers that only the fluid can exert a drag force over the particles, but the latter do not influence the flow field. As a consequence, the fluid flow can be solved in a first step and then introduce its influence in the particle dynamics through the drag force. The case studied in this dissertation (Chapter 10) considers that the MRF is under a simple shear flow. Thus, it is not even necessary to numerically solve the flow field; this is simply given by $\vec{v}(z) = \dot{\gamma} z \hat{y}$.

The particle dynamics problem was tackled using DEM [24,25]. This method, together with other classical ones (e.g. Molecular Dynamics, Dissipative Particle Dynamics or Brownian Dynamics) [26], pursues a Lagrangian description of the particulate systems. The MRF is considered as a large number N of particles that interact with each other, with the surrounding fluid and with the confining boundaries (if applies). These interactions are supposed to be known analytically (what in most of the cases implies a strong approximation to real interactions) at any time. Therefore each particle dynamics can be solved by integrating its law of motion [27]. In DEM, the equation to be integrated is the Newton's second law.

In our simulations, MMA is assumed (see Sec. 3.2.1) with saturated dipoles. Therefore, the dipole strength is fixed but its direction is governed by the Newton's second law for the angular motion where only the magnetic torque $\vec{T}_m$ (Eq. (3.47)) is regarded (see

below). Because of the MMA, the magnetic particle-particle interaction is reduced to the dipolar one $\vec{F}_d$ (Eq. (3.46)).

In Secs. 3.1 and 3.2, we considered that the particles interact mainly through magnetostatics and hydrodynamic forces. According to the latter, contacts between particles are impossible to occur because the hydrodynamic (lubrication) forces between two approaching spheres diverges as they go closer and closer. As a result, no further interactions would have to be included. However, this ideal picture is broken when short-range interactions (e.g. van der Waals forces always present in real systems) or particle roughness appear. What is more, our simulations do not account for lubrication theory neither, thus, a contact-repulsive force is needed in order to prevent particle overlapping.

Currently, the level of understanding of real contact forces is very poor. Pioneering publications on the modeling of MRFs using DEM-like simulations, e.g. Ref. [28], implemented a contact-repulsive force using an exponential function of the interparticle distance simply because this functional form yielded structures that closely 'resembled' those experimentally observed. On the contrary, in DEM simulations contact forces are traditionally supposed to come from particle deformation during contact. The deformation is typically approximated by a spring whose elongation is equal to the particle overlapping (i.e. elastic Hertzian contacts) [29]. In our DEM simulations we use the Hertzian contact approximation:

$$\vec{F}_{rep} = \frac{1}{3}\frac{E}{1-\nu^2}\sqrt{d h_{\alpha\beta}^3}\,\frac{\vec{R}_{\alpha\beta}}{R_{\alpha\beta}} \tag{4.22}$$

where $\vec{R}_{\alpha\beta} = \vec{r}_\alpha - \vec{r}_\beta$, $h_{\alpha\beta} = d - R_{\alpha\beta}$ is the particle overlapping, E and ν are the particle Young's modulus and Poisson's ratio respectively. Note that only when there is overlapping $\left(h_{\alpha\beta} > 0\right)$ repulsion forces can be evaluated. It is worth mentioning that the Hertzian contact is introducing another force scale, in this case $F_{rep} \sim E d^{1/2}$. Nevertheless, for the parameters used in this dissertation, repulsion-to-magnetic and repulsion-to-hydrodynamic forces ratios are, in the worst cases, around 10^6 and 10^{11} respectively. Therefore, it can be seen that a hard sphere potential is properly simulated to avoid particle overlapping and consequently F_{rep} should not modify, by itself, the rheology of the system [30].

Finally, in the computation of the drag -hydrodynamic- force, the Stokes' law (Eq. (3.21)) is used. Bearing in mind the other previous interactions, the equations of motion for the translational and the rotational degrees of freedom of a particle α are given by:

$$m\frac{d^2\vec{r}_\alpha}{dt^2} = 3\pi\eta_c d\left(\frac{d\vec{r}_\alpha}{dt} - \vec{v}\right) + \sum_{\beta\neq\alpha}^{N}\left(\vec{F}_d + \vec{F}_{rep}\right) \tag{4.23}$$

$$\tilde{I}\frac{d^2\vec{\vartheta}_\alpha}{dt^2} = \vec{T}_m \tag{4.24}$$

where $\vec{\vartheta}_\alpha$ is the particle orientation, $\vec{v}$ is the flow field in simple shear flow as stated at the beginning of this section and the summation runs over β particles that are closer to the particle α than a cutoff distance.

Once the forces and torques are computed over all particles at a given time, their position and velocity $\vec{u}_\alpha = d\vec{r}_\alpha/dt$ in the next time step are obtained by the explicit time integration of Eqs. (4.23) and (4.24) using a velocity Verlet scheme [31]:

$$\vec{r}_\alpha(t+\Delta t) = \vec{r}_\alpha(t) + \vec{u}_\alpha(t)\Delta t + \frac{\vec{F}_\alpha(t)\Delta t^2}{2m} \tag{4.25}$$

$$\vec{u}_\alpha(t+\Delta t) = \vec{u}_\alpha(t) + \frac{\left(\vec{F}_\alpha(t) + \vec{F}_\alpha(t+\Delta t)\right)\Delta t}{2m} \tag{4.26}$$

where $\vec{F}_\alpha$ is the total force (i.e. RHS of Eq. (4.23)) acting over particle α. Analogous expressions are used for rotational degrees of freedom just substituting translational magnitudes $\left(\vec{r}_\alpha, \vec{u}_\alpha, \vec{F}_\alpha, m\right)$ by rotational ones $\left(\vec{\vartheta}_\alpha, \vec{\omega}_\alpha, \vec{T}_m, \tilde{I}\right)$. In Eqs. (4.25) and (4.26), the integration time step is adaptively computed to guarantee convergence of the numerical scheme and also to save computational effort. To get the first goal, Δt must be short enough in comparison to the smaller time scale of the problem. In our simulations, this scale is usually controlled by the Hertzian repulsion giving a characteristic time per collision of [27,32]:

$$t_{col} \sim 3.21 \left(\frac{3}{2}\frac{(1-\nu^2)m}{E\sqrt{d}}\right)^{2/5} u_n^{-1/5} \tag{4.27}$$

where u_n is the relative normal velocity of the colliding particles at the beginning of the collision, that is, when $h_{\alpha\beta} = 0$. With this, a time step was chosen so that shortest collision in the simulation is tracked around 50 steps.

It is worth noting that t_{col} goes down as u_n increases. This is a great inconvenience when studying MRFs in the pre-yield regime with DEM-like methods (see Sec. 3.4.2) since particles in this stage move at a very short timescale (Eq. (3.60)). The problem has to be overcome using a very small fixed Δt which leads to a high computational effort. In Chapter 8, a computation scheme without this shortcoming, but restricted to the pre-yield regime, is proposed as an alternative to DEM-like methods.

Regarding the values that $\vec{r}_\alpha$ can reach, particles are placed in a tetragonal simulation box whose volume V is chosen according to the simulated MRF volume fraction $V = N\pi d^3/(6\phi)$. Periodic boundary conditions are imposed in boundaries normal to the flow and vorticity direction. This is equivalent to replicate the particle configuration, at each time step, at the four sides of the explicitly simulated box. Particles in these replicated boxes are usually called 'image-particles' and, although their motion is not solved since they are just a replica of the original particles, they are also taken into account when the total force and/or the local field are computed over an original particle (if they are inside the aforementioned cutoff distance).

On the contrary, boundaries normal to the gradient/applied field direction mimic the rheometer walls by placing there an array of non-magnetic 'wall-particles' having the same characteristics (d, m, E, ν) than MRF ones but without an associated dipole. 'Wall-particles' move with a prescribed translational velocity in order to meet the velocity of the flow field at their position and are not allowed to rotate. Thus, their equations of motion are not solved. In this way, MRF particles can interact with 'wall-particles' only through contact forces. This constitutes a step forward in the particle-wall model traditionally used in MR simulations. This traditional model considers walls as perfect

surfaces and consists in imposing a no-slip condition to the MRF particles as well, that is, it is supposed that any particle close enough to the walls will stick to them acquiring their tangential velocity (the normal velocity is still given by the equations of motion). Clearly, this is an idealization that do not have to be of interest in all MRF simulations (e.g., it completely neglects 'wall-slip' phenomena). In its turn, the use of 'wall-particles' allows a more realistic treatment based on physical interactions and only a slight increase in the computational effort [33].

As initial conditions, all MRF particles are at rest, randomly distributed and oriented. As soon as the simulation starts, the shear rate and the magnetic field are applied. During time evolution, the shear stress coming from particle interaction is computed according to Eq. (3.57). For these simulations, it reads as follows:

$$\langle \widetilde{xF} \rangle_{zy} = -\frac{1}{V} \sum_{\alpha}^{N} (\vec{r}_\alpha \cdot \hat{z}) \left(\left(\vec{F}_d + \vec{F}_{rep} \right) \cdot \hat{y} \right) \tag{4.28}$$

The system is let to reach a stationary state and only when this is reached, $\langle \widetilde{xF} \rangle_{zy}$ is averaged also over time to obtain the total shear stress:

$$\tau = \eta_c \dot{\gamma} + \langle \widetilde{xF} \rangle_{zy} \tag{4.29}$$

Note that Eq. (4.29) is the same as Eq.(3.66) excluding the hydrodynamic interactions that are not accounted for in this one-way coupling scheme.

4.2.2 Finite Element Method

In most cases, physical magnitudes are not governed by simple laws that are analytically solvable under any circumstance. On the contrary, they usually come from partial differential equations, PDEs, that relate the physical magnitude (dependent variable) to its changes (derivatives) with time and space (independent variables).

In addition, to be well-posed, these physical magnitudes are not only given by their PDEs but also by a number of boundary conditions (as many as the order of the PDE). Therefore, even when the PDE is simple, e.g. a linear one, complex boundary conditions can make the problem analytically unsolvable. Examples of these situations have already appeared in this text: Maxwell equations together with their continuity ones at magnetic/non-magnetic interphases (Eqs. from (3.32) to (3.37)) or Stokes (Eq. (3.11)) and Navier-Stokes (Eq. (3.2)) equations together with the no-slip condition (Eq. (3.3)) and the continuity equation (Eq. (3.1)).

As it has been shown in Chapter 3, attempts to analytically solve these equations always require elaborated developments that are limited by (very often strong) assumptions and that eventually needs a numerical technique to provide the final solution. Alternatively, previous PDEs can be solved numerically from the beginning, obtaining complete solutions although a not so deep insight in comparison to analytical studies. In this dissertation, the numerical resolution of PDEs was addressed using FEM, in particular, to solve the magnetic field distribution inside the MRF microstructure (from Chapter 5 to Chapter 7) and the magnetic field distribution and flow fields within the rheometer cell (Chapter 9).

Due to the different nature of these scenarios, in this section we will not focus on any of them in particular. Instead we will just highlight the main steps in FEM computations in order to understand their advantages and limitations. Further details on the

implementation and particularization to magnetostatic problems or their use as a CFD tool can be found elsewhere [34,35].

For the sake of simplicity, we consider only stationary problems ruled by one PDE with a scalar solution. Let us note $\mathcal{A}(\cdot)$ the PDE operator of m-th order (i.e. the highest derivate in $\mathcal{A}$ is of order m) defined in a given volume V, g a constraint function given by the PDE and $\mathcal{B}(\cdot)$ the set of boundary conditions to be met in the volume boundary S. To solve the PDE consists in finding a function f (dependent only on the position) that fulfills:

$$\mathcal{A}(f) = g \tag{4.30}$$

in any point of V and

$$\mathcal{B}(f) = 0 \tag{4.31}$$

in any point of S. Due to obvious reasons, this formulation is called pointwise or strong form. However, it can be shown that it is equivalent to the weak form that states the solution f also fulfills:

$$\int_V u\mathcal{A}(f)dV + \int_S u\mathcal{B}(f)dS = \int_V ugdV \tag{4.32}$$

for any function u (dependent also on the position).

FEM starts from the weak from and, in its more common formulation (i.e. the Galerkin method), it approximates f and u by finite expansions:

$$f \sim \sum_{i=1}^{n} \varepsilon_i \psi_i \tag{4.33a}$$

$$u \sim \sum_{i=1}^{n} \epsilon_i \psi_i \tag{4.33b}$$

where n stands for the total number of degrees of freedom, ψ_i are known functions (called shape or basis functions) and ε_i and ϵ_i are unknown constants (independent on the position) coefficients.

Substituting Eqs. (4.33) in Eq. (4.32), supposing that both $\mathcal{A}$ and $\mathcal{B}$ are linear and rearranging we arrive to:

$$\sum_{j=1}^{n} \epsilon_j \left[\sum_{i=1}^{n} \left(\varepsilon_i \int_V \psi_j \mathcal{A}(\psi_i)dV + \varepsilon_i \int_S \psi_j \mathcal{B}(\psi_i)dS \right) - \int_V \psi_j g dV \right] = 0 \tag{4.34}$$

As no particularization has been done on the function u, the ϵ_j coefficients are arbitrary and hence, the only way that Eq. (4.34) holds is by equating each square bracket to zero or:

$$\sum_{i=1}^{n} \varepsilon_i \left(\int_V \psi_j \mathcal{A}(\psi_i) dV + \int_S \psi_j \mathcal{B}(\psi_i) dS \right) = \int_V \psi_j g dV \tag{4.35}$$

for $j = 1, 2, \ldots, n$. This can be written in a more compact form as:

$$\widetilde{K}\vec{\varepsilon} = \vec{b} \tag{4.36}$$

where $\vec{\varepsilon}$ is the degrees of freedom vector while $\widetilde{K}$ and $\vec{b}$ are the so-called stiffness matrix (note that its dimension is $n \times n$) and constraints vector, respectively:

$$K_{ij} = K_{ji} = \int_V \psi_j \mathcal{A}(\psi_i) dV + \int_S \psi_j \mathcal{B}(\psi_i) dS \tag{4.37}$$

$$b_j = \int_V \psi_j g dV \tag{4.38}$$

Since the basis functions ψ_i are chosen by the user, and $\mathcal{A}$, $\mathcal{B}$ and g are given by the PDE, all terms in $\widetilde{K}$ and $\vec{b}$ are known. Thus, with FEM, it is possible to pass from solving a PDE to solving a system of n algebraic equations with n uknowns $(\varepsilon_1, \ldots, \varepsilon_n)$. In particular, FEM reduces the initial problem to another one where the hardest numerical step is the inversion of the stiffness matrix.

Till now, nothing has been said about the basis functions ψ_i. Indeed, according to the weak formulation, any kind of function can be chosen whenever it can expand the solution f. In the practice, this entails two basic requirements. Firstly, as a solution of Eq. (4.30), f is m times derivable and thus, each ψ_i should be also m times derivable. Secondly, f must meet the boundary conditions, Eq. (4.31), and as it is going to be expressed as a linear combination of ψ_i, the combination of these latter must fulfill Eq. (4.31) as well.

The first condition can be easily met by choosing ψ_i as polynomials (of degree m or higher in order not to artificially impose that the solution has zero $(m+1)$-th derivatives). Nevertheless, a linear combination of these functions is rarely able to agree with the boundary conditions as well, especially, taking into consideration that the boundary S can have a complex shape. For this reason, both V and S are split in small and simpler subdomains, called elements, yielding a mesh where it should be more feasible to fulfill the boundary conditions.

Each mesh element is parametrized by a group of points (its vertices, edge midpoints, faces centers…) called nodes, $\vec{r}_i$. Related to each node, a basis function ψ_i is chosen as a piecewise polynomial, of degree m, that is defined over a small support. This support only spreads over all those adjacent elements that share the point $\vec{r}_i$ as a node and becomes zero at any other node: $\psi_i(\vec{r}_j) = \delta_{ij}$, where δ_{ij} is the Kronecker delta. Evaluating the approximate solution expansion, Eq. (4.33a), in one particular node it becomes easy to understand the meaning of the degrees of freedom:

$$f(\vec{r}_i) \sim \sum_{j=1}^{n} \varepsilon_j \psi_j(\vec{r}_i) = \sum_{j=1}^{n} \varepsilon_j \delta_{ij} = \varepsilon_i \tag{4.39}$$

The value for the degree of freedom ε_i resultant from solving Eq. (4.36) is just the approximated solution at the node $\vec{r}_i$. On the other hand, if the expansion is evaluated in a point $\vec{r}$ contained in an element, but that it is not a node, only those basis functions

defined at the element nodes will contribute to the final value of $f(\vec{r})$ (because only these functions have a support that contains the point $\vec{r}$, the rest are zero there).

Furthermore, the use of piecewise functions greatly simplifies the computation of $\widetilde{K}$ as only those terms including basis functions whose supports overlap each other are different from zero. A typical example of this kind of basis function with order $m = 1$ and 1D is the triangular one:

$$\psi_i(x) = \mathrm{T}(x - x_i) = \begin{cases} \dfrac{x - x_{i-1}}{x_i - x_{i-1}} & \text{if } x_{i-1} \leq x < x_i \\ \dfrac{x_{i+1} - x}{x_{i+1} - x_i} & \text{if } x_i \leq x \leq x_{i+1} \\ 0 & \text{otherwise} \end{cases} \tag{4.40}$$

As it can be seen, ψ_i is non-zero only in the 1D elements (i.e. segments) that share the node x_i as a limit: the segment $[x_{i-1}, x_i]$ and the segment $[x_i, x_{i+1}]$. Therefore, given (for example) $x \in [x_i, x_{i+1}]$, $f(x) = \varepsilon_i \mathrm{T}(x - x_i) + \varepsilon_{i+1} \mathrm{T}(x - x_{i+1})$.

From the previous discussion, it can be noticed that the use of n piecewise functions in the expansion of Eq. (4.33a) really implies to define a series of n nodes that discretize the space V in elements where the solution is approximated by a polynomial function. Then, it is clear to deduce that closer nodes yield results that are more accurate: by splitting the whole domain V in very small elements, it is expected the change of f in one of them to be smooth, and therefore, easy to approximate by a simple polynomial.

Of course, a compromise must always be reached since the larger the number of nodes also implies the larger the stiffness matrix dimension and thus the higher computational cost required to solve the system of Eq. (4.36). Because of this, regular meshes (i.e. where all elements have the same size) are rarely used. Instead, the element size is adapted according to the expected gradient of the solution: finer elements are used in regions of large gradients while coarser elements are used to discretize the regions where changes of f are expected to be small. In the best scenario, these gradients are only anticipated but their values are not known. Therefore, the use of FEM simulations always involves a convergence study where the mesh is made finer and finer up to a point when the solution becomes weakly dependent on the mesh and remains below a desired tolerance.

The description above constitutes the basics of FEM. Once all inputs of $\widetilde{K}$ and $\vec{b}$ have been calculated, it is necessary just to solve numerically Eq. (4.36) or equivalently to compute $\widetilde{K}^{-1}$. To do so, several well-known techniques are available. On the one hand, there exist direct methods (e.g. LU factorization) that depend weakly on the mesh but use a large amount of memory, typically $\mathcal{O}(n^2)$- $\mathcal{O}(n^3)$ in 3D. On the other hand, there exist indirect methods (e.g. Newton-Raphson) with smaller memory requirements, $\sim\mathcal{O}(n)$, but whose convergence depends on the initial seed and also on the quality of the mesh (i.e. how well the nodes and basis functions adapt to real gradients of the solution).

It must be reminded again that the explanation above concerns stationary and linear problems whose solution is a scalar f. However, FEM can be applied equally to time-dependent and non-linear PDEs that couple different magnitudes.

Time dependency is accounted for by allowing $\varepsilon_i = \varepsilon_i(t)$ but keeping $\psi_i = \psi_i(\vec{r})$. As a result, a different matrix expression from Eq. (4.36) is obtained:

$$\tilde{L}\frac{d\vec{\varepsilon}}{dt} + \tilde{K}\vec{\varepsilon} = \vec{b} \tag{4.41}$$

where $\tilde{L}$ is called the mass matrix and is computed similarly to $\tilde{K}$. Note that $\tilde{K}$ and $\vec{b}$ could have change slightly their definition in the time-dependent problem but the new definitions can be obtained following the same steps done to get Eqs. (4.37) and (4.38). Equation (4.41) can be integrated by numerical methods, for example using Runge-Kutta methods, or discretized (in time) by finite difference schemes. Alternatively, to save computational effort, finite differences can be applied directly to the original PDE to get rid of the time derivative and then apply FEM as in a stationary problem.

In the case that the original PDE contains non-linear terms $q(f)$, for example, non-linear constitutive equations in magnetostatic problems or the convective term in fluid flow ones, these PDE are frequently linearized with the Newton method: $q(f) = q(f^*) + f \cdot q'(f^*)$ where f^* is guesstimated value of the solution and the prime stands for the differentiation with respect to f. As a consequence, in these kind of problems both the stiffness matrix and constraints vector depend on the solution, $\tilde{K} = \tilde{K}(\vec{\varepsilon})$ and $\vec{b} = \vec{b}(\vec{\varepsilon})$, restricting Eq. (4.36) resolution to iterative methods only [36].

Finally, if a set of PDEs couples several magnitudes: f_1, …, f_l; (for example, pressure and velocity components in incompressible fluids or the previous ones together with the temperature for the compressible case) then each of these magnitudes must be expanded in a series of basis functions that depending on the PDEs can be of the same degree or not:

$$f_i \sim \sum_{j=1}^{n_i} \varepsilon_{i,j}\psi_{i,j} \tag{4.42}$$

In addition, the same mesh or a specific one can be used for each magnitude according to the problem behavior and magnitude gradients. The total number of degrees of freedom will be $n = n_1 + \cdots + n_l$ increasing the computational effort because of the higher stiffness matrix dimension.

References

[1] Wereley, N. (Ed.). Magnetorheology: advances and applications (Vol. 6) (Royal Society of Chemistry, Cambridge, 2013).

[2] Ruiz-López, J. A., Wang, Z. W., Fernández-Toledano, J. C., Hidalgo-Álvarez, R., and de Vicente, J. (2016). Start-up rheometry of highly polydisperse magnetorheological fluids: experiments and simulations. Rheologica Acta, 55(3), 245-256.

[3] Bombard, A. J., Gonçalves, F. R., Morillas, J. R., and de Vicente, J. (2014). Magnetorheology of dimorphic magnetorheological fluids based on nanofibers. Smart Materials and Structures, 23(12), 125013.

[4] Laun, H. M., Schmidt, G., Gabriel, C., and Kieburg, C. (2008). Reliable plate–plate MRF magnetorheometry based on validated radial magnetic flux density profile simulations. Rheologica Acta, 47(9), 1049-1059.

[5] Jones, T. B. Electromechanics of particles (Cambridge University Press, New York, 1995).

[6] Laun, H. M., Gabriel, C., and Kieburg, C. (2010). Twin gap magnetorheometer using ferromagnetic steel plates - performance and validation. Journal of Rheology, 54(2), 327-354.

[7] Cutillas, S., Bossis, G., and Cebers, A. (1998). Flow-induced transition from cylindrical to layered patterns in magnetorheological suspensions. Physical Review E, 57(1), 804.

[8] Wang, Z., Shahrivar, K., and de Vicente, J. (2014). Creep and recovery of magnetorheological fluids: Experiments and simulations. Journal of Rheology, 58(6), 1725-1750.

[9] Chhabra, R. P., and Richardson, J. F. Non-Newtonian flow and applied rheology: engineering applications (Butterworth-Heinemann, Oxford, 2008).

[10] Jönkkäri, I., and Syrjälä, S. (2010). Evaluation of techniques for measuring the yield stress of a magnetorheological fluid. Applied Rheology, 20(4), 41-47.

[11] Barnes, H. A. (1999). The yield stress—a review or ‘παντα ρει’—everything flows?. Journal of Non-Newtonian Fluid Mechanics, 81(1-2), 133-178.

[12] Mezger, T. G. The rheology handbook: for users of rotational and oscillatory rheometers (Vincentz Network GmbH & Co KG, Hannover, 2006).

[13] Mewis, J., and Wagner, N. J. Colloidal suspension rheology (Cambridge University Press, New York, 2012).

[14] Macosko, C. W. Rheology: Principles, Measurements, and Applications. (Wiley-VCH, New York, 1994).

[15] Barnes, H. A., and Walters, K. (1985). The yield stress myth?. Rheologica Acta, 24(4), 323-326.

[16] Ewoldt, R. H., Johnston, M. T., and Caretta, L. M. (2015). Experimental challenges of shear rheology: how to avoid bad data. In: Spagnoile, S. (Ed.) Complex fluids in biological systems (Springer, New York).

[17] Barnes, H. A. (1995). A review of the slip (wall depletion) of polymer solutions, emulsions and particle suspensions in viscometers: its cause, character, and cure. Journal of Non-Newtonian Fluid Mechanics, 56(3), 221-251.

[18] Cloitre, M., and Bonnecaze, R. T. (2017). A review on wall slip in high solid dispersions. Rheologica Acta, 56(3), 283-305.

[19] Yoshimura, A., and Prud'homme, R. K. (1988). Wall slip corrections for Couette and parallel disk viscometers. Journal of Rheology, 32(1), 53-67.

[20] Jönkkäri, I., Kostamo, E., Kostamo, J., Syrjala, S., and Pietola, M. (2012). Effect of the plate surface characteristics and gap height on yield stresses of a magnetorheological fluid. Smart Materials and Structures, 21(7), 075030.

[21] Laun, H. M., Gabriel, C., and Kieburg, C. (2011). Wall material and roughness effects on transmittable shear stresses of magnetorheological fluids in plate–plate magnetorheometry. Rheologica Acta, 50(2), 141-157.

[22] de Vicente, J., López-López, M. T., Durán, J. D., and González-Caballero, F. (2004). Shear flow behavior of confined magnetorheological fluids at low magnetic field strengths. Rheologica Acta, 44(1), 94-103.

[23] Lemaire, E., and Bossis, G. (1991). Yield stress and wall effects in magnetic colloidal suspensions. Journal of Physics D: Applied Physics, 24(8), 1473.

[24] Cundall, P. A., and Strack, O. D. (1979). A discrete numerical model for granular assemblies. Geotechnique, 29(1), 47-65.

[25] Zhu, H. P., Zhou, Z. Y., Yang, R. Y., and Yu, A. B. (2007). Discrete particle simulation of particulate systems: theoretical developments. Chemical Engineering Science, 62(13), 3378-3396.

[26] Satoh, A. Modeling of magnetic particle suspensions for simulations (CRC Press, Boca Raton, 2017).

[27] Li, S., Marshall, J. S., Liu, G., and Yao, Q. (2011). Adhesive particulate flow: The discrete-element method and its application in energy and environmental engineering. Progress in Energy and Combustion Science, 37(6), 633-668.

[28] Klingenberg, D. J., Van Swol, F., and Zukoski, C. F. (1989). Dynamic simulation of electrorheological suspensions. The Journal of Chemical Physics, 91(12), 7888-7895.

[29] Andreotti, B., Forterre, Y., and Pouliquen, O. Granular media: between fluid and solid. (Cambridge University Press, Cambridge, 2013).

[30] Mari, R., Seto, R., Morris, J. F., and Denn, M. M. (2014). Shear thickening, frictionless and frictional rheologies in non-Brownian suspensions. Journal of Rheology, 58(6), 1693-1724.

[31] Allen, M. P., and Tildesley, D. J. Computer simulation of liquids. (Oxford University Press, New York, 1991).

[32] Lagger, H. G. PhD thesis. University of Freiburg, Freiburg, 2014.

[33] Lagger, H. G., Bierwisch, C., Korvink, J. G., and Moseler, M. (2014). Discrete element study of viscous flow in magnetorheological fluids. Rheologica Acta, 53(5-6), 417-443.

[34] Huebner, K. H., Dewhirst, D. L., Smith, D. E., and Byrom, T. G. The finite element method for engineers (John Wiley & Sons, Hoboken, 2001).

[35] Zienkiewicz, O. C., Taylor, R. L., and Zhu, J. Z. The finite element method: its basis and fundamentals (Butterworth-Heinemann, Oxford, 2005).

[36] Kundu, P. K., Cohen, I. M., and Hu, H. H. Fluid mechanics (Academic Press, Burlington, 2008).

Chapter 5. On the Yield Stress in Magnetorheological Fluids: a Direct Comparison between 3D Simulations and Experiments

Jose R. Morillas and Juan de Vicente

This article is published in: Composites Part B: Engineering, 160, 626-631 (2019).

DOI: https://doi.org/10.1016/j.compositesb.2018.12.114

Abstract

Undoubtedly, the yield stress is the most relevant rheological property of a magnetorheological (MR) fluid. However, available analytical and simulation methodologies to compute the magnetostatic interparticle interactions that govern the yield stress, fail at large particle concentrations and large strain levels. In this communication we propose a 3D finite element methodology (FEM), to compute the yield stress, that grounds on a reduced magnetic field formulation and periodic boundary conditions. This approach takes into account multibody and multipolar interactions and satisfactorily simulates large concentrations and strains. Experiments are also carried out in a torsional magnetorheometer for a wide range of MR formulations. Experimental results obtained are in very good agreement with FEM simulations.

5.1 Introduction

Magnetorheological (MR) fluids are typically constituted by dispersion of micronsized magnetizable iron particles in a carrier fluid. In the quasistatic regime (no-flow), their rheological properties are strongly determined by field-induced magnetostatic interparticle interactions. In particular, when the magnetic field strength and/or particle concentration are large enough, the composite exhibits a field-dependent yield stress and viscoelasticity [1,2].

Frequently, magnetostatic interparticle interactions are estimated using the mean magnetization approximation where each particle is assimilated by a point dipole at its center that is proportional to the particle volume and magnetization level [3,4]. However, this approximation is only strictly valid under two circumstances: (1) particles are far apart from each other so that they feel a homogeneous field, and (2) particle magnetization is fully saturated so multipolar terms disappear. Nevertheless, in practice, the magnetic field strength applied is large enough for the particles to approach up to physical contact and small enough for the particles not being fully saturated [3].

Improvements to get a more accurate estimation of the magnetic interactions between particles involve, for instance, the use of multipolar expansion methods and capacitance matrices techniques [5,6]. However, these approaches are only applicable in the case of

linear magnetic materials and do not consider magnetic saturation. In this context, Finite Element Method (FEM) simulations are of great interest because they provide a solution to this non-linear multibody and multipolar problem by directly solving Maxwell's equations in the simulation domain when continuity equations for electromagnetic fields are applied.

Previous studies on MR fluids using FEM can be classified into two groups. On the one hand, we identify those studies that compute magnetic interparticle forces between two isolated particles [7-9]. On the other hand we find studies that compute the yield stress (and the storage modulus) of an ensemble of particles arranged in an infinite chain or cubic lattice [10-13]. Interestingly, common to all previous studies, the external magnetic field is introduced in the model via Boundary Conditions (BCs), i.e. the magnetic field is prescribed at a BC. Of course, this is not a problem for low particle concentrations but it is definitely an issue for large particle concentrations of interest in applications because of multibody contributions. Furthermore, another complication arises because the computational domain must be deformed when shearing the composite and hence the mirror symmetry BCs are lost and the magnetic field direction is not aligned with the lattice anymore. In view of these two disadvantages, available FEM simulation methodologies are rigorously limited to low concentrations and small strain levels [12,13]. In this communication, a method is proposed that is based on a reduced formulation of the magnetic field with periodic BCs to overcome these limitations.

5.2 Numerical analysis

The magnetic field distribution is calculated in the static state. Taking into consideration that there are not free current densities, it can be seen from Ampere's law that the magnetic field strength is derivable from a scalar potential:

$$\vec{H} = -\nabla V \tag{5.1}$$

In the case of interest in this work, the total magnetic field has two contributions: (i) a homogeneous background field (the external magnetic field) and (ii) a perturbation due to the presence of the magnetizable particles. Therefore, Eq. (5.1) can be rewritten as follows:

$$\vec{H} = \vec{H}_{ext} - \nabla V_p \tag{5.2}$$

where $\vec{H}_{ext} = H_{ext}\hat{z}$ is the external applied field and V_p is the perturbation scalar potential. The main advantage of this reduced field formulation is that the external magnetic field is set in the model as a domain property (and not a boundary one). In other words, the magnetic field strength/direction is not imposed at the boundaries.

Next, Eq. (5.2) is coupled with Gauss law for the magnetic field flux density $\vec{B}$:

$$\nabla \cdot \vec{B} = \mu_0 \nabla \cdot \left(\mu_r \vec{H}\right) = 0 \tag{5.3}$$

Here μ_r is the relative magnetic permeability of the materials involved (μ_{rc} for the continuous media and μ_{rp} for the dispersed phase). In a typical MR fluid the carrier is non-magnetic (i.e. $\mu_{rc} = 1$) while the dispersed particles are magnetic (i.e. $\mu_{rp} > 1$). Unless otherwise stated, the non-linear magnetization of the particles is modeled here assuming isotropic materials that follow the Fröhlich-Kennelly constitutive equation:

$$\mu_{rp} = 1 + \frac{(\mu_i - 1)M_s}{M_s + (\mu_i - 1)H} \tag{5.4}$$

In the evaluation of Eq. (5.4) we take $\mu_i \equiv \mu_{rpi} = 1000$ as the initial permeability of the particles and $M_s = 1600$ kA/m as the saturation magnetization of the particles.

Finally, Eqs. (5.2) and (5.3) are numerically solved via FEM using the COMSOL Multiphysics software.

In order to demonstrate the capability of this methodology, next we focus first in the simplest case. This corresponds to single-particle width chains, that is, particles arranged in a tetragonal lattice with lateral distance w between them (Fig. 5.1a). In this configuration, the computational domain can be chosen as the unit cell of the lattice. Its height h is given by the particle diameter d whereas the width of the simulation box w is given by the particle volume fraction ϕ as follows $w = \sqrt{d^2\pi/6\phi}$. It is important to note that the use of a simple tetragonal lattice at high particle concentrations is not justified. However, it will be demonstrated below, that the Body Centered (BCT) lattice gives very similar results.

Periodic or mirror symmetries can be imposed as BCs if the lattice is not strained. However, when the lattice is sheared at an angle θ normal to the field direction (for example in y direction according to Fig. 5.1), the chains in the lattice undergo an affine deformation. As a consequence, the tetragonal lattice becomes a monoclinic one whose tilt angle θ verifies $\gamma = \tan\theta$ (Fig. 5.1b). In this configuration, mirror symmetries at the boundaries are not applicable and only periodic BCs can be imposed.

In both tetragonal and monoclinic lattices, a mirror symmetry exists along x direction. As a result, the computational domain can be reduced to one half of the lattice unit cell (Fig. 5.1d). As it can be seen, since periodic BCs are used, shear straining the lattice is reduced to straining the computational domain/unit cell (see dotted box in Fig. 5.1c).

Once the magnetic field distribution is obtained in the whole computational domain, the magnetostatic interaction force is calculated from Maxwell's stress tensor $\tilde{T}$:

$$\tilde{T} = \widetilde{BH} - \tilde{\delta}\frac{BH}{2} \tag{5.5}$$

where $\tilde{\delta}$ is the unit diagonal tensor. Here, the force on the lower half of the lattice due to the upper half is computed by integrating $\tilde{T}$ over the red plane in Fig. 5.1d.

In order to calculate the shear stress, only the force in the shear direction is needed. The force in the shear direction F_y is computed as follows:

$$F_y = \int_S \hat{y}^T \cdot \tilde{T} \cdot \hat{n} ds \tag{5.6}$$

where $\hat{y}^T$ is the transposed unit vector in the y direction and $\hat{n} = \hat{z}$ is the unit vector normal to the integration surface. Note that in the infinity, the averaged field in x- and y-direction are zero and therefore there is not any contribution to the force coming from the rest of the surface which encompasses the lower half of the lattice.

Once the magnetic force F_y is calculated for every strain, the shear stress τ can be obtained dividing the force in the shear direction by the surface area of application, $\tau = 2\,F_y/w^2$, where the factor 2 in this expression comes from the fact that only one half of the unit

cell is simulated. In this way, a shear stress versus strain curve is obtained and the yield stress, τ_0, is identified as the maximum of this curve.

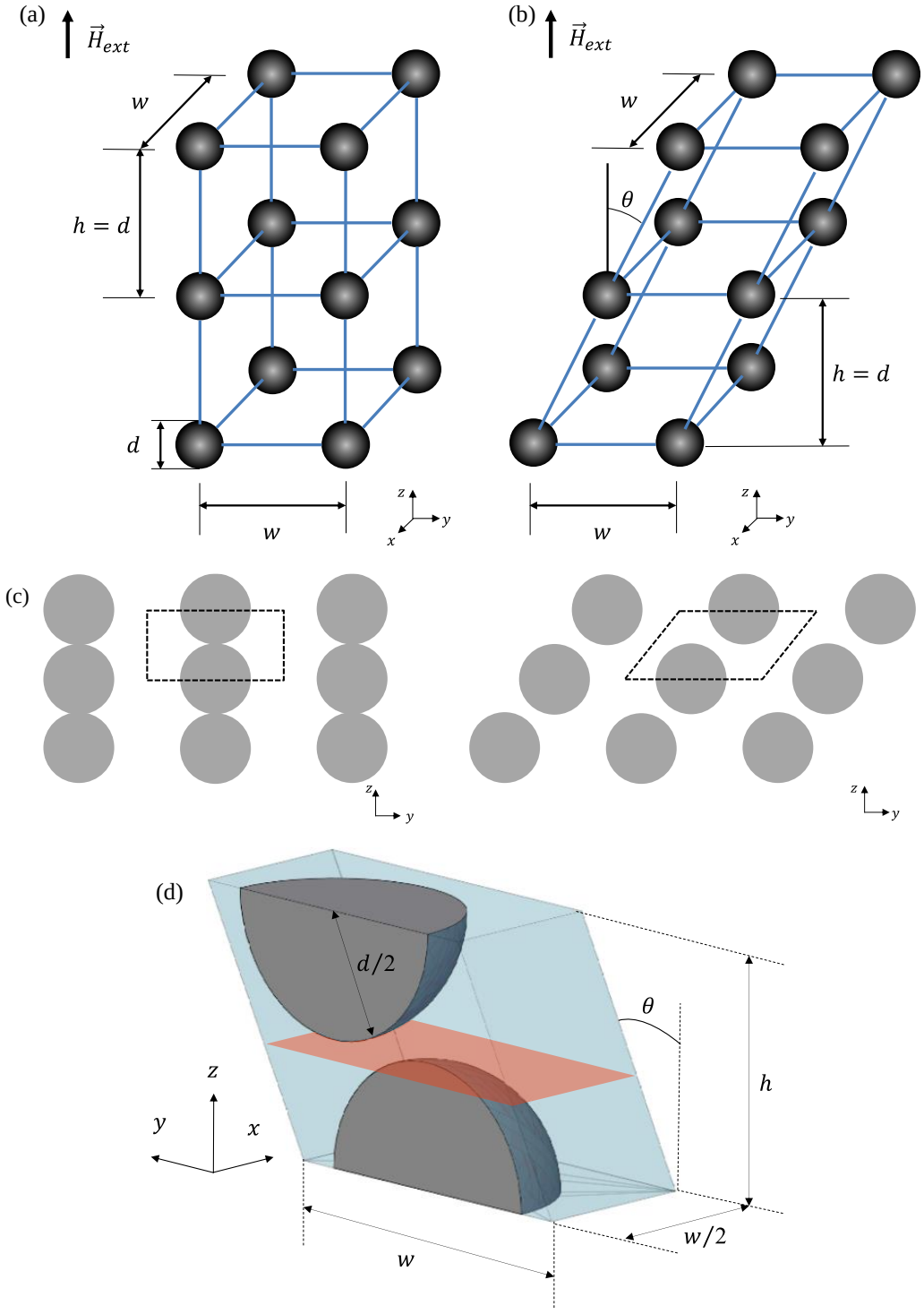

Figure 5.1: (a) The particles are arranged in a tetragonal lattice under the presence of a magnetic field. (b) The tetragonal lattice becomes a monoclinic one if a shear strain $\gamma = \tan\theta$ is applied in the y direction. (c) To transform a tetragonal lattice into a monoclinic one is equivalent to strain the original unit cell (plotted in dashed lines). (d) Computational domain used to simulate the monoclinic lattice. Mirror symmetries are applied in boundaries normal to $\hat{x}$. Periodic BCs are imposed in the rest of boundaries. The surface used to integrate Maxwell's stress tensor is plotted in red (see text).

5.3 Results and discussion

The consistency of the simulation methodology was tested first in the magnetic saturation regime. For this aim, FEM simulations were carried out imposing a particle magnetization $\vec{M} = M_s\hat{z}$. Furthermore, numerical calculations were performed modeling a monoclinic lattice of point dipoles with the same primitive vectors as the simulated lattice used in FEM calculations. The dipole strength was chosen to be $\vec{m} = \pi\mu_0\mu_{rc}d^3M_s/6\,\hat{z}$ with $\mu_{rc} = 1$, and a cutoff distance of $r_{cut} = 160d$ was used (note that computations with larger cutoff distances, till $460d$, only differ by 10^{-4} %).

Results corresponding to these two methods are plotted in Fig. 5.2. Fig. 5.2a shows the scaled shear stress as a function of the strain for FEM simulations (black squares) and numerical calculations (red circles). As observed, there is a very good agreement between the two methods.

Energy calculations constitute another alternative to validate FEM simulations. The idea behind is that the tetragonal lattice ($\theta = 0$) corresponds to the lowest particle energetic state in comparison with the monoclinic lattice for any $\theta > 0$. Therefore, when the tetragonal lattice is strained a shear stress appears to recover the most favorable energetic state.

The free energy per unit volume of the lattice F can be calculated as $F = F_0 - W$, where F_0 is the free energy per unit volume in the absence of a magnetic field and W is the magnetic energy per unit volume [14]:

$$W = \frac{1}{V_{cell}}\int_{V_{cell}}\left(\int_0^{\vec{H}}\vec{B}d\vec{H}'\right)dv \tag{5.7}$$

The inner integral in Eq. (5.7) depends on the magnetic constitutive equation of the materials within the lattice. Therefore, for those points within the cell that are occupied by the carrier fluid (non-magnetic material) the integral yields the familiar form of magnetic energy for a linear medium: $\int_0^{\vec{H}}\vec{B}d\vec{H}' = BH/2$. On the other hand, as stated before, particles were modeled as a non-linear isotropic material (see Eq. (5.4)). As a result, the inner integral for those regions occupied by the particles reads as follows:

$$\begin{aligned}\int_0^H BdH' &= \mu_0\int_0^H \mu_{rp}H'dH' \\ &= \mu_0\left\{\frac{H^2}{2} + HM_s - \frac{M_s^2}{\mu_i - 1}\ln\left[1 + (\mu_i - 1)\frac{H}{M_s}\right]\right\}\end{aligned} \tag{5.8}$$

Finally, from classical electromagnetism, the relation between shear stress and magnetic energy is simply given by:

$$\tau = -\frac{\partial W}{\partial \gamma} \tag{5.9}$$

In Fig. 5.2b we show a direct comparison between scaled yield stresses as identified as the maximum in stress vs. strain curves obtained from Maxwell's stress tensor integration and energy differentiation. Data contained in Fig. 5.2b cover both linear and non-linear regimes. As observed, there is a good agreement between both calculation methodologies.

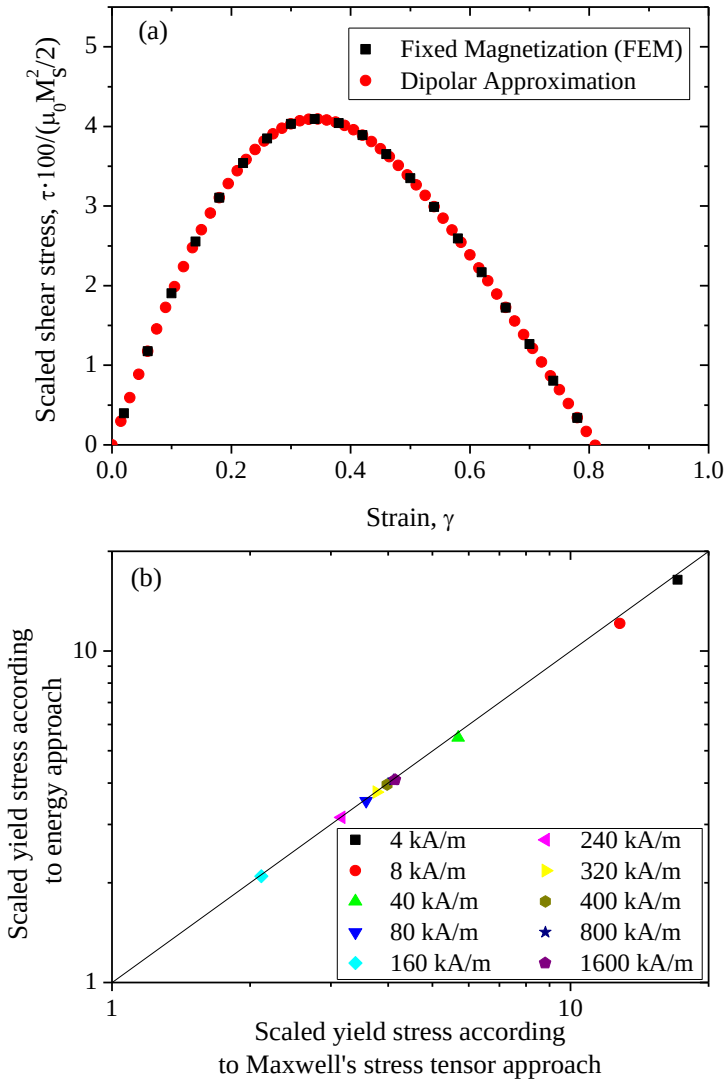

Figure 5.2: (a) Scaled shear stress versus shear strain in the saturated regime for $\phi = 0.2$. Black squares correspond to FEM simulations for permanently magnetized particles in the $\hat{z}$ direction. Red circles correspond to the numerical calculations for a lattice of magnetic dipoles. (b) Scaled yield stress calculated by differentiating the energy density (y-axis) versus the scaled yield stress calculated by integrating Maxwell's stress tensor (x-axis) for $\phi = 0.2$. The stress data are scaled by H_{ext}^2 if $H_{ext} < 160$ kA/m and by M_s^2 if $H_{ext} \geq 160$ kA/m.

Now that the FEM simulations are tested for saturation and using the free energy approach we move on to show the results. Simulated scaled shear stress versus shear strain data are shown in Fig. 5.3 for $\phi = 0.2$ and $d = 1$ μm. In Fig. 5.3a we show data for low magnetic field strengths where the particles operate in the linear magnetostatic regime ($\tau \propto H_{ext}^2$), while in Fig. 5.3b we show data for large magnetic field strengths where the particles operate in the saturation magnetostatic regime ($\tau \propto M_s^2$). The fact that the curves do not collapse with the field was expected in view of the appearance of saturated regions at the poles.

In the linear magnetization regime, our simulations for $\phi = 0.2$ give a one order of magnitude larger stress level if compared to previous FEM simulations (cf. solid line). This discrepancy is expected to be due to inappropriate boundary conditions imposed in previous simulations [12,13] and the difference is expected to be even larger for larger

particle concentrations. Note that in previous FEM simulations reported in the literature, it is the external magnetic vector potential $\vec{A}_{ext}$ that is imposed on the boundary. Hence, the shear stress level is significantly below our FEM simulations because the boundary gets closer to the particles when the concentration and/or strain increases.

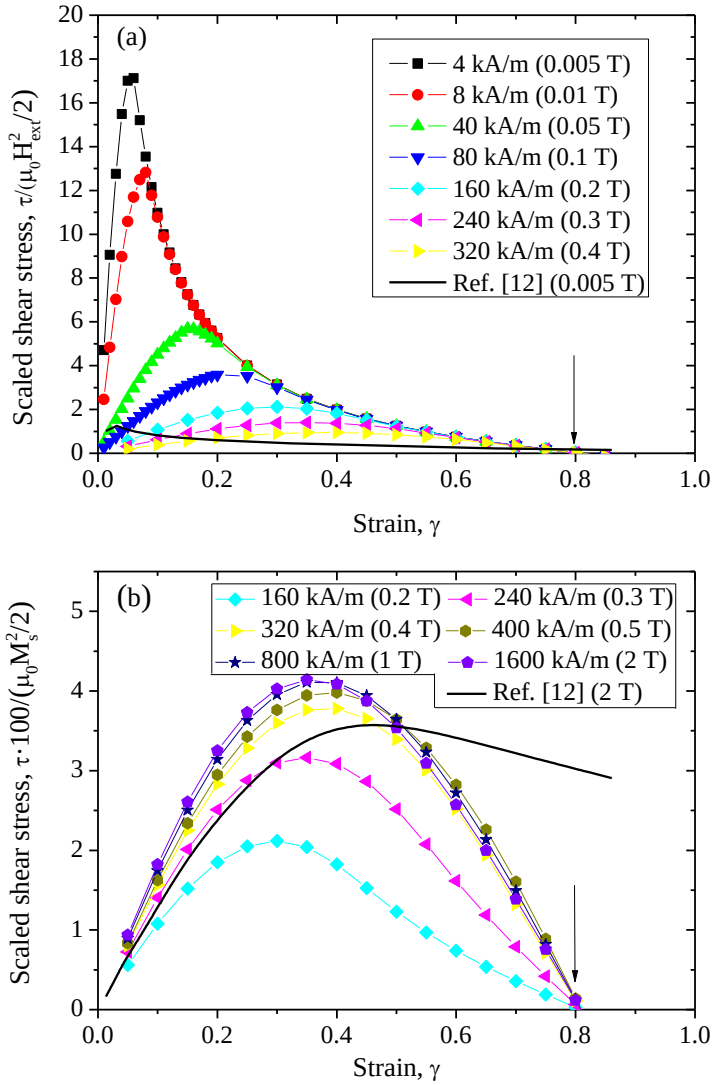

Figure 5.3: Scaled shear stress as a function of shear strain for different applied external magnetic fields and $\phi = 0.2$. (a) In the low field regime the shear stress is scaled by H_{ext}^2. (b) In the saturated regime the shear stress is scaled by M_s^2. Solid lines correspond to numerical calculations from Ref. [12].

Regarding the saturated regime, Fig. 5.3b demonstrates a much better agreement between our FEM simulations and those by previous authors (cf. solid line). This is coherent with the fact that the particular way to impose the external field (either using boundary conditions, Ref. [12], or reduced field formulation, this communication) is irrelevant in saturation.

An important observation from the inspection of Fig. 5.3 is that the stress becomes negative when the strain is large enough because F_y changes sign. A geometrical analysis gives a critical strain value for the crossover of $\gamma_c = \sqrt{\pi/24\phi}$ in good agreement with our simulations (cf. vertical arrow in Fig. 5.3). This observed sign reversal occurs in

striking contrast to previous simulations in the literature where the stress tends to zero but is always positive -independently of the strain- (see Ref. [12]). The reason for this is that in previous FEM simulations reported in the literature the strain deformation is simplified by an elongation of the chains followed by the rotation of the elongated chains at an angle $\theta = \operatorname{atan}\gamma$ (e.g. see Refs. [12,13]). However, this method is not truly equivalent to a real strain because in practice, the magnetization vector within every particle is aligned with the external magnetic field and not with the chain axis. At this point it is important to remark that an affine deformation is not expected to occur in real experiments on MR fluids essentially because the structures become unstable above the yielding point.

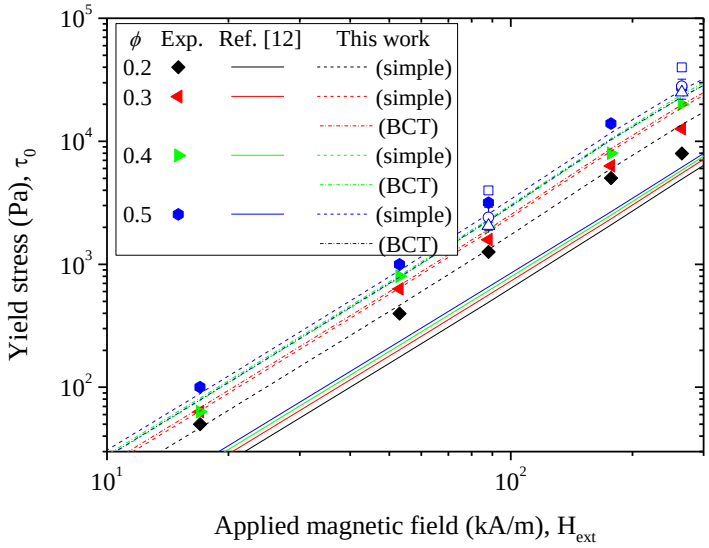

Figure 5.4: Yield stress as a function of the external magnetic field strength for concentrated carbonyl iron suspensions. Solid symbols: Experiments from Ref. [3]. Open symbols: Experiments from this communication. Open squares: glycerol 88 wt% with 125 mPa·s, open circles: silicone oils with 464 mPa·s and open triangles: silicone oils with 971 mPa·s. Solid lines: Simulations following Ref. [12]. Dashed lines: FEM simulations from this communication for tetragonal lattices. Dash-dotted lines: FEM simulations from this communication for BCT lattices.

In Fig. 5.4 we show FEM simulated yield stresses at different magnetic fields and particle concentrations (dashed lines). In the same figure, these results are plotted together with experiments [3] (solid symbols) and simulations [12] (solid lines) from the literature. Solid symbols correspond to HQ grade carbonyl iron (BASF SE) suspensions in a silicone oil of viscosity 20 mPa·s (Sigma Aldrich). These data are taken directly from Ref. [3] (see Fig. 6a in Ref. [3]). Additionally, new experiments were performed in order to demonstrate the applicability of the model with other different carriers. Open symbols in Fig. 5.4 correspond to 50 vol% HQ iron suspensions in carriers of different viscosities and chemical characteristics (open squares: glycerol 88 wt% with 125 mPa·s, open circles: silicone oils with 464 mPa·s and open triangles: silicone oils with 971 mPa·s). The fact that the experimental yield stresses do not depend on the particular carrier composition, for a given particle concentration, demonstrates that the experimental yield stress is solely driven by magnetostatic interactions and is therefore comparable to FEM calculations. To be consistent, both FEM simulations shown in Fig. 5.4 were carried out using the magnetization curve of the carbonyl iron powder as measured in a Squid magnetometer. As observed, a very good agreement is found between experiments (symbols) and our 3D FEM simulations (dashed lines). Simulations from the literature (solid lines) are clearly below the experiments again suggesting that the boundary

conditions typically used in the literature are not correct and that the elongation + rotation decomposition is not appropriate. For completeness, in Fig. 5.4 we also include FEM calculations for BCT packings in 30, 40 and 50 vol% MR fluids (see dash-dotted lines). The results are very similar to tetragonal lattices hence suggesting that the particular packing does not play a key role in the yielding process.

5.4 Conclusions

In conclusion, we propose a methodology that is capable to precisely compute magnetostatic interparticle interactions in model MR fluids for large particle loadings and strain levels. The method is based on periodic BCs and a reduced field formulation. The results are tested against numerical calculations in the magnetic saturation regime and energy minimization principles. Also, 3D simulation data are compared to yield stress experiments in concentrated MR fluids (above 10 vol%) and simulations available in the literature. There is a surprisingly good agreement between experiments and 3D FEM simulations. Although the results given in this letter are limited to the case of tetragonal and BCT lattices, the model can be easily extended to other lattices.

Acknowledgements

This work was supported by MINECO MAT 2016-78778-R and PCIN-2015-051 projects (Spain), European Regional Development Fund (ERDF) and by Junta de Andalucía P11-FQM-7074 project (Spain). J. R. Morillas acknowledges FPU14/01576 fellowship.

References

[1] Ginder, J. M. (1998). Behavior of magnetorheological fluids. MRS Bulletin, 23(8), 26-29.

[2] Park, B. J., Fang, F. F., and Choi, H. J. (2010). Magnetorheology: materials and application. Soft Matter, 6(21), 5246-5253.

[3] Ruiz-López, J. A., Fernández-Toledano, J. C., Hidalgo-Álvarez, R., and de Vicente, J. (2016). Testing the mean magnetization approximation, dimensionless and scaling numbers in magnetorheology. Soft Matter, 12(5), 1468-1476.

[4] Ruiz-López, J. A., Hidalgo-Álvarez, R., and de Vicente, J. (2017). Towards a universal master curve in magnetorheology. Smart Materials and Structures, 26(5), 054001.

[5] Clercx, H. J. H., and Bossis, G. (1993). Many-body electrostatic interactions in electrorheological fluids. Physical Review E, 48(4), 2721.

[6] Bonnecaze, R. T., and Brady, J. F. (1992). Dynamic simulation of an electrorheological fluid. The Journal of Chemical Physics, 96(3), 2183-2202.

[7] Klingenberg, D. J., Ulicny, J. C., and Golden, M. A. (2007). Mason numbers for magnetorheology. Journal of Rheology, 51(5), 883-893.

[8] Ocalan, M. PhD thesis. Massachusetts Institute of Technology, Cambridge, 2011.

[9] Vereda, F., Segovia-Gutiérrez, J. P., de Vicente, J., and Hidalgo-Álvarez, R. (2014). Particle roughness in magnetorheology: effect on the strength of the field-induced structures. Journal of Physics D: Applied Physics, 48(1), 015309.

[10] Davis, L. C. (1992). Finite-element analysis of particle-particle forces in electrorheological fluids. Applied Physics Letters, 60(3), 319-321.

[11] Davis, L. C. (1992). Polarization forces and conductivity effects in electrorheological fluids. Journal of Applied Physics, 72(4), 1334-1340.

[12] Ginder, J. M., and Davis, L. C. (1994). Shear stresses in magnetorheological fluids: role of magnetic saturation. Applied Physics Letters, 65(26), 3410-3412.

[13] Ginder, J. M., Davis, L. C., and Elie, L. D. (1996). Rheology of magnetorheological fluids: Models and measurements. International Journal of Modern Physics B, 10(23n24), 3293-3303.

[14] López-López, M. T., Kuzhir, P., Caballero-Hernandez, J., Rodríguez-Arco, L., Duran, J. D., and Bossis, G. (2012). Yield stress in magnetorheological suspensions near the limit of maximum-packing fraction. Journal of Rheology, 56(5), 1209.

Chapter 6. Yielding Behavior of Model Magnetorheological Fluids

Jose R. Morillas and Juan de Vicente

This article is published in: Soft Matter, 15(16), 3330-3342 (2019).

DOI: https://doi.org/10.1039/c9sm00275h

Abstract

The yielding behavior of magnetorheological fluids is revisited through the use of finite element method calculations on model structures and carefully conducted experiments in a magnetorheometer. Model structures investigated in this work are monoclinic lattices with simple and body centered bases. From the simulation point of view we emphasize the influence of the interparticle gap separation. From the experimental point of view we elucidate the importance of the magnetic field application and the occurrence of slip at the confining surfaces. Simulations demonstrate that the yield stress τ_0 scales with the interparticle center-to-center distance h as $\tau_0/\langle M\rangle^2 \propto h^{-6}$ where $\langle M\rangle$ is the particle magnetization. A good agreement is found when the simulated yield stresses are compared with the experimental ones, independent of the particular packing and interparticle gap.

6.1 Introduction

Soft matter is generally constituted by structured multi-phased materials in out-of-equilibrium configurations. Understanding their mechanical behavior, and in particular, the appearance of a yield stress is challenging [1]. In this context, the use of model systems may help to rationalize the analysis of more complex ones. A particularly interesting model system is a non-Brownian colloidal suspension, constituted by only two-phases, where the dispersed particles are preassembled in a lattice and whose interactions can be externally controlled through magnetic fields.

Magnetorheological (MR) materials are 'smart' magnetic-field responsive two-phase systems that exhibit a dramatic rheological change under the presence of a magnetic field [2-8]. When the field is applied, the dispersed particles become magnetized and interact via magnetostatic interparticle forces giving rise to an apparent yield stress and a non-negligible storage modulus. Most previous simulation works assume dipolar magnetostatic interactions between the particles [9-11] and the influence of multipole interactions has been scarcely investigated [12-14]. Among the different techniques employed to calculate multipole magnetostatic interactions in magnetorheology, Finite Element Method (FEM) is undoubtedly the most widely used [14-23].

Traditionally two different approaches are followed in the literature when dealing with FEM simulations. In a first set of publications, the computational domain encloses one or two particles in an attempt to determine the interaction between: (i) isolated particles or infinitely long single-particle width chains [24] or (ii) doublets of particles [25]. This

approach is especially useful to study the influence of surface roughness, interparticle distance, particle shape, and magnetic properties of the particles. In these simulations an external homogeneous magnetic field is introduced in the model through the boundary conditions, meaning the magnitude and direction of the magnetic field vector in one of the boundaries of the computational domain are assumed to match the external magnetic field. As a consequence, a compromise must be reached when choosing the domain size. Ideally, it must be large enough for the external magnetic field boundary condition to be valid but also small enough to reach sufficiently large particle volume fractions, which is often the case in MR fluid applications.

In a second set of publications the computational domain is the unit cell of a particle-based lattice with periodic boundary conditions. Tetragonal lattices are typically used [26,27]. However, axisymmetric domains are also employed in other publications [13,28]. This second approach is especially useful to calculate the yield stress and storage modulus in quasi-static conditions. In these simulations, mirror symmetries are also used and the external magnetic field is again introduced as a boundary condition. Two major complications arise in these particular simulations. The first drawback is a limitation in the maximum particle loading that can be achieved. The reason for this is that the size of the computational box reduces when the concentration increases and therefore the external magnetic field cannot be rigorously fixed at the boundary. The second limitation appears when the lattice is sheared and the unit cell loses its mirror symmetries in the boundaries, and the external magnetic field is no longer aligned with the lattice.

In brief, major problems regarding the simulation of the yield stress of MR composites with traditional FEM approaches are related to imposing the external magnetic field as a boundary condition close to the particle and properly modeling a true shear strain without losing lattice symmetries. These problems limit the traditional simulation strategies to small concentration and small shear strains. In this context, a novel FEM simulation methodology has been recently proposed for the calculation of the shear stress for all achievable particle loadings and strain levels [29]. In the present manuscript we use this model to study the influence of interparticle separation and thoroughly compare the simulation predictions with new carefully conducted experiments in a wide range of magnetic field strengths and particle concentrations. Note that the interparticle separation distance is crucial in practical applications where carbonyl iron particles are oxidized on their surface and magnetic core-core contact is prevented [17].

6.2 Simulation model

The methodology is based on a reduced magnetic field formulation to calculate multipolar contributions with periodic boundary conditions in order to compute multibody interactions. The essentials of this model are summarized below. For more details see Morillas and de Vicente [29].

The total magnetic field is decomposed into two contributions for the external magnetic field to be set as a domain property instead of a boundary property: (i) a homogenous background field (the external magnetic field) and (ii) a perturbation due to the presence of the magnetizable particles:

$$\vec{H} = \vec{H}_{ext} - \nabla V_p \tag{6.1}$$

Here $\vec{H}_{ext} = H_{ext}\hat{z}$ is the external applied field and V_p is the perturbation magnetic scalar potential.

Next, the magnetic field distribution is calculated in the steady state, in the absence of free current densities, by numerically solving:

$$\vec{H} = -\nabla V \tag{6.2a}$$

$$\nabla \cdot \vec{B} = \mu_0 \nabla \cdot \left(\mu_r \vec{H}\right) = 0 \tag{6.2b}$$

To solve Eq. (6.2) via FEM we used COMSOL Multiphysics software. Here $\vec{B}$ is the magnetic induction, μ_0 is the permeability of vacuum, and μ_r is the relative magnetic permeability of the particle and carrier fluid phases. Unless otherwise stated, we used the Fröhlich-Kennelly equation to calculate the magnetic permeability of the particles. As typically done in the literature, we assumed $\mu_i = 1000$ as their relative initial permeability and $M_s =$ 1600 kA/m as their saturation magnetization. However, the experimental magnetization curve will be used when comparing with the experiments (see Figs. 6.9-6.11).

In Fig. 6.1 we show the computational domains used in this work, which consists of unit cells in two model structures. In Fig. 6.1a we show the simplest possible unit cell for a tetragonal lattice that evolves into a monoclinic lattice upon shearing an amount γ in an affine deformation. This lattice, which we will refer to as the simple basis (SB), corresponds to a set of single-particle width chains aligned with the field direction with a constant lateral distance w_s between them (see Fig. 6.1a). Its height h_s is dictated by the particle diameter $h_s = d$ ($d =$ 1 μm through this work), whereas its width w_s is a function of the particle volume fraction ϕ_p as follows $w_s = \left(d^2\pi/6\phi_p\right)^{1/2}$. Since periodic boundary conditions are used, shear straining the lattice is equivalent to straining the computational domain/unit cell.

In Fig. 6.1b we show the computational domain used to model the same monoclinic lattice but with a 'body centered' basis (BCB). The reason why this structure is worth investigating is that, at least for magnetic dipoles in the non-strained state, a BC tetragonal lattice is the most favorable arrangement from an energetic point of view (i.e. it is the minimum energy configuration) [30]. As it can be seen, the BCB is shifted vertically a given distance from the center of the unit cell (in particular a distance of $d/4$ in Fig. 6.1b). This is mandatory due to computational requirements: if the central particle of the basis were in the center of the unit cell there would be two tangential points at the contact points between the central particle poles and top/bottom boundaries of the computational domain. These two singularities would make it not possible to properly mesh the computational domain. In this context, please note that in the tetragonal case (non-strained; $\gamma = 0$) regardless of the basis, a contact point appears between the poles of the particles. Therefore, the case $\gamma = 0$ is not studied in this work. Nevertheless, due to the symmetry of the problem, it can be stated that in this configuration the force in the strain direction is zero.

Bearing in mind that in the BCB there are two magnetic particles per unit cell, the height of the BCB is given by $h_{bc} = d$ while its width is still a function of the particle volume fraction as follows $w_{bc} = \left(d^2\pi/3\phi_p\right)^{1/2}$. It is also worth to note here that not all strains can be evaluated in the BCB. Under affine deformation particles displace horizontally with constant z values, therefore at large enough particle volume fractions and strains the

particles in the compression axis will eventually reach the central particle. At this stage, larger strains are not simulated because the interpenetration of the particles is not allowed. Following geometrical arguments, it can be seen that for a given particle volume fraction above $\phi_p = 0.35$ the maximum allowable strain is $\gamma_{max} = \sqrt{\pi/3\phi_p} - \sqrt{3 - \pi/3\phi_p}$. If $\phi_p < 0.35$ particles at the unit cell corners will not touch the central particle for any strain.

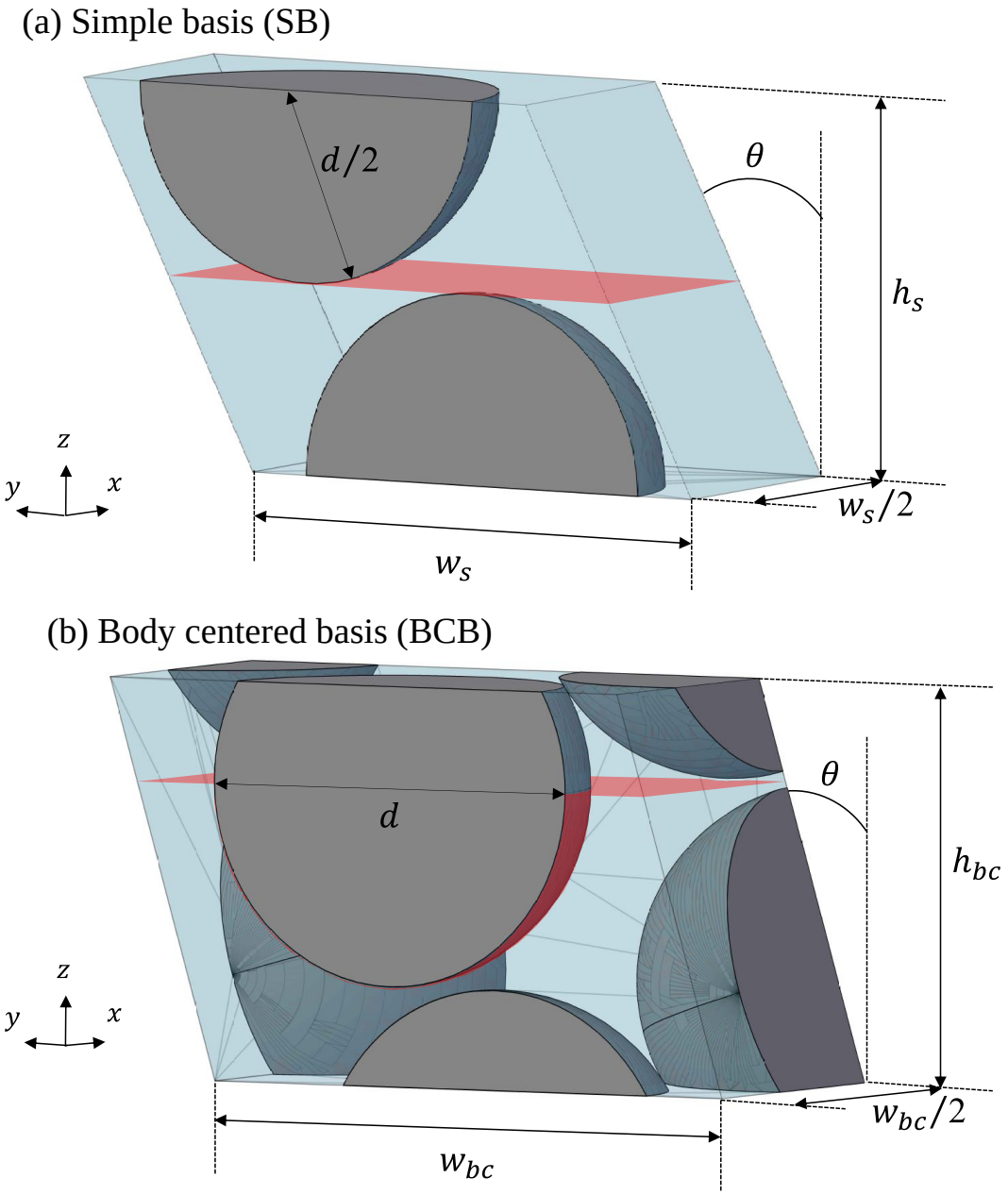

Figure 6.1: Computational domains used to simulate a monoclinic lattice with tilt angle $\theta = \operatorname{atan}\gamma$ in: (a) simple basis SB and (b) body centered basis BCB. Mirror symmetries are applied in boundaries normal to $\hat{x}$. Periodic boundary conditions are imposed in the rest of boundaries. To compute the force, the Maxwell's stress tensor is integrated on the red surface.

Once the magnetic field strength distribution is computed in the simulation cell, the interparticle force in the shear direction is determined by integration of the Maxwell's stress tensor over a closed surface S:

$$F_y = \int_S \hat{y}^T \cdot \left(\widetilde{BH} - \tilde{\delta} \frac{BH}{2} \right) \cdot \hat{n} ds \tag{6.3}$$

where $\tilde{\delta}$ is the unit diagonal tensor, $\hat{y}^T$ is the transposed unit vector in the y (shear) direction and $\hat{n}$ the unit vector normal to the integration surface. Due to the boundary conditions used in this work, the integration surface S can be reduced to a surface that intersects the lateral planes at the same height. In the case of the SB, the shadowed red plane highlighted in Fig. 6.1a can be chosen. However, in the BCB this plane is no longer useful because it crosses the central particle. Therefore, the surface employed in this work is represented by the red surface shown in Fig. 6.1b. Essentially, it is the same plane as the SB but it includes a spherical surface surrounding the bottom half of the central particle.

Having determined the magnetic interparticle force F_y for each strain, the shear stress τ is obtained by simply dividing the force in the shear direction by the surface area as follows:

$$\tau = 2 \frac{F_y}{w^2} \tag{6.4}$$

Note that the factor 2 in Eq. (6.4) comes from the fact that only one half of the unit cell is simulated. Using this simulation model, a shear stress versus strain curve can be obtained and the yield stress τ_0 is identified as the maximum of this curve.

6.3 Experiments

Experiments were carried out in suspensions prepared by dispersion of carbonyl iron particles in a mixture of water:glycerol (30:70 wt%) of viscosity 10 mPa·s at different particle concentrations ($\phi_p = 0.5$, 1, 5 and 10 vol%). Iron particles were kindly provided by BASF SE (HQ grade – mean diameter 1 μm) and glycerol was purchased from Scharlau (88 wt%).

The magnetization curve of the iron particles was determined in a Squid magnetometer (Quantum Design MPMS XL) at room temperature (the full magnetization versus field curve is, for example, published in Ref. [31]). From this curve, the initial magnetic permeability and saturation magnetization of the particles was obtained. In particular, these carbonyl iron particles have an initial relative magnetic permeability around 5 and a saturation magnetization of 1600 kA/m.

Rheological tests were carried out in a commercial magnetocell device (MRD70, MCR501 Anton Paar) in plate-plate configuration (1 mm gap) and isothermal conditions (25 ºC). The maximum magnetic field strength achieved was 265 kA/m. Steady shear flow tests were carried out according to the following protocol: First, the sample was redispersed (2 min stirring with a spatula + 2 min ultrasounds sonication bath + 2 min stirring with a spatula). Next, the sample was loaded on the rheometer base and the upper plate was displaced downwards until the plate separation reached the programmed gap. Then, the magnetic field was applied. Finally, a stress controlled ramp was imposed (15 pts./decade) concurrently with the applied magnetic field.

In an attempt to be as close as possible to the equilibrium configurations, we carefully controlled the way to superimpose the magnetic field on the suspensions. For this, two cases were considered. In the first case, a magnetic field of strength H_{ext} was suddenly

applied (fast field ramp) and the sample was allowed to structure during 1 min before the stress ramp starts. In the second case, the magnetic field strength was incrementally increased from 0 to H_{ext} for a stepwise sweep consisting of 16 steps of 10 seconds each (slow field ramp). Each step was split in two parts: during the first 7 seconds a magnetic field of strength $nH_{ext}/17$ (where n is the number of the step in the sweep) is applied to aggregate the particles, next, the magnetic field is switched off in the last 3 seconds of the step to allow the particles to conform by diffusion. In the step number 17 a magnetic field strength H_{ext} is applied during 7 seconds and kept constant during the stress ramp test. This particular protocol was inspired by previous works [32-34] and, *in principle*, should allow the particles to reach an equilibrium configuration.

In order to identify the importance of any possible wall slip occurring between the sample and the confining plates, we used surfaces with different roughness and/or texture. Experiments were conducted with sandblasted plates with a surface roughness of $R_q = 0.410 \pm 0.016$ μm and $R_a = 0.323 \pm 0.012$ μm. Also, texturized surfaces were used with radial grooves of 250 μm depth and 250 μm width. In these latter experiments, bottom and upper plates contained a pattern of 16 radial grooves.

Once the stress ramp test is finished, the steady shear flow curve is obtained. Typically, shear stress versus shear rate curves exhibited a very sharp transition from a quasi-solid to a purely viscous regime. The yield stress (corrected by the Weissenberg–Rabinowitsch–Mooney formula [35]) is taken here as the last data point before the sudden jump in shear rate. Only in those cases where the particle volume fraction and magnetic field strengths were very small, the transition was smoother and therefore the yield stress was obtained using the tangent method [36,37].

6.4 Results and discussion

6.4.1 Stress-strain curves: influence of interparticle gap

Simulated shear stress versus shear strain curves are shown in Fig. 6.2 for a particle concentration of $\phi_p = 0.2$ in a single-particle width chain structure (SB). In these figures, we show the influence of the magnetic field strength ($H_{ext} = 4$ – 4000 kA/m) and interparticle gap separation ($\Delta = 0$ and $\Delta = 0.015d$). In all cases, a maximum in the curves is clearly observed that corresponds to the yielding point of the structures.

The influence of a gap between the particles (Δ), its effect on particle magnetization and on the axial magnetic force have been previously studied for isolated chains [38]. That work demonstrated how increasing the gap reduces the magnetic field magnitude and magnetization in the polar regions of the particles, and therefore the magnetostatic interaction force decreases. The simulation methodology used in the present work is capable to predict the influence of interparticle gap in the yield stress by simply changing the dimensions of the simulation unit cell as follows:

$$h = d + \Delta \tag{6.5a}$$

$$w = \sqrt{\frac{h^2\pi}{C\phi_p}} \tag{6.5b}$$

Here $C = 6$ or 3 depending on the SB or BCB basis, respectively. Note that, the lateral separation between chains is also affected by the interparticle gap. Keeping the particle

volume fraction constant, w increases with Δ. Therefore, when an interparticle gap is considered, ϕ_p stands for the volume fraction of a suspension based on core-shell particles with core diameter d and shell thickness $\Delta/2$. Note that this particular configuration is closer to the experiments where magnetizable particles are typically oxidized on their surface [17]. As a result of the core-shell structure, the magnetic volume fraction ϕ_m is not exactly the same as the particle volume fraction ϕ_p. The two volume fractions are related through $\phi_m = \phi_p(d/h)^3$.

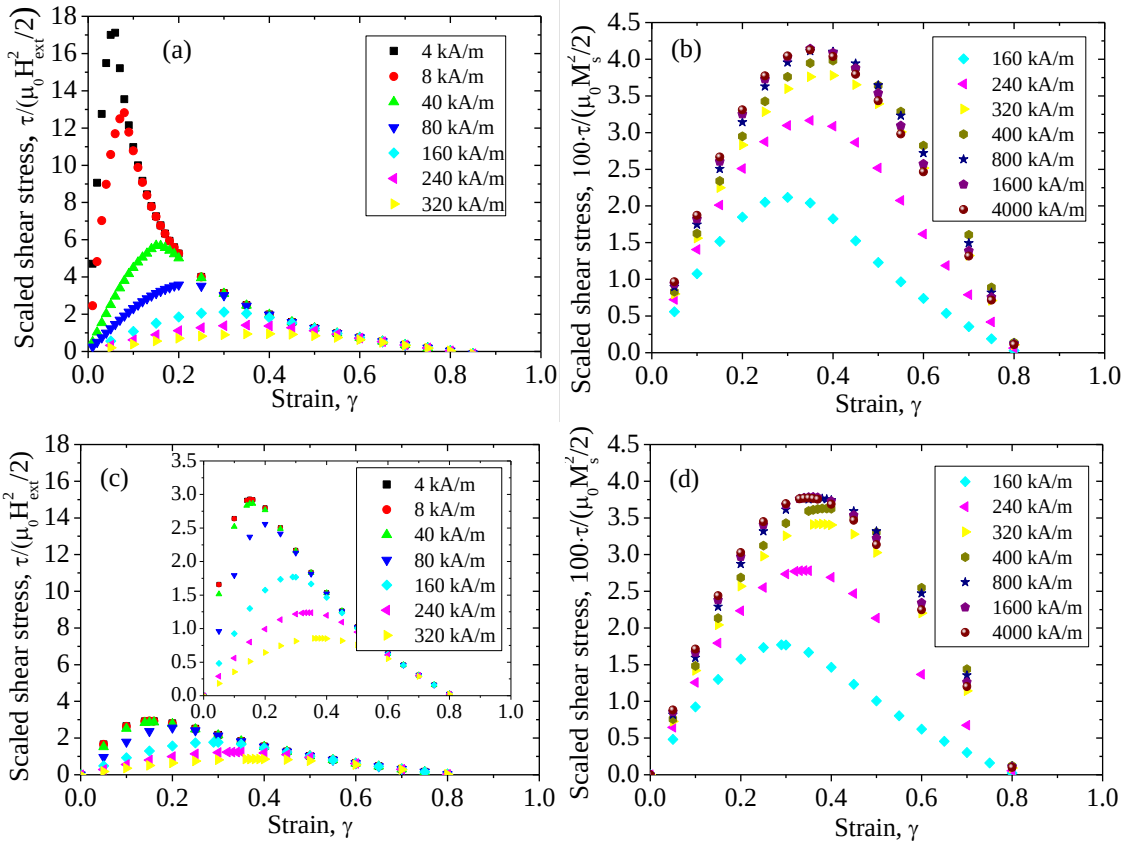

Figure 6.2: Scaled shear stress versus strain curves for $\phi_p = 0.2$ and different applied external magnetic fields in a single-particle width chain structure (SB). a) Small fields, $\Delta = 0$. b) Large fields, $\Delta = 0$. c) Small fields, $\Delta = 0.015d$. d) Large fields, $\Delta = 0.015d$. The shear stress is scaled by $\mu_0 H_{ext}^2/2$ and $\mu_0 M_S^2/2$ for small and large fields respectively. a) and b) are adapted from Ref. [29].

In Figs. 6.2a and 6.2c we show results for low magnetic fields, while in Figs. 6.2b and 6.2d we show results for high magnetic fields. It can be clearly seen that the shear stress is dramatically reduced for even small changes of Δ in the case of the smaller magnetic fields (compare Figs. 6.2a and 6.2c). In the case of saturating fields the influence of Δ is less important (compare Figs. 6.2b and 6.2d). This finding can be explained taking into consideration that in the saturated regime, saturated regions within the particles act as dipoles, whose interaction is of longer range than multipolar interactions. A small separation between these regions is not supposed to significantly affect the shear stress in the saturation regime.

As expected, in the low field regime (see Fig. 6.2a), a scaling of the stress by H_{ext}^2 fails regardless of the field strength when $\Delta = 0$ at low strains. This was expected because the particles are so close that their polar regions saturate. Conversely, this scaling is

appropriate for fields up to 40 kA/m when $\Delta = 0.015d$ (see inset in Fig. 6.2c). This observation reinforces the previous reasoning: if an interparticle gap exists, the multipolar terms do not play a major role, therefore field enhancement will be reduced along with the magnetization. As it was pointed out by Ref. [13], if the saturation magnetization is not reached, magnetic interaction increases proportionally with H_{ext}^2, explaining the good fitting to this scaling in Fig. 6.2c with $\Delta \neq 0$ and low fields.

The dependence of the yield stress on the interparticle gap is more clearly seen in Fig. 6.3. In this figure we show the scaled yield stress as a function of $h = d + \Delta$. Although still valid, the aforementioned scaling does not give any insight into the influence of the local magnetic field on the yield stress. With this in mind, two normalizations are evaluated in Fig. 6.3. In Fig. 6.3a, the yield stress is scaled by the particle magnetization evaluated at the internal magnetic field within the particle H_{int} (i.e. the external field plus the demagnetization field) under the assumption that the particle is isolated. This kind of scaling should be insensitive to the nonlinear magnetic behavior, however it yields a good collapse only at large h values when magnetic cores are far enough from each other thus avoiding a noticeable coupling between the magnetization of the cores. Multipolar effects can still be seen at small gaps giving rise to a yield stress enhancement in the linear magnetic field regime.

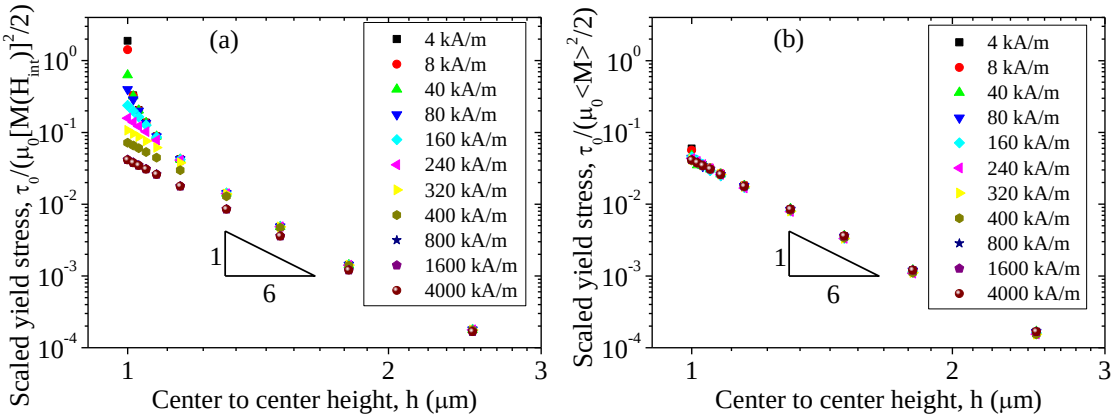

Figure 6.3: Scaled yield stress as a function of the distance between centers $h = d + \Delta$ for different external fields in a simple basis at $\phi_p = 0.2$. In a) the yield stress is scaled using the particle magnetization at its internal magnetic field H_{int} while in b) the yield stress is scaled using the true magnetization as obtained from the magnetization average over the particle volume $\langle M \rangle$.

In an attempt to improve the overlapping, in Fig. 6.3b we scale the yield stress by the true particle magnetization, in other words, including the magnetization enhancement due to the field originated by the surrounding particles. As observed, a better collapse can be seen for all simulated fields. Magnetization values used in the construction of Fig. 6.3b come from the volume average of the magnetization at the particle volume. The fact that the data do not collapse at the two smallest fields is due to the existence of multipole effects.

Finally, it is worth to note that in the saturation regime (800-4000 kA/m) both kinds of scalings yield the same result for the yield stress. This was expected because only in this case the magnetization is constant and uniform within the particle, independent of local field effects. With this in mind, the yield stress scales with the center-to-center distance

as a power law function with exponent -6. This behavior can be easily understood taking into consideration that the dipolar forces scale as h^{-4} and therefore $\tau_0 \propto F_0/w^2 \propto h^{-6}$.

6.4.2 Minimum energy configuration: comparison between simple and body centered bases

As stated previously, the equilibrium structure for a MR fluid under a DC uniaxial magnetic field is expected to be a BC tetragonal lattice. However, as far as we know, this statement has only been demonstrated for interacting dipoles [30]. Hence, our first goal was to compare the magnetic energy of SB and BCB in linear and saturation regimes. Note that, a direct comparison between SB and BCB in a tetragonal lattice (non-strained state) is only possible when $\Delta \neq 0$. Otherwise, a tangential point between particles in contact would not allow the domain to mesh. To circumvent this problem, a monoclinic lattice will be simulated and the energy related to the tetragonal lattice should be inferred in the limit where $\gamma = 0$. The cell magnetic energy density W will be calculated similar to Ref. [29]:

$$W = \frac{1}{V_{cell}} \int_{V_{cell}} \left(\int_0^{\vec{H}} \vec{B} d\vec{H}' \right) dv \tag{6.6}$$

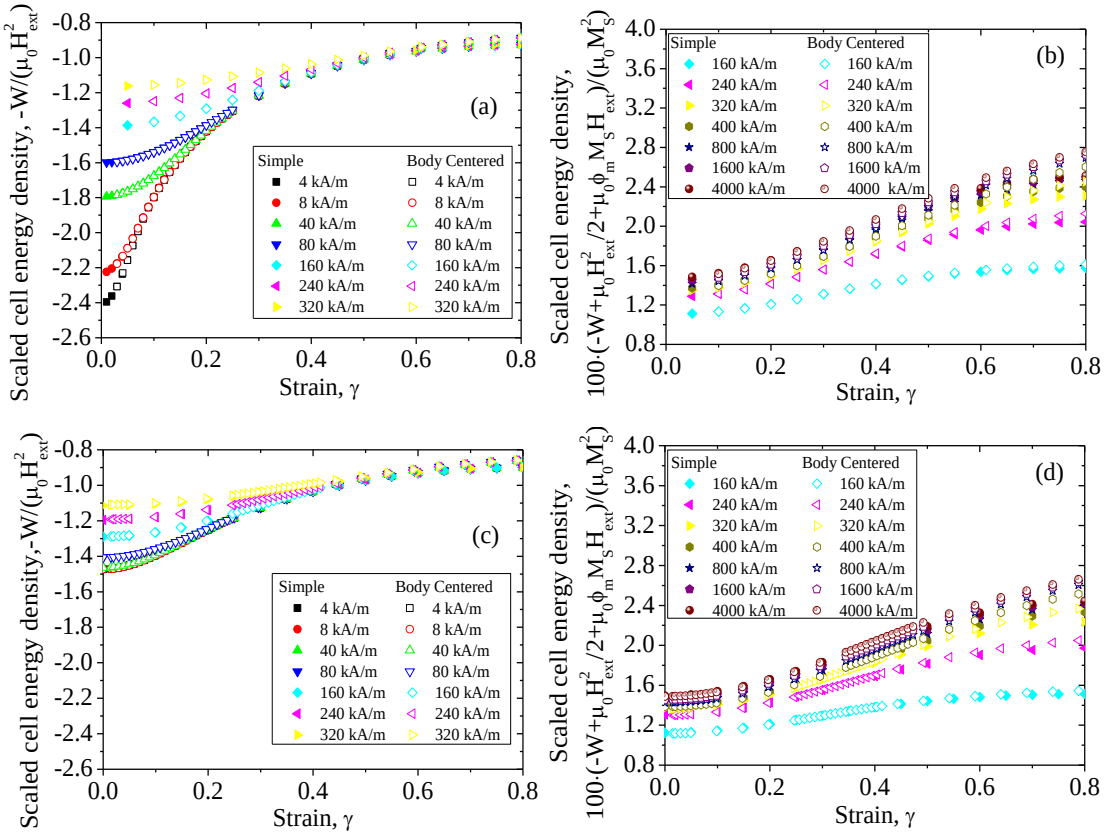

Figure 6.4: Scaled cell magnetic energy density for SB (filled symbols) and BCB (empty symbols). $\phi_p = 0.2$. a) Small fields, $\Delta = 0$. b) Large fields, $\Delta = 0$. c) Small fields, $\Delta = 0.015d$. b) Large fields, $\Delta = 0.015d$.

In Fig. 6.4 we show W for $\phi_p = 0.2$ in the absence ($\Delta = 0$) and presence of an interparticle gap ($\Delta = 0.015d$) with different magnetic fields in the case of SB and BCB. In Figs. 6.4a and 6.4c we show the results for low fields while in Figs. 6.4b and 6.4d we show results for high fields. As observed, regardless of the field strength, no differences are found

between the two kinds of bases. This observation can be understood bearing in mind that for small and moderate concentrations, the lateral distance between chains in the lattice with BCB is too large for the vertical misalignment between the particles to play a role.

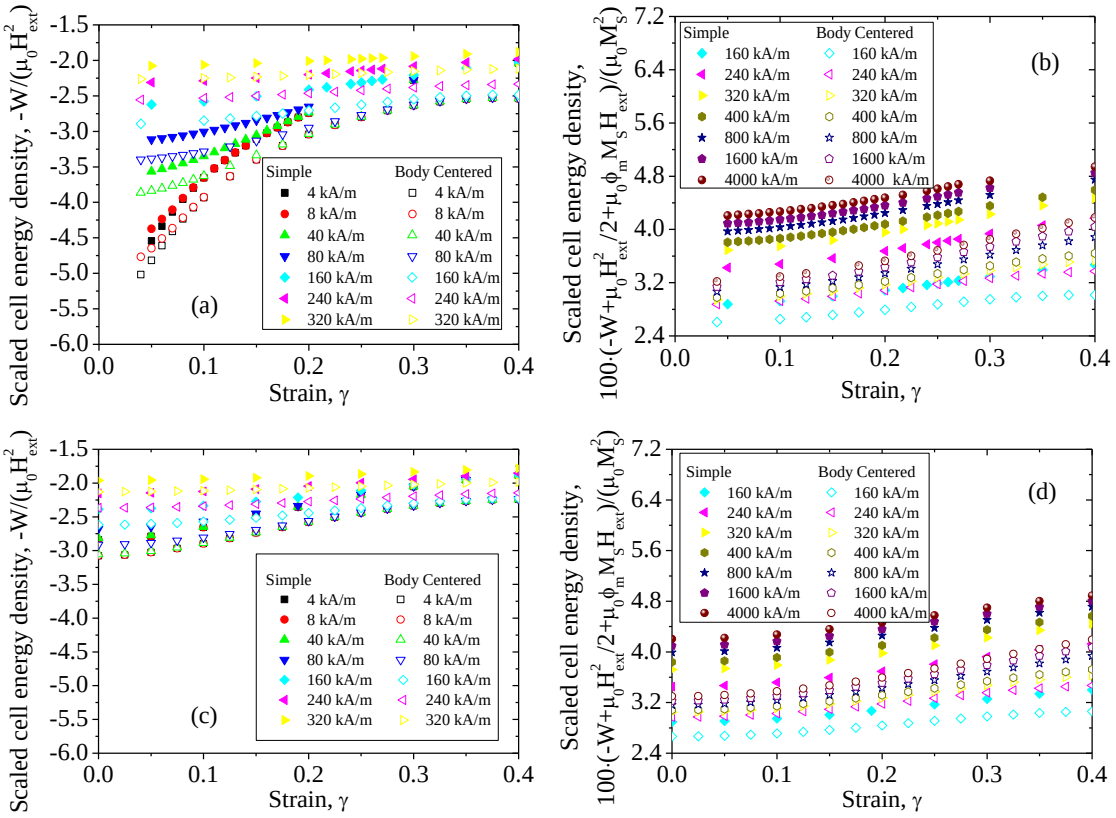

Figure 6.5: Scaled cell magnetic energy density for SB (filled symbols) and BCB (empty symbols). $\phi_p = 0.5$. a) Small fields, $\Delta = 0$. b) Large fields, $\Delta = 0$. c) Small fields, $\Delta = 0.015d$. b) Large fields, $\Delta = 0.015d$.

Data for low fields reported in Fig. 6.4a are normalized by $\mu_0 H_{ext}^2$. Similar to what happens to the shear stress, the normalization by H_{ext}^2 works properly only for small fields and sufficiently large strains to avoid the magnetic saturation at the polar regions of the particles. Figure 6.4b shows that in the saturated regime, a reduced energy $-W + \mu_0 H_{ext}^2/2 + \phi_m \mu_0 M_s H_{ext}$ is found to be normalized by $\mu_0 M_s^2$. This points out that in this regime, the total energy can be split in three contributions: particle interaction (proportional to $\mu_0 M_s^2$), external magnetic field ($\mu_0 H_{ext}^2/2$), and particle-external field interaction ($\mu_0 \phi_m M_s H_{ext}$).

In Fig. 6.5 we show results for $\phi_p = 0.5$. For this higher concentration, the BCB is clearly energetically more favorable than the SB both in the low and high field regime for any simulated strain. Furthermore, taking into consideration that the energy derivative is the shear stress (with opposite sign) and knowing that the shear stress is zero in the non-strained state, it could be inferred that the energy will not decrease sharply as the strain approaches $\gamma = 0$. Consequently, it is expected that the energy in the BCB remains below the SB even in the non-strained state indicating that the former is a more stable configuration.

In Figs. 6.4c, 6.4d, 6.5c and 6.5d, the magnetic energy density is represented for $\Delta = 0.015d$. It can be seen that, for low magnetic fields, the existence of an interparticle gap prevents the saturation of the poles thus extending to smaller strains the interval where

the normalization by H_{ext}^2 is successful. For large fields, the incorporation of an interparticle gap does not have a remarkable effect in the normalization because even without it, magnetostatic interactions are dominated by dipolar ones. As it was expected, for both linear and saturated magnetic regimes, the magnetic interaction along the chains is attractive and therefore the existence of an interparticle gap increases the energy of the system.

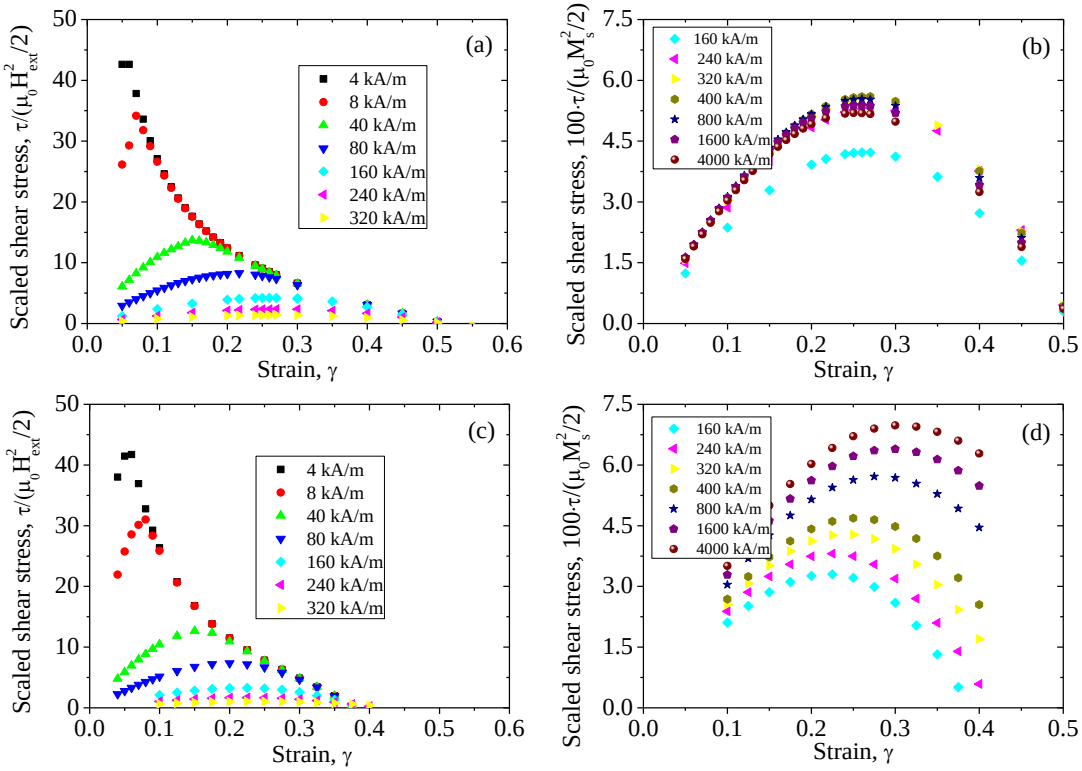

Figure 6.6: Scaled shear stress versus strain curves for $\phi_p = 0.5$, $\Delta = 0$ and different applied external magnetic fields. Top row: SB. Bottom row: BCB. The shear stress is scaled according to the low field regime (H_{ext}^2, left column) and saturated regime (M_s^2, right column).

As demonstrated in Figs. 6.4 and 6.5, the particular preassembly of the particles, in SB or BCB, is critical only at high concentrations when the distance between neighboring chains is small. Consequently, in Fig. 6.6 the shear stress versus strain curves are represented for both bases only when $\phi_p = 0.5$. Surprisingly, in the low field regime, although the BCB is energetically more favorable, a lower yield stress is exhibited if compared to the SB (compare Figs. 6.6a and 6.6c). This can be understood analyzing the yield strain, that is, the strain corresponding to the maximum stress. It can be seen that in the BCB the yield strain is lower than in the SB hence hampering the shear stress to reach higher values. This is related with the particle arrangement within the unit cell. For the BCB, as the strain is increased, the particles located in the compression axis get closer to the central particle hence generating a force that is opposed to the strain direction therefore reducing the shear stress. The effect of neighboring particles can also be appreciated in the strain at which the shear stress changes its sign. In the SB this point is independent of the magnetic field and can be simply obtained from geometrical arguments. In the BCB this reasoning is not true. Note that in a real system a negative stress is not observed.

Another important observation comes from a close look to Fig. 6.6b. It is observed that contrary to intuition, the shear stress values do not saturate at high magnetic fields (i.e. the stress slightly decreases at high fields). This behavior is observed with and without an interparticle gap but only at high volume fractions (compare Figs. 6.6b and 6.7b). A similar observation has also been reported by other authors [16]. The reason for this could be in the magnetic behavior of the particles. In our case, the magnetizable particles are modeled as non-linear isotropic materials. The magnetization vector components are not related to each other; while the z component could be saturated for sufficiently large H_{ext} values (note that $H_z = H_{z,p} + H_{ext}$), the y and x components could not saturate because they only depend on the respective components of $\vec{H}$, which do not have a contribution from the external magnetic field H_{ext} that always points in the z direction. In Fig. 6.6d we show that the stress monotonically increases with the field strength. This was expected and, in fact, for fully saturated particles one gets the same curve as that shown in Fig. 6.6d for 4000 kA/m. As observed, a larger field strength is needed for the stress to level off in the BCB.

Similar to what happened for the smaller volume fraction investigated, the influence of the interparticle gap is very strong for small fields (see Figs. 6.7a and 6.7c), reducing the shear stress one order of magnitude. For saturating fields (see Figs. 6.7b and 6.7d), the shear stress decreases, which is expected because the magnetic cores are more separated inside each chain.

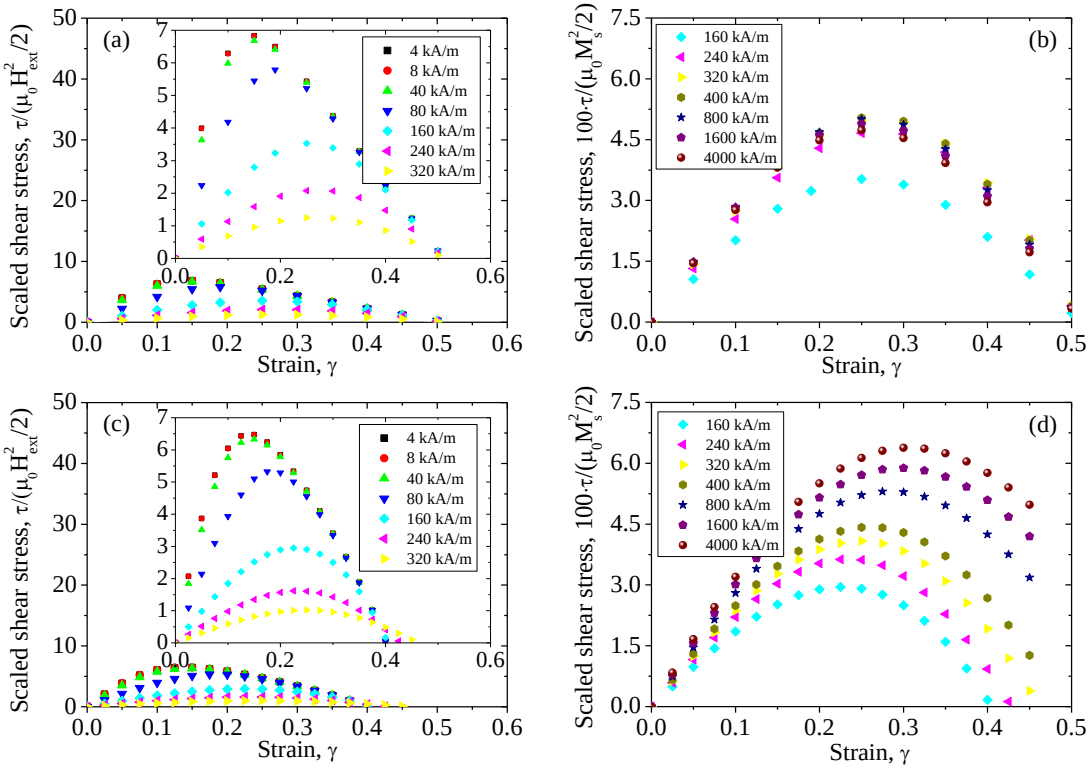

Figure 6.7: Scaled shear stress versus strain curves for $\phi_p = 0.5$, $\Delta = 0.015d$ and different applied external magnetic fields. Top row: SB. Bottom row: BCB. The shear stress is scaled according to the low field regime (H_{ext}^2, left column) and saturated regime (M_s^2, right column).

6.4.3 Comparison with experimental data

In Fig. 6.8 we show the most representative experimental results for conventional MR fluids subjected to field strengths of 265 kA/m. Higher fields can be achieved in this experimental setup, however the resulting field is not homogeneous in the sample volume giving rise to magnetophoretic forces and concentration gradients that influence shear stress measurements [39-41]. Experimental data in the magnetic saturation regime have been recently reported by Ref. [41].

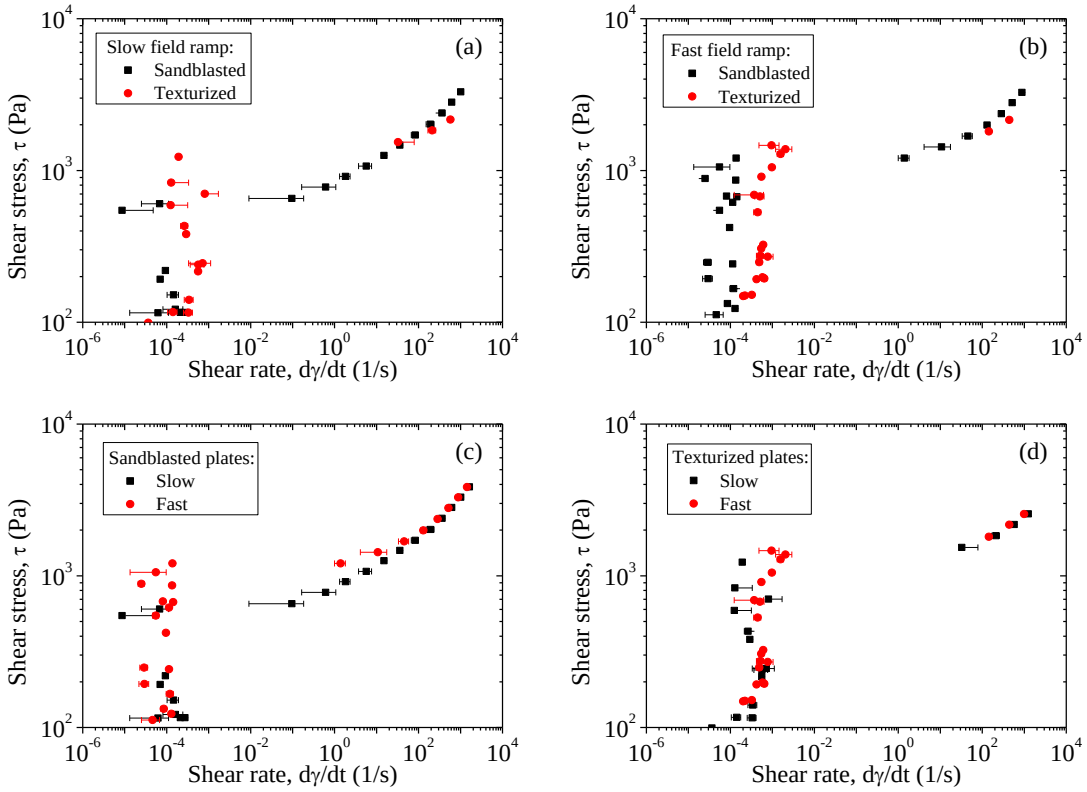

Figure 6.8: Typical experimental rheograms to show the influence of plate texturization and magnetic field application. Particle volume fraction 5 vol%. External magnetic field strength 265 kA/m. a) slow field ramp for sandblasted and texturized plates, b) fast field ramp for sandblasted and texturized plates, c) sandblasted plates for slow field ramp and fast field ramp, d) texturized plates for slow field ramp and fast field ramp. All experimental data shown in this figure were corrected using the Weissenberg–Rabinowitsch–Mooney correction.

In Fig. 6.8a we show results corresponding to the slow field ramp for sandblasted and texturized plates. The yield stress obtained in the case of texturized plates is clearly larger than in sandblasted plates. This suggests that wall slip, if exists, is smaller in the case of texturized plates than in sandblasted plates. In Fig. 6.8b we show results corresponding to the fast field ramp for sandblasted and texturized plates. Again, texturized plates give larger stress values if compared to sandblasted plates. In Fig. 6.8c we show results corresponding to the sandblasted plates for slow field ramps and fast field ramps. For the gap investigated in this work (1 mm), slow field ramps are typically associated to wall slip in contrast to fast field ramps. This explains why in this case (fast field ramps) the yield stress is higher. For completeness, in Fig. 6.8d we show results corresponding to the texturized plates for a slow field ramp and a fast field ramp. In this case, we observe that both slow and fast field ramps yield similar results. To summarize, wall slip is found to

occur also with sandblasted plates. Only when texturized plates are used the wall slip is completely prevented and the application of slow or fast field ramps does not make a difference.

In Fig. 6.9 we show the yield stress obtained from experiments (symbols) and simulations (SB and BCB depicted by thin and thick lines, respectively). Experimental data for concentrations below 20 vol% correspond to measurements with texturized plates and fast field ramps. As demonstrated in Fig. 6.8, this particular configuration avoids the occurrence of wall slip and provides the most reproducible results. Experimental data for concentrations above 20 vol% are taken from Ref. [42]. As observed, a reasonably good agreement exists between experiments and both the SB and BCB simulation cases for all the concentrations investigated. Simulations using the BCB yield results that (in the worst case) only differ by 12% with the SB simulations. Deviations at high magnetic fields may come from the stronger opposition of the kinetically arrested field-induced structures to relax towards more energetically favorable states.

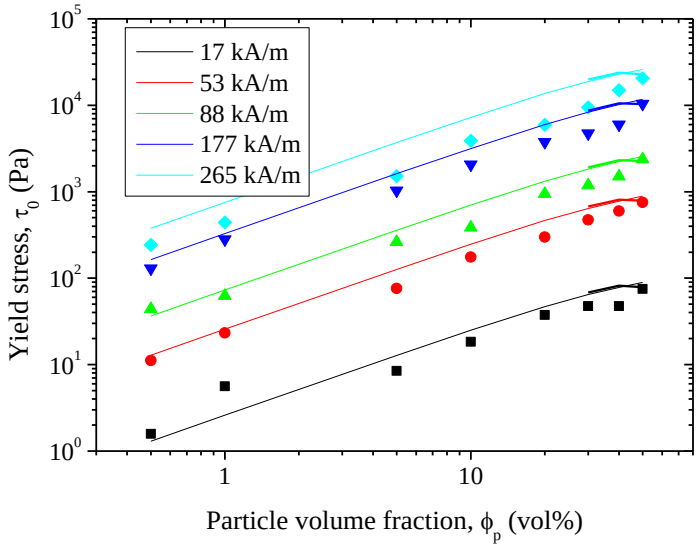

Figure 6.9: Comparison of the yield stress obtained from simulations with SB (thin lines) or BCB (thick lines) and experiments (symbols). Experimental data for concentrations above 20 vol% are taken from Ref. [42]. Experimental data for concentrations below 20 vol% are measured in this work. They correspond to texturized parallel plates and fast field ramps. All experimental data shown in this figure were corrected using the Weissenberg–Rabinowitsch–Mooney correction. In the simulations we used the experimental magnetization curve for the carbonyl iron particles.

From the simulation data shown in Fig. 6.9 it can be concluded that the yield stress follows a power law relationship with the external field H_{ext} and volume fraction ϕ_p:

$$\tau_0 = \begin{cases} AH_{ext}^{a}\phi_p^{\alpha} & \phi_p \leq 0.1 \\ BH_{ext}^{b}\phi_p^{\beta} & \phi_p > 0.1 \end{cases} \tag{6.7}$$

The best fitting parameters were $A = 0.66 \pm 0.06$, $a = 2.071 \pm 0.015$, $\alpha = 0.9746 \pm 0.0011$, $B = 0.62 \pm 0.11$, $b = 2.00 \pm 0.03$, and $\beta = 0.749 \pm 0.011$. Note that H_{ext} must be expressed in kA/m to get τ_0 in Pa. As expected, in the linear regime the external magnetic field exponent is close to 2. With regards to the volume fraction dependence, the yield stress increases almost linearly in the diluted regime. This observation is in good agreement with mechanical models based on isolated chains [43,44]. For higher

concentrations the yield stress levels off in agreement with Ref. [45] and the slope decreases.

Regarding the interparticle gap effect, simulations described in the Secs. 6.4.1 and 6.4.2 using the Fröhlich-Kennelly constitutive equation ($\mu_i = 1000$ and $M_s = 1600$ kA/m) showed yield stress differences as large as 80% with only a small gap of $\Delta = 0.015d$ (see Figs. 6.2, 6.6 and 6.7). However, when the experimental magnetization curve for the carbonyl iron powder is used in the simulations ($\mu_i \sim 5$), these differences are reduced to 20% for the most unfavorable case, small fields and large concentrations (results not shown here for brevity). For sufficiently large fields, when the particles are fully saturated and dipolar interactions govern, the differences are reduced even further to only 8%. Overall, the existence of an interparticle gap is especially important at low fields, and in this case, a precise estimation of the particle initial permeability is needed.

From an experimental point of view, it is difficult to assess the influence of the interparticle gap in the yield stress especially taking into consideration the microparticles used in this work (bare magnetic carbonyl iron cores of 1 μm diameter). Generally speaking, interparticle gaps always occur due to polydispersity, roughness, and surface oxidation. In addition, the interparticle gap is not expected to be the same in all contact points, therefore the choice of this parameter in the simulation model is not straightforward. Although the inclusion of a gap could make simulations fit better to the experiments, we think that a deeper study on this topic should be done by using well defined core-shell particles. In summary, the good agreement between experiments and simulations, with $\Delta = 0$ as shown in Fig. 6.9, demonstrates that the effect of the interparticle gap is negligible for the MR fluids with low initial permeability that are investigated in this work.

The simulated yield strain (associated to the yield stress) is shown in Fig. 6.10 with lines. Thin lines correspond to SB and thick lines correspond to BCB. Consistent with the discussion above, and similarly to Fig. 6.9, the experimental magnetization curve for the carbonyl iron particles is used and the interparticle gap is neglected ($\Delta = 0$). Together with the simulation data we also show experiments from the literature using dynamic oscillatory shear tests (from Fig. 7d in Ref. [45]). In particular, in Fig. 6.10 we include what Ref. [45] denotes the 'crossover strain'. The 'crossover strain' is defined as the strain at which both storage and loss moduli have the same value $G' = G''$ and it is related to the onset of flow of the MR fluid. As observed from Fig. 6.10, the simulations give the correct order of magnitude for particle volume fractions below 10 vol%. In this regime the chains do not see each other and the yield strain is dictated by the relative positions of the particles within individual chains. As a result, the volume fraction dependence is negligible below 10 vol%.

For higher concentrations (above 10 vol%), the particle chains are closer and interchain interactions develop. Simulations predict a decrease in the yield strain that can be interpreted from a geometric point of view. As the particle volume fraction increases, the critical strain associated with the stress reversal (change in sign) decreases [29]. Therefore, the stress versus strain curve has to reach its maximum (i.e. the yield stress) at smaller yield strains before becoming negative. Contrary to simulations, experiments exhibit two different trends. For the smallest fields investigated, the yield strain decreases with the volume fraction in good agreement with the simulations. However, for the largest fields investigated, the yield strain increases with the volume fraction. According to Ref. [45], this behavior originates from the fact that, at high concentrations, there exist connections between aggregates (inter-connections) and between particles forming each

aggregate (intra-connections). The latter are stronger than the former so when the MR fluid undergoes a stress, the resulting strain is not homogeneous but smaller inside the aggregates. As a result, larger strains are needed to yield. This discrepancy between simulations and experiments at high loadings can be understood bearing in mind that, in simulations, due to the use of periodic boundary conditions and affine deformation, (i) the strain is the same in the whole lattice and (ii) the particles are placed in a periodic lattice (i.e. there are not aggregates). Consequently, a distinction between inter- and intra-connections is not appropriate.

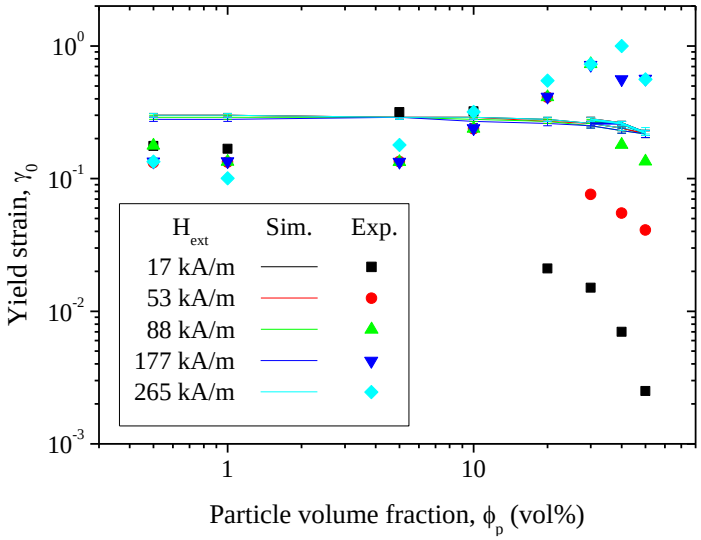

Figure 6.10: Comparison of the yield strain obtained from simulations with SB (thin lines) or BCB (thick lines) and experiments (symbols). Experimental data are taken from Ref. [45]. In the simulations we used the experimental magnetization curve for the carbonyl iron particles.

6.4.4 Universal Master Curve

In this section we aim to explore the consistency of the current simulations in the frame of the universal master curve proposed by Ref. [42] for steady shear.

Because of its non-Brownian character, the steady shear flow behavior of MR fluids can be collapsed on a master curve if the dimensionless viscosity η/η_∞ (i.e. the ratio between the shear viscosity and the high shear viscosity) is plotted as a function of the Mason number $\mathrm{Mn}_{\langle M\rangle}$, which is the ratio between hydrodynamic and magnetostatic forces [25,42]:

$$\mathrm{Mn}_{\langle M\rangle} = \frac{72\eta_c\dot{\gamma}}{\mu_0\mu_{cr}\langle M\rangle^2} \tag{6.8}$$

Here $\langle M\rangle$ is the particle magnetization, μ_{cr} is the carrier fluid relative magnetic permeability, and η_c is the viscosity of the carrier fluid. Depending on the constitutive equation of the MR fluid, different master curves can be constructed. However, a very simple curve that provides a very good fit to the experimental data in a wide range of field strengths and concentrations is the Casson model [46]:

$$\frac{\eta}{\eta_\infty} = 1 + \frac{\mathrm{Mn}^*_{\langle M\rangle}}{\mathrm{Mn}_{\langle M\rangle}} + 2\sqrt{\frac{\mathrm{Mn}^*_{\langle M\rangle}}{\mathrm{Mn}_{\langle M\rangle}}} \tag{6.9}$$

Here $\mathrm{Mn}^*_{\langle M\rangle}$ is a critical Mason number that determines the transition from the magnetostatic controlled regime to the hydrodynamic one [42]:

$$\mathrm{Mn}^*_{\langle M\rangle} = \frac{72\tau_y}{\mu_0\mu_{cr}\langle M\rangle^2}\frac{\eta_c}{\eta_\infty} \tag{6.10}$$

where τ_y is the dynamic yield stress (dependent on the particle magnetization and particle volume fraction). Note that, in line with Eq. (6.9), if $\mathrm{Mn}^*_{\langle M\rangle}$ is known then the flow curve of any MR fluid collapses on a single master curve when it is plotted versus $\mathrm{Mn}^*_{\langle M\rangle}/\mathrm{Mn}_{\langle M\rangle}$.

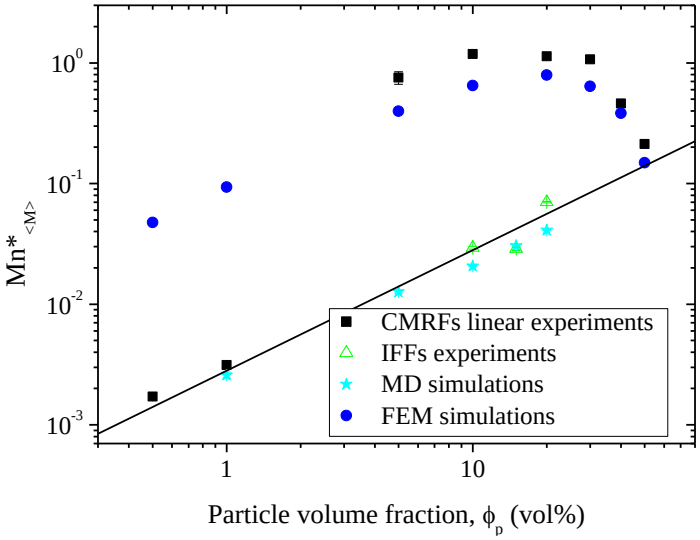

Figure 6.11: Particle volume fraction dependence of the critical Mason number $\mathrm{Mn}^*_{\langle M\rangle}$. Squares: experiments on conventional MR fluids (CMRFs) in the linear magnetostatic regime. Triangles: experiments on inverse ferrofluids (IFFs). Stars: MD simulations. Circles: FEM simulations from the present work. Experiments were carried out under stress control. Squares, triangles and stars are obtained from Ref. [42]. The line corresponds to $\mathrm{Mn}^*_{\langle M\rangle} = 0.25\phi^{1.03}$.

Using particle-level molecular dynamics (MD) simulations, Ref. [47] obtained a best-fitting expression $\mathrm{Mn}^*_{\langle M\rangle} = 0.25\phi^{1.03}$ that satisfactorily predicted the steady shear flow behavior of inverse ferrofluids (IFFs). However, this equation failed to explain the experimental results for MR fluids with concentrations above 5 vol% (see Fig. 5 in Ref. [42]). In this concentrated regime, the discrepancies between experiments and MD simulations are expected to come from both the Stokes' drag and dipolar approximations. The first issue can be partially circumvented by supposing that the high shear rate viscosity is given by a Quemada-like expression: $\eta_c/\eta_\infty = (1 - \phi/\phi_0)^2$ with $\phi_0 = 0.64$ as the maximum packing fraction [47]. With regards to the second issue, several approaches have been used to solve magnetostatic multipolar interactions [14,23] generally involving a high computational cost and simplifications (e.g. very small number of particles in 2D systems).

Taking into consideration the good correspondence between experiments and FEM simulations in Fig. 6.9, we computed $\mathrm{Mn}^*_{\langle M\rangle}$ through Eq. (6.10) using the static yield stress, instead of the dynamic yield stress, and $\langle M\rangle$ as obtained by the magnetization average over the particle volume. In Fig. 6.11 we plot the field averaged $\mathrm{Mn}^*_{\langle M\rangle}$ as obtained from the FEM simulations (circles). Together with FEM simulations we also plot MD simulations data (stars) and experimental results for conventional MR fluids in the linear regime (squares) and IFFs (triangles) extracted from Fig. 5 in Ref. [42]. As expected, FEM simulations agree better than MD simulations with the experimental data for conventional MR fluids at the higher particle loadings.

Another important observation is that FEM simulations strongly overestimate the experimental data of conventional MR fluids in the dilute regime reported by Ref. [42]. In view of the results presented in this manuscript, the disagreement at low concentrations may come from the existence of wall slip. Note that the experiments by Ref. [42]. were not carried out with texturized plates.

6.5 Conclusions

The yielding behavior of MR fluids is revisited using Finite Element Method calculations on preassembled structures and carefully conducted experiments in a torsional magnetorheometer. On the one hand, a reduced field formulation is used that allows us to explore the influence of different packings (e.g. simple and body centered bases) and interparticle gaps (e.g. due to surface oxidation of iron microparticles). On the other hand, experiments are conducted in texturized geometries and near-to-equilibrium field configurations.

Independent of the field strength, the minimum energy configuration corresponds to the BC configuration in contrast to the simple basis. However, the influence of the particular packing arrangement on the yield stress is only relevant for very high particle concentrations ($\phi_p \sim 0.5$). Compared to the simple basis, BC packings give a smaller yield stress in the linear regime because of geometrical constrains in an affine deformation.

Simulations reveal that the existence of an interparticle gap Δ does not play a role in the saturation regime. However, there is a remarkable influence of the interparticle gap at low magnetic field strengths. The yield stress dramatically decreases as the interparticle gap increases. In this context, the interparticle gap effect becomes more important with larger initial magnetic permeability of the particles. Finally, the yield stress τ_0 scales with the interparticle center-to-center height h as $\tau_0/\langle M\rangle^2 \propto h^{-6}$ where $\langle M\rangle$ is the particle magnetization.

Similar to other colloidal suspensions and physical gels, magnetorheological experiments demonstrate that wall slip and sedimentation may play a crucial role in the determination of the yield stress for MR fluids. To avoid wall slip and sedimentation it is recommended to use texturized surfaces and fast field ramps, respectively. Overall, experiments demonstrate a reasonably good agreement with simulations (there are no free fitting parameters) independent of the particular packing and interparticle gap.

Finally, compared to MD simulations, FEM simulations are in much better agreement with experimental data of conventional MR fluids at high particle volume fractions. This demonstrates the importance of multipolar magnetostatic interactions and suggests that the static yield stress is very close to the dynamic yield stress at high loadings.

Acknowledgements

This work was supported by MINECO MAT 2016-78778-R and PCIN-2015-051 projects (Spain) and European Regional Development Fund (ERDF). J. R. Morillas acknowledges FPU14/01576 fellowship. We acknowledge Matthew Terkel for proofreading the manuscript.

References

[1] Chen, D. T., Wen, Q., Janmey, P. A., Crocker, J. C., and Yodh, A. G. (2010). Rheology of soft materials. Annual Review of Condensed Matter Physics, 1(1), 301-322.

[2] de Vicente, J., Klingenberg, D. J., and Hidalgo-Álvarez, R. (2011). Magnetorheological fluids: a review. Soft Matter, 7(8), 3701-3710.

[3] Wereley, N. (Ed.). Magnetorheology: advances and applications (Vol. 6) (Royal Society of Chemistry, Cambridge, 2013).

[4] Ahamed, R., Choi, S. B., and Ferdaus, M. M. (2018). A state of art on magneto-rheological materials and their potential applications. Journal of Intelligent Material Systems and Structures, 29(10), 2051-2095.

[5] Ahmad Khairi, M. H., Mazlan, S. A., Choi, S. B., Abdul Aziz, S. A., Mohamad, N., Hapipi, N. M., and Nordin, N. (2019). Role of Additives in Enhancing the Rheological Properties of Magnetorheological Solids: A Review. Advanced Engineering Materials, 21(3), 1800696.

[6] Berasategui, J., Gomez, A., Martinez-Agirre, M., Elejabarrieta, M. J., and Bou-Ali, M. M. (2018). Magnetorheological damper behaviour in accordance with flow mode. The European Physical Journal Applied Physics, 84(2), 21101.

[7] Chen, S., Li, R., Li, X., and Wang, X. (2018). Magnetic field induced surface micro-deformation of Magnetorheological Elastomers for roughness control. Frontiers in Materials, 5, 76.

[8] Seo, Y. P., Han, S., Choi, J., Takahara, A., Choi, H. J., and Seo, Y. (2018). Searching for a stable high-performance magnetorheological suspension. Advanced Materials, 30(42), 1704769.

[9] Segovia-Gutierrez, J. P., de Vicente, J., Hidalgo-Álvarez, R., and Puertas, A. M. (2013). Brownian dynamics simulations in magnetorheology and comparison with experiments. Soft Matter, 9(29), 6970-6977.

[10] Vågberg, D., and Tighe, B. P. (2017). On the apparent yield stress in non-Brownian magnetorheological fluids. Soft Matter, 13(39), 7207-7221.

[11] Pei, L., Pang, H., Chen, K., Xuan, S., and Gong, X. (2018). Simulation of the optimal diameter and wall thickness of hollow Fe 3 O 4 microspheres in magnetorheological fluids. Soft Matter, 14(24), 5080-5091.

[12] Klingenberg, D. J., van Swol, F., and Zukoski, C. F. (1991). The small shear rate response of electrorheological suspensions. II. Extension beyond the point–dipole limit. The Journal of Chemical Physics, 94(9), 6170-6178.

[13] Ginder, J. M., and Davis, L. C. (1994). Shear stresses in magnetorheological fluids: role of magnetic saturation. Applied Physics Letters, 65(26), 3410-3412.

[14] Kang, T. G., Hulsen, M. A., and den Toonder, J. M. (2012). Dynamics of magnetic chains in a shear flow under the influence of a uniform magnetic field. Physics of Fluids, 24(4), 042001.

[15] Bossis, G., Lācis, S., Meunier, A., and Volkova, O. (2002). Magnetorheological fluids. Journal of Magnetism and Magnetic Materials, 252, 224-228.

[16] Lācis, S., Zavickis, E., and Bossis, G. (2002). Magnetic interactions of chains formed by ferromagnetic spheres. International Journal of Modern Physics B, 16(17n18), 2307-2313.

[17] de Vicente, J., Bossis, G., Lācis, S., and Guyot, M. (2002). Permeability measurements in cobalt ferrite and carbonyl iron powders and suspensions. Journal of Magnetism and Magnetic Materials, 251(1), 100-108.

[18] Cīmurs, J., Evertovskis, J., and Lācis, S. (2010). Dipole Aproximation Limits for Magnetic Interaction Forces Between Spheres. In Proceedings of the International Scientific Colloquium Modelling for Material Processing (University of Latvia, Riga).

[19] Han, Y., Hong, W., and Faidley, L. E. (2013). Field-stiffening effect of magneto-rheological elastomers. International Journal of Solids and Structures, 50(14-15), 2281-2288.

[20] Javili, A., Chatzigeorgiou, G., and Steinmann, P. (2013). Computational homogenization in magneto-mechanics. International Journal of Solids and Structures, 50(25-26), 4197-4216.

[21] Spieler, C., Kästner, M., Goldmann, J., Brummund, J., and Ulbricht, V. (2013). XFEM modeling and homogenization of magnetoactive composites. Acta Mechanica, 224(11), 2453-2469.

[22] Chen, S. W., Li, R., Zhang, Z., and Wang, X. J. (2016). Micromechanical analysis on tensile modulus of structured magneto-rheological elastomer. Smart Materials and Structures, 25(3), 035001.

[23] Hashemi, M. R., Manzari, M. T., and Fatehi, R. (2017). Non-linear stress response of non-gap-spanning magnetic chains suspended in a Newtonian fluid under oscillatory shear test: A direct numerical simulation. Physics of Fluids, 29(10), 107106.

[24] Vereda, F., Segovia-Gutiérrez, J. P., de Vicente, J., and Hidalgo-Álvarez, R. (2014). Particle roughness in magnetorheology: effect on the strength of the field-induced structures. Journal of Physics D: Applied Physics, 48(1), 015309.

[25] Klingenberg, D. J., Ulicny, J. C., and Golden, M. A. (2007). Mason numbers for magnetorheology. Journal of Rheology, 51(5), 883-893.

[26] Davis, L. C. (1992). Finite-element analysis of particle-particle forces in electrorheological fluids. Applied Physics Letters, 60(3), 319-321.

[27] Davis, L. C. (1992). Polarization forces and conductivity effects in electrorheological fluids. Journal of Applied Physics, 72(4), 1334-1340.

[28] Ginder, J. M., Davis, L. C., and Elie, L. D. (1996). Rheology of magnetorheological fluids: Models and measurements. International Journal of Modern Physics B, 10(23n24), 3293-3303.

[29] Morillas, J. R., and de Vicente, J. (2019). On the yield stress in magnetorheological fluids: a direct comparison between 3D simulations and experiments. Composites Part B: Engineering, 160, 626-631.

[30] Tao, R., and Sun, J. M. (1991). Three-dimensional structure of induced electrorheological solid. Physical Review Letters, 67(3), 398.

[31] Bombard, A. J., Joekes, I., Alcantara, M. R., and Knobel, M. (2003). Magnetic susceptibility and saturation magnetization of some carbonyl iron powders used in magnetorheological fluids. Materials Science Forum, 416-418, 753-758.

[32] Mohebi, M., Jamasbi, N., and Liu, J. (1996). Simulation of the formation of nonequilibrium structures in magnetorheological fluids subject to an external magnetic field. Physical review E, 54(5), 5407.

[33] Cutillas, S., Bossis, G., and Cebers, A. (1998). Flow-induced transition from cylindrical to layered patterns in magnetorheological suspensions. Physical Review E, 57(1), 804.

[34] Bauer, J. L., Kurian, M. J., Stauffer, J., and Furst, E. M. (2016). Suppressing the Rayleigh–Plateau Instability in Field-Directed Colloidal Assembly. Langmuir, 32(26), 6618-6623.

[35] Macosko, C. W. Rheology: Principles, Measurements, and Applications. (Wiley-VCH, New York, 1994).

[36] Mezger, T. G. The rheology handbook: for users of rotational and oscillatory rheometers (Vincentz Network GmbH & Co KG, Hannover, 2006).

[37] Ramos, J., Klingenberg, D. J., Hidalgo-Álvarez, R., and de Vicente, J. (2011). Steady shear magnetorheology of inverse ferrofluids. Journal of Rheology, 55(1), 127-152.

[38] Ocalan, M. PhD thesis. Massachusetts Institute of Technology, Cambridge, 2011.

[39] Laun, H. M., Schmidt, G., Gabriel, C., and Kieburg, C. (2008). Reliable plate–plate MRF magnetorheometry based on validated radial magnetic flux density profile simulations. Rheologica Acta, 47(9), 1049-1059.

[40] Jonkkari, I., Kostamo, E., Kostamo, J., Syrjala, S., and Pietola, M. (2012). Effect of the plate surface characteristics and gap height on yield stresses of a magnetorheological fluid. Smart Materials and Structures, 21(7), 075030.

[41] Morillas, J. R., Yang, J., and de Vicente, J. (2018). Double-gap plate–plate magnetorheology. Journal of Rheology, 62(6), 1485-1494.

[42] Ruiz-López, J. A., Fernández-Toledano, J. C., Hidalgo-Álvarez, R., and de Vicente, J. (2016). Testing the mean magnetization approximation, dimensionless and scaling numbers in magnetorheology. Soft Matter, 12(5), 1468-1476.

[43] Klingenberg, D. J., and Zukoski IV, C. F. (1990). Studies on the steady-shear behavior of electrorheological suspensions. Langmuir, 6(1), 15-24.

[44] de Gans, B. J. (1999). Non-linear magnetorheological behaviour of an inverse ferrofluid. Faraday Discussions, 112, 209-224.

[45] Segovia-Gutiérrez, J. P., Berli, C. L. A., and de Vicente, J. (2012). Nonlinear viscoelasticity and two-step yielding in magnetorheology: A colloidal gel approach to understand the effect of particle concentration. Journal of Rheology, 56(6), 1429-1448.

[46] Berli, C. L., and de Vicente, J. (2012). A structural viscosity model for magnetorheology. Applied Physics Letters, 101(2), 021903.

[47] Ruiz-López, J. A., Hidalgo-Álvarez, R., and de Vicente, J. (2017). Towards a universal master curve in magnetorheology. Smart Materials and Structures, 26(5), 054001.

Chapter 7. On the Importance of Interchain Interaction and Rotational Contribution to the Computation of the Yield Stress in Magnetorheology

Jose R. Morillas and Juan de Vicente

This article is published in: Smart Materials and Structures, 28, 08LT01 (2019).

DOI: https://doi.org/10.1088/1361-665X/ab2470

Abstract

Traditionally, Finite Element Method Magnetostatics (FEMM) simulations used in magnetorheology consider that the shearing affine deformation of the particle lattice can be divided in two motions: first, an elongation, and second, a rotation of the elongated structure. This allows reducing the magnetostatic problem to an axisymmetric one with a smaller computational cost. However, supposed symmetries also impose, without any physical reason, that both the magnetic field direction and particle magnetization are aligned with the chain axis for any strain. The first assumption leads to an incorrect interchain interaction while the second one neglects the magnetization rotation during the strain process. In this letter we analyze the limitations within these classical assumptions under the frame of a recently proposed reduced field formulation that is capable to truly simulate large shear strains and concentrations in model structures [Compos. Part B: Eng. 160 626-31].

7.1 Introduction

Conventional magnetorheological (MR) fluids are suspensions of micronsized magnetizable carbonyl iron particles in liquid carriers. Under the presence of magnetic fields the particles magnetize and form field-directed structures [1-3]. Ginder and coworkers were probably the first to report on the importance of the local magnetic saturation of the particles in the rheological response of MR fluids using Finite Element Method Magnetostatic (FEMM) simulations [4-6]. Their work gave an explanation to the sub-quadratic power law and high field saturation that is observed in the yield stress of MR fluids. The latter observation is in clear contrast to their electrorheological counterparts where the maximum yield stress is achieved at the dielectric breakdown [7].

The starting point in classical FEMM simulations of interest in magnetorheology is a preassembled structure subjected to an external/applied field (in the z direction). The simulations assume that the field-induced structure has a cylindrical symmetry oriented with the applied field regardless the strain (i.e. axisymmetric model) bounded by a mirror symmetry. These simplifications imply also some consequences from a physical point of view.

Firstly, the particle magnetization $\vec{M}$ is supposed to be aligned with the chain axis and therefore with the relative position vector joining two particles i and j in a chain $\vec{R}_{ij} = \vec{r}_i - \vec{r}_j$. As a result, the magnetostatic interaction between particles in the chain is always attractive and only the elongational contribution to the stress is taken into consideration. However, magnetic interaction is anisotropic, that is, it does not only depend on the interparticle distance $\left|\vec{R}_{ij}\right|$ but also on the relative orientation between $\vec{M}$ and $\vec{R}_{ij}$. Thus, using an axisymmetric model completely neglects the real misalignment between $\vec{M}$ and $\vec{R}_{ij}$ and with this the rotational contribution to the stress as well.

Secondly, due to the mirror symmetry at the external boundary of the computational domain, the magnetic field here is supposed to be collinear with the chain axis. This is equivalent to surround the explicitly simulated chain with a magnetic body capable to cancel the radial component of the magnetic field. In the non-strained state the mirror symmetric boundary condition is fulfilled. However as soon as the system is sheared that symmetry is lost and the interchain interactions incorrectly accounted for.

As a consequence of the assumed cylindrical and mirror symmetries, it is not surprising that these simulations underestimate the experimental yield stress data (e.g. see Fig. 7.1 below). Recently, a novel FEMM simulation methodology [10] has been proposed to overcome the shortcomings of the classical model. This new approach is based on a reduced field formulation, which does not need to impose the magnetic field vector on any boundary, and periodic boundary conditions, which simplifies the simulation of the shearing deformation of a particle lattice. With this new approach interchain interactions are correctly simulated in truly sheared lattices where there is not any restriction regarding the orientation of the particle magnetization vector.

In Fig. 7.1 we compare the yield stress as obtained using the method proposed by Ref. [4] (in solid lines) and the method proposed by Ref. [10] (in dashed lines). Together with simulations we also include experimental data obtained in a magnetorheometer. Note that in order for the comparison to be appropriate, the experimental magnetization curve of the carbonyl iron powder was used in the two simulations. As observed, Ginder and Davis' simulations [4] underestimate the experimental data, especially, at high volume fractions. However, simulations proposed in Ref. [10] are in better agreement with experiments.

In the following sections the differences between Ginder and Davis' and Morillas and de Vicente's FEMM analyses are discussed in detail in 3D geometries and supposing the Fröhlich-Kennelly constitutive equation for the magnetic particles (initial permeability: 1000, saturation magnetization: 1600 kA/m) [11]. In particular we will address differences on: (i) how to compute interparticle forces, (ii) how to shear strain the lattice without keeping particle magnetization aligned with chain axis and (iii) how to impose the external field in the model without supposing the total field direction and thus modifying real interchain interactions. Next, we will thoroughly analyze each one.

Note that, none of the simulations proposed in Refs. [4] nor [10] take into account the real structures present in a MR fluid under a simple shear kinematics; they work with a highly symmetric arrangement of particles in order to accurately resolve magnetic interactions. To compute true magnetic forces in realistic structures, more complex numerical methods must be implemented in order to couple magnetostatic interactions (solved by FEMM) with particle motion through Newton's second law (solved by Molecular Dynamics like methods) [12,13]. However, the computational cost of these

numerical schemes only allows simulating very small systems with tens of particles (below 50) in two dimensions, therefore moving away from concentrated MR fluids that are of interest in current applications.

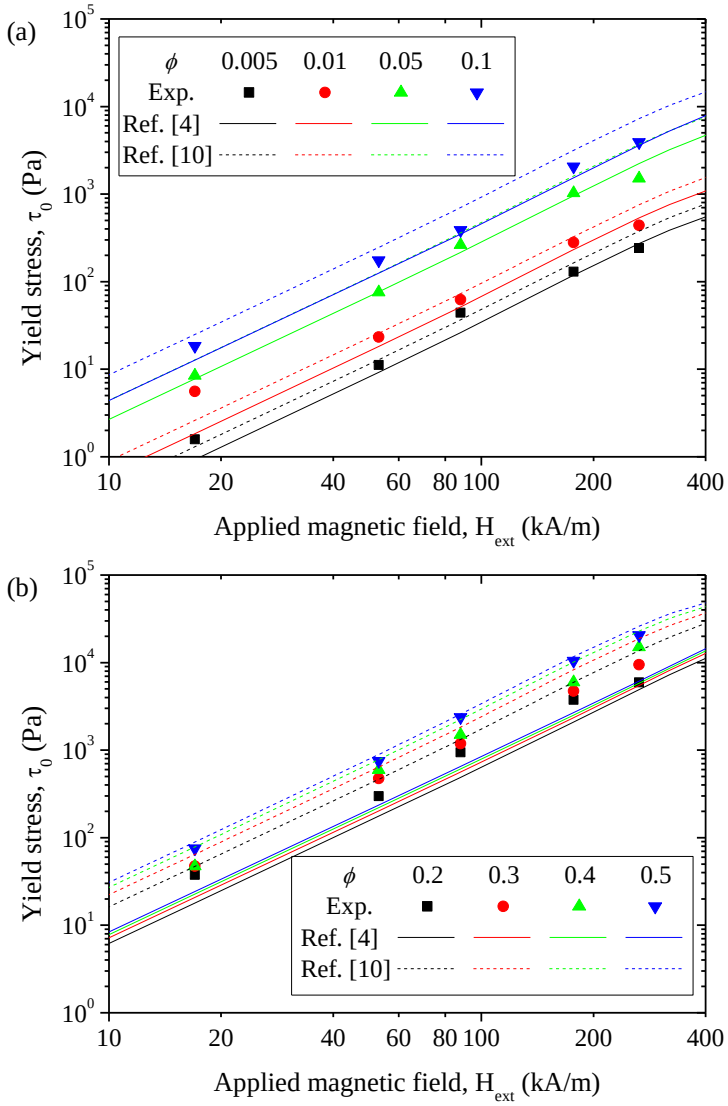

Figure 7.1: Yield stress τ_0 as a function of the applied magnetic field strength H_{ext}. Points: experiments from Refs. [8] ($\phi = 0.005$, 0.01, 0.05 and 0.1) and [9] ($\phi = 0.2$, 0.3, 0.4 and 0.5). Solid lines: simulation method proposed by Ref. [4]. Dashed lines: simulation method proposed by Ref. [10] supposing a simple monoclinic lattice. Both sets of simulations were performed taking into consideration the experimental magnetization curve of the iron powder used in the experiments. Experimental data were all corrected using the Weissenberg-Rabinowitsch-Mooney equation. a) low particle concentrations. b) large particle concentrations.

7.2 Computation of the interparticle forces

On the one hand, in Ginder and Davis' simulations [4], the total force exerted by the upper half of a chain on its lower half is computed by integrating the 'reduced' Maxwell stress tensor over the plane that halves the chain (see Eq. (1) in Ref. [4]). The term 'reduced' was used in that paper because only the field perturbation coming from the particles $\vec{H}$ –

$\vec{H}_0$ was considered in the tensor. Here $\vec{H}$ was the total magnetic field and $\vec{H}_0$ denoted an effective applied field computed as an average along the cell height (see Eq. (2) in Ref. [4]). However, according to classical electromagnetism theory, there is not any reason to use a reduced field instead of the total field in the computation of the forces [14,15]. Moreover, the Maxwell stress tensor has to be integrated over a closed surface in order to yield the force acting on the encompassed magnetic body. Nothing is said about this issue in Ref. [4].

On the other hand, in Ref. [10] the total force exerted by the upper part of the lattice on the lower one is computed by using the total field $\vec{H}$ (regarded as a background field identified with the external one $\vec{H}_{ext}$ plus the field coming from the particles) and a closed surface S. This surface is sketched with red dashed lines in Fig. 7.2 for a lattice that is strained at an angle $\theta = \operatorname{atan}\gamma$ in the y direction. As it can be seen, the surface S is composed by:

- S_t: A top plane with unit normal vector $\hat{z}$ halving the unit cell (Fig. 7.2a).
- S_b: A bottom plane with unit normal vector $-\hat{z}$ (Fig. 7.2c).
- S_l: Two lateral planes, tilted according to the strain γ with unit normal vectors $\pm\hat{e}_2 = \pm(\hat{y} - \gamma\hat{z})/\sqrt{1+\gamma^2}$ that coincide with the lateral boundaries of the unit cell (Figs. 7.2a and 7.2b). $\hat{e}_2$ will be later a basis vector of a coordinate system (see below, Fig. 7.3). The associated cell boundaries are defined as periodic walls.
- S_f: Two front planes with unit normal vectors $\pm\hat{x}$. These planes are not shown in Fig. 7.2 for the sake of clarity but they coincide with the front and rear boundaries of the unit cell. The associated cell boundaries are defined as mirror symmetric planes.

As will be demonstrated below, only the integration over the top and bottom planes (S_t and S_b) are needed to be carried out to compute the total force.

First, the integration of the Maxwell stress tensor over each S_l plane gives a value that is different from zero. However, because the two planes are defined as periodic walls, the results of the integrations are the same but with opposite sign (note that their unit normal vectors have opposite direction). Second, the integration over S_f is also zero because these planes are defined as mirror symmetries and as a result, the x component of the magnetic field strength and flux density is zero $H_x = B_x = 0$. Third, the integration over S_t is straightforward once the magnetic field is computed on the surface. Fourth, the integration over S_b is more elaborate. Since we are interested in the total force acting over the bottom half of the lattice, the tilted lateral planes and the frontal ones should go down till the end of the lattice (pointed with a horizontal solid line in Figs. 7.2b). Once the planes exit the lattice, any horizontal position below the lattice bottom boundary can be used to close the surface. However, it should be remembered that near to the end of the lattice the magnetic field distribution is not known (i.e. FEMM solution is only valid in the bulk of the lattice, where a large number of particles surround the explicitly simulated one). A solution to this problem is to lengthen lateral and frontal planes till a distance that is large enough to see the lattice as a homogeneous body (body 1 in Figs. 7.2c). Note that, although they go out from the lattice, lateral and frontal planes are still periodic and mirror symmetric respectively. Therefore, the integration over them does not contribute to the total force.

When the lattice is seen as a homogeneous body, the magnetic field can be theoretically calculated by solving a typical electromagnetism boundary problem (Figs. 7.2c) with two

homogeneous media (1 and 2) separated by an interface with unit normal vector $\hat{n}$ ($\hat{n} = -\hat{z}$ in Figs. 7.2c). Through this interface, the normal component of the magnetic flux density and the tangential component of the magnetic field strength are preserved through the continuity equations (i.e. $B_{1,n} = B_{2,n}$ and $H_{1,t} = H_{2,t}$).

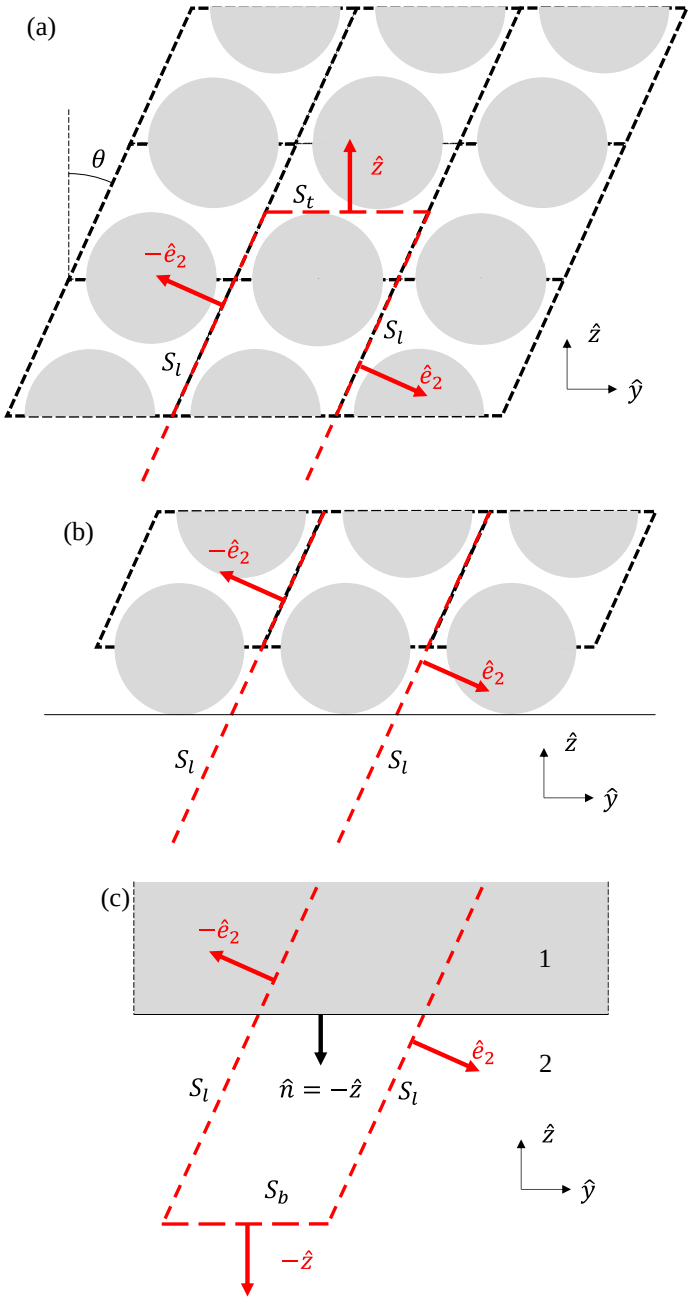

Figure 7.2: Sketch of a monoclinic lattice sheared at an angle θ. Its unit cell is plotted with black dashed lines. (a) In the bulk of the lattice. (b) At the bottom row of the lattice. (c) Far away from the lattice where it is seen as a continuous and homogeneous (grey) medium. Red dashed lines show the surface over which the Maxwell stress tensor is integrated.

In addition, since the lattice is considered as a continuous and homogeneous medium, the magnetic flux density and magnetic field strength inside the lattice can be identified with their volume averages over the unit cell: $\vec{B}_1 = \langle \vec{B} \rangle$, $\vec{H}_1 = \langle \vec{H} \rangle$ being $\vec{B}$ and $\vec{H}$ the fields obtained using FEMM simulations. Thus, with this identification and knowing the

orientation of the lattice interface, previous continuity conditions for each field component can be solved yielding the magnetic flux density and magnetic field strength far away from the lattice, just at the plane S_b where the Maxwell stress tensor needs to be integrated to close the total surface S. Note that, identifying the values of $\vec{B}_1$ and $\vec{H}_1$ with the corresponding average values in the lattice, no demagnetization effects are considered. This agrees with the picture of an infinite (unbounded) lattice created by the periodic conditions imposed in the FEMM unit cell.

As an example, in the particular case of a lattice that is placed in a non-magnetic media with $\hat{n}$ parallel to the external magnetic field strength $\vec{H}_{ext}$ (aligned with the z direction), the boundary condition problem yields:

$$\vec{B}_2 = \mu_0\big(\langle H_x\rangle\hat{x} + \langle H_y\rangle\hat{y}\big) + \langle B_z\rangle\hat{z} \tag{7.1a}$$

$$\vec{H}_2 = \frac{\vec{B}_2}{\mu_0} \tag{7.1b}$$

where, in addition, $\langle H_x\rangle = \langle H_y\rangle = 0$ due to the symmetries of the problem. Bearing this in mind, the shear force F_y in the y direction is computed using the Maxwell stress tensor $\tilde{T} = \widetilde{BH} - \tilde{\delta}\, BH/2$ (where $\tilde{\delta}$ is the unit diagonal tensor) as follows:

$$\begin{aligned} F_y = \int_S \hat{y}^T\cdot\tilde{T}\cdot\hat{n}ds &= \int_{S_t}\hat{y}^T\cdot\tilde{T}\cdot\hat{z}ds - \int_{S_b}\hat{y}^T\cdot\tilde{T}\cdot\hat{z}ds \\ &= \int_{S_t} H_z B_y ds - \int_{S_b} H_{2,z}B_{2,y}ds \\ &= \int_{S_t} H_z B_y ds - \int_{S_b}\langle B_z\rangle\langle H_y\rangle ds = \int_{S_t} H_z B_y ds \end{aligned} \tag{7.2}$$

where $\hat{y}^T$ is the transposed unit vector in the (shear) y direction. In Eq. (7.2) it has already been taken into consideration that the contributions from S_l and S_f are null. The shear force in the x direction F_x can be computed in a similar way. However, $F_x = 0$ because of the symmetry of the lattice for all cases investigated in this manuscript.

Finally, the normal force F_z in z direction is calculated as follows:

$$\begin{aligned} F_z = \int_S \hat{z}^T\cdot\tilde{T}\cdot\hat{n}ds &= \int_{S_t}\hat{z}^T\cdot\tilde{T}\cdot\hat{z}ds - \int_{S_b}\hat{z}^T\cdot\tilde{T}\cdot\hat{z}ds \\ &= \int_{S_t}\frac{1}{2}\big(H_zB_z - H_xB_x - H_yB_y\big)ds \\ &- \int_{S_b}\frac{1}{2}\big(H_{2,z}B_{2,z} - H_{2,x}B_{2,x} - H_{2,y}B_{2,y}\big)ds \\ &= \int_{S_t}\frac{1}{2}\big(H_zB_z - H_xB_x - H_yB_y\big)ds \\ &- \int_{S_b}\frac{\langle B_z\rangle^2}{2\mu_0}ds \end{aligned} \tag{7.3}$$

As observed in Eqs. (7.2) and (7.3), this route yields different expressions for the interparticle forces in comparison to those used in Ref. [4] (see their Eq. (1)). However,

both approaches contain an averaged field: while in Ref. [4] the effective applied field $\vec{H}_0$ is proposed as an estimation of the background field (note that in Ref. [10], thanks to its reduced formulation, the background field is exactly $\vec{H}_{ext}$), in Ref. [10] the averaged field is introduced as the magnetic field far away from the lattice. In the following, the method proposed in Ref. [10] will be used to compute the interparticle forces.

7.3 Elongation + rotation versus a true shear strain

A very common approximation when shear straining an isolated chain of particles is its elongation followed by a rotation (e.g. Refs. [4,5,16]). This approximation effectively mimics the actual deformation for very small strains but fails in the case of intermediate and large strains [10]. In their article, Ginder and Davis [4] used this decomposition because it allows them to keep the computational domain axisymmetric during the elongation stage. At a certain strain level γ the chain is rotated at an angle $\theta = \operatorname{atan}\gamma$ and the force along the chain axis, F_{axis}, is projected in the shear direction multiplying by a factor $\sin\theta$. Finally, as the chain is tilted, the field aligned with its axis is not the external one but its projection, and therefore the results have to be corrected by a factor $\cos\theta$. As a consequence, in the simulations proposed by Ref. [4] the chain rotation is accounted for by a factor $\sin\theta\cos\theta = \gamma/(1+\gamma^2)$ (see Eq. (3) in that work).

In this section the shear stress coming from, first, elongating and, then, rotating the chain is compared with that obtained from a true shearing motion. In the first set of simulations, the elongation + rotation kinematics is performed on a rectangular simulation box (see black box in Fig. 7.3a) with height $h = d\sqrt{1+\gamma^2}$ and width $w = \sqrt{\pi d^3/6\phi h}$ using a reduced field formulation and periodic boundary conditions. Here, d is the particle diameter and ϕ is the particle volume fraction. This simulation approach is the 3D analogue of the axisymmetric computational domain used by Ref. [4]. As a result of the imposed periodic boundary conditions, the final system is a tetragonal lattice with vectors $\vec{a}_1 = w\hat{x}$, $\vec{a}_2 = w\hat{y}$ and $\vec{a}_3 = h\hat{z}$ (see Fig. 7.3a, note that mirror symmetries would yield the same lattice as $\vec{H}_{ext}$ is aligned with the chain axis). Once the magnetic field distribution is solved for different strain levels γ, the normal force in the lattice (i.e. along the chain axis direction) is computed using Maxwell stress tensor (Eq. (7.3)) and corrected by the same factor used by Ref. [4] $\sin\theta\cos\theta = \gamma/(1+\gamma^2)$ to account for the eventual rotation.

The true shear strain is modelled following Ref. [10]. The resultant lattice in this case is a monoclinic one (of simple basis) with lattice vectors $\vec{b}_1 = w'\hat{x}$, $\vec{b}_2 = w'\hat{y}$ and $\vec{b}_3 = h'(\gamma\hat{y}+\hat{z}) = h'\sqrt{1+\gamma^2}\hat{e}_3$ with $w' = d\sqrt{\pi/6\phi}$ and $h' = d$ the lateral and vertical interparticle distances respectively (see Fig. 7.3b).

In Fig. 7.4 we show the shear stress τ versus shear strain γ curves for different volume fractions ϕ and external magnetic field strengths H_{ext} (in the linear, left, and saturation, right, regimes) using the 3D extension of the classical elongation + rotation decomposition approach as described by Ref. [4] (solid squares in Fig. 7.4) and truly shearing the system as described by Ref. [10] (lines in Fig. 7.4).

Note that the symbols included in Fig. 7.4 are limited to a maximum strain level $\gamma_m = \sqrt{\pi^2/(36\phi^2)-1}$ in view of the unit cell dimensions (h and w) due to geometrical constrains (i.e. particle overlapping). For $\gamma > \gamma_m$ the particles overlap and therefore the

analysis by Ref. [4] is not applicable. However, it is worth to remark that particle overlapping is avoided in the method proposed by Ref. [10].

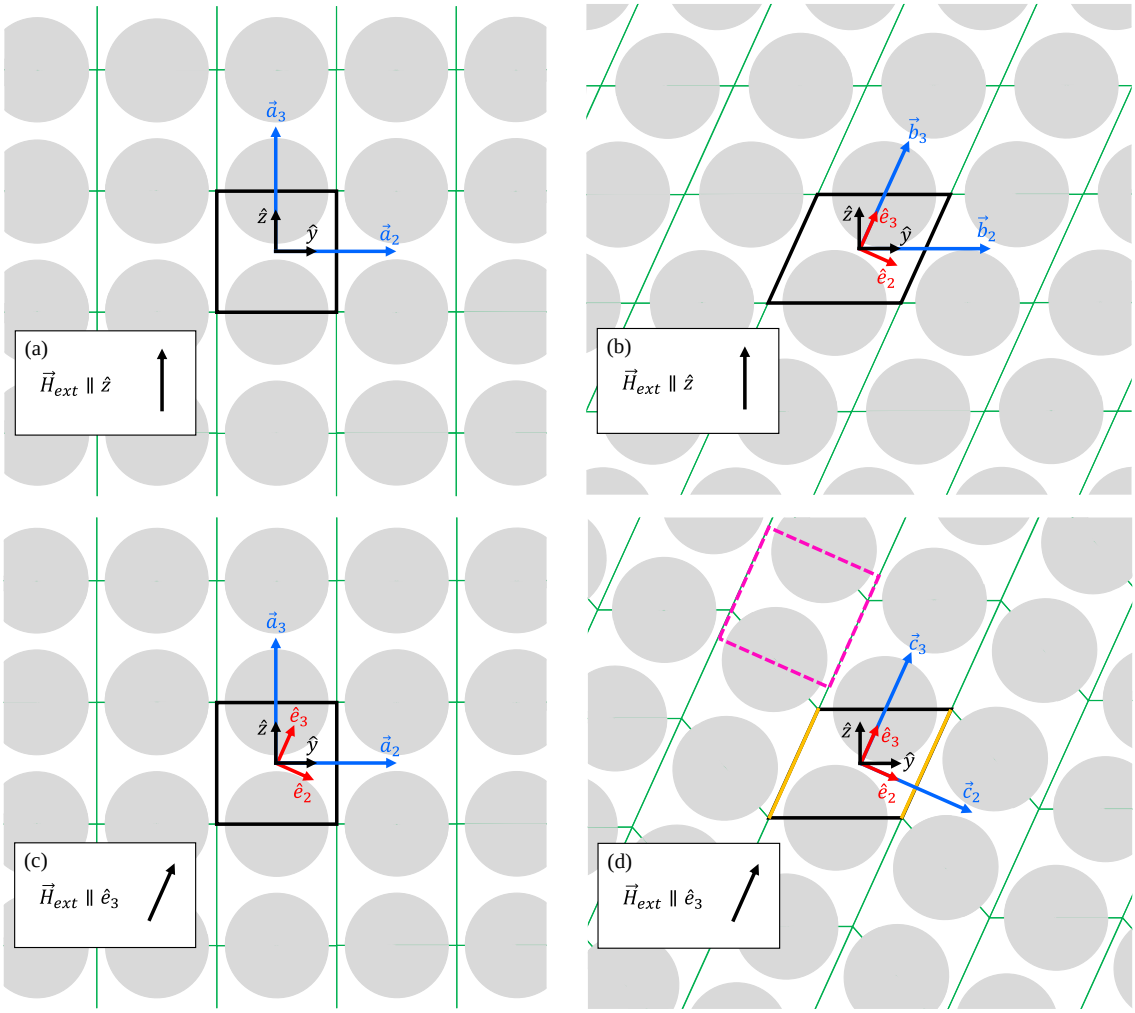

Figure 7.3: Unit cells and generated lattices using periodic (black lines) and mirror symmetry (yellow lines) boundary conditions. (a) Tetragonal lattice under elongation according to Ref. [4]. (b) Monoclinic lattice generated from (a), when it is not elongated, by affine shear deformation. (c) Same than (a) but explicitly rotating the external magnetic field. (d) Tetragonal lattice rotated together with the $\{\hat{e}_1, \hat{e}_2, \hat{e}_3\}$ basis (its unit cell is highlighted with magenta dashed lines).

In view of Fig. 7.4, the two methods provide very similar results in the linear regime for low and moderate concentrations. This result was expected at low strain levels. However, the fact that the two methods (decomposition D and true T) also provide similar data for large strains is striking. An explanation for this can be given if shear stress τ is written in terms of the traction force orientation $\beta = F_y/F_z$ and traction force norm $t = \sqrt{F_y^2 + F_z^2}/A$ (where $A = w^2$ or w'^2 in the decomposition and true method respectively) as $\tau = t\beta/\sqrt{1+\beta^2}$. In Sec. 7.5, both traction orientation and norm are plotted for the different cases studied in this work. Note that, in the decomposition method proposed by Ref. [4], the traction orientation is the same as the applied strain $\beta_D = \gamma$ (see Figs. 7.5a, 7.5c and 7.5e). When the applied strain γ is small, the traction norm simulated by the two methods is very similar $t_D = t_T$ (see Figs. 7.5b, 7.5d and 7.5f) and we can distinguish two scenarios: low and high fields. For small field strengths, the true traction orientation

is equal to the applied strain γ and consequently it is also equal to the traction orientation as obtained by decomposition ($\beta_T = \gamma = \beta_D$). Therefore the stress predicted by the decomposition method τ_D and the true one τ_T are the same $\tau_D = \tau_T$. However, as the strain is increased $t_T < t_D$ and $\beta_T > \beta_D$ so it is possible that both effects balance themselves and then $\tau_D = \tau_T$.

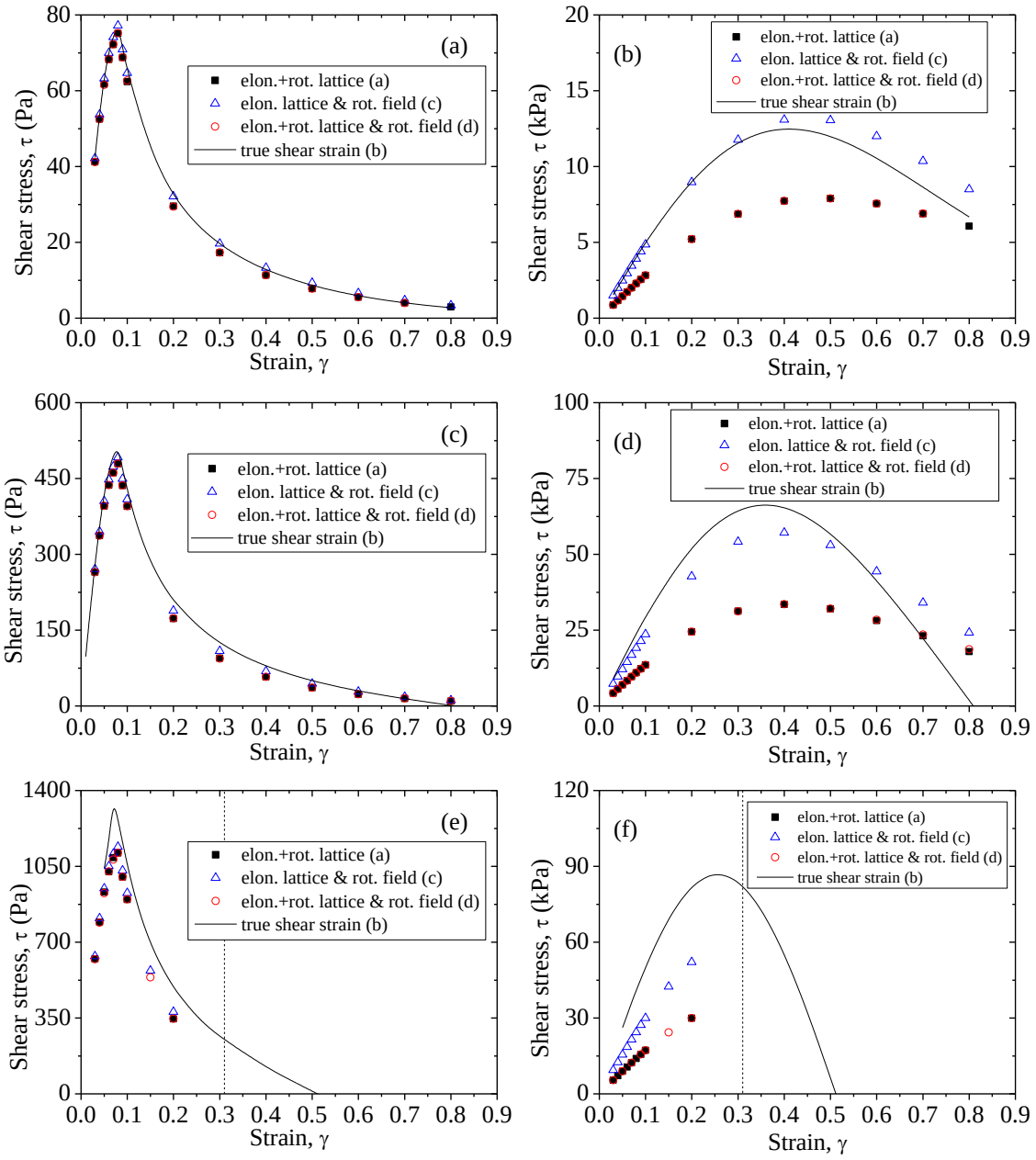

Figure 7.4: Shear stress τ versus strain γ curves under different external magnetic fields (left column-linear regime, $H_{ext} = 8$ kA/m; right column-saturation regime, $H_{ext} = 1600$ kA/m) and volume fractions (top row 3 vol%, middle row 20 vol% and bottom row 50 vol%). Squares: elongating + rotating the lattice according to Ref. [4]. Triangles: elongating the lattice & rotating the field. Circles: elongating + rotating the lattice & rotating the field. Lines: truly straining the lattice. Letters in brackets inside the graphs legends correspond to the different cases shown in Fig. 7.3. The vertical dashed line corresponds to the maximum strain γ_m that can be simulated before particle overlapping occurs.

On the other hand, for large field strengths $\beta_T > \gamma = \beta_D$ even at small strains (see Figs. 7.5a, 7.5c and 7.5e) and therefore $\tau_D < \tau_T$ (see Fig. 7.4). This observation was already pointed out by Ref. [17]. In that paper, using a dipolar approach (valid in saturation), the shear modulus (in dilute systems and at low strain) was analytically calculated for isolated chains. They proved that the contributions from elongation and particle dipole rotation are of the same order of magnitude in the saturation regime (where the particle permeability is close to 1). The observations by Ref. [17] are in good qualitative agreement with our observations at low strains where the true stress is approximately twofold the one obtained by decomposition. This would explain the disagreement: for low strains this elongation + rotation simulations (points) fail as they do not account explicitly for rotation. For high strains in addition to the previous failure, shearing the chain is not well approximated by its elongation + rotation deformation.

In order to ascertain what is the range of applicability of the referred elongation + rotation approximation, the previous simulations were repeated using the same computational domain and boundary conditions (and thus, simulating the same tetragonal lattice) but, as the lattice is elongated, the external magnetic field is rotated accordingly to the applied strain: $\vec{H}_{ext} = H_{ext}\hat{e}_3$ (see Fig. 7.3c). Note that, in this case, mirror symmetries cannot be applied due to the misalignment between the external field and the chain axis. In this way, the field rotation is directly implemented in the FEMM simulations and deviations from the true shear simulations are only expected to come from the failure of the elongation + rotation geometrical approximation. In this case, since the chain axis is not parallel to the external field it is not necessary to project the normal force nor the field. Instead, the force in the direction normal to the external magnetic field ($-\hat{e}_2$ see Fig. 7.3c) is computed by integration of the appropriate Maxwell stress tensor components:

$$F_{e_2} = \int_S -\hat{e}_2^T \cdot \tilde{T} \cdot \hat{n} ds \tag{7.4}$$

Results from this set of simulations are plotted (triangles) in Fig. 7.4 as well. For the smallest fields there is also a reasonably good agreement. More importantly, for the largest fields the collapse is significantly improved, especially at small volume fractions. This is also expected because the elongation + rotation approximation is only appropriate for small concentrations (i.e. isolated chains). Overall, Fig. 7.4 suggests that the elongation + rotation approximation is only applicable for small strains (below $\gamma = 0.2$).

To conclude this section, from Fig. 7.4 it can be inferred that the correction proposed by Ref. [4] to take into consideration the rotation of the chain (i.e. the prefactor $\cos\theta$) is not accurate enough to satisfactorily implement the elongation + rotation approximation. Even though using that prefactor the magnetic field is projected in the chain axis direction, hence reducing particle interaction ($\cos\theta < 1$), a key point here is the misalignment between the external field (and particle magnetization) and the chain axis, which cannot be achieved in Ginder and Davis' axisymmetric model [4].

7.4 Boundary conditions: fixing magnetic potential vs periodic BCs and reduced field formulation

Another difference between Ginder and Davis' approach [4] and the method proposed by Ref. [10] is the way to introduce the external magnetic field. Thanks to the reduced field formulation, in Ref. [10], the external magnetic field is imposed as a domain property.

On the other hand, the approximation by Ref. [4] employs the magnetic vector potential and fixes its value along an external boundary. As a consequence, the total magnetic field is not fixed anywhere, however its direction is always parallel to the chain axis in the external boundary (i.e. mirror symmetry).

In this section, we study the influence of the way the field is applied on the shear stress versus shear strain curve. In order not to couple this problem with the elongation + rotation approximation, the shear strain of the chains will be implemented by shear straining the computational domain and applying periodic conditions only on top and bottom walls of the unit cell (black lines in Fig. 7.3d). Finally, in the sheared walls the total magnetic field direction is fixed along them to align this field with the chain axis as it is done in Ref. [4] (mirror symmetries-yellow lines in Fig. 7.3d). To sum up, taking into consideration the computational domain used by Ref. [10], periodic boundary conditions are imposed in both top and bottom walls while the rest of boundaries are defined as mirror symmetries.

Since the shear motion is achieved by tilting the computational domain its dimensions are h' and w'. By replicating the unit cell with the new imposed boundary conditions it can be seen that the new lattice vectors are (see Fig. 7.3d):

$$\vec{c}_1 = w'\hat{x} \tag{7.5a}$$

$$\vec{c}_2 = \frac{w'}{\sqrt{1+\gamma^2}}\frac{\hat{y}-\gamma\hat{z}}{\sqrt{1+\gamma^2}} \tag{7.5b}$$

$$\vec{c}_3 = h'(\gamma\hat{y}+\hat{z}) \tag{7.5c}$$

However, they can be written in a simpler form using another basis $\{\hat{e}_1, \hat{e}_2, \hat{e}_3\}$ where $\hat{e}_1 = \hat{x}$ and $\hat{e}_2$ and $\hat{e}_3$ were already defined in Secs. 7.2 and 7.3 respectively, thus:

$$\vec{c}_1 = w'\hat{e}_1 \tag{7.6a}$$

$$\vec{c}_2 = \frac{w'}{\sqrt{1+\gamma^2}}\hat{e}_2 \tag{7.6b}$$

$$\vec{c}_3 = h\hat{e}_3 \tag{7.6c}$$

In this new basis it can be clearly seen that the resultant lattice is a tetragonal one (with a unit cell represented by the magenta dashed box in Fig. 7.3d) similar to that used in the Sec. 7.3 (compare definitions of both lattice vectors sets) but with the following differences:

- While in the first tetragonal lattice $\{\vec{a}_1, \vec{a}_2, \vec{a}_3\}$ both (x and y) lateral dimensions adjust to keep the volume fraction constant during elongation, in the second one $\{\vec{c}_1, \vec{c}_2, \vec{c}_3\}$ the dimension along the x direction is fixed.
- 'Shearing' the first tetragonal lattice simply implies to elongate it, however in the second one, in addition to elongation, the lattice undergoes through a rotation $\theta = \operatorname{atan}\gamma$ (note that the versors $\hat{e}_2$ and $\hat{e}_3$ rotate around the x axis).

Up to now, all boundary conditions used have an influence on the magnetic field direction but nothing has been said about its magnitude. To work in similar conditions to Ref. [4] (without fixing the total magnetic field magnitude anywhere) the reduced field formulation will be used again imposing only the external magnetic field parallel to the chain axis (i.e. $\vec{H}_{ext} \parallel \hat{e}_3$).

As the chain axis is aligned for every strain with the lateral boundaries, this condition is equivalent to rotate the external magnetic field an angle $\theta = \operatorname{atan}\gamma$. This means that, for each strain, the lattice and the external field rotate the same angle and the problem reduces to the first one where chains are only elongated in the field direction (but remembering that only one dimension of the computational domain changes to keep the volume fraction constant). In Fig. 7.4, the shear stress curves obtained with this method (red open circles) are plotted together with previous results. It can be observed that, although both kinds of tetragonal lattices are elongated in different ways, this does not introduce noticeable changes in the shear stress versus strain curve. For strain levels below $\gamma = 0.2$ differences in the unit cell width are smaller than 2% while for large strains the width of the computation box is already large enough so that boundary conditions (which are the same in both lattices) do not influence the final solution.

Finally note that, as it was stated before, the whole lattice is rotated while it is strained. Consequently, the interface referred in Sec. 7.2 splitting both homogeneous media will also rotate. Indeed, its normal vector is parallel to the tilted surfaces of the unit cell $\hat{n} = -\hat{e}_3$. Consequently, the value of the magnetic field (and its flux density) far away from the lattice will depend on the strain and will be given by continuity equations. In particular:

$$B_{2,x} = \mu_0 \langle H_x \rangle \tag{7.7a}$$

$$B_{2,y} = \frac{\mu_0\big(\langle H_y \rangle - \gamma \langle H_z \rangle\big) + \gamma^2 \langle B_y \rangle + \gamma \langle B_z \rangle}{1+\gamma^2} \tag{7.7b}$$

$$B_{2,z} = \frac{\mu_0\big(\gamma^2 \langle H_z \rangle - \gamma \langle H_y \rangle\big) + \gamma \langle B_y \rangle + \langle B_z \rangle}{1+\gamma^2} \tag{7.7c}$$

and $\vec{H}_2 = \vec{B}_2/\mu_0$.

From this section it can be concluded that the use of mirror symmetries as lateral boundary conditions (that is, aligning the total magnetic field at the boundaries with the chain axis) completely fails in simulating a shear strain motion. Nonetheless, at least, the use of mirror symmetries results in a tetragonal lattice (that elongates and rotates) and therefore includes multibody interactions. At this point, it is worth to remark that, although Ginder and Davis' method [4] applies these particular boundary conditions, their model is axisymmetric. Thus, the simulated geometry will not mimic a true lattice for high concentrations (small interchain distance) when lateral interactions are expected to play a role.

In summary, classical axisymmetric FEMM simulations have, as main advantage, a reduced computational cost. However, in this manuscript it has been demonstrated that their predictions are solely right at small field strengths (in the linear regime) and small shear strains ($\gamma < 0.2$). In this particular small-field and small-strain operation regime, magnetostatic interactions are multipolar, directed along the chain axis and dictated by the interparticle distance. As a result, interchain interactions are satisfactorily captured and the rotational contribution to the stress is negligible in comparison to the elongational one. Nevertheless, for large field strengths and strain levels, the classical axisymmetric FEMM simulations fail to describe the true strain process because the interchain interactions and the rotational contributions are not satisfactorily captured. In this large-field and large-strain operation regime the model proposed by Morillas and de Vicente [10] should be used.

Acknowledgements

This work was supported by MINECO MAT 2016-78778-R and PCIN-2015-051 projects (Spain) and European Regional Development Fund (ERDF). J. R. Morillas acknowledges FPU14/01576 fellowship.

7.5 Appendix

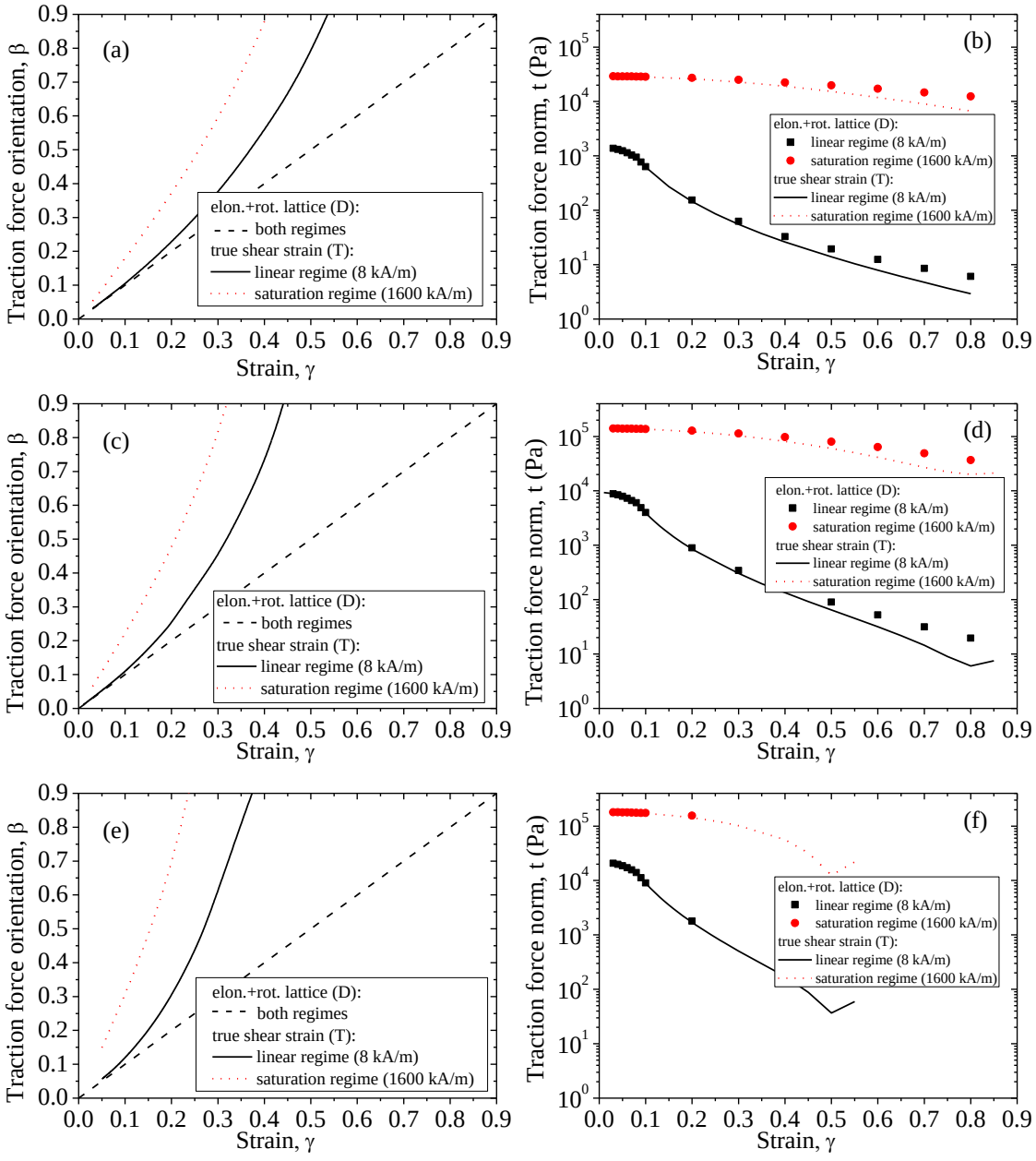

Figure 7.5: Traction force orientation $\beta = F_y/F_z$ (left column-dashed line) and norm $t = \sqrt{F_y^2 + F_z^2}/A$ (right column-points) for different volume fractions (top row 3 vol%, middle row 20 vol% and bottom row 50 vol%) and magnetic field strengths according to Ginder and Davis' axysimmetric approach [4]. Results from truly shearing the lattice are also plotted with solid and dotted lines.

References

[1] Wereley, N. (Ed.). Magnetorheology: advances and applications (Vol. 6) (Royal Society of Chemistry, Cambridge, 2013).

[2] Ghaffari, A., Hashemabadi, S. H., and Ashtiani, M. (2015). A review on the simulation and modeling of magnetorheological fluids. Journal of Intelligent Material Systems and Structures, 26(8), 881-904.

[3] Ahamed, R., Choi, S. B., and Ferdaus, M. M. (2018). A state of art on magneto-rheological materials and their potential applications. Journal of Intelligent Material Systems and Structures, 29(10), 2051-2095.

[4] Ginder, J. M., and Davis, L. C. (1994). Shear stresses in magnetorheological fluids: role of magnetic saturation. Applied Physics Letters, 65(26), 3410-3412.

[5] Ginder, J. M., Davis, L. C., and Elie, L. D. (1996). Rheology of magnetorheological fluids: Models and measurements. International Journal of Modern Physics B, 10(23n24), 3293-3303.

[6] Bossis, G., Grasselli, Y., and Ciffreo, A. (2019). The role of volume fraction and additives on the rheology of suspensions of micron sized iron particles. Frontiers in Materials, 6, 4.

[7] Ruzicka, M. Electrorheological fluids: modeling and mathematical theory (Springer-Verlag, Berlin, 2000).

[8] Morillas, J. R., and de Vicente, J. (2019). Yielding behavior of model magnetorheological fluids. Soft Matter, 15(16), 3330-3342.

[9] Ruiz-López, J. A., Fernández-Toledano, J. C., Hidalgo-Álvarez, R., and de Vicente, J. (2016). Testing the mean magnetization approximation, dimensionless and scaling numbers in magnetorheology. Soft Matter, 12(5), 1468-1476.

[10] Morillas, J. R., and de Vicente, J. (2019). On the yield stress in magnetorheological fluids: a direct comparison between 3D simulations and experiments. Composites Part B: Engineering, 160, 626-631.

[11] Jiles, D. Introduction to magnetism and magnetic materials (CRC Press, Boca Raton, 2015).

[12] Kang, T. G., Hulsen, M. A., & den Toonder, J. M. (2012). Dynamics of magnetic chains in a shear flow under the influence of a uniform magnetic field. Physics of Fluids, 24(4), 042001.

[13] Hashemi, M. R., Manzari, M. T., & Fatehi, R. (2017). Non-linear stress response of non-gap-spanning magnetic chains suspended in a Newtonian fluid under oscillatory shear test: A direct numerical simulation. Physics of Fluids, 29(10), 107106.

[14] Griffiths, D. J. Introduction to Electrodynamics (Prentice Hall, Upper Saddle River, 1999).

[15] Franklin, J. Classical Electromagnetism (Pearson Addison-Wesley, San Francisco, 2005)

[16] Bossis, G., Lacis, S., Meunier, A., & Volkova, O. (2002). Magnetorheological fluids. Journal of Magnetism and Magnetic Materials, 252, 224-228.

[17] Davis, L. C. (1992). Polarization forces and conductivity effects in electrorheological fluids. Journal of Applied physics, 72(4), 1334-1340.

Chapter 8. Magnetorheology in Saturating Fields

Jose R. Morillas and Juan de Vicente

This article is published in: Physical Review E, 99(6), 062604 (2019).

DOI: https://doi.org/10.1103/PhysRevE.99.062604

Abstract

Understanding magnetorheology in saturating fields is crucial for success in high torque applications. In this manuscript we use numerical computations, analytical developments and experimental data (using a double-gap magnetocell) to study the saturation behavior of model magnetorheological fluids for different particle loadings. Numerical calculations demonstrate a non-linear dependence of both shear and normal stresses with particle concentration in contrast with analytical predictions. These predictions are in very good agreement with numerical calculations at low volume fractions when the interchain interactions can be safely neglected. Numerical calculations for the (yield) shear stress overestimate experimental data for small and medium concentrations. However, a reasonably good qualitative agreement is found for the larger particle loadings. Normal stresses are extraordinarily sensitive to the particular microstructure; experiments suggest sample dilatation in good agreement with simulations in lattices with a body centered (BC) basis.

8.1 Introduction

Magnetorheological (MR) fluids of interest in mechanical applications are prepared by dispersion of magnetizable carbonyl iron particles in a Newtonian oily phase. The importance of these materials stems from the fact that their rheological properties can be externally controlled through the superposition of magnetic fields; an apparent yield stress appears if the field strength is large enough. The reason for this is the formation of particle-based columnar structures in the field direction that are capable to transfer the torque between the confining surfaces. The maximum strength of any MR fluid is attained at saturating fields (i.e. sufficiently large field strengths for the magnetization of the particles to saturate) [1-4].

In saturation, the magnetized particles can be simply replaced by a fixed magnetic dipole moment placed at its center. With this, the theoretical description of the rheological behavior of a MR fluid is strongly simplified [5,6]. However, performing experiments in saturation is not straightforward; in order to saturate the particles an electromagnetic circuit must be used and, as a result, the field inhomogeneity within the sample typically increases. Just recently, it has been demonstrated that using a double-gap magnetocell it is possible to measure the rheological properties of MR fluids in homogeneous saturating fields [7].

Apart from increasing the external magnetic field strength, the other simplest route to enhance the MR effect is to increase the particle volume fraction [8,9]. As a result, it is of great interest to ascertain the influence of particle loading in the rheological behavior of saturated MR fluids. Several attempts have been reported in the literature for low volume fractions that predict a linear dependence [10]. However, increasing the particle loading strongly complicates the analysis because multibody interactions come into play. In this manuscript we perform numerical calculations to compute the shear and normal stresses in model preassembled structures. The results are then compared to analytical calculations that are valid for low volume fractions. Finally, experiments are carried out in a double-gap magnetocell device to measure shear stress and normal stress differences at saturation for a wide range of particle concentrations.

8.2 Preassembled structures: numerical calculations

In this section we compute shear and normal stresses in preassembled structures subjected to a simple shear deformation $\gamma = \tan\theta$ in the y direction under an external field that is applied in the z direction (see Fig. 8.1). At rest, in the undistorted state, the particles are preassembled in a tetragonal lattice. For simplicity, in the body text of this manuscript we will restrict the analysis to simple tetragonal lattices. However, the same approach used here can be extended to other more complex lattices. In particular, in Sec. 8.7 we show the derivation for the body centered (BC) basis.

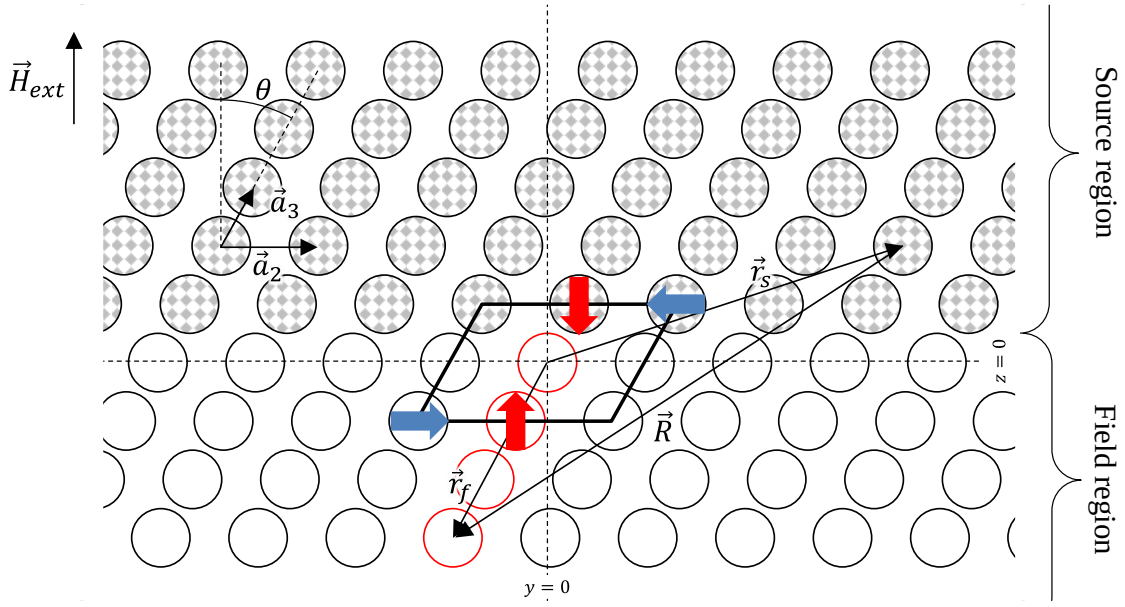

Figure 8.1: Schematics of the particle arrangement. Simulated lattice under a strain $\gamma = \tan\theta$ and an external applied magnetic field $\vec{H}_{ext}$. Only the particles sheet at $x = 0$ is plotted. Dashed lines determine the origin of the coordinate system. The upper (source) region of the lattice is represented with dotted circles while the bottom (field) region is represented with empty circles. In this sketch, the vector $\vec{R}$ joins the (0,3,2) source particle with the (0,0,-3) field particle. Due to the lattice symmetry, only the force acting over the red field particles needs to be computed. The sign criteria is represented by the black trapezium: blue (red) arrows represent positive field-driven shear (normal) stresses acting on the microstructure.

When sheared at a given strain level γ we assume that the particles undergo an affine deformation and therefore the particles rearrange in a monoclinic lattice. Consequently,

for any applied strain, the particle position vector $\vec{r}$ can be written in terms of the lattice unit vectors (see Fig. 8.1):

$$\vec{a}_1 = w\hat{x} \tag{8.1a}$$

$$\vec{a}_2 = w\hat{y} \tag{8.1b}$$

$$\vec{a}_3 = h(\gamma\hat{y} + \hat{z}) \tag{8.1c}$$

Here $h = d$ is the vertical distance between two consecutive particles along a chain (i.e. the particle diameter d), $w = h\sqrt{\pi/6\phi}$ is the horizontal distance between chains (i.e. the width of the lattice unit cell) and ϕ is the particle volume fraction. Note that ϕ remains constant during the straining motion because the volume of the unit cell is conserved. It is also worth to note that magnetic-non magnetic, core-shell, composite particles can also be simulated following this approach by simply making $h > d$.

The magnetic field inside the lattice is the summation of the external applied field plus the perturbation due to the magnetized particles. Under strong enough external fields, the total field will be dominated by the external one and therefore, under the assumption of isotropic magnetizable particles, the latter will fully saturate in the external field direction. As a result, the particles can be substituted by point dipoles of strength $\vec{m} = M_s V_m \hat{z}$ where M_s is the saturation magnetization and V_m is the magnetic volume of the particles ($V_m = \pi d^3/6$ for spherical particles). With this assumption, a *field* (f) particle experiences a dipolar force due to a *source* (s) particle through:

$$\vec{F}_{fs} = \frac{3\mu_0}{4\pi R^4}\left[2\vec{m}(\vec{m}\cdot\hat{R}) + m^2\hat{R} - 5(\vec{m}\cdot\hat{R})^2\hat{R}\right] \tag{8.2}$$

Here μ_0 is the permeability of vacuum and $\vec{R}$ is the position vector of the field particle with respect to the source particle (see Fig. 8.1). $\vec{R}$ can be written in terms of the position vector of the field and source particles as follows:

$$\vec{r}_f = l_f\vec{a}_1 + m_f\vec{a}_2 + n_f\vec{a}_3 \tag{8.3a}$$

$$\vec{r}_s = l_s\vec{a}_1 + m_s\vec{a}_2 + n_s\vec{a}_3 \tag{8.3b}$$

$$\vec{R} = \vec{r}_f - \vec{r}_s = (l_f - l_s)w\hat{x} + [(m_f - m_s)w + (n_f - n_s)\gamma h]\hat{y} + (n_f - n_s)h\hat{z} \tag{8.3c}$$

where (l, m, n) are the (integer) 'coordinates' of the field and source particles within the lattice.

Shear/normal stresses in the lattice can be obtained from the total force experienced (in the shear/normal direction) by the *field region* of the lattice due to the *source region* divided by the total surface area of the interface separating both regions. The choice between *field* and *source regions* will depend on the internal stress which is pursued. In the case of stresses acting over a plane with normal vector $\hat{z}$, the *field region* will be the bottom region (that is, $n_f \leq 0$) and the *source region* will be the upper region ($n_s > 0$) (see Fig. 8.1).

Moreover, due to the translational symmetry of the lattice in x and y directions, the shear/normal stress can also be calculated from the total shear/normal force, due to all the particles contained in the *source region* ($n_s > 0$), acting on all the particles contained in one arbitrary chain (for simplicity: $l_f = m_f = 0$). In particular, the shear/normal stress

can be obtained dividing the force acting on those particles in the chain that belong to the *field region* ($l_f = m_f = 0$, $n_f \leq 0$) by the area per chain w^2 (see red highlighted circles in Fig. 8.1).

Through this section and the next one (Sec. 8.3), only shear (τ_{zy}) and normal (σ_{zz}) stresses, both acting over the plane with normal vector $\hat{z}$, are considered. However, in Sec. 8.8 the computation of the normal stress σ_{yy} (acting over a plane with normal vector $\hat{y}$) is addressed in the non-strained state as well. As it will be seen later, this quantity is also necessary to compute the thrust developed by MR fluids under the presence of a magnetic field.

At this point, it must be remarked that periodic dipole lattice models have already been employed in the literature to study MR elastomers (e.g. see Refs. [11] or [12] and references therein). However, those works are based on an energetic approach that requires, at least, a differentiation to obtain the stress (and therefore the viscoelastic moduli). Moreover, in the energetic approach only the generalized force related to the generalized coordinate is accessible. In this way, only shear stresses are computable when the lattice is shear strained while only normal stresses are computable when the lattice is elongated. Since the simulations presented in this work are directly based on forces computation, they do not have the aforementioned shortcomings and thus are more versatile. In particular, the methodology presented here is capable to provide both shear and normal stress information under a shearing motion.

Finally, to keep the model as simple as possible, we only considered magnetostatic interparticle forces between non-deformable spheres prepositioned in periodic arrays. Other contact and colloidal forces were neglected in the analysis (e.g. Brownian, dispersion, electrostatic and gravitational). Torque effects on the shear strained lattice were not considered in the analyses. For the experimental field strength used in this work, torque effects on yield and normal stresses are below 6% and 10%, respectively. As a result, they do not seem to play a crucial role in the mechanical behavior of the system. Moreover this torque contribution is difficult to be assessed from an experimental point of view.

8.2.1 Shear stress

To compute the shear stress $\tau_{zy} = \tau$ for a given applied strain γ we need to calculate, for every field particle, the projection of the force $\vec{F}_{fs}$ along the shear direction $(\hat{y})$ as follows:

$$F_{zy} = \sum_{\substack{n_f \leq 0 \\ l_f = m_f = 0}} \sum_{\substack{n_s > 0 \\ \forall\, l_s, m_s}} \vec{F}_{fs} \cdot \hat{y} = \sum_{\substack{n_f \leq 0 \\ l_f = m_f = 0}} \sum_{\substack{n_s > 0 \\ \forall\, l_s, m_s}} \frac{3\mu_0 m^2}{4\pi} \frac{R_y}{R^5} \left(5 \frac{R_x^2 + R_y^2}{R^2} - 4 \right) \tag{8.4}$$

where the subscripts z and y just remind that the force F_{zy} has y direction and is related to a plane with normal vector $\hat{z}$. From Eqs. (8.3) and (8.4) we conclude that if the particles in the lattice are directly touching, that is $h = d$, each component of the vector $\vec{R}$ is proportional to d and hence the force scales with $\propto d^2$. As a consequence, since the stress

is computed dividing the force by the surface area $w^2 \propto d^2$, the dependence of the stress with the diameter of the particles is lost. Note that this statement is applicable not only to shear stresses but also to normal stresses (see below).

As it was pointed out previously, the total shear force is computed by summation of the force component, along the shear direction, acting on each field particle in a chain $(0,0,n_f)$ due to all source particles in the source region (l_s, m_s, n_s). Ideally, the summation should go through all possible combinations of n_f, l_s, m_s and n_s with $n_f \leq 0$ and $n_s > 0$. Of course, this yields an infinite number of combinations because the lattice is unbounded. However, as it is typically done in the literature, a cutoff distance r_{cut} is introduced taking advantage of the fact that the dipolar interaction decreases with the distance. Therefore, for a given field particle, only those source particles fulfilling $R < r_{cut}$ will eventually contribute to the total force. As a result, n_f runs from 0 till the closest integer to $-r_{cut}/h$: for smaller n_f the cutoff sphere (i.e. sphere of radius r_{cut}) is placed completely inside the field region of the lattice and therefore no source particles are accounted for. Through this work, a cutoff distance of $r_{cut} = 160h$ is used. It is important to note that this value is large enough for not to have any size effect on the shear stress calculations shown in this manuscript (differences with larger cutoff distances below 0.02%). The process explained above is repeated for different strain levels in order to construct the shear stress versus shear strain curve and eventually determine the maximum (yield) shear stress.

In view of the method employed to compute the shear stress, a positive (negative) shear stress implies that the bottom half of the lattice (i.e. field region) feels a force in the same (opposite) direction as the applied strain. Using Newton's third law, the upper half of the lattice (i.e. the source region) feels a force in opposite (same) direction as the strain that compensates, in mechanical equilibrium, the external shear force imposed by the rheometer. Note that in modern plate-plate torsional rheometers the torque sensor is attached to the upper movable plate so one has experimental access to the stresses acting on the upper part of the lattice (see Fig. 8.1). From now on, the sign for the stresses represented in the figures are those corresponding to the structures and not to the rheometer's plate.

8.2.2 Normal stress

In contrast to shear stress calculations described in Sec. 8.2.1, the normal stress σ_{zz} cannot be computed by simply projecting the magnetostatic force acting on the field particles $\vec{F}_{fs}$ along the magnetic field direction (i.e. z direction) using

$$F_{zz} = \sum_{\substack{n_f \leq 0 \\ l_f = m_f = 0}} \sum_{\substack{n_s > 0 \\ \forall\, l_s, m_s}} \vec{F}_{fs} \cdot \hat{z} = \sum_{\substack{n_f \leq 0 \\ l_f = m_f = 0}} \sum_{\substack{n_s > 0 \\ \forall\, l_s, m_s}} \frac{3\mu_0 m^2}{4\pi} \frac{R_z}{R^5} \left(5 \frac{R_x^2 + R_y^2}{R^2} - 2 \right) \tag{8.5}$$

and the cutoff radius r_{cut} introduced in Sec. 8.2.1. Calculations using Eq. (8.5) give larger normal stresses than expected because the dipoles outside the cutoff sphere are not considered. To illustrate this issue we will use the decomposition employed by Lorentz to calculate the local field [13-16]. According to this, the total magnetic field at any field point of an unbounded dipole lattice can be decomposed in two parts: Firstly, a discrete

(*dis*) region contribution coming from near source dipoles inside the so-called Lorentz's sphere. Secondly, a continuous (*cont*) region contribution arising from the dipoles outside the Lorentz's sphere. Source dipoles outside the Lorentz's sphere are so far away from the field point that the interdipole distance in the source region is negligible and therefore they truly act as a continuous medium. This continuous contribution comes from a uniformly magnetized continuous body containing a spherical cavity (the Lorentz's sphere) inside. It does not depend on the radius of the Lorentz's sphere and, thus, regardless of the size for the discrete region, the continuous contribution needs to be computed.

The Lorentz's sphere can be identified with the cutoff sphere previously introduced in the shear stress computation (see Sec. 8.2.1): only those dipoles inside the sphere are considered in a discrete way when the total field/force is computed over a field dipole. Therefore, similar to Lorentz's approach where the total field is given by a discrete contribution plus a continuous contribution, it is expected that Eq. (8.5) (i.e. the discrete contribution) will not provide the total normal force. In addition to discrete source particles within the cutoff sphere, any field particle will feel the force due to the rest of source particles outside the cutoff sphere (Fig. 8.2a).

Similar to Lorentz's model, source particles outside the cutoff sphere are so far away from the field particle that they are seen as a continuum (in the following, the *continuous region*). In addition, since the field particles are truly magnetic dipoles, the *continuous region* should act over them through a force coming from the magnetic field gradient it generates $\vec{B}_{cont}$ as follows [16]:

$$\vec{F}_{cont} = \nabla\left(\vec{m} \cdot \vec{B}_{cont}\right) = (\vec{m} \cdot \nabla)\vec{B}_{cont} = m\frac{\partial \vec{B}_{cont}}{\partial z} \tag{8.6}$$

In Eq. (8.6) it has been already taken into consideration that field dipoles are constant and aligned with the external magnetic field (i.e. in the z direction).

As the *continuous region* is based on constant dipoles (all of them having the same magnitude and direction), this region is uniformly magnetized $\vec{M}_{cont} = \phi M_s \hat{z}$ and the magnetic field it creates only depends on the magnetic charge surface density $\rho_s = \vec{M}_{cont} \cdot \hat{n}$ where $\hat{n}$ is the normal vector of the boundary surface delimiting the *continuous region*.

In view of Fig. 8.2, it can be seen that ρ_s is distributed along a flat plane (with a hole of radius ρ_0, Fig. 8.2b) and the inner surface of a spherical cap (of radius r_{cut} and maximum polar angle θ_f, Fig. 8.2c). Therefore, it is possible to compute $\vec{F}_{cont}$ following the next steps: (i) Calculate the magnetic field distribution created by the plane with a circular hole $\vec{B}_{cont,p}$. Bearing in mind the axial symmetry of the geometry, only $\vec{B}_{cont}$ along the symmetry axis (i.e. the dash-dotted line in Figs. 8.2b and 8.2c) is needed. (ii) Calculate $\partial\vec{B}_{cont,p}/\partial z$ at the position of a field dipole and introduce it in Eq. (8.6). (iii) Repeat step (ii) for all field dipole positions and add their contribution to the discrete normal force F_{zz} (Eq. (8.5)). (iv) Repeat all the previous steps for the field due to the spherical cap surface $\vec{B}_{cont,c}$.

At this stage it is easy to understand why the *continuous region* does not contribute to the shear stress calculations described in Sec. 8.2.1. The reason for this is that the *continuous region* is magnetized in the same direction than the symmetry axis: the surface density ρ_s

is axisymmetric. As a direct consequence, the y component of $\vec{B}_{cont}$ along this axis is null and thus, according to Eq. (8.6), the *continuous region* does not contribute to the shear stress.

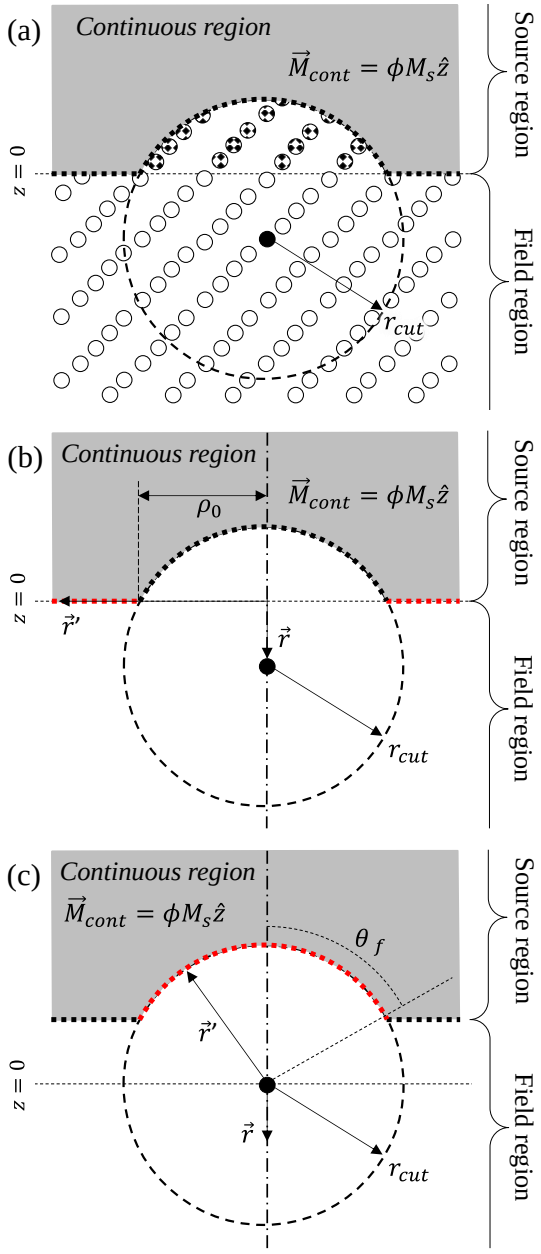

Figure 8.2: (a) According to Lorentz's model, a given field particle (black circle) will feel the force due to all source particles inside the cutoff sphere (dotted particles) plus a contribution from the *continuous region* (grey region) based on those source particles outside the cutoff sphere. As the *continuous region* is uniformly magnetized, its contribution will depend on its surface density distributed along its boundary surface (dotted line). This surface is axisymmetric and can be split in a flat plane with a hole of radius ρ_0 (b-red dotted line) and the inner surface of a spherical cap of radius r_{cut} and maximum polar angle θ_f (c-red dotted line).

Alternatively to steps (i)-(iv), it is worthwhile to note that in view of Newton's third law, it would also be possible to compute the force acting on the *continuous region* due to the field dipoles (see Sec. 8.8). The advantage is that the field due to magnetic dipoles (in the

field region) is simpler to calculate and the differentiation in Eq. (8.6) is not needed. Furthermore, this is possibly more convenient in non-axisymmetric problems where the magnetization is not aligned with the axis and the continuous source region is expected to contribute to both shear and normal stresses.

In Secs. 8.2.2.1 and 8.2.2.2, the force due to the *continuous region* is computed following the aforementioned steps (i)-(iv). Through these sections, field points (i.e. the points where the magnetic field is to be computed) will be denoted with $\vec{r}$ while source surface density positions will be denoted with $\vec{r}'$ (Figs. 8.2b and 8.2c).

8.2.2.1 *Normal stress created by the plane with a hole*

In view of Fig. 8.2b it can be seen that $\vec{r}' = \rho'(\cos\varphi'\,\hat{x} + \sin\varphi'\,\hat{y})$, $\vec{r} = z\hat{z}$ and $\hat{n} = -\hat{z}$. Therefore, the field $\vec{B}_{cont,p}$ created by the flat plane with the ρ_0 radius hole is given by:

$$\begin{aligned}\vec{B}_{cont,p} &= \frac{\mu_0}{4\pi}\int \rho_s(\vec{r}')\frac{\vec{r}-\vec{r}'}{|\vec{r}-\vec{r}'|^3}ds' \\ &= -\frac{\mu_0}{4\pi}\int_0^{2\pi}\int_{\rho_0}^{\infty}\phi M_s\frac{z\hat{z}-\rho'(\cos\varphi'\,\hat{x}+\sin\varphi'\,\hat{y})}{\left(z^2+\rho'^2\right)^{\frac{3}{2}}}\rho' d\rho' d\varphi' \\ &= -\frac{\mu_0\phi M_s}{2}\frac{z\hat{z}}{\left(\rho_0^2+z^2\right)^{1/2}}\end{aligned} \tag{8.7}$$

Hence, substituting Eq. (8.7) in Eq. (8.6) (i.e. differentiating and multiplying by the dipole strength) we get:

$$\vec{F}_{cont,p} = -\frac{\mu_0\phi M_s^2\pi d^3}{12}\frac{\rho_0^2}{\left(\rho_0^2+z^2\right)^{3/2}}\hat{z} \tag{8.8}$$

In addition, the radius of the hole depends on the position of the field point through $\rho_0^2 + z^2 = r_{cut}^2$ (see Fig. 8.2b). Substituting this relationship in Eq. (8.8) and dividing by the area per chain $w^2 = d^2\,\pi/6\phi$ one gets the correction to the normal stress due to the plane with the hole corresponding to one field particle located at z:

$$\sigma_{zz}^{cont,p} = -\frac{\mu_0\phi^2 M_s^2}{2}\frac{d}{r_{cut}}\left(1-\left(\frac{z}{r_{cut}}\right)^2\right) \tag{8.9}$$

For the lattices considered in this work, the vertical position of the field particles is given by $z = n_f d$. Thus, the contribution due to all field particles is:

$$\sigma_{zz}^{cont,p} = -\frac{\mu_0\phi^2 M_s^2}{2}\frac{d}{r_{cut}}\sum_{n_f=-r_{cut}/d}^{0}\left(1-\left(\frac{n_f d}{r_{cut}}\right)^2\right) \tag{8.10}$$

Interestingly, in contrast to the local field correction proposed by Lorentz, the normal stress correction does depend on the cutoff distance (see Eq. (8.10)). However, it should be remembered that, according to Lorentz's model, this cutoff distance must be large enough to approximate the source region as a continuum, thus in the previous summation, $n = r_{cut}/d$ must tend to infinity. Taking the limit $n \to \infty$, Eq. (8.10) simplifies as follows:

$$\sigma_{zz}^{cont,p} = -\frac{\mu_0 \phi^2 M_s^2}{2} \lim_{n\to\infty} \frac{1}{n} \sum_{n_f=-n}^{0} \left(1 - \left(\frac{n_f}{n}\right)^2\right)$$
$$= -\frac{\mu_0 \phi^2 M_s^2}{2} \int_0^1 (1 - x^2) dx = -\frac{\mu_0 \phi^2 M_s^2}{3} \tag{8.11}$$

8.2.2.2 *Normal stress created by the cap surface*

In Fig. 8.2c we show the coordinate system employed to compute the normal stress contribution from the spherical cap surface. Note that the origin is displaced with respect to the coordinate system used through Sec. 8.2: $\vec{r}' = r_{cut}(\sin\theta' \cos\varphi' \hat{x} + \sin\theta' \sin\varphi' \hat{y} + \cos\theta' \hat{z})$, $\vec{r} = z\hat{z}$ and $\hat{n} = -\vec{r}'/r_{cut}$. In principle, the same protocol used for the plane with a hole can be repeated here, however, computing the field created by the spherical cap surface just at its center (where the field particle is placed) leads to a cumbersome integral. In this case it is easier to calculate, first, the z derivative of $\vec{B}_{cont,c}$ and then integrate this result for the whole cap surface. This is valid as the integration is done over source coordinates $\vec{r}'$ while derivation is done with respect of field coordinates $\vec{r}$ and both sets of coordinates are independent:

$$\frac{\partial \vec{B}_{cont,c}}{\partial z}$$
$$= \frac{\mu_0 \phi M_s r_{cut}^2}{2} \hat{z} \int_0^{\theta_f} \frac{\cos\theta' \sin\theta' \left(-r_{cut}^2 + 3r_{cut}^2 \cos^2\theta'\right)}{\left(r_{cut}^2 + z^2 - 2z r_{cut} \cos\theta'\right)^{5/2}} d\theta'$$
$$+ \frac{\mu_0 \phi M_s r_{cut}^2}{2} \hat{z} \int_0^{\theta_f} \frac{\cos\theta' \sin\theta' \left(2z^2 - 4z r_{cut} \cos\theta'\right)}{\left(r_{cut}^2 + z^2 - 2z r_{cut} \cos\theta'\right)^{5/2}} d\theta' \tag{8.12}$$

where the azimuthal coordinate has already been integrated. Evaluating the derivative at the field particle position $z = 0$ and integrating we arrive to:

$$\left.\frac{\partial \vec{B}_{cont,c}}{\partial z}\right]_{z=0} = \frac{\mu_0 \phi M_s}{2 r_{cut}} \hat{z} \int_0^{\theta_f} \frac{1}{8} (2\sin 2\theta' + 3\sin 4\theta') d\theta'$$
$$= -\frac{\mu_0 \phi M_s}{2 r_{cut}} \hat{z} \left(\frac{3}{4}\cos^4\theta_f - \frac{1}{2}\cos^2\theta_f - \frac{1}{4}\right) \tag{8.13}$$

Multiplying Eq. (8.13) by the dipole strength, and in view of Eq. (8.6), the force experienced by the field dipole under the spherical cap of maximum angle θ_f is obtained:

$$\vec{F}_{cont,c} = -\frac{\mu_0 \phi M_s^2 \pi d^3}{12 r_{cut}} \hat{z} \left(\frac{3}{4}\cos^4\theta_f - \frac{1}{2}\cos^2\theta_f - \frac{1}{4}\right) \tag{8.14}$$

Looking at Fig. 8.2c, it can be seen that θ_f is related to the vertical position of the field particle z (now, this vertical position is referred to the original coordinate system of the lattice) through $\cos\theta_f = z/r_{cut}$. Substituting $\cos\theta_f = z/r_{cut}$ in Eq. (8.14) and dividing by w^2 we get the correction due to the spherical cap surface for every field particle:

$$\sigma_{zz}^{cont,c} = -\frac{\mu_0 \phi^2 M_s^2}{2} \frac{d}{r_{cut}} \left(\frac{3}{4} \left(\frac{z}{r_{cut}} \right)^4 - \frac{1}{2} \left(\frac{z}{r_{cut}} \right)^2 - \frac{1}{4} \right) \tag{8.15}$$

Finally, following the previous reasoning to consider all field particles:

$$\begin{aligned} \sigma_{zz}^{cont,c} &= -\frac{\mu_0 \phi^2 M_s^2}{2} \lim_{n \to \infty} \frac{1}{n} \sum_{n_f=-n}^{0} \left(\frac{3}{4} \left(\frac{n_f}{n} \right)^4 - \frac{1}{2} \left(\frac{n_f}{n} \right)^2 - \frac{1}{4} \right) \\ &= -\frac{\mu_0 \phi^2 M_s^2}{2} \int_0^1 \left(\frac{3}{4} x^4 - \frac{1}{2} x^2 - \frac{1}{4} \right) dx \\ &= \frac{2\mu_0 \phi^2 M_s^2}{15} \end{aligned} \tag{8.16}$$

8.2.2.3 *Total normal stress*

The total normal stress is obtained by summation of the different contributions. First, the discrete contribution that is computed numerically through all source dipoles inside the cutoff sphere σ_{zz}^{dis} according to Eq. (8.5). Second, the continuous contribution from the plane containing the circular hole $\sigma_{zz}^{cont,p}$ (Eq. (8.11)). Third, the continuous contribution from the cap surface $\sigma_{zz}^{cont,c}$ (Eq. (8.16)):

$$\begin{aligned} \sigma_{zz} = \sigma_{zz}^{dis} + \sigma_{zz}^{cont} &= \sigma_{zz}^{dis} + \sigma_{zz}^{cont,p} + \sigma_{zz}^{cont,c} \\ &= \sigma_{zz}^{dis} - \frac{\mu_0 \phi^2 M_s^2}{5} \end{aligned} \tag{8.17}$$

As observed in Eq. (8.17), the continuous contribution $\sigma_{zz}^{cont} = -\mu_0 \phi^2 M_s^2/5$ tends to reduce the normal stress ($\sigma_{zz}^{cont} < 0$), it is especially important at high volume fractions ($\propto \phi^2$) and independent on the strain since all source particles outside the cutoff sphere have been substituted by a continuous medium. Similar to what happened with the shear stress τ, if $h = d$, all terms in Eq. (8.17) are independent on the diameter of the particles d.

At this stage, it is important to remark that computed forces in Eq. (8.17) act over the bottom half of the lattice (i.e. field region). Hence, a positive normal stress σ_{zz} (equivalently a force) implies that this part of the lattice is suffering an upwards force. Due to Newton's third law, the upper part of the lattice will feel the same force but in opposite direction, that is, downwards. Consequently, for positive normal stresses the lattice is under compression (see Fig. 8.1).

8.3 Single-particle width chains: analytical model

It is straightforward to obtain analytical expressions for shear τ and normal σ_{zz} stresses if the particles are arranged within single-particle width chains and the interaction between particles from different chains is neglected. In this section we show a simple way to compute the shear and normal stress. The results, analytically obtained, are expected to match the numerical calculations in the case of low volume fractions where the interchain interactions can be neglected. Note that a similar approach has been used by Refs. [17-19].

Since only one chain is considered in the analysis, the vector joining the source dipole with the field dipole is given by $l_f = l_s = m_s = m_f = 0$, hence Eq. (8.3) is reduced to:

$$\vec{R} = -R\left(\frac{\gamma\hat{y} + \hat{z}}{\sqrt{\gamma^2 + 1}}\right) \tag{8.18a}$$

$$R = \left|n_f - n_s\right| h\sqrt{\gamma^2 + 1} \tag{8.18b}$$

8.3.1 Shear stress

The force exerted by all the source dipoles (located in the upper half of the chain) on the field dipoles (located in the lower half of the chain) in the shear direction will be given by Eq. (8.4) for the particular case of an isolated chain. Therefore, substituting Eq. (8.18) in Eq. (8.4) we get:

$$\begin{aligned} F_{zy} &= \sum_{n_f \le 0}\sum_{n_s > 0} \frac{3\mu_0 m^2}{4\pi R^4}\sqrt{\frac{\gamma^2}{1+\gamma^2}}\left(4 - 5\frac{\gamma^2}{1+\gamma^2}\right) \\ &= \frac{3\mu_0 m^2}{4\pi}\sqrt{\frac{\gamma^2}{1+\gamma^2}}\left(4 - 5\frac{\gamma^2}{1+\gamma^2}\right)\sum_{n_f \le 0}\sum_{n_s > 0}\frac{1}{R^4} \\ &= \frac{3\mu_0 m^2}{4\pi h^4}\frac{\gamma(4-\gamma^2)}{(1+\gamma^2)^{7/2}}\sum_{n_f \le 0}\sum_{n_s > 0}\frac{1}{\left|n_f - n_s\right|^4} \end{aligned} \tag{8.19}$$

where the double summation is given by the Zeta Riemann function as follows:

$$\sum_{n_f \le 0}\sum_{n_s > 0}\frac{1}{\left|n_f - n_s\right|^4} = \sum_i \frac{i}{i^4} = \sum_i \frac{1}{i^3} = \xi(3) \sim 1.202 \tag{8.20}$$

Substituting Eq. (8.20) in Eq. (8.19) we arrive to:

$$F_{zy} = \frac{3\mu_0 m^2 \xi(3)}{4\pi h^4}\frac{\gamma(4-\gamma^2)}{(1+\gamma^2)^{7/2}} = \frac{3\mu_0 m^2 \xi(3)}{4\pi h^4} f(\gamma) \tag{8.21}$$

In view of Eq. (8.21), the yield stress corresponds to the maximum of F_{zy} which is obtained for $\gamma_0 = 0.389$ with $f(\gamma_0) = 0.914$. Note that for saturated dipoles considered here, the yield strain γ_0 does not depend on the number of particles in the chain (i.e. there are not multibody effects for γ_0): as it can be seen in Eq. (8.19) all information regarding the length of the chain is contained in the double summation which is a constant with no effects on the critical point where the maximum of F_{zy} appears. Therefore, a doublet of saturated dipoles has the same γ_0 than a longer chain.

Next, the yield stress is simply calculated dividing F_{zy} by the surface area per chain in the tetragonal/monoclinic lattice w^2. With this, using $h = d$ and $m = M_s\,\pi d^3/6$ we arrive to:

$$\tau_0 = \frac{3\mu_0 m^2 \xi(3)}{4\pi h^4 w^2} f(\gamma_0) = \frac{\xi(3) f(\gamma_0)}{8}\mu_0 M_s^2 \phi \sim 0.137\mu_0 M_s^2 \phi \tag{8.22}$$

where the particle volume fraction ϕ is related to the surface area per chain through $hw^2 = \pi d^3/6\phi$. Equation (8.22) can be obtained using an energetic approach as well

(instead of the force approach followed in this section). In Sec. 8.9 we show the derivation of Eq. (8.22) using the energetic method.

A similar result for the yield stress was obtained in Ref. [20] (see Eq. (9) in that paper) with the only difference of the prefactor; 0.086 instead of 0.137. This discrepancy comes from the axisymmetric model used in that work which is also revisited in Sec. 8.9.

8.3.2 Normal stress

In this section we aim to determine the normal stress σ_{zz} generated on the chain when it is subjected to a shearing deformation. Therefore, introducing Eq. (8.18) in Eq. (8.5):

$$\begin{aligned} F_{zz} &= \sum_{n_f \leq 0} \sum_{n_s > 0} \frac{3\mu_0 m^2}{4\pi R^4} \sqrt{\frac{1}{1+\gamma^2}} \left(2 - 5\frac{\gamma^2}{1+\gamma^2}\right) \\ &= \frac{3\mu_0 m^2}{4\pi h^4} \frac{2-3\gamma^2}{(1+\gamma^2)^{7/2}} \sum_{n_c \leq 0} \sum_{n_f > 0} \frac{1}{|n_f - n_s|^4} \\ &= \frac{3\mu_0 m^2 \xi(3)}{4\pi h^4} \frac{2-3\gamma^2}{(1+\gamma^2)^{7/2}} \end{aligned} \tag{8.23}$$

Evaluating the force F_{zz} for a strain level $\gamma = 0$, dividing by the surface area per chain w^2 and substituting $h = d$ and $m = M_s\, \pi d^3/6$ we obtain the following expression for the normal stress:

$$\sigma_{zz}(\gamma = 0) = \frac{3\mu_0 m^2 \xi(3)}{2\pi h^4 w^2} = \frac{\xi(3)}{4} \mu_0 M_s^2 \phi \sim 0.3 \mu_0 M_s^2 \phi \tag{8.24}$$

Note that in this analytical development, the double summation in Eq. (8.23) takes into consideration all particles along the chain. Therefore it is not necessary to introduce a cutoff distance nor to correct the previous expression with the continuous contribution σ_{zz}^{cont} used in Sec. 8.2.2. Note also that Eq. (8.24) is exactly the last contribution described in Ref. [21] (see Eq. (43) in that paper) for the electrorheological analogues.

8.4 Experiments

Rheological experiments were conducted to measure shear and normal stresses at saturation. For this purpose, a recently developed double-gap magnetocell was used [7]. With this geometry it is possible to reach saturating fields with sufficiently accurate field homogeneity. In particular, the ferromagnetic Tool #2 described in Ref. [7] was employed.

Samples used in this work were conventional MR fluids based on EW grade carbonyl iron microparticles (BASF SE) dispersed at different volume fractions (from 0.05 to 0.5) in glycerol 88 wt% (125 mPa·s, Scharlau). These iron microparticles have a saturation magnetization of M_s =1600 kA/m that is reached for external fields of approximately 1000 kA/m. This particular value for the saturation magnetization will be used in the equations contained in Secs. 8.2 and 8.3. Similar values for the saturation magnetization have been reported in the literature for carbonyl iron particles [22,23].

The yield stress was evaluated through stress-controlled rheograms. The experimental protocol was: (i) pre-shear interval (30 s at a shear rate of 33 s^{-1}) to erase the previous mechanical history of the sample, (ii) application of an external magnetic field of 1002

kA/m (experimentally measured in the gap without sample) during 1 min at rest, (iii) still in the presence of the field, a stress log ramp (15 points per decade) is applied. From these tests, the yield stress is identified with the data point immediately previous to the sample breakage.

Different from shear stress, normal stresses cannot be measured directly. Instead, the rheological accessible magnitude in a plate-plate torsional geometry is the thrust t exerted by the sample over the upper plate. This can be related to the first N_1 and second N_2 normal stress differences through:

$$N_1 - N_2 = \frac{t}{\pi r_p^2}\left(2 + \frac{d \ln t}{d \ln \dot{\gamma}}\right) \tag{8.25}$$

where $N_1 = \sigma_{yy} - \sigma_{zz}$, $N_2 = \sigma_{zz} - \sigma_{xx}$, $\dot{\gamma}$ is the magnitude of the shear rate tensor (i.e. the applied shear rate) and r_p the plate radius.

To measure the normal stress differences, the double-gap magnetocell device was also employed but only filling the bottom gap in the geometry. The same previous protocol was used simply changing step (iii). In this case, while the magnetic field is applied, the thrust t on the upper plate is recorded as the strain is increased from 0 to 0.5 at a shear rate of 0.001 s^{-1}. For this small value, it can be shown that logarithmic derivative in Eq. (8.25) is close to zero [2].

8.5 Results and discussion

8.5.1 Shear stresses

In Fig. 8.3 we show the shear stress τ versus shear strain γ results for a range of volume fractions ($\phi = 0.05$ - 0.5). Figure 8.3a contains calculations for the simple basis while Fig. 8.3b contains calculations for the BC basis. Lines in Fig. 8.3a (Fig. 8.3b) correspond to numerical calculations for saturated dipoles obtained as described in Sec. 8.2.1 (Sec. 8.7). Symbols correspond to Finite Element Method simulations using a recently developed model by Ref. [24] for the particular case of perfectly aligned saturated dipoles in the field direction. As expected, a very good agreement is found indicating that the chosen cutoff distance r_{cut} is large enough to properly model an unbounded lattice. As observed, for sufficiently large particle volume fractions, calculations for the BC basis provide larger stresses than the simple basis. This is related to the more energetically stable configuration provided by the BC basis, only noticeable at the high volume fractions when interchain interactions are not negligible. In all cases, the curves shown in Fig. 8.3 clearly exhibit a well defined peak that is associated to the yield point (τ_0, γ_0). Note that in the BC basis, large strains are not allowed at the highest volume fraction ($\phi = 0.5$) [25] since they would imply particle penetration.

In Fig. 8.4, the yield stress τ_0 is shown as a function of the volume fraction ϕ. A linear relationship is found for very small particle loadings. This is a general observation that is applicable for non-saturating fields as well. There are many references in the literature supporting this observation (e.g. Refs. [26-28] and references therein). However, for very large particle concentrations the yield stress exhibits a maximum (at approx. 0.4 for the simple basis and 0.45 for the BC basis). A maximum in the yield stress has also been reported in experiments using inverse ferrofluids [8] and theoretical analyses (macroscopic models in Ref. [8] and microscopic models, which incorporate interchain interactions, in Ref. [29]). Interestingly, the dipolar approximation applies in previous

publications where a maximum in the yield stress is observed. In contrast, when multipolar magnetostatic interactions need to be considered, the maximum in the yield stress does not appear [24,25]. In that case, a nearly linear dependence is obtained which is also supported experimentally [8,24,25].

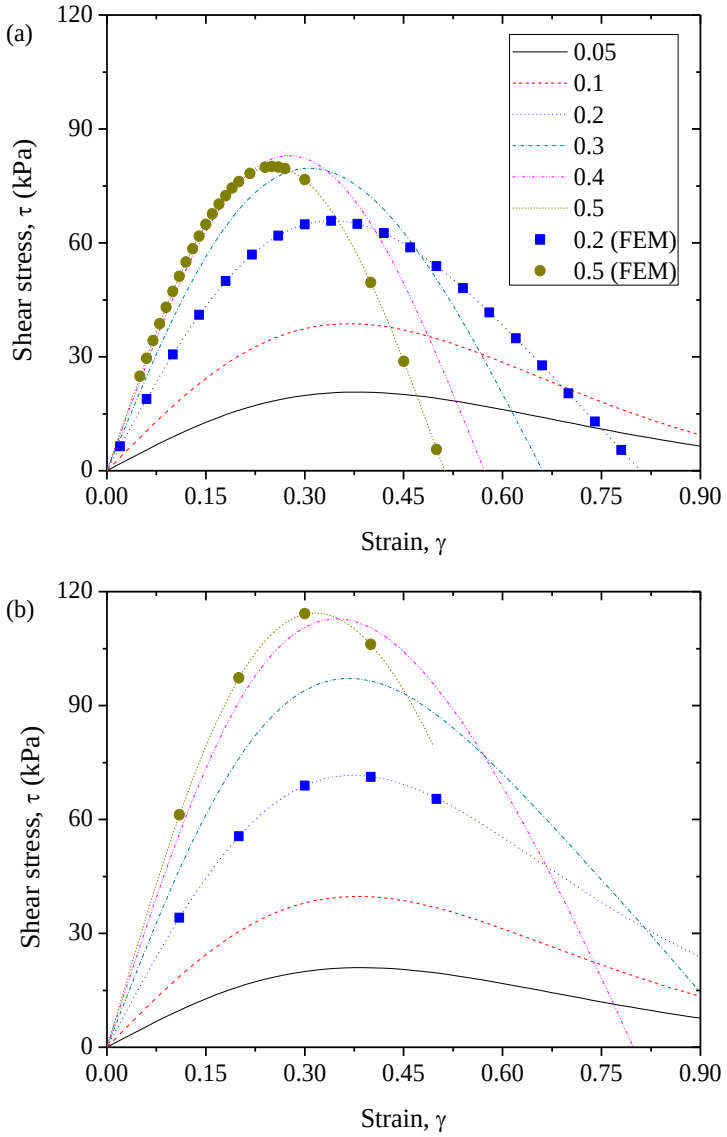

Figure 8.3: Shear stress τ as a function of the applied shear strain γ for different volume fractions ϕ. Numerical calculations are plotted with lines while results using FEM simulations for saturated dipoles as proposed in Ref. [24] are plotted with symbols. (a) Simple basis (see Sec. 8.2.1). (b) BC basis (see Sec. 8.7).

Together with simulation data we also show the analytical prediction (Eq. (8.22)) obtained in Sec. 8.3.1. As observed, this expression is in very good agreement with the simulations for sufficiently small volume fractions. This is better appreciated in Fig. 8.4b where we show the data in log-log scales. As expected, the analytic expression does not show a maximum because interchain interactions are not taken into account.

Experimental data obtained in this manuscript are also included in Fig. 8.4 as blue up triangles. As it can be seen, experiments are always below simulations except at the highest concentrations where they tend to level off at a plateau that is reasonably close to the simple basis prediction. In this figure, we also include experimental results for the

same iron microparticles dispersed in silicon oil (see green down triangles in Fig. 8.4, from Ref. [7]). Comparing up and down triangles we conclude that no significant differences can be observed pointing out that the carrier fluid is not playing a main role (as anticipated in the pre-yield regime) and that magnetic saturation is reached. Deviations between experiments and numerical/analytical calculations are expected because of strong/ideal assumptions in the calculations: periodic arrangement at an energy minimum, homogeneous strain in the sample, etc.

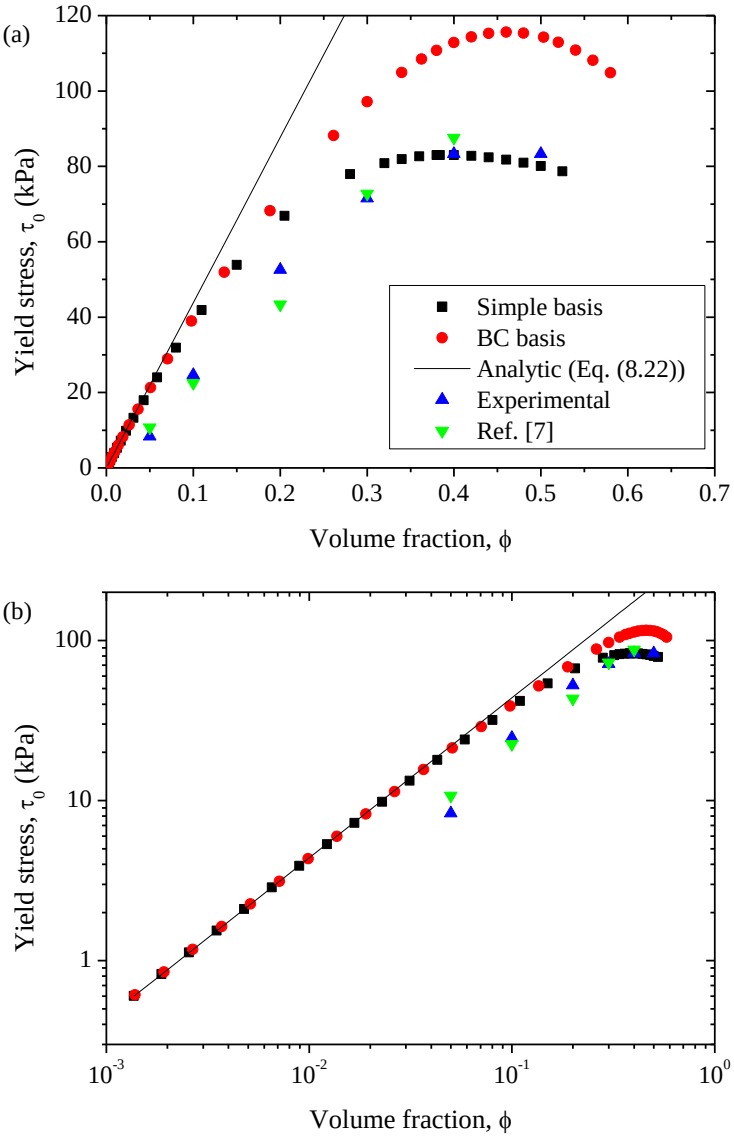

Figure 8.4: Yield stress τ_0 dependence on particle volume fraction ϕ according to simulations for simple (black squares) and BC (red circles) bases, analytical calculation for low concentrations (black line) and experiments (triangles). Blue up triangles correspond to experiments from this manuscript. Green down triangles correspond to experiments by Ref. [7] for a magnetic field strength of 979 kA/m. (a) lin-lin representation. (b) log-log representation.

In Fig. 8.5 we show the volume fraction dependence of the yield strain γ_0. As expected from Sec. 8.3.1, for small volume fractions, when the lateral interactions between chains are negligible, the yield strain is practically constant and equal to 0.389 independently of the basis (see black dashed line in Fig. 8.5). A very similar value (0.39) was found in Ref.

[30] for a chain of magnetic droplets at high magnetic fields. When the volume fraction increases the yield strain goes down. In the simple basis, this trend can be explained taking into consideration that the shear stress changes its sign at a critical strain γ_c which also depends on the volume fraction (see Fig. 8.3a): $\gamma_c = \sqrt{\pi/(24\phi)}$ [24]. When the periodic lattice is strained, the shear stress versus strain curves are expected to show periodicity as well. Thus, under the assumption that the stress versus strain curves can be approximated by simple sine waves, its period should be $2\gamma_c$ and the point where the maximum (i.e. yield stress) is reached should be $\gamma_c/2 = \sqrt{\pi/(96\phi)}$. This dependence is plotted with a magenta dotted line in Fig. 8.5 and seems to be in good agreement with simulation results at high volume fractions. This observation reveals that the periodic behavior in the shear stress-strain curve is not that simple and other harmonics must be considered. As observed in Fig. 8.5, the BC basis accommodates larger shear strains before sample breakage.

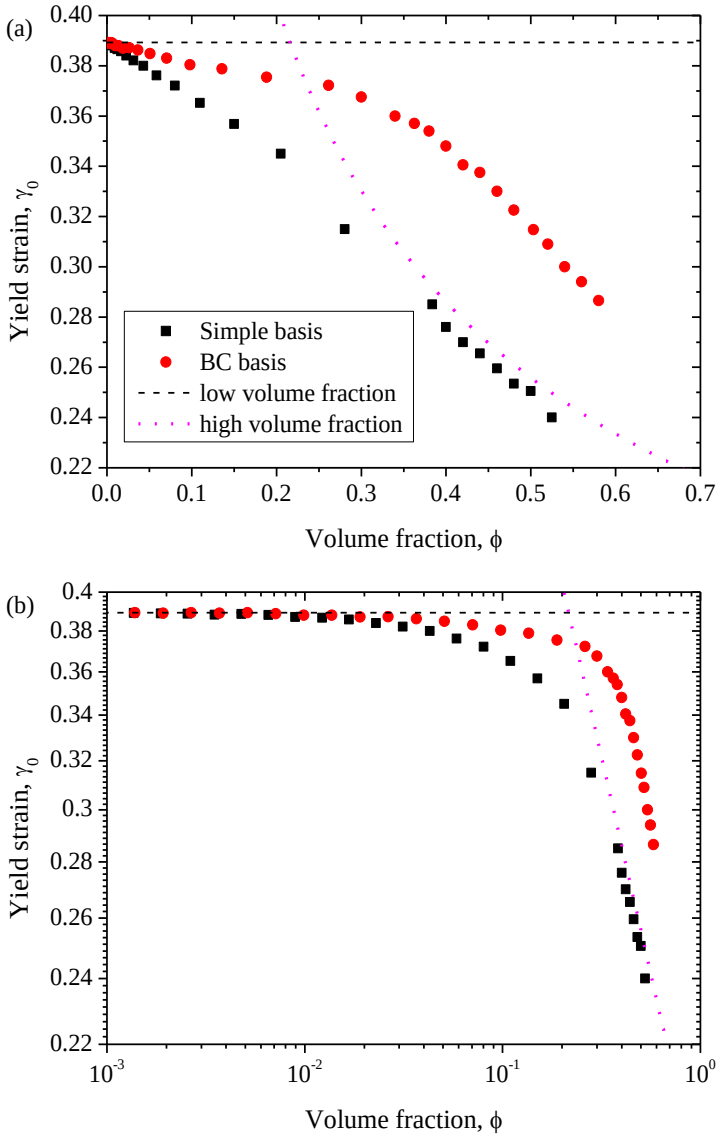

Figure 8.5: Yield strain γ_0 dependence on particle volume fraction ϕ according to simulations in simple (black squares) and BC (red circles) bases, analytic value for low concentrations (black dashed line) and approximation at high concentrations (magenta dotted line) only valid for simple basis. (a) lin-lin representation. (b) log-log representation.

Experimental shear strain data corresponding to the yield point are shown together with numerical calculations for simple and BC bases in Table 8.1. First, it is worth to note a significant error in the experimental determination. Only for the smallest particle concentrations ($\phi = 0.05$ and 0.1) there is an acceptable agreement between experiments and simulations. For larger concentrations clear deviations between experiments and numerical calculations exist that demonstrate the strong sensitivity of the yield strain to the particle microstructure [31]. We would like to remark here that deviations still exist when comparing with yield strains obtained from LAOS experiments as proposed in Ref. [9].

Volume fraction ϕ	Experimental yield strain	Simulated yield strain for a simple basis ($\pm$ 0.015)	Simulated yield strain for a BC basis ($\pm$ 0.015)
0.05	0.44 ± 0.07	0.375	0.390
0.1	0.34 ± 0.03	0.375	0.375
0.2	0.50 ± 0.06	0.345	0.375
0.3	0.020 ± 0.010	0.300	0.360
0.4	0.036 ± 0.016	0.270	0.345
0.5	0.0044 ± 0.0021	0.255	0.315

Table 8.1: Experimental and simulated yield strain γ_0 data for different volume fractions ϕ. Experimental values correspond to the data point just before sample breakage.

8.5.2 Normal stresses

In Figs. 8.6a and 8.6b we show the calculations for the normal stress σ_{zz} (in simple and BC bases, respectively) as a function of the strain γ at different particle concentrations ϕ. Together with the numerical calculations we also show FEM calculations following Ref. [32]. As expected, a very good collapse is obtained. It is worthwhile to emphasize that normal stresses as obtained by FEM come from the application of Maxwell's stress tensor in the unit cell [32] without the necessity to introduce any *continuous region* correction. This is so because in FEM simulations all the information related to the source particles is taken into account by directly solving Maxwell's equations together with periodic conditions at the unit cell boundaries.

At $\gamma = 0$, regardless of the basis, $\sigma_{zz}(\gamma = 0) > 0$ for the studied volume fractions. *A priori*, this would mean that the sample is under compression pulling the rheometer's plates. When the start-up test is initiated, the normal stress σ_{zz} decreases (in clear contrast to shear stress calculations, see Fig. 8.3) and the sample relaxes.

As observed, the normal stress σ_{zz} is strongly sensitive to the particular microstructure (compare Fig. 8.6a and Fig. 8.6b). For a simple basis the normal stress is positive and decreases with the strain before the sample breakage (see vertical arrows in Fig. 8.6a). However, for the most concentrated systems in the BC basis the normal stress reverses sign before sample breakage (see vertical arrows in Fig. 8.6b). As a result, the structure would push apart the rheometer's plates before the flow onset.

The fact that the lattice is under compression (pull together the plates of the rheometer) or dilatation (push the plates apart) along the field direction does not depend only on the normal stress σ_{zz}. Instead, it is the difference $N_1 - N_2 = \sigma_{xx} + \sigma_{yy} - 2\sigma_{zz}$ which dictates the sign of the thrust developed by the lattice. Thus, it is necessary to compute normal stresses also in the shear (σ_{yy}) and vorticity (σ_{xx}) directions. For simplicity, in the following, we restrict our discussion to the non-strained state, $\gamma = 0$. In this case, due to the symmetries of the tetragonal lattice $\sigma_{xx} = \sigma_{yy}$ and therefore $N_1 - N_2 = 2(\sigma_{yy} - \sigma_{zz})$. The computation of σ_{yy} in the non-strained state is addressed in Sec. 8.8 using the method proposed in Sec. 8.2.

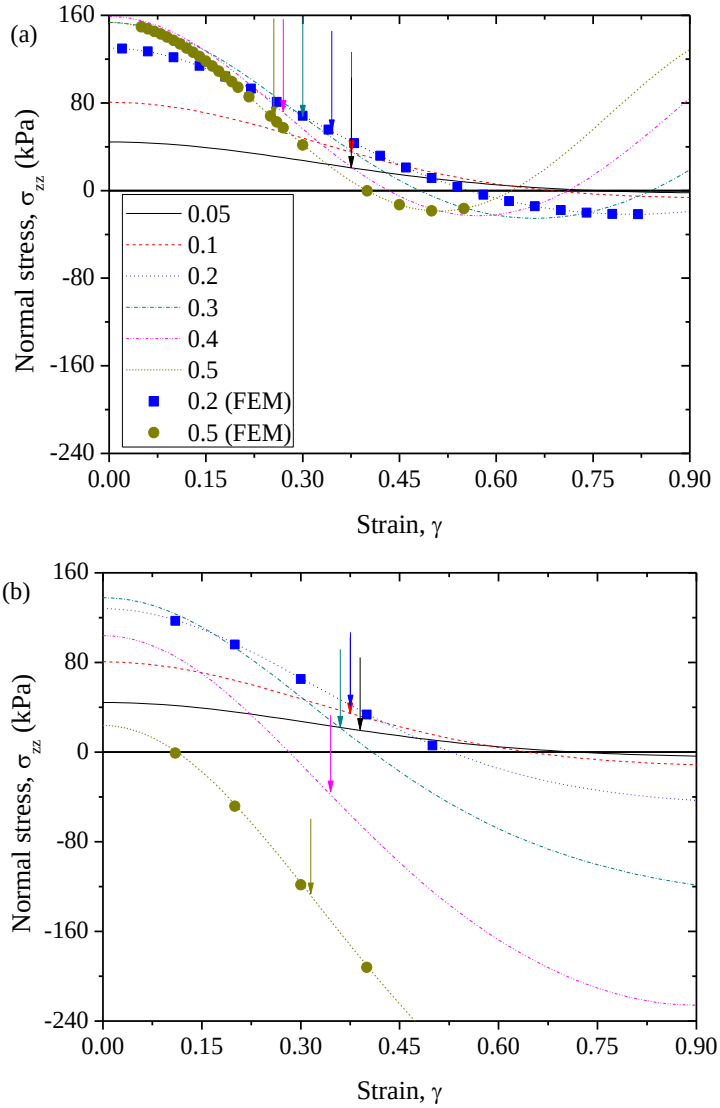

Figure 8.6: Normal stress σ_{zz} as a function of the applied shear strain γ for different volume fractions ϕ. Results from the numerical calculations are plotted with lines while the results from FEM simulations proposed in Ref. [32] are plotted with symbols. Vertical arrows correspond to the yield strain γ_0 as obtained from Fig. 8.3. (a) Simple basis. (b) BC basis.

In Fig. 8.7a we show the simulated normal stresses, $\sigma_{zz}(\gamma = 0)$ and $\sigma_{yy}(\gamma = 0)$, as a function of the particle volume fraction ϕ for simple and BC bases. Normal stresses in the field direction $\sigma_{zz}(\gamma = 0)$ for the BC basis (red solid circles) remain below those of

the simple basis (black solid squares) and the maximum shifts towards smaller concentrations. Interestingly, in the BC basis the normal stress $\sigma_{zz}(\gamma = 0)$ reverses sign for concentrations above $\phi = 0.53$.

Results for $\sigma_{yy}(\gamma = 0)$ are also plotted in Fig. 8.7a with solid green triangles (simple basis) and solid blue diamonds (BC basis). In the simple basis, independent on the volume fraction, the normal stress in the shear direction is negative, as expected taking into consideration that the dipolar interaction is repulsive when the particles are aligned normal to their dipole direction (see Sec. 8.8 for a discussion on the sign of σ_{yy}). Similar to what happened to $\sigma_{zz}(\gamma = 0)$, the BC basis shows a more complex behavior, especially at high concentrations where $\sigma_{yy}(\gamma = 0)$ becomes positive (that is, the lattice tends to stretch along the field direction).

Open squares and circles in Fig. 8.7a correspond to simulated $\sigma_{zz}(\gamma = 0)$ that do not include the *continuous region* correction (so-called 'uncorrected' values; that is, results from Eq. (8.5) for the simple basis and Eq. (8.29) for the BC basis). As it can be seen, the correction plays a crucial role for medium and high concentrations regardless of the basis. Firstly, if the correction is not included in the simple basis, differences of 20% at $\phi = 0.2$ and increasing till 117% at $\phi = 0.5$ are found. In fact, the correction is responsible for the appearance of a maximum in $\sigma_{zz}(\gamma = 0)$ (cf. black solid squares in Fig. 8.7a). Secondly, if the correction is not included for the BC basis, $\sigma_{zz}(\gamma = 0)$ would always be positive and similar to the level achieved in the simple basis. Uncorrected normal stresses in the simple basis monotonically increase with the particle concentration in contrast to BC results where the maximum is already seen.

Uncorrected values of the normal stress in the shear direction $\sigma_{yy}(\gamma = 0)$ are also shown in Fig. 8.7a (see open triangles, Eq. (8.30), and diamonds, Eq. (8.31)). Simple basis results are always negative (contributing to sample compression in the field direction). On the contrary, a change in sign is found in the BC basis near to the maximum packing.

In Fig. 8.7a we also show the analytical prediction according to the micromechanical model as a solid straight line (Eq. (8.24)) for $\sigma_{zz}(\gamma = 0)$. As expected, the analytical prediction is in very good agreement with the simulations in simple and BC bases at low concentrations. This correspondence can be seen clearer in Fig. 8.7b where log-log scales are used. The symbol code is the same than in Fig. 8.7a but now the original negative values are plotted with lighter colors. For high concentrations, the normal stress increases (in absolute value) very sharply as it goes closer to the maximum packing fraction.

In Fig. 8.7c we better appreciate the volume fraction dependence of $\sigma_{yy}(\gamma = 0)$ in the dilute regime. Again, in this figure dark (light) symbols stand for the positive (negative) values of $\sigma_{yy}(\gamma = 0)$ previously plotted in Fig. 8.7a. Clearly, for small volume fractions $\sigma_{yy}(\gamma = 0)$ is orders of magnitude smaller than $\sigma_{zz}(\gamma = 0)$. Looking at the dilute regime (approx. $\phi < 0.1$), uncorrected $\sigma_{yy}(\gamma = 0)$ values (open symbols) suggest a dependence on ϕ^2 that cancels out with the *continuous region* contribution σ_{yy}^{cont} (that exactly depends on ϕ^2 but has opposite sign, Eq. (8.35)). As it can be seen, corrected values (solid symbols) alternate between positive (dark color) and negative values (light color) pointing that $\sigma_{yy}(\gamma = 0)$ is zero and those small deviations are due to numerical errors. The fact that $\sigma_{yy}(\gamma = 0) = 0$ was expected in the dilute regime because of the absence of lateral interactions.

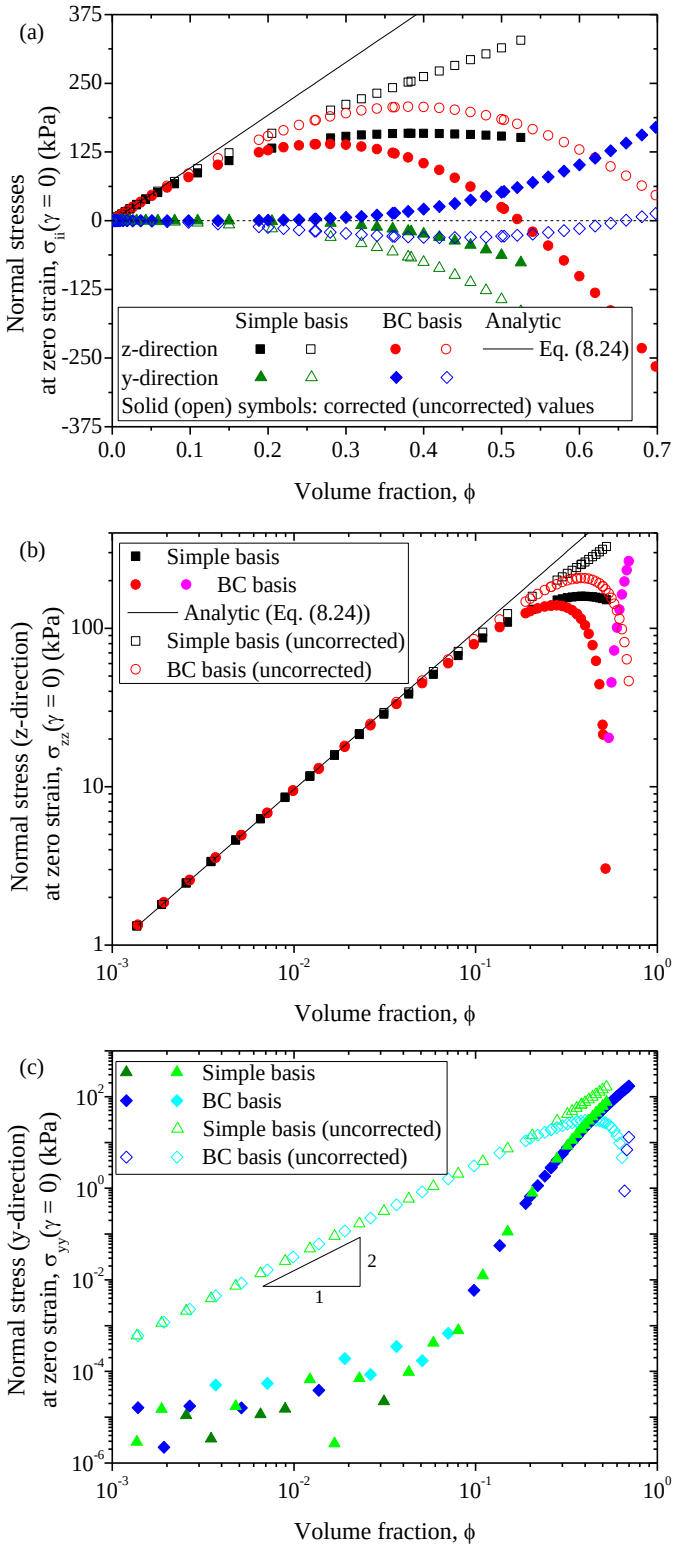

Figure 8.7: (a) Normal stresses at zero strain in the field and shear direction, $\sigma_{zz}(\gamma = 0)$ and $\sigma_{yy}(\gamma = 0)$, versus particle volume fraction ϕ according to numerical simulations in simple basis (black squares and green triangles) and BC basis (red circles and blue diamonds). Simulations without the continuous region correction are plotted with open symbols. Analytical calculation for normal stress in the field direction at low concentrations is plotted with a black line. (b) and (c) log-log representation for normal stresses at zero strain in the field and shear direction respectively (original negative values are plotted with lighter colors).

Once both normal stresses in the field (σ_{zz}) and shear (σ_{yy}) directions are known, $(N_1 - N_2)/2$ can be computed. Results are shown in Fig. 8.8 as a function of the volume fraction. In this figure, negative $N_1 - N_2$ values (i.e. $\sigma_{zz} > \sigma_{yy}$) indicate a compressed state in the field direction (i.e. the lattice would pull from the plates of the rheometer) while positive values are related to a stretched state pushing the plates apart. As expected, at small volume fractions, $(N_1 - N_2)/2$ is controlled by $\sigma_{zz}(\gamma = 0)$ being independent of the kind of basis (compare Figs. 8.7b and 8.8b). Consequently, the analytical prediction derived in Eq. (8.24) is a good estimator of the stress state. As the volume fraction increases, the simple basis keeps in the compressed state while the BC basis dilates for volume fractions above 0.47.

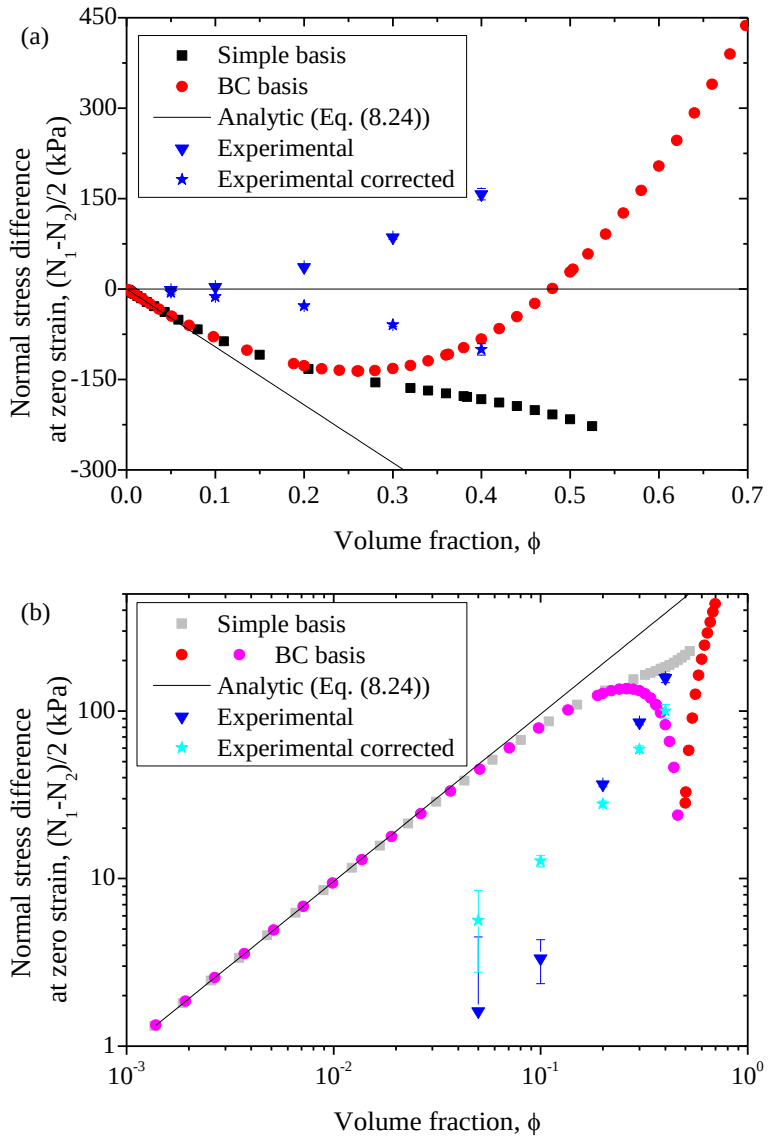

Figure 8.8: Normal stress difference at zero strain $(N_1 - N_2)/2$ versus particle volume fraction ϕ according to numerical simulations in simple (squares) and BC (circles) bases. Also plotted with a line is the analytical approximation for low concentrations (Eq. (8.24)). The maximum normal stress difference measured while straining the sample in start-up tests is plotted with triangles and the related value, once corrected using the Maxwell stress jump $[\sigma_M]$, with stars. (a) lin-lin representation. (b) log-log representation (negative values are plotted with lighter colors).

The experimental normal stress difference $(N_1 - N_2)/2$ is also plotted in Fig. 8.8 (maximum value during start-up test) with triangles. For all explored concentrations, a positive thrust is measured. This experimental observation is in striking contrast with the simulation results that predict a negative normal stress difference (i.e. $N_1 - N_2 < 0$) at low volume fractions. It is also important to note that in contrast to the calculated shear stresses, the normal stresses are very sensitive to the particular microstructure showing opposite tendencies depending on the basis and concentration.

The model proposed in this manuscript supposes infinite (unbounded) lattices. This approximation seems reasonable taking into consideration the great difference between particles-sample typical length scales (1 μm-1 mm). However the current model neglects boundary effects such as demagnetization charges or discontinuities in the Maxwell stress tensor at the interfaces. The latter has shown to be a non-negligible positive contribution to the thrust: $[\sigma_M] = \mu_0 \phi^2 M_s^2/2$ [33]. If we subtract $[\sigma_M]$ from the experimental $(N_1 - N_2)/2$ data we get the stars shown in Fig. 8.8. At this point, it must be said that the previous definition for $[\sigma_M]$ is valid in the case of samples placed between non-magnetic plates while those used in the current experiments were ferromagnetic. Interestingly, thrust measurements were repeated using a titanium geometry giving no significant differences with respect to the ferromagnetic tools.

As observed in Fig. 8.8, corrected experimental data have the same sign as the simulations. However, experimental values are clearly smaller (in absolute value) than the simulations and only at the highest concentrations lie between the simple and the BC bases. The explanation for this could be that the microstructure evolves during the start-up test forming highly packed aggregates that better resemble a lattice with a BC basis. At this point it is worth to note that the literature on this topic is not conclusive at all. A vast majority of experimental publications dealing with MR fluids [2,34-36] and anisotropic (i.e. field oriented) MR elastomers [37-39] report a positive normal stress difference. However, other publications found the opposite trend in similar MR elastomers [40,41]. From a theoretical point of view, a positive normal stress in the field direction σ_{zz}, implying negative thrusts, appears when the field-induced structures are aligned with the field (see for instance Refs. [21,31,42] for isolated chains and [43] for particle lattices). In contrast, a positive normal thrust is reported when the structure contains defects (e.g. introducing wavy chains [44], no-percolating elongated aggregates [38,45], or shape effects due to demagnetization fields in Ref. [12]).

8.6 Conclusions

We investigate the influence of the particle concentration on field-induced shear and normal stresses of magnetorheological (MR) fluids at rest and under standard shearing flows in the magnetic saturation regime. Both shear and normal stresses are well described by analytical expressions in the dilute regime. However, for larger particle concentrations (above 10 vol% in the case of carbonyl iron) a numerical approach is needed. Two tetragonal and monoclinic lattice arrangements are investigated in this manuscript: simple and BC bases. Numerical calculations are found to be in good agreement with Finite Element Calculations described in Ref. [24].

Shear stress versus shear strain curves exhibit a well-defined maximum that is associated to the yield stress (τ_0). More importantly, a maximum is found when the yield stress is represented as a function of the particle concentration. Numerical calculations slightly overestimate the experimental results due to defects in the experimental field-induced

structures that may be far from energy minimum configurations. Some work is currently being done in this direction.

Finally, calculated normal stress differences ($N_1 - N_2$) at zero strain (in a tetragonal lattice) are always negative in simple basis but show a sign reversal in the BC basis at large concentrations. Similar to shear stresses, simulated normal stress differences overestimate experimental results again.

Acknowledgements

This work was supported by MINECO MAT 2016-78778-R and PCIN-2015-051 projects (Spain) and European Regional Development Fund (ERDF). J. R. Morillas acknowledges FPU14/01576 fellowship.

8.7 Appendix A: force calculations for a body centered BC basis

The analysis described in Sec. 8.2 assumes that there is only one magnetic particle linked to each node (l, m, n) of the lattice. Consequently, resulting arrangements are the tetragonal ($\gamma = 0$) or monoclinic ($\gamma \neq 0$) lattices with the simple basis. However, it is possible to adapt these simulations to cover other bases as well. In particular, in this appendix we show the results for the body centered (BC) basis. The BC basis has shown to be a more favorable configuration, from an energetic point of view, than the simple basis [25,46].

The BC basis consists of two particles, one particle (A) placed at the lattice nodes and another particle (B) displaced from the nodes a quantity $\vec{\alpha} = [w_{bc}\hat{x} + (w_{bc} + h\gamma)\hat{y} + h\hat{z}]/2$. Here, $w_{bc}/2$ is the lateral distance between chains based on A and B particles, w_{bc} is the lateral distance between chains of the same kind of particles and $h = d$ is the vertical distance between particles along the chain (regardless of its kind). As it happens in the simple basis, since the lattice is isotropic in the x and y directions, w_{bc} can be obtained from the particle volume fraction as $w_{bc} = h\sqrt{\pi/3\phi}$. Taking this into consideration, the particle position in the lattice can still be written in terms of the lattice vectors (Eq. (8.1)) as follows:

$$\vec{r}_{A,-} = l_-\vec{a}_1 + m_-\vec{a}_2 + n_-\vec{a}_3 \tag{8.26a}$$

$$\vec{r}_{B,-} = \vec{r}_{A,-} + \vec{\alpha} \tag{8.26b}$$

Here, the hyphen – denotes that each particle A or B can act as a field or source particle. As a consequence, up to three kinds of vectors, joining source and field particles, must be considered:

$$\vec{R}_{AA} = \vec{R}_{BB} = \vec{r}_{A,f} - \vec{r}_{A,s} = \vec{r}_{B,f} - \vec{r}_{B,s} = \vec{R} \tag{8.27a}$$

$$\vec{R}_{AB} = \vec{r}_{B,f} - \vec{r}_{A,s} = \vec{R} + \vec{\alpha} \tag{8.27b}$$

$$\vec{R}_{BA} = \vec{r}_{A,f} - \vec{r}_{B,s} = \vec{R} - \vec{\alpha} \tag{8.27c}$$

where $\vec{R}$ given by Eq. (8.3). Once we know the particle position, it is possible to compute both shear and normal stresses following the same reasoning described in Sec. 8.2, but

bearing in mind that for each allowed combination of n_f, l_s, m_s and n_s there will be two field particles (one of kind A and another of kind B) and two source particles (again of kinds A and B). Thereby, the shear force in the BC basis is computed as follows:

$$F_{zy} = \frac{3\mu_0 m^2}{4\pi} \sum_{\substack{n_f \leq 0 \\ l_f = m_f = 0 \; \forall \; l_s, m_s}} \sum_{n_s > 0} \left[2\frac{R_y}{R^5}\left(5\frac{R_x^2 + R_y^2}{R^2} - 4\right) + \frac{R_{AB,y}}{R_{AB}^5}\left(5\frac{R_{AB,x}^2 + R_{AB,y}^2}{R_{AB}^2} - 4\right) + \frac{R_{BA,y}}{R_{BA}^5}\left(5\frac{R_{BA,x}^2 + R_{BA,y}^2}{R_{BA}^2} - 4\right)\right] \tag{8.28}$$

The first term in the square brackets stands for the interaction between AA and BB particles (note the prefactor 2) while the second and third terms correspond to AB and BA interactions, respectively. Similar to the analysis for the simple basis, in the previous summation only source particles within the cutoff distance r_{cut} are accounted for. In the same way, the discrete contribution to the normal force is given by:

$$F_{zz} = \frac{3\mu_0 m^2}{4\pi} \sum_{\substack{n_f \leq 0 \\ l_f = m_f = 0 \; \forall \; l_s, m_s}} \sum_{n_s > 0} \left[2\frac{R_z}{R^5}\left(5\frac{R_x^2 + R_y^2}{R^2} - 2\right) + \frac{R_{AB,z}}{R_{AB}^5}\left(5\frac{R_{AB,x}^2 + R_{AB,y}^2}{R_{AB}^2} - 2\right) + \frac{R_{BA,z}}{R_{BA}^5}\left(5\frac{R_{BA,x}^2 + R_{BA,y}^2}{R_{BA}^2} - 2\right)\right] \tag{8.29}$$

The contribution to the normal stress from the *continuous region* remains unchanged because any information on the internal microstructure is lost. Note also that when the force is computed over all field particles, in the case of the BC basis, this force should be twice the force than the simple basis case because there are two particles per node n_f. However, the area per chain in the BC basis is also twice the area per chain in the simple case $w_{bc}^2 = 2w^2$ and therefore the normal stress correction does not change.

Using the analogous expressions for the shear and normal stresses, the analysis described in the body text for the simple basis can now repeated for the BC basis.

8.8 Appendix B: computation of the normal stress in the shear direction at zero strain

Internal stresses do not only depend on the force direction, but also on the plane over which they are applied. In Sec. 8.2 this plane was chosen to be normal to the field direction $\hat{z}$, and thus, only the shear τ_{zy} and normal σ_{zz} stresses were computed.

In this appendix we sketch the main steps to compute the normal stress in the shear direction σ_{yy}. The reason for this is that σ_{yy} is necessary in the evaluation of the thrust developed by the lattice (see Eq. (8.25)). The discussion here will focus only in the non-strained state and consequently, due to the symmetries of the tetragonal lattice, the results will be equally valid for the vorticity direction σ_{xx}.

The computation of the total force in the shear direction is done following the same reasoning described in Sec. 8.2.1 but bearing in mind that this force is going to be applied over a plane with normal vector $\hat{y}$. If this imaginary plane is supposed to go through the origin of coordinates, it will split the lattice in two halves, one on the left based on particles with $y \leq 0$ and another on the right based on particles with $y > 0$.

The choice of field and source particles is arbitrary. However, to be consistent with Sec. 8.2, field particles will be in the left half ($m_f \leq 0$ according to Eq. (8.3)) while source particles will be on the right half ($m_s > 0$ in Eq. (8.3)) as it is sketched in Fig. 8.9a. Taking this into consideration, the total force in the shear direction is given by the analogous expression to Eq. (8.4) for a simple basis:

$$F_{yy} = \sum_{\substack{m_f \leq 0 \\ l_f = n_f = 0}} \sum_{\substack{m_s > 0 \\ \forall\, l_s, n_s}} \vec{F}_{fs} \cdot \hat{y} = \sum_{\substack{m_f \leq 0 \\ n_f = m_f = 0}} \sum_{\substack{m_s > 0 \\ \forall\, l_s, n_s}} \frac{3\mu_0 m^2}{4\pi} \frac{R_y}{R^5} \left(5 \frac{R_x^2 + R_y^2}{R^2} - 4 \right) \tag{8.30}$$

In the case of a BC basis, starting from Eq. (8.28), we arrive to:

$$F_{yy} = \frac{3\mu_0 m^2}{4\pi} \sum_{\substack{m_f \leq 0 \\ l_f = n_f = 0}} \sum_{\substack{m_s > 0 \\ \forall\, l_s, n_s}} \left[2 \frac{R_y}{R^5} \left(5 \frac{R_x^2 + R_y^2}{R^2} - 4 \right) + \frac{R_{AB,y}}{R_{AB}^5} \left(5 \frac{R_{AB,x}^2 + R_{AB,y}^2}{R_{AB}^2} - 4 \right) + \frac{R_{BA,y}}{R_{BA}^5} \left(5 \frac{R_{BA,x}^2 + R_{BA,y}^2}{R_{BA}^2} - 4 \right) \right] \tag{8.31}$$

In both bases, the summation over source indexes should be run only over source particles inside the cutoff sphere. Finally, it is also necessary to remind that the unit area per particle in the shear direction is hw (hw_{bc} for BC case) instead of w^2 (w_{bc}^2 for the BC case).

Taking into consideration that the field region is the left half of the lattice ($m_f \leq 0$), a positive value of the force implies a stretched state where both halves of the lattice tend to join together.

Similar to what happens to σ_{zz}, Eqs. (8.30) and (8.31) need to be corrected by the continuous region contribution. This region is still uniformly magnetized, $\vec{M}_{cont} = \phi M_s \hat{z}$, and therefore its action over field particles will depend on the magnetic charge surface density ρ_s distributed over its boundary surface. This surface is sketched in Fig. 8.9b and can be decomposed in the same way as in the σ_{zz} case: flat plane with hole of radius ρ_0 plus a spherical cap surface of radius r_{cut} and maximum polar angle θ_f.

However, now the flat plane is not charged because the magnetization is parallel to the boundary surface: $\rho_s = -\vec{M}_{cont} \cdot \hat{y} = 0$. Consequently, source density positions will be given only by the cap surface $\vec{r}' = r_{cut}(\sin\theta' \cos\varphi'\, \hat{x} + \cos\theta'\, \hat{y} - \sin\theta' \sin\varphi'\, \hat{z})$. With this notation, the normal vector to the cap surface is $\hat{n} = -\vec{r}'/r_{cut}$ and the surface density is $\rho_s = \vec{M}_{cont} \cdot \hat{n} = \phi M_s \sin\theta' \sin\varphi'$.

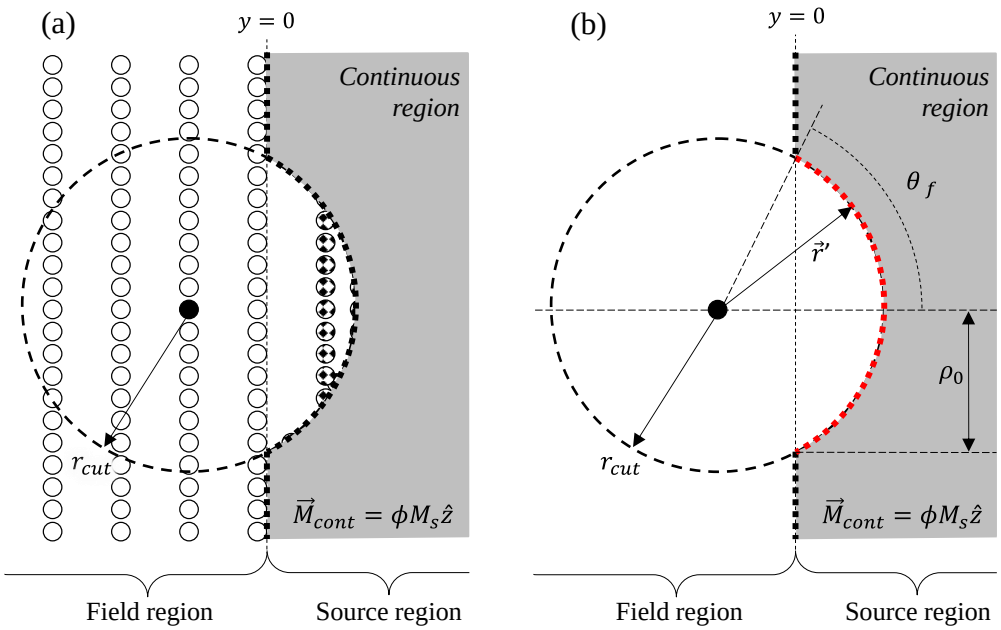

Figure 8.9: (a) Source and field regions used to compute the normal stress in the shear direction. A field particle (black circle) will feel the force due to all source particles inside the cutoff sphere (dotted circles) plus a contribution from the *continuous region* (grey region). (b) The *continuous region* contribution is due to only the cap surface (dotted red line).

Note that ρ_s depends on φ' and thus it is not axisymmetric. Due to this fact, the use of Eq. (8.6) to derive σ_{yy}^{cont} can lead to a complex computation. As it was noted in Sec. 8.2.2, in these cases, it is easier to compute the force exerted by each field dipole over the source density and eventually change the sign of the resultant force by means of Newton's third law. As the surface density is based on punctual charges, the force over a differential element of the surface will be given by $\vec{F}_d = \rho_s \vec{B}_d$ where the sub index d means that the force is due to a dipole (not due to the *continuous region*) and $\vec{B}_d$ is the field created the field dipole:

$$\vec{B}_d = \frac{\mu_0 m}{4\pi} \frac{3r_z'\vec{r}' - |\vec{r}'|^2 \hat{z}}{|\vec{r}'|^5} \tag{8.32}$$

Integrating over the whole surface of the cap, the total force exerted over the continuous region by a field dipole is obtained as follows:

$$\begin{aligned}
\vec{F}_d &= \int \rho_s \vec{B}_d ds \\
&= \frac{\mu_0 m \phi M_s}{4\pi} \int_0^{\theta_f} \int_0^{2\pi} \sin\theta' \sin\varphi' \frac{3r_z'\vec{r}' - |\vec{r}'|^2 \hat{z}}{|\vec{r}'|^5} r_{cut}^2 \sin\theta' \, d\theta' d\varphi' \\
&= -\frac{3\mu_0 m \phi M_s}{4 r_{cut}} \hat{y} \int_0^{\theta_f} \sin^3\theta' \cos\theta' \, d\theta' = -\frac{3\mu_0 m \phi M_s}{4 r_{cut}} \frac{\sin^4\theta_f}{4} \hat{y}
\end{aligned} \tag{8.33}$$

As it can be seen, Eq. (8.33) gives the force exerted by a field dipole from which the spherical cap has a maximum polar angle of θ_f. This amplitude will depend on the field dipole position. From Fig. 8.9b, and using trigonometric relationships it can be proved

that $\sin\theta_f = \left(1 - y^2/r_{cut}^2\right)^{1/2}$ where y is the distance between the field dipole and the source region. Changing the sign of $\vec{F}_d$ (to compute the force exerted by the continuous region over the field dipole), substituting the magnitude of the dipole m and dividing by the unit area hw one gets the correction to the normal stress for one field particle located at y:

$$\sigma_{yy}^{cont} = \frac{3\mu_0\phi^2 M_s^2}{16}\frac{w}{r_{cut}}\left(1 - \left(\frac{y}{r_{cut}}\right)^2\right)^2 \tag{8.34}$$

In the simple tetragonal lattice, field particles are placed at $y = m_f w$ (following the same reasoning shown in Sec. 8.7, results are also valid for BC basis), thus adding the correction for all field particles and taking the continuum limit $n = r_{cut}/w \to \infty$ we get:

$$\begin{aligned}\sigma_{yy}^{cont} &= \frac{3\mu_0\phi^2 M_s^2}{16}\lim_{n\to\infty}\frac{1}{n}\sum_{m_f=-n}^{0}\left(1 - 2\left(\frac{m_f}{n}\right)^2 + \left(\frac{m_f}{n}\right)^4\right) \\ &= \frac{3\mu_0\phi^2 M_s^2}{16}\int_0^1 (1 - 2x^2 + x^4)dx = \frac{\mu_0\phi^2 M_s^2}{10}\end{aligned} \tag{8.35}$$

8.9 Appendix C: energetic approach to determine the shear stress versus strain curve

In this section, we derive the analytical expressions for the force/shear stress versus strain curve (Eq. (8.21)) and yield stress versus volume fraction curve (Eq. (8.22)) for an isolated chain using an energetic approach.

We start from the magnetic interaction energy between two dipoles i and j separated a distance R in a chain tilted an angle θ [20,47]:

$$U = \frac{\mu_0 m^2}{4\pi R^3}(1 - 3\cos^2\theta) \tag{8.36}$$

Taking into consideration Eq. (8.18), Eq. (8.36) can be written as a function of the shear strain γ as follows:

$$\begin{aligned}U &= \frac{\mu_0 m^2}{4\pi h^3 |i-j|^3}\frac{1}{(1+\gamma^2)^{3/2}}\left(1 - \frac{3}{1+\gamma^2}\right) \\ &= \frac{\mu_0 m^2}{4\pi h^3 |i-j|^3}\frac{\gamma^2 - 2}{(1+\gamma^2)^{5/2}}\end{aligned} \tag{8.37}$$

Therefore, the total magnetic energy of the system is the summation over all the pairs of particles in the chain:

$$\begin{aligned}U_{tot} &= \sum_i \sum_{j>i} \frac{\mu_0 m^2}{4\pi h^3 |i-j|^3}\frac{\gamma^2 - 2}{(1+\gamma^2)^{5/2}} \\ &= \frac{\mu_0 m^2}{4\pi h}\frac{\gamma^2 - 2}{(1+\gamma^2)^{5/2}}\sum_i \sum_{j>i}\frac{1}{|i-j|^3}\end{aligned} \tag{8.38}$$

It is important to note that the indexes in the summations contained in Eq. (8.38) run differently than in Eq. (8.19). In Eq. (8.19) we computed the force due to the upper half of the chain on the lower half of the chain. In that case, field particles are those with $n_f \leq 0$ while source particles are those with $n_s > 0$. On the other hand, in Eq. (8.38) we are computing the total energy of the chain and accordingly, it is not necessary to distinguish between field or source dipoles: all particles belonging to the chain are sources independently of their position. Thus, i runs along the whole chain (positive and negative i values). For a given i value, j must be larger than i to avoid counting twice the same pair of particles.

In Eq. (8.38), the inner summation corresponds to $i < j < \infty$ or equivalently (by subtracting i) $0 < j - i < \infty$, hence the inner summation is simply:

$$\sum_{j>i} \frac{1}{|i-j|^3} = \sum_{j-i>0} \frac{1}{|i-j|^3} = \sum_{j-i>0} \frac{1}{|j-i|^3} = \xi(3) \tag{8.39}$$

Obviously, if we carry out the summation within U_{tot} over all the particles we obtain an infinite energy because there is an infinite number of particles in the system. Thus, it is more convenient to use the energy density u_{tot} as follows:

$$\begin{aligned} u_{tot} = \frac{U_{tot}}{L_{tot} w^2} &= \frac{\mu_0 m^2}{4\pi h^3} \frac{\gamma^2 - 2}{(1+\gamma^2)^{5/2}} \frac{\sum_i \xi(3)}{w^2 \sum_i h} \\ &= \frac{\mu_0 m^2 \xi(3)}{4\pi h^4 w^2} \frac{\gamma^2 - 2}{(1+\gamma^2)^{5/2}} \end{aligned} \tag{8.40}$$

In Eq. (8.40) we have considered that the surface area associated to a chain is given by w^2 and its total length is $L_{tot} = \sum_i h$.

From classical electromagnetism, the resulting stress upon shearing the chain is given by:

$$\tau = \frac{\partial u_{tot}}{\partial \gamma} = \frac{\mu_0 m^2 \xi(3)}{4\pi h^4 w^2} \frac{3\gamma(4-\gamma^2)}{(1+\gamma^2)^{7/2}} = \frac{3\mu_0 m^2 \xi(3)}{4\pi h^4 w^2} f(\gamma) \tag{8.41}$$

where $f(\gamma)$ is the same function previously found with the force calculation provided in Sec. 8.3.1 (see Eq. (8.21)). Consistently, using this energetic approach we obtain the same value for the yield stress only by evaluating $f(\gamma)$ at its maximum and substituting $m = M_s \pi d^3/6$, $h = d$ and $hw^2 = \pi d^3/6\phi$ in Eq. (8.41):

$$\tau_0 = \frac{\xi(3) f(\gamma_0)}{8} \mu_0 M_s^2 \phi \sim 0.137 \mu_0 M_s^2 \phi \tag{8.42}$$

Note that this energetic approach was also followed in Ref. [20] although the final result differs by the numerical factor in Eq. (8.42). This discrepancy comes from the axisymmetric model used in that work. According to this, shearing a chain is approximated by its elongation for a constant volume fraction. Therefore, the vector joining two dipoles, i and j, within the elongated chain $\left(\vec{R}_{el}\right)$ and the area per chain $\left(w_{el}^2\right)$ are given by [20]:

$$\vec{R}_{el} = -R_{el}\hat{z} \tag{8.43a}$$

$$R_{el} = |i-j| d \sqrt{\gamma^2 + 1} \tag{8.43b}$$

$$w_{el}^2 = \frac{\pi d^2}{6\phi\sqrt{1+\gamma^2}} \tag{8.44}$$

Note that in this axisymmetric approximation, $\vec{R}_{el}$ is always directed along the chain (compare to the true shear strain in Eq. (8.18)) and both vertical separation between two consecutive particles $h_{el} = d\sqrt{\gamma^2+1}$ and w_{el}^2 depend on the strain, while in a true shear strain deformation these quantities are constant ($h = d,\ w^2 = h^2\pi/6\phi$) in coherence with an affine deformation. In addition, since the chain axis is collinear with the dipoles of the particles during the whole strain, the interaction energy between any two dipoles within the chain is obtained from Eq. (8.36) making $\theta = 0$:

$$U_{el} = -\frac{\mu_0 m^2}{2\pi R_{el}^3} \tag{8.45}$$

Summing over all pairs of dipoles in the chain and dividing by its total volume as it was done previously for a true shear strain deformation, it can be shown that the magnetic energy density for the whole chain is:

$$u_{el,tot} = \frac{U_{el,tot}}{L_{el,tot} w_{el}^2} = -\frac{\mu_0 m^2 \xi(3)}{2\pi h_{el}^4 w_{el}^2} \tag{8.46}$$

and the corresponding shear stress:

$$\tau_{el} = \frac{\partial u_{el,tot}}{\partial\gamma} = -\frac{\mu_0 m^2 \xi(3)}{2\pi}\frac{\partial}{\partial\gamma}\left(\frac{1}{h_{el}^4 w_{el}^2}\right) = \frac{9\mu_0 m^2 \xi(3)\phi}{\pi^2 d^6} g(\gamma) \tag{8.47}$$

where $g(\gamma) = \gamma/(1+\gamma^2)^{5/2}$. The maximum of this function corresponds to $\gamma_{el,0} = 0.5$. Substituting $\gamma_{el,0}$ and $m = M_s\,\pi d^3/6$ in Eq. (8.47) one arrives to Eq. (9) of Ref. [20]:

$$\tau_{el,0} = \frac{4}{5^{5/2}}\xi(3)\phi\mu_0 M_s^2 \sim 0.086\phi\mu_0 M_s^2 \tag{8.48}$$

Comparing Eqs. (8.42) and (8.48), it can be seen how neglecting particle dipole rotation during the shear straining motion can underestimate the yield stress in nearly 40%. This issue was previously pointed out by [48] for the case of the shear modulus where the difference reached 50%.

References

[1] Genç, S., and Phulé, P. P. (2002). Rheological properties of magnetorheological fluids. Smart Materials and Structures, 11(1), 140.

[2] Laun, H. M., Gabriel, C., and Schmidt, G. (2008). Primary and secondary normal stress differences of a magnetorheological fluid (MRF) up to magnetic flux densities of 1 T. Journal of Non-Newtonian Fluid Mechanics, 148(1-3), 47-56.

[3] Burguera, E. F., Love, B. J., Sahul, R., Ngatu, G., and Wereley, N. M. (2008). A physical basis for stability in bimodal dispersions including micrometer-sized particles and nanoparticles using both linear and non-linear models to describe yield. Journal of Intelligent Material Systems and Structures, 19(11), 1361-1367.

[4] Bossis, G., Grasselli, Y., and Ciffreo, A. (2019). The role of volume fraction and additives on the rheology of suspensions of micron sized iron particles. Frontiers in Materials, 6, 4.

[5] Keaveny, E. E., and Maxey, M. R. (2008). Modeling the magnetic interactions between paramagnetic beads in magnetorheological fluids. Journal of Computational Physics, 227(22), 9554-9571.

[6] Han, K., Feng, Y. T., and Owen, D. R. J. (2010). Three-dimensional modelling and simulation of magnetorheological fluids. International Journal for Numerical Methods in Engineering, 84(11), 1273-1302.

[7] Morillas, J. R., Yang, J., and de Vicente, J. (2018). Double-gap plate–plate magnetorheology. Journal of Rheology, 62(6), 1485-1494.

[8] Volkova, O., Bossis, G., Guyot, M., Bashtovoi, V., and Reks, A. (2000). Magnetorheology of magnetic holes compared to magnetic particles. Journal of Rheology, 44(1), 91-104.

[9] Segovia-Gutiérrez, J. P., Berli, C. L. A., and de Vicente, J. (2012). Nonlinear viscoelasticity and two-step yielding in magnetorheology: A colloidal gel approach to understand the effect of particle concentration. Journal of Rheology, 56(6), 1429-1448.

[10] Ginder, J. M. (1998). Behavior of magnetorheological fluids. MRS Bulletin, 23(8), 26-29.

[11] Zhu, Y. S., Gong, X. L., Dang, H., Zhang, X. Z., and Zhang, P. Q. (2013). Numerical analysis on magnetic-induced shear modulus of magnetorheological elastomers based on multi-chain model. Chinese Journal of Chemical Physics, 19(2), 126.

[12] Ivaneyko, D., Toshchevikov, V., Saphiannikova, M., and Heinrich, G. (2014). Mechanical properties of magneto-sensitive elastomers: unification of the continuum-mechanics and microscopic theoretical approaches. Soft Matter, 10(13), 2213-2225.

[13] Lorentz, H. A. The theory of electrons and its applications to the phenomena of light and radiant heat (G.E. Stechert & co., New York, 1916).

[14] Reitz, J. R., and Milford, F. J. Foundations of Electro Magnetic Theory (Addison-Wesley, Reading, 1960).

[15] Panofsky, W. K. H, and Phillips, M. Classical Electricity and Magnetism (Addison-Wesley, Reading, 1962).

[16] Wangsness, R. K. Electromagnetic fields (John Wiley & Sons, New York, 1979).

[17] Martin, J. E., and Anderson, R. A. (1996). Chain model of electrorheology. The Journal of Chemical Physics, 104(12), 4814-4827.

[18] de Gans, B. J. (1999). Non-linear magnetorheological behaviour of an inverse ferrofluid. Faraday Discussions, 112, 209-224.

[19] de Vicente, J., López-López, M. T., Durán, J. D., and González-Caballero, F. (2004). Shear flow behavior of confined magnetorheological fluids at low magnetic field strengths. Rheologica Acta, 44(1), 94-103.

[20] Ginder, J. M., Davis, L. C., and Elie, L. D. (1996). Rheology of magnetorheological fluids: Models and measurements. International Journal of Modern Physics B, 10(23n24), 3293-3303.

[21] Shkel, Y. M., and Klingenberg, D. J. (1999). A continuum approach to electrorheology. Journal of Rheology, 43(5), 1307-1322.

[22] Bombard, A. J., Joekes, I., Alcantara, M. R., and Knobel, M. (2003). Magnetic susceptibility and saturation magnetization of some carbonyl iron powders used in magnetorheological fluids. Materials Science Forum, 416-418, 753-758.

[23] Vereda, F., de Vicente, J., Segovia-Gutiérrez, J. P., and Hidalgo-Álvarez, R. (2011). On the effect of particle porosity and roughness in magnetorheology. Journal of Applied Physics, 110(6), 063520.

[24] Morillas, J. R., and de Vicente, J. (2019). On the yield stress in magnetorheological fluids: a direct comparison between 3D simulations and experiments. Composites Part B: Engineering, 160, 626-631.

[25] Morillas, J. R., and de Vicente, J. (2019). Yielding behavior of model magnetorheological fluids. Soft Matter, 15(16), 3330-3342.

[26] Chin, B. D., Park, J. H., Kwon, M. H., and Park, O. O. (2001). Rheological properties and dispersion stability of magnetorheological (MR) suspensions. Rheologica Acta, 40(3), 211-219.

[27] de Vicente, J., Klingenberg, D. J., and Hidalgo-Álvarez, R. (2011). Magnetorheological fluids: a review. Soft Matter, 7(8), 3701-3710.

[28] Wereley, N. (Ed.). Magnetorheology: advances and applications (Vol. 6) (Royal Society of Chemistry, Cambridge, 2013).

[29] Bossis, G., Lemaire, E., Volkova, O., and Clercx, H. (1997). Yield stress in magnetorheological and electrorheological fluids: A comparison between microscopic and macroscopic structural models. Journal of Rheology, 41(3), 687-704.

[30] Furst, E. M., and Gast, A. P. (2000). Micromechanics of magnetorheological suspensions. Physical Review E, 61(6), 6732.

[31] Jolly, M. R., Carlson, J. D., Muñoz, B. C., and Bullions, T. A. (1996). The magnetoviscoelastic response of elastomer composites consisting of ferrous particles embedded in a polymer matrix. Journal of Intelligent Material Systems and Structures, 7(6), 613-622.

[32] Morillas, J. R., and de Vicente, J. (2019). On the importance of interchain interaction and rotational contribution to the computation of the yield stress in magnetorheology. Smart Materials and Structures, 28(8), 08LT01.

[33] López-López, M. T., Kuzhir, P., Durán, J. D., and Bossis, G. (2010). Normal stresses in a shear flow of magnetorheological suspensions: viscoelastic versus Maxwell stresses. Journal of Rheology, 54(5), 1119-1136.

[34] de Vicente, J., González-Caballero, F., Bossis, G., and Volkova, O. (2002). Normal force study in concentrated carbonyl iron magnetorheological suspensions. Journal of Rheology, 46(5), 1295-1303.

[35] See, H., and Tanner, R. (2003). Shear rate dependence of the normal force of a magnetorheological suspension. Rheologica Acta, 42(1-2), 166-170.

[36] Pang, H., Pei, L., Sun, C., and Gong, X. (2018). Normal stress in magnetorheological polymer gel under large amplitude oscillatory shear. Journal of Rheology, 62(6), 1409-1418.

[37] Ginder, J. M., Clark, S. M., Schlotter, W. F., and Nichols, M. E. (2002). Magnetostrictive phenomena in magnetorheological elastomers. International Journal of Modern Physics B, 16(17n18), 2412-2418.

[38] Guan, X., Dong, X., and Ou, J. (2008). Magnetostrictive effect of magnetorheological elastomer. Journal of Magnetism and Magnetic Materials, 320(3-4), 158-163.

[39] Danas, K., Kankanala, S. V., and Triantafyllidis, N. (2012). Experiments and modeling of iron-particle-filled magnetorheological elastomers. Journal of the Mechanics and Physics of Solids, 60(1), 120-138.

[40] Zhou, G. Y., and Jiang, Z. Y. (2004). Deformation in magnetorheological elastomer and elastomer–ferromagnet composite driven by a magnetic field. Smart Materials and Structures, 13(2), 309.

[41] Coquelle, E., and Bossis, G. (2005). Magnetostriction and piezoresistivity in elastomers filled with magnetic particles. Journal of Advanced Science, 17(1+ 2), 132-138.

[42] Ginder, J. M., and Davis, L. C. (1994). Shear stresses in magnetorheological fluids: role of magnetic saturation. Applied Physics Letters, 65(26), 3410-3412.

[43] Ivaneyko, D., Toshchevikov, V. P., Saphiannikova, M., and Heinrich, G. (2011). Magneto-sensitive Elastomers in a Homogeneous Magnetic Field: A Regular Rectangular Lattice Model. Macromolecular Theory and Simulations, 20(6), 411-424.

[44] Han, Y., Hong, W., and Faidley, L. E. (2013). Field-stiffening effect of magneto-rheological elastomers. International Journal of Solids and Structures, 50(14-15), 2281-2288.

[45] Stolbov, O. V., Raikher, Y. L., and Balasoiu, M. (2011). Modelling of magnetodipolar striction in soft magnetic elastomers. Soft Matter, 7(18), 8484-8487.

[46] Tao, R., and Sun, J. M. (1991). Three-dimensional structure of induced electrorheological solid. Physical Review Letters, 67(3), 398.

[47] de Vicente, J. (2013). Magnetorheology: A review. The Ibero-American Journal of Rheology, 1, 1-18.

[48] Davis, L. C. (1992). Polarization forces and conductivity effects in electrorheological fluids. Journal of Applied physics, 72(4), 1334-1340.

Chapter 9. Double-gap Plate-plate Magnetorheology

Jose R. Morillas, Jianjian Yang and Juan de Vicente

This article is published in: Journal of Rheology, 62(6), 1485-1494 (2018).

DOI: https://doi.org/10.1122/1.5052247

Abstract

A double-gap (DG) magnetorheological (MR) cell is designed, constructed and validated using Finite Element Method Magnetostatics (FEMM) simulations, Computational Fluid Dynamics (CFD) calculations and experimental data with Newtonian fluids and conventional MR fluids for a range of particle concentrations and external magnetic field strengths. This new cell is a generalization of the twin-gap (TG) device. It is capable to reach very large magnetic field strengths and shear rates avoiding normal force overload. More importantly, it is optimized for magnetic field homogeneity.

9.1 Introduction

Conventional magnetorheological (MR) fluids are dispersions of non-Brownian magnetizable particles in non-magnetic liquid carriers. In the absence of magnetic fields MR fluids behave as traditional dispersions [1]. However, under the presence of magnetic fields the particles aggregate forming mesostructures in the field direction giving rise to the appearance of a yield stress [2-9].

The rheological characterization of MR fluids is typically carried out in torsional rheometers using parallel plates ‘pp’ (in contrast to cone-plates ‘cp’ and concentric cylinders ‘cc’ configurations) [10]. The ‘pp’ geometry exhibits some advantages from both theoretical and practical points of view. In the ‘pp’ geometry, field-induced structures, under sufficiently large fields, have the same length. Additionally, the superposition of a magnetic field is not a very complicated task. In the late 90’s the magnetic fields were simply generated through the use of open coils surrounding the disks [11-14]. In this setup the maximum magnetic fields achieved were of the order of 10 kA/m and their homogeneity, within the sample volume, was very good (below 10%). Later, early this century, electromagnetic circuits were implemented in the design in an attempt to achieve larger field strengths (≈ 100 kA/m) sacrificing the field homogeneity [15-22]. When using electromagnetic circuits, the hole in the upper yoke unavoidably contributes with a field strength reduction (approximately 10% in the Anton Paar magnetocell). Also, the measurable yield stress is limited by the saturation in the normal force transducer of the device (in commercial rheometers it is typically of the order of 50 N). Independently of the setup employed to generate the magnetic field, in a ‘pp’ configuration, the maximum shear rates are limited to ≈ 1000 s^{-1} before sample loss due to centrifugal forces. To overcome some of these problems, Laun *et al.* [23] came up with a twin-gap (TG) design using ferromagnetic tools. The advantages of this device are a

larger maximum magnetic field (up to 1.5 T) with improved homogeneity, a larger maximum shear rate (up to 10000 s^{-1}) and normal force compensation.

In an attempt to improve the TG setup, in this manuscript we study a generalization of this design by allowing the two shear gaps to be different in size. This 'double-gap' (DG) design is validated using Finite Element Method Magnetostatic (FEMM) calculations, Computational Fluid Dynamics (CFD) simulations and experimental tests in a torsional rheometer. Interestingly, this new cell is capable to generate very homogeneous saturating magnetic fields and therefore, for the first time, allows us to interrogate MR fluids in the magnetic saturation regime.

9.2 Materials and methods

Carbonyl iron microparticles used in this work were kindly provided by BASF SE, Germany. In particular, we used the EW grade carbonyl iron powder. Silicone oils (SO350 with viscosity $\eta_{SO350} = 0.3406$ Pa·s and SO500 with viscosity $\eta_{SO500} = 0.4642$ Pa·s at 25 ºC) were obtained from Sigma-Aldrich and used without further purification. MR fluids were prepared by vigorous dispersion of the iron microparticles in the oils using a centrifugal mixer.

Rheological tests were carried out in a commercial magnetorheometer (MCR501, Anton Paar, SE Germany) with the MRD 70/1T field generator (Anton Paar, SE Germany) attached to the rheometer base. Three different geometries were studied: (i) conventional single-gap (SG), (ii) twin-gap (TG) and (iii) double-gap (DG) magnetocells. In SG tests we used the commercial non-ferromagnetic (titanium) rotor with a lower brass disk and a spacer ring [19,20]. In TG and DG tests we used ferromagnetic plates of two different materials: soft iron (RS Amidata) and Mumetal (Magnetic Shield Corporation). The magnetic properties of these materials are shown in Sec. 9.9.1 (see Fig. 9.11). Geometrical details of the plates employed in the experiments are included in Table 9.1.

	Radius (R_r)	Thickness (h_r)	Material
Tool #1	9.972 mm	1.44 mm	Titanium
Tool #2	7.950 mm	2.36 mm	Soft iron
Tool #3	8.010 mm	1.04 mm	Soft iron
Tool #4	7.995 mm	2.34 mm	Mumetal
Tool #5	8.075 mm	3.05 mm	Soft iron

Table 9.1: Geometrical characteristics of the rotating plates employed in the rheological experiments.

The DG magnetocell was a modification of the commercial Anton Paar MRD magnetocell. A schematics of the DG magnetocell is depicted in Fig. 9.1. As observed, it closely resembles the TG device designed by Laun *et al.* [23] (see Fig. 2 in their paper) with two major differences: (i) The sample rests directly on top of the surface of the bottom yoke (the original brass disk is removed). (ii) The two shear gaps (bottom and up) are not necessarily the same size ($h_b \neq h_u$).

Laboratory experiments were performed in three different steps as follows: first, the sample was preconditioned at a constant shear rate of approximately 100 s^{-1} for 30 s to prevent the particles from settling and to erase the mechanical history. Second, the

magnetic field was suddenly applied in the gradient direction and the suspension was left to equilibrate for 1 min in order to aggregate the particles. Finally, a steady shear test was carried out still in the presence of a magnetic field. All tests were performed at 25 °C.

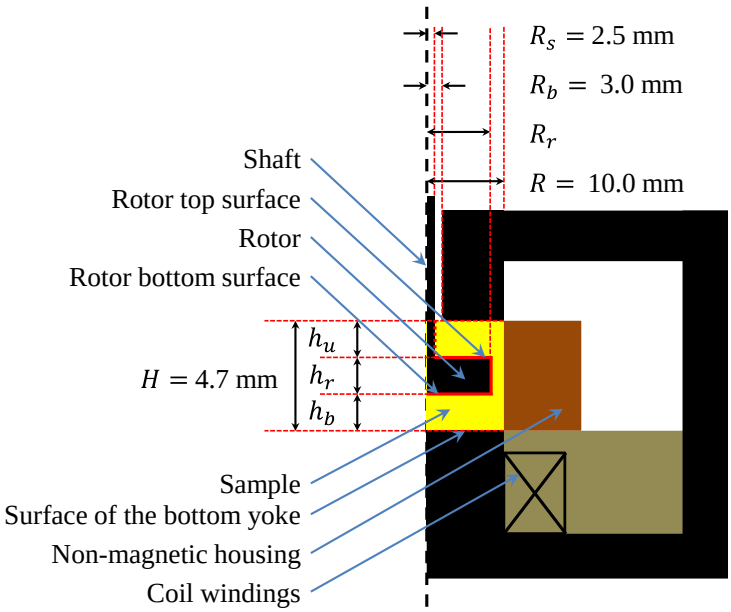

Figure 9.1: Schematics of the double-gap (DG) magnetocell. This design is a modification of the Anton Paar MRD 70/1T magnetocell. This includes the commercial ferromagnetic spacer ring of thickness 1.29 mm.

Numerical simulations were carried out to compute the magnetic field distribution (strength and homogeneity) in the magnetocells and the shear stress acting on the rotating plate. For this aim we used COMSOL Multiphysics. In the first case, the magnetic field distribution was obtained by solving Maxwell's equations in the stationary state (i.e. FEMM simulations). The axisymmetric computational domain is sketched in Fig. 9.1, it is based on the magnetic circuit (yokes), non-/magnetic rotor, sample region and coils through feeding current flows. The particular magnetic properties of each piece were taken into consideration in these simulations. The whole device was placed within a large external (cylindrical) box where boundary conditions were defined. In particular, the normal component of the magnetic field on each boundary (top, bottom and lateral cylindrical wall) was set to be zero. The size of the box was prescribed at a distance to sufficiently remove any size effects but still be manageable for calculations. A height of $2.3h_{mc}$ and a radius of $2r_{mc}$ (being h_{mc} and r_{mc} magnetocell's height and radius) was used; a larger simulation box did not give different results (e.g. differences are below 0.1% for a box size of $4.6h_{mc} \times 4r_{mc}$). The mesh was generated in a similar way; simulations were carried out for finer and finer meshes until no significant difference was observed in the results. The mesh density changed depending on the computational domain region. The densest mesh was located within the gap between yokes (mesh element size ~ 0.1 mm) while it became coarser as it went away from that place (0.5 mm in the yokes, 2 mm in the coil windings and 14 mm in the external cylinder next to its boundaries).

In the second case, Cauchy and continuity equations were solved again in stationary state (i.e. CFD simulations) within an axisymmetric domain enclosing the sample (yellow region in Fig. 9.1). The fluid domain was discretized using a structured regular mesh with a mean element size of 0.055 mm. The finer mesh was close to the rotor corner (element size of 0.01 mm). More details about these CFD simulations are provided in Sec. 9.5.

9.3 Magnetic field strength and homogeneity

In this section, FEMM simulations are carried out to find the operation conditions that guarantee field homogeneity in the shearing cell. Simulations are always done in empty cells (i.e. without sample) in order for the results not to depend on the particular material tested.

Figure 9.2 shows the magnetic flux density in the rotor axis direction B_v as a function of the solenoid current for an empty gap in a SG device using the commercial titanium plate (Tool #1). Both experimental measurements and FEMM simulations are shown together for three different radial positions. This figure clearly demonstrates the consistency of the simulations and a noticeable magnetic field gradient in the radial direction that has been reported in the past to promote the migration of the particles to the rim of the plate [20,24,25]. As observed, the inhomogeneity in the field is more pronounced the larger the current (i.e. close to saturation).

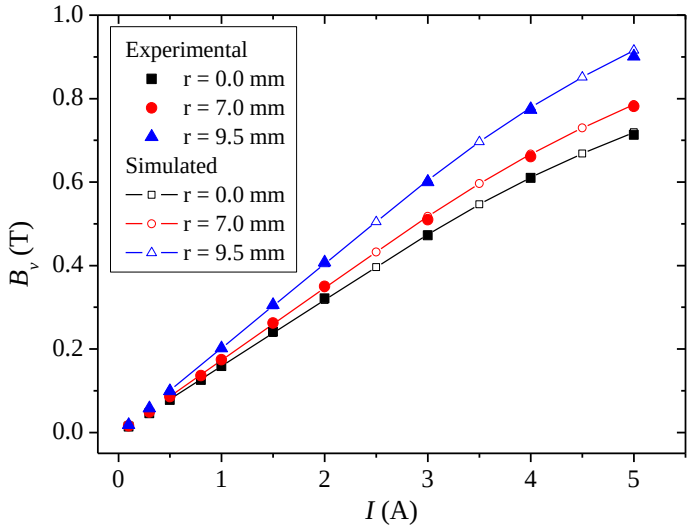

Figure 9.2: Vertical component of the magnetic flux density B_v in the empty gap as a function of solenoid current I for three different radial positions (r = 0.0, 7.0 and 9.5 mm) in the SG device. Solid symbols: Experimental data; Open symbols + line: FEMM simulations. The magnetic flux density in the empty gap was measured directly on top of the lower yoke by means of a Hall probe (FW Bell STH17-0404 with a strip of 1 mm thickness, 4 mm breadth and 101 mm length). The sensitive area of the probe is located at a distance of 0.85 mm from the strip tip. Simulation data reported in the figure exactly correspond to the actual position of the probe.

FEMM simulations for the new magnetocell device are shown in Fig. 9.3. These particular simulations correspond to a ferromagnetic (soft iron) plate (R_r = 7.95 mm; h_r = 1 mm) placed in the middle of the gap between the two yokes ($h_b = h_u$ = 1.85 mm in TG configuration). As observed, the radial profile is quite flat in the region of interest occupied by the sample. However, in the flat region, the flux density in the bottom shear gap is clearly higher than the upper one by 13 % for 5 A, 19 % for 3 A and 48 % for 1 A (cf. Fig. 9.3). This was expected (because of the central bore in the upper yoke) but it is obviously undesirable. The maximum fields achieved are of the order of 1 T (similar to the TG device [23]).

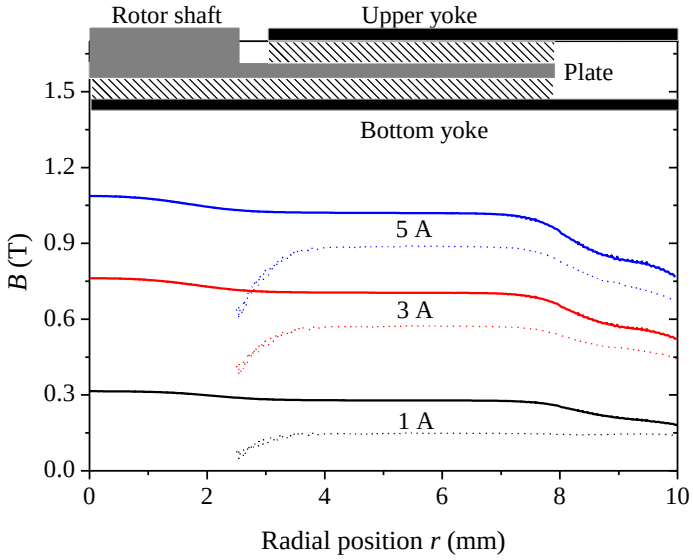

Figure 9.3: Simulated radial flux density norm profiles for a TG device in the middle of the shear gaps for three different solenoid currents (1, 3 and 5 A). Bottom gap: solid lines; upper gap: dashed lines. Numerical simulations correspond to $R_r = 7.95$ mm, $h_r = 1$ mm and $h_b = h_u = 1.85$ mm.

Apart from achieving a large magnetic field strength in the shear gaps, averaged field homogeneity must also be ensured. A dimensionless number that quantifies the change in the magnetic field (CMF) within the volume occupied by the fluid (Σ) is given by:

$$CMF = \frac{\bar{B}_b - \bar{B}_u}{\bar{B}_u} \tag{9.1}$$

where $\bar{B} = \int_\Sigma B(r,z)ds/\Sigma$ is the average magnetic flux density and B is the magnetic field norm. In Eq. (9.1), $\bar{B}_b$ stands for the average magnetic flux density in the volume occupied by the fluid in the lower shear gap (i.e. for $r < R_r$; see bottom hatched region in Fig. 9.3). On the other hand, $\bar{B}_u$ represents the average magnetic flux density in the volume occupied by the fluid in the upper shear gap (i.e. for $R_b < r < R_r$; see upper hatched region in Fig. 9.3). Simulations on the radial dependence of the magnetic flux density gradient are shown in Sec. 9.9.2 (see Fig. 9.12).

The simplest way to reduce CMF consists in displacing the plate upwards (increasing h_b/decreasing h_u) in order to compensate the field reduction due to the central bore in the upper yoke. By doing so, the average flux densities ($\bar{B}_b$ and $\bar{B}_u$) are also modified. Figure 9.4 demonstrates the impact of displacing the plate in the vertical direction in both magnetic flux density $\bar{B}$ and homogeneity CMF. Figure 9.4a shows the dependence of $\bar{B}_b$ and $\bar{B}_u$ with h_b for different solenoid currents I. As observed, for a given current level, $\bar{B}_b > \bar{B}_u$ for low h_b (in agreement with Fig. 9.3). However, upon increasing h_b the averaged fields tend to approach each other until $\bar{B}_b = \bar{B}_u$ at a crossover field value $\bar{B}_x \equiv \bar{B}_b = \bar{B}_u$. In Fig. 9.4b we show the dependence of $\bar{B}_x$ with I. Obviously, the magnetic flux achieved increases with the current. The black solid line in Fig. 9.4b corresponds to a linear fit. Finally, in Fig. 9.4c we show CMF as a function of h_b for different currents I. These curves demonstrate that the homogeneity is improved when h_b increases as otherwise expected. The optimal value slightly decreases with the current and is approximately $h_b = 3.5$ mm.

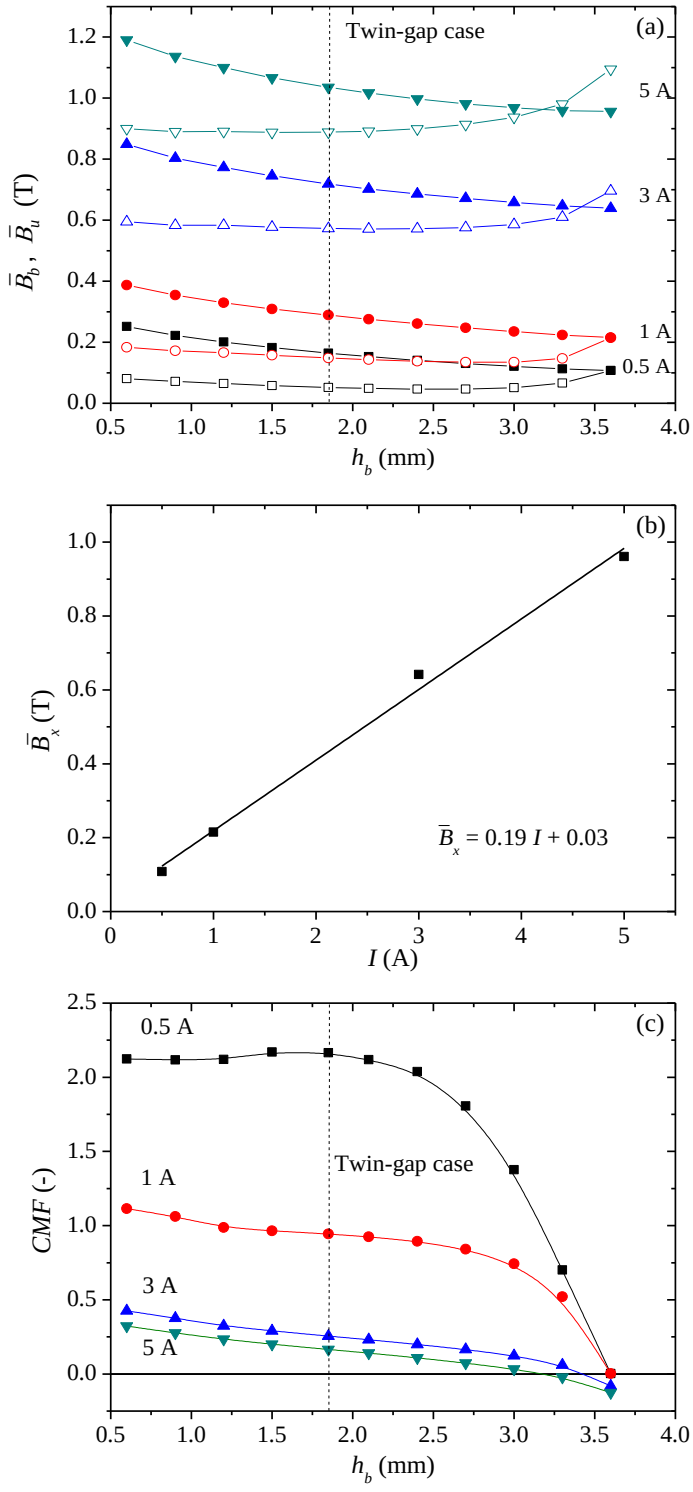

Figure 9.4: a) Average magnetic flux density $\bar{B}$ variation in the bottom gap $\bar{B}_b$ (closed symbols) and upper gap $\bar{B}_u$ (open symbols) vs bottom gap thickness h_b for different solenoid currents I. b) Crossover field value $\bar{B}_x$ as a function of I. The straight solid line is the best fitting linear regression equation to the data. c) Homogeneity (CMF) in the DG magnetocell for different vertical positions of the plate (specified by bottom gap thickness h_b) at a range of I values. The vertical dashed line in a) and c) corresponds to the TG case ($h_b = h_u = 1.85$ mm). Simulations correspond to $R_r = 7.95$ mm and $h_r = 1$ mm.

Up to now, we have assumed that the plate has a prescribed thickness of $h_r = 1$ mm. However, apart from increasing the solenoid current (cf. Fig. 9.4b), a simple way to increase $\bar{B}_x$ consists in increasing h_r (i.e. reducing the magnetic reluctance of the circuit). As a result, the goal now is, given h_r, to determine h_b in order to generate the largest field possible for the same averaged $\bar{B}_x$ value in the two shear gaps. With this in mind, we performed an extensive set of simulations for plates having different thicknesses h_r at different vertical positions h_b. The results are contained in Fig. 9.5. In Fig. 9.5a we show $\bar{B}_b$ and $\bar{B}_u$ as a function of h_b for different h_r values and a constant $I = 5$ A. The data demonstrate that the crossover point $\bar{B}_x$ is more quickly achieved for the thicker plates when displacing the plate upwards. Also, $\bar{B}_x$ can reach an astonishingly large value of ≈ 1.7 T when $h_r = 3$ mm, which is a very large field specially taking into account that we are simulating empty gaps. In Fig. 9.5b we show CMF as a function of h_b for different h_r values and a constant $I = 5$ A. These data clearly show that the homogeneity is achieved for smaller h_b values when h_r increases.

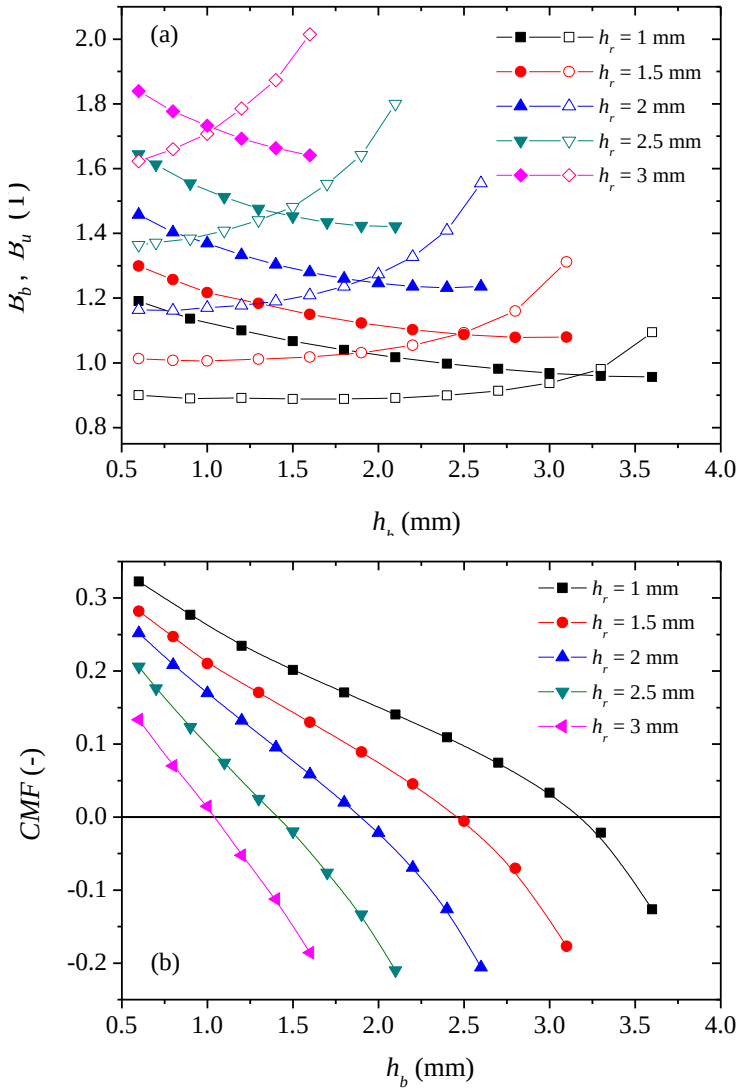

Figure 9.5: a) Average magnetic flux density $\bar{B}$ variation in the bottom gap $\bar{B}_b$ (closed symbols) and upper gap $\bar{B}_u$ (open symbols) vs bottom gap thickness h_b for different plate thickness h_r at a solenoid current of $I = 5$ A. b) Field homogeneity (CMF) corresponding to the data shown in (a), calculated with Eq. (9.1). The radius of the plate is $R_r = 7.95$ mm.

A more detailed analysis on the influence of h_r is shown in Fig. 9.6. In particular, in Fig. 9.6a we show $h_{b,x}$ values corresponding to the crossover ($CMF = 0$) versus h_r for three different currents ($I = 0.5$ A, 3 A and 5 A) while in Fig. 9.6b we show $\bar{B}_x$ as a function of h_r for three different currents ($I = 0.5$ A, 3 A and 5 A). It is important to note that the maximum h_r value simulated in this work corresponds to $h_r = 3$ mm. This upper limit in h_r is of practical interest. Due to geometrical constrictions, thicker plates would be too close to the lower and upper yokes and therefore direct contact would be possible because of the tolerances in the misalignment of the tools.

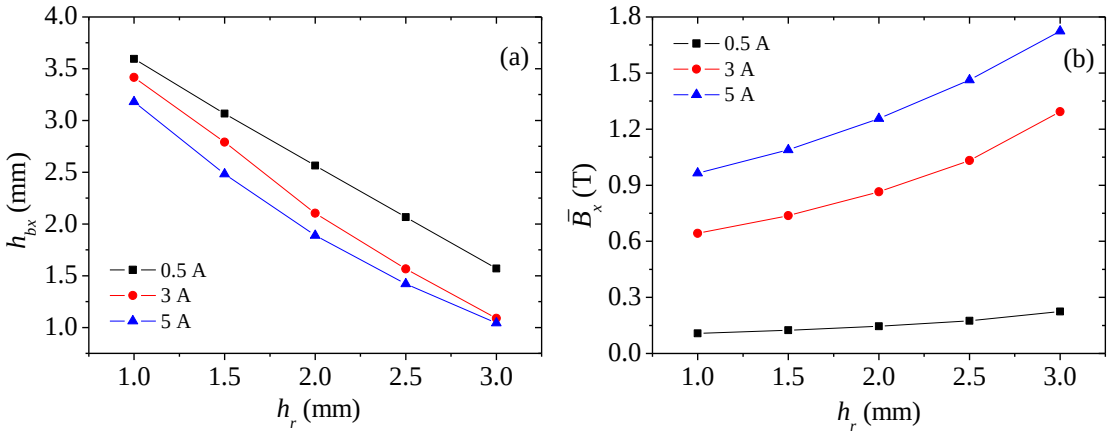

Figure 9.6: a) $h_{b,x}$ values corresponding to the crossover ($CMF = 0$) versus h_r for three different currents ($I = 0.5$ A, 3 A and 5 A). b) $\bar{B}_x$ as a function of h_r for three different currents ($I = 0.5$ A, 3 A and 5 A).

From the previous discussion, it could be inferred that the ferromagnetic upper plate should not feel any force when placed at $h_{b,x}$ because, in this particular case, the condition for magnetic field homogeneity is accomplished (i.e. $CMF = 0$). However, although in this case the fields match in upper and bottom gaps, the magnetic field along the shaft of the upper plate is not the same as in the shear gaps and therefore, the upper plate experiences an effective magnetic field gradient responsible for a non-negligible normal force (also in the absence of sample). Nevertheless, even in the most unfavorable conditions (i.e. $I = 5$ A), this normal force remains below the rheometer's normal force limit (50 N). Simulations on the normal force acting on the plate are shown in Sec. 9.9.3 (see Fig. 9.13). Overall, DG and TG geometries are capable to balance normal forces developed by the sample (due to their double gap). However, the upper plate still suffers an external magnetic body force (also without sample) hence contributing to a non-negligible normal force.

In summary, results shown up to now demonstrate that there are essentially three routes to match the magnetic flux density in both shear gaps. They involve tuning: (i) the current I, (ii) the thickness of plate h_r and (iii) the vertical position of the plate h_b.

9.4 Analytical calculation of the shear rate and shear stress

The total torque M acting on the rotor surfaces due to the confined fluid mainly consists of three contributions: On the one hand, a contribution from the bottom and upper shear gaps ($M_b + M_u$) and on the other hand, a contribution from the cylindrical (i.e. lateral) shear gap (M_c) (see solid thick red lines in Fig. 9.1):

$$M = M_b + M_u + M_c \tag{9.2}$$

Strictly speaking, the torque coming from the rotor shaft surface should also have been taken into account (see dashed thick red line in Fig. 9.1). However, this contribution can be neglected (see below).

In the analysis we considered the case of a power-law fluid. The reason for this is that this particular constitutive equation serves as a bridge between Newtonian and yield stress fluids of interest in this work. Note also that MR fluids typically behave as power-law fluids in a very wide range of shear rates. In the case of power-law fluids the shear stress-shear rate relationship is given by:

$$\tau = m\dot{\gamma}^n \tag{9.3}$$

where m is the flow consistency index and n is the flow behavior index. Accordingly, Newtonian fluids correspond to $n = 1$ while yield stress fluids correspond to $n = 0$.

No matter the constitutive equation of the fluid, for viscometric flows, the shear rate in the bottom, upper and cylindrical shear gaps can be expressed as a function of the angular velocity of the plate Ω and geometrical dimensions as follows:

$$\dot{\gamma}_b(r) = \frac{r\Omega}{h_b};\ \ \dot{\gamma}_{R_r,b} \equiv \dot{\gamma}_b(R_r) = \frac{R_r\Omega}{h_b} \tag{9.4a}$$

$$\dot{\gamma}_u(r) = \frac{r\Omega}{h_u};\ \ \dot{\gamma}_{R_r,u} \equiv \dot{\gamma}_u(R_r) = \frac{R_r\Omega}{h_u} \tag{9.4b}$$

$$\dot{\gamma}_c = \frac{2\Omega}{1-\beta} \text{ with } \beta = \left(\frac{R_r}{R}\right)^2 \tag{9.4c}$$

The torque acting on the rotating plate due to a power-law fluid can be computed by integration:

$$\begin{aligned} M &= \int_{\substack{\text{total}\\\text{surface}}} r\tau dS \\ &= \int_{\substack{\text{bottom}\\\text{surface}}} rm[\dot{\gamma}_b(r)]^n dS + \int_{\substack{\text{upper}\\\text{surface}}} rm[\dot{\gamma}_u(r)]^n dS \\ &+ \int_{\substack{\text{lateral}\\\text{surface}}} rm(\dot{\gamma}_c)^n dS \end{aligned} \tag{9.5}$$

Using cylindrical coordinates and substituting the expressions for the shear rates (Eq. (9.4)) in Eq. (9.5) we arrive to:

$$\begin{aligned} M = &\int_0^{R_r} rm\left(\frac{r\Omega}{h_b}\right)^n r d\varphi dr + \int_{R_b}^{R_r} rm\left(\frac{r\Omega}{h_u}\right)^n r d\varphi dr \\ &+ \int_0^{h_r} R_r m\left(\frac{2\Omega}{1-\beta}\right)^n R_r d\varphi dh \end{aligned} \tag{9.6}$$

Here R_b is the radius of the axis hole (see Fig. 9.1). Hence, after integration of Eq. (9.6), the following theoretical expression is obtained for the total torque:

$$M = 2\pi m\left[\left(\frac{R_r\Omega}{h_b}\right)^n \frac{R_r^3}{3+n} + \left(\frac{\Omega}{h_u}\right)^n \frac{R_r^{3+n} - R_b^{3+n}}{3+n} + \left(\frac{2\Omega}{1-\beta}\right)^n R_r^2 h_r\right] \tag{9.7}$$

For convenience, the total torque can be expressed as a function of the rim shear stress in the bottom gap $\tau_{R_r,b} = m\dot{\gamma}_{R_r,b}^n = m(R_r\Omega/h_b)^n$ as follows:

$$M = \tau_{R_r,b}\frac{2\pi R_r^3}{3+n}\left[1 + \left(\frac{h_b}{h_u}\right)^n\left(1 - \left(\frac{R_b}{R_r}\right)^{3+n}\right) + (3 + n)\frac{h_r h_b^n}{R_r^{n+1}}\left(\frac{2}{1-\beta}\right)^n\right] \tag{9.8a}$$

$$\tau_{R_r,b} = \frac{(3+n)M}{2\pi R_r^3}\left[1 + \left(\frac{h_b}{h_u}\right)^n\left(1 - \left(\frac{R_b}{R_r}\right)^{3+n}\right) + (3 + n)\frac{h_r h_b^n}{R_r^{n+1}}\left(\frac{2}{1-\beta}\right)^n\right]^{-1} \tag{9.8b}$$

In the particular case of Newtonian fluids ($\tau = \eta\dot{\gamma}$, $n = 1$), Eq. (9.8) can be written as a function of the rim shear stress in the bottom gap $\tau_{R_r,b} = \eta\dot{\gamma}_{R_r,b} = \eta\, R_r\Omega/h_b$ as follows:

$$M = \tau_{R_r,b}\frac{\pi R_r^3}{2}\left[1 + \frac{h_b}{h_u}\left(1 - \left(\frac{R_b}{R_r}\right)^4\right) + \frac{8h_r h_b}{R_r^2(1-\beta)}\right] \tag{9.9a}$$

$$\tau_{R_r,b} = M\frac{2}{\pi R_r^3}\left[1 + \frac{h_b}{h_u}\left(1 - \left(\frac{R_b}{R_r}\right)^4\right) + \frac{8h_r h_b}{R_r^2(1-\beta)}\right]^{-1} \tag{9.9b}$$

Similarly, in the particular case of yield stress fluids ($\tau = \tau_y = \text{const.}$, $n = 0$), Eq. (9.8) is written as follows:

$$M = \tau_y\frac{2\pi R_r^3}{3}\left[2 - \left(\frac{R_b}{R_r}\right)^3 + 3\frac{h_r}{R_r}\right] \tag{9.10a}$$

$$\tau_y = \frac{3M}{2\pi R_r^3}\left[2 - \left(\frac{R_b}{R_r}\right)^3 + 3\frac{h_r}{R_r}\right]^{-1} \tag{9.10b}$$

Neglecting the lateral surface contribution (i.e., the last term in Eq. (9.10)) we arrive to:

$$M = \tau_y\frac{2\pi R_r^3}{3}\left[2 - \left(\frac{R_b}{R_r}\right)^3\right] \tag{9.11a}$$

$$\tau_y = M\frac{3}{2\pi R_r^3}\left[2 - \left(\frac{R_b}{R_r}\right)^3\right]^{-1} \tag{9.11b}$$

Note that in the particular case of MR fluids, the stress acting on the lateral surface can be safely neglected because the magnetic field, and therefore the field-induced (stress-bearing) structures, are collinear with the vorticity direction.

9.5 Numerical calculation of the shear rate and shear stress

The fluid flow was solved using non-Newtonian Computational Fluid Dynamics (CFD). In a typical simulation for a power-law fluid the constitutive equation is prescribed (Eq. (9.3), imposing m and n) and the simulations performed at a range of angular speeds Ω.

Cauchy (in the stationary state) and Continuity equations apply with appropriate boundary conditions for the fluid flow:

$$\rho(\vec{u}\cdot\nabla)\vec{u} = \nabla\cdot\left[-P\bar{\bar{I}} + \bar{\bar{\tau}}\right] + \rho\vec{g} \tag{9.12a}$$

$$\rho\nabla\cdot\vec{u} = 0 \tag{9.12b}$$

where ρ is the density, $\vec{u}$ is the flow velocity, P is the pressure, $\vec{g}$ represents body accelerations acting on the continuum (in the simulations contained in this work $\vec{g} = 0$), $\bar{\bar{I}}$ is the identity tensor and $\bar{\bar{\tau}}$ is the viscous stress tensor for the simulated fluid in laminar flow:

$$\bar{\bar{\tau}} = \eta\bar{\bar{\dot{\gamma}}} \tag{9.13}$$

Here, the shear rate $\bar{\bar{\dot{\gamma}}}$ is given by $\bar{\bar{\dot{\gamma}}} = \nabla\vec{u} + (\nabla\vec{u})^T$, the shear viscosity is $\eta = m\dot{\gamma}^{n-1}$ and the magnitude of the shear rate tensor is $\dot{\gamma} = \left(\bar{\bar{\dot{\gamma}}}:\bar{\bar{\dot{\gamma}}}\right)^{1/2}/2$.

The boundary conditions for the velocity and pressure are as follows:

$$\vec{u}_{wall} = 0 \tag{9.14a}$$

$$u_\theta = \Omega r \tag{9.14b}$$

$$f_0 = 0 \tag{9.14c}$$

Equation (9.14a) prevents slip at the housing wall and yokes' surfaces, Eq. (8.14b) imposes the rotation of the upper plate and finally Eq. (9.14c) sets the normal force to zero in the small open gap between rotor shaft and the upper yoke.

Once the velocity $\vec{u}$ and pressure fields P are computed, the viscous stress tensor $\bar{\bar{\tau}}$ is calculated from Eq. (9.13) and, finally, the torque M is calculated by integration as follows:

$$M = \hat{z}\cdot\int\vec{r}\times\bar{\bar{\tau}}\cdot d\vec{s} \tag{9.15}$$

Here, the cross symbol '×' denotes a vector product and $\hat{z}$ is the unit vector in the vertical (axis) direction. The previous integral is done over all rotor's surfaces, that is, (dashed and solid) thick red lines in Fig. 9.1. This means that we are also including the surface of the rotor shaft, which had not been considered in the analytical derivation of Eq. (9.8). Nevertheless, data do not change significantly if the integration is carried out only over the solid thick red lines (the differences are below 1.4%).

9.6 Experimental validation with Newtonian fluids

First, we compare the analytical predictions with numerical simulations for a DG geometry with different h_b. In Fig. 9.7 we compare the radial dependence of the reduced shear rate ($\dot{\gamma}/\Omega$) acting on the lower surface of the rotating plate for a Newtonian liquid

(with viscosity 1 Pa·s) for a small angular velocity (1 s^{-1}). The agreement between the analytical calculations and numerical simulations is very good for $r < 6$ mm. However, as expected, the theoretical prediction (Eq. (9.4a), solid line) underestimates the simulated shear rate (symbols) at the rim of the plate because of the edge effects. At this point it is worth to note that a very good agreement was also found for power law fluids (results not included here for brevity).

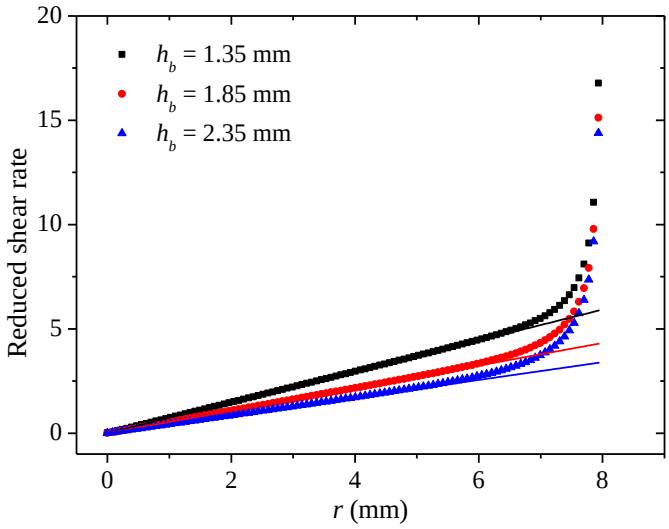

Figure 9.7: Reduced shear rate $(\dot{\gamma}/\Omega)$ as a function of the radial distance (r) acting on the lower surface of the plate for an angular speed of Ω = 1 s^{-1}. In the simulation of the DG geometry we assumed a Newtonian fluid with a viscosity of 1 Pa·s, $R_r = 7.95$ mm and $h_r = 1$ mm. Solid lines correspond to the theoretical prediction (Eq. (9.4a)).

Experiments were also carried out with Newtonian fluids. In Fig. 9.8 we compare experimental data with predictions on two silicone oils (SO350 and SO500) for TG and DG geometries. On the one hand, in Figs. 9.8a and 9.8b we show the torque data M as a function of the angular velocity Ω. Symbols correspond to experimental raw data for M and Ω as obtained directly from the rheometer. The solid lines correspond to CFD calculations (Eq. (9.15)). As observed a reasonably good agreement is found between experiments and simulations in both TG and DG devices. On the other hand, in Figs. 9.8c and 9.8d, we show the shear viscosity $\tau_{R_r,b}/\dot{\gamma}_{R_r,b}$ as a function of the shear rate $\dot{\gamma}_{R_r,b}$ at the rim in lin-log representation. Solid symbols correspond to experimental data as obtained after manipulation of the raw torque and angular velocity data using Eqs. (9.9b) and (9.4a), respectively. For completeness, in Figs. 9.8c and 9.8d we also include open symbols corresponding to experimental measurements in a single-gap (SG) geometry ('pp' and 'cp' give the same results for Newtonian fluids). These figures demonstrate that the conversion from torque/angular velocity to shear stress/shear rate is done properly even when the contribution due to rotor shaft is omitted in the analytical calculation. The slight shear thinning that is observed at low shear rates in TG and DG geometries may be due to surface tension torque and/or finite precision and roughness at the edge of these geometries [26].

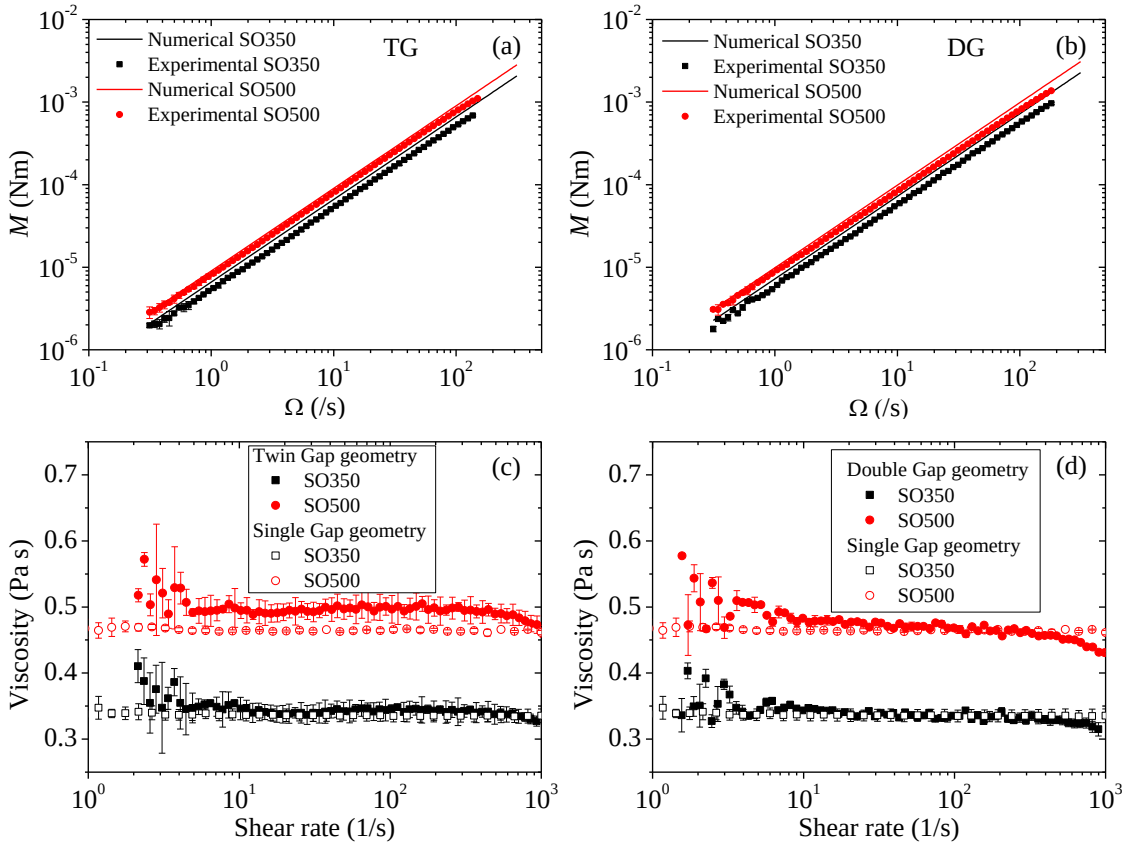

Figure 9.8: Validation of the TG and DG devices with two Newtonian silicone oils (SO350 and SO500). First row: comparison between numerical (lines) and experimental (symbols) torque M versus angular speed Ω curves in TG (a) and DG (b) geometries. Second row: comparison between experimental constitutive curves obtained with single gap (SG) geometry and both TG (c) and DG (d) geometries. In the TG case $R_r = 7.950$ mm, $h_r = 2.36$ mm and $h_b = h_u = 1.17$ mm while in the DG case $R_r = 7.950$ mm, $h_r = 2.36$ mm, $h_b = 1.60$ mm and $h_u = 0.74$ mm. Experiments in SG tests were carried out for a gap of 300 μm.

9.7 Experimental validation with MR fluids

In this section we start with the analysis of conventional MR fluids. In this manuscript, the conventional MR fluids are prepared by dispersion of 20 vol% carbonyl iron particles in a silicone oil. In the absence of magnetic fields, these suspensions are expected not to exhibit a yield stress. However, in practice the iron particles are slightly aggregated and the suspensions do not behave as perfect Newtonian fluids in the sense that the stress is not truly proportional to the shear rate. As a result, the application of Eq. (9.9b) is questionable. To circumvent this problem we consider that the MR fluids behave as power-law fluids with a shear rate-dependent flow behavior index n. With this, the conversion from torque to shear stress can be simply carried out using Eq. (9.8b) with a local flow behavior index given by $n = d\log(M)/d\log(\Omega)$.

A three step process was followed to compute the shear stress and shear rate in the DG cell: (i) First the local flow index n was computed in the range of angular velocities Ω explored. (ii) Then the shear rate at the bottom of the rotor $\dot{\gamma}_{R_r,b}$ was obtained from Ω

using Eq. (9.4a). (iii) Finally, the shear stress at the bottom rim $\tau_{R_r,b}$ was calculated from the torque M and local flow behavior index n using Eq. (9.8b).

In Fig. 9.9 we compare predictions with experimental data on 20 vol% EW carbonyl iron based MR fluids in SG, TG and DG geometries in the absence of a magnetic field. Black squares correspond to experimental data in the commercial SG device. They were obtained using the Weissenberg-Rabinowitsch-Mooney (WRM) correction [27]. Red circles and blue triangles correspond to TG and DG results, respectively. They were obtained using the protocol described in the paragraph above. Finally, red and blue lines correspond to TG and DG results supposing Newtonian fluids (Eq. (9.9b)). As observed, there is not much difference between using the local flow behavior index in Eq. (9.8b) or the Newtonian approximation (Eq. (9.9b)) because the suspensions are only slightly shear thinning. As expected, the rheograms for the suspensions do not depend on the particular geometry employed.

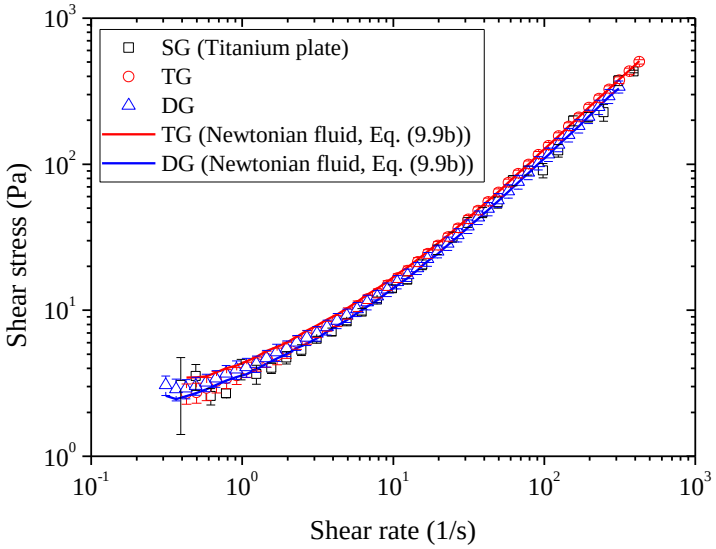

Figure 9.9: Flow curves (stress versus shear rate) corresponding to 20 vol% EW iron particles dispersed in silicone oil (SO350) in the absence of magnetic fields. Symbols correspond to experimental data using single-gap SG ($h_b = 1.6$ mm; due to sample wettability and large shear gap, a brass ring was employed to maintain the sample in place during the measurements), twin-gap TG ($R_r = 7.950$ mm, $h_r = 2.36$ mm and $h_b = h_u = 1.17$ mm) and double-gap DG ($R_r = 7.950$ mm, $h_r = 2.36$ mm, $h_b = 1.6$ mm and $h_u = 0.74$ mm) devices. Solid lines correspond to the predictions for TG and DG geometries under the assumption that the suspension behaves as a Newtonian fluid (Eq. (9.9b)).

The next step was to superimpose a magnetic field to the MR fluid in order to induce particle-particle magnetostatic interactions and therefore an apparent yield stress in the suspensions. In this manuscript we are interested in saturating (and homogeneous) magnetic fields. This point guarantees the applicability of Eq. (9.11b) to compute the shear stress from the torque acting on the plate. In Fig. 9.10a we show $\tau_{R_r,b}$ as a function of $\dot{\gamma}_{R_r,b}$ under magnetic fields where the homogeneity condition is fulfilled ($CMF = 0$; i.e. same averaged field in the upper and bottom shear gaps; see Sec. 9.3). Experimental stress data shown in Fig. 9.10a do not significantly change with the shear rate suggesting that the suspension behaves as a plastic-like material with a yield stress. This validates

the use of Eq.(9.11b) in the computation of the stress from the torque. As expected, the stress increases with the magnetic field strength.

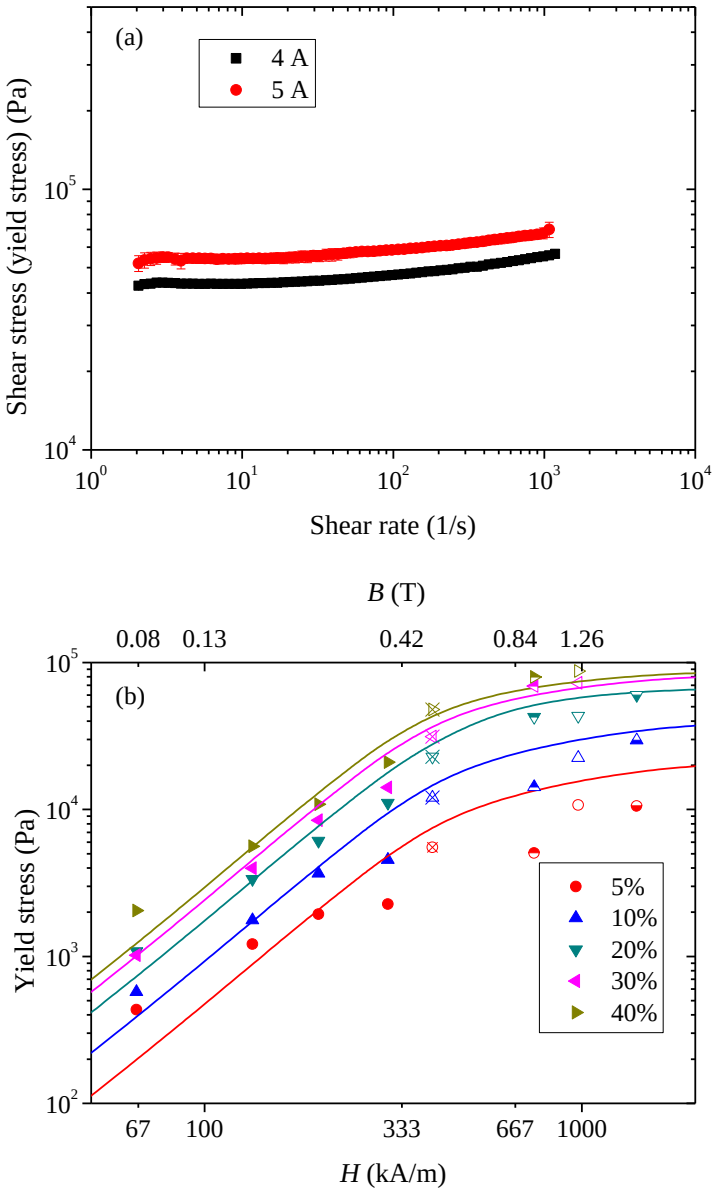

Figure 9.10: a) Experimental shear stress vs shear rate data evaluated at the bottom rim of the DG device with $\bar{B}_x = \bar{B}_u = \bar{B}_b$. The plate used had a radius R_r =7.950 mm and a thickness $h_r = 2.36$ mm. Black squares: $I = 4$ A, $h_b = 1.6$ mm, $h_u = 0.74$ mm and $\bar{B}_x = \bar{B}_b = \bar{B}_u = 1.23$ T. Red circles: $I = 5$ A, $h_b = 1.52$ mm, $h_u = 0.82$ mm and $\bar{B}_x = \bar{B}_b = \bar{B}_u = 1.40$ T. These magnetic flux densities correspond to simulations without sample in the cell (i.e. external fields). b) Yield stress as a function of the external magnetic field strength H as obtained using the SG (solid symbols) and DG devices with different soft iron plates (open symbols-Tool #2, filled half up-Tool #3, filled half down-Tool #5) and Mumetal plate (crossed symbols-Tool #4) using Eq. (9.11b). Also included are the simulation data following [28] (solid lines). Experiments in SG tests were carried out for a gap of 300 μm.

The apparent yield stress τ_y can be obtained from Fig. 9.10a by extrapolation of the shear stress to low shear rates. In Fig. 9.10b we show the resulting τ_y data as a function of the

magnetic field strength H together with experiments on the same MR fluids but using the commercial SG device. Open symbols correspond to the DG device (Tool #2) while solid symbols correspond to the SG device. Even though SG data suggest that τ_y is close to saturation for $H \approx 300$ kA/m, experiments performed with DG cell provide a clearly larger yield stress. This suggests that the saturation observed in the SG tool may be an artifact, possibly due to slippage and/or particle migration because of nonuniformity in the magnetic field distribution [24,25].

In principle, in order to fully cover the interval between SG measurements (solid symbols) and DG measurements (open symbols) new tests should be carried out for smaller solenoid currents. However, from the inspection of Fig. 9.6a it is clear that for smaller currents ($I < 4$ A), the rotor employed in the experiments (Tool #2 from Table 9.1) cannot provide the desired field homogeneity $CMF = 0$ for a practical upper gap height h_u. In this context, note that h_u must be sufficiently large in order to prevent physical contact between the rotor plate and the upper yoke. To solve this issue, and in view of Sec. 9.3, a thinner plate can be used. In this sense, we repeated previous experiments with a plate with $h_r = 1$ mm (Tool #3) that creates a field around 0.9 T if the bottom gap is $h_b = 3$ mm and the current is $I = 5$ A (see Fig. 9.6a). Yield stresses measured with this plate are shown in Fig. 9.10b with filled half up symbols.

All the discussion exposed until now supposes that the rotor is made of soft iron. However, other magnetic materials can be employed as well. To show this, a Mumetal plate (Tool #4) was also used in this work. This material has a lower magnetic response (see Fig. 9.11) and allows to work with smaller and still homogeneous magnetic fields by properly choosing h_b (checked again by FEMM simulations). Experimental data obtained with the Mumetal plate are plotted in Fig. 9.10b with crossed symbols. Interestingly, both data points coming from Tools #3 and #4 satisfactorily bridge SG and DG measurements.

Finally, as it was pointed out in Fig. 9.6b, the highest achievable magnetic field with this DG device is 1.7 T for a 3 mm thickness rotor. Yield stress data obtained with this plate (Tool #5) is shown also in Fig. 9.10b with filled half down symbols. Note that in this case, most concentrated samples (30 and 40 vol%) could not be measured as the developed torque overcomes the maximum allowed by the rheometer (230 mN·m). In Fig. 9.10b we also include FEMM numerical predictions in preassembled structures (plotted with solid lines) following the methodology proposed in Ref. [28]. Briefly, in a first step, the particles are preassembled in infinite monoclinic lattices. Then, these lattices are tilted, according to the applied strain, by simulating the lattice unit cell and imposing periodic boundary conditions. The yield stress is computed from the maximum of stress versus strain curves using the Maxwell stress tensor. In these simulations, the magnetic properties of the particles are taken into account by explicitly introducing their magnetization curve (see Fig. 9.11) as a magnetostatic constitutive equation (for more details please see Ref. [28]). As observed in Fig. 9.10b, FEMM simulation results are in qualitatively good agreement with experiments.

9.8 Conclusions

A major challenge in magnetorheology is to obtain reliable data in the magnetic saturation regime at the same time the magnetic field distribution remains homogeneous within the sample volume. Available commercial devices are capable to reach fields of the order of 1 T but the price to be paid is the generation of field gradients that artifact the

measurements; typically the yield stress levels off earlier than expected (i.e. at smaller magnetic field strengths) in view of the magnetization curves of the materials involved.

The double-gap device described in this work is capable to generate highly homogeneous fields by appropriately choosing the plate thickness and gap size. The device has been fully characterized using magnetostatic and fluid dynamics simulations. Additionally, experiments on Newtonian fluids demonstrate that the shear stress calculation is correct. Finally, experiments on conventional MR fluids are reported for the first time in magnetic saturation. These experiments are in good agreement with FEMM simulations in preassembled structures.

Acknowledgements

This work was supported by MINECO MAT 2016-78778-R and PCIN-2015-051 projects (Spain), European Regional Development Fund (ERDF) and by Junta de Andalucía P11-FQM-7074 project (Spain). J. R. Morillas acknowledges FPU14/01576 fellowship. J. J. Yang acknowledges Chinese State Scholarship Fund.

9.9 Supplementary material

The Supplementary Material contains the magnetization curves for all materials investigated in this manuscript. It also includes additional information on the magnetic field homogeneity, field gradients and normal forces generated in the DG device.

9.9.1 Magnetic properties of the materials

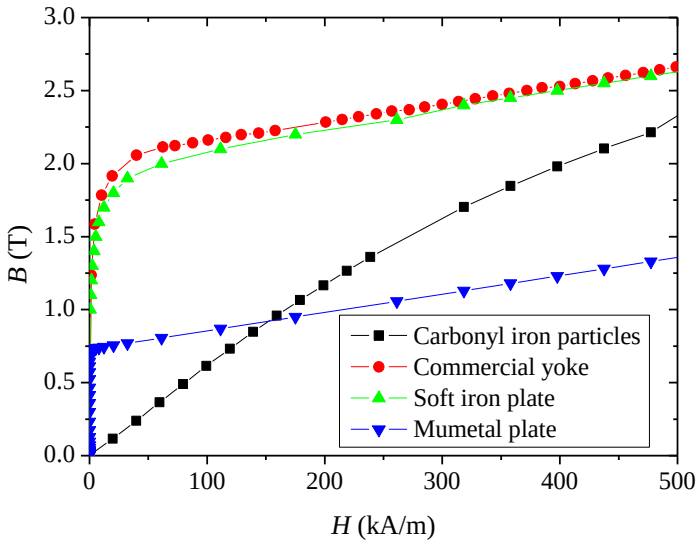

Figure 9.11: Magnetic flux density B versus magnetic field strength H for different magnetic materials used in this work: Squares.- carbonyl iron microparticles, Circles.- commercial yoke MRD device from [24], Up triangles.- soft iron plate (soft iron, without losses, from the material library in COMSOL Multiphysics' AC/DC Module) and down triangles.- Mumetal plate (from supplier datasheet).

In order to perform the FEMM numerical simulations, the (magnetic) constitutive equations of the different materials must be introduced in the model. Figure 9.11 shows the BH curves for the different materials employed.

9.9.2 Magnetic field homogeneity in the radial direction

In the main text, the magnetic field homogeneity was discussed in terms of the averaged fields over the bottom and upper shear gaps. However, nothing was said about the magnetic field profile (i.e. the radial dependence) in the shear gap.

As demonstrated in the manuscript (see Fig. 9.2), the SG device suffers from an important magnetic field gradient (i.e. the field changes with the radial position) that is responsible for undesirable particle migration within the gap. This feature can be better seen in Fig. 9.12 where the gradient in the radial direction of the magnetic field is directly plotted (black line). Clearly, the magnetic field is not constant along radial position and increases as we move outwards to the rim. On the other hand, the DG device shows a much flatter profile as it is inferred from its nearly zero gradient up to $r/R_r = 0.6$.

It is also important to note that, in both cases (SG and DG), the field gradient cannot be fully prevented at the rim due to edge effects originated by the bottom yoke and the rotor (this last one only applies in the DG device).

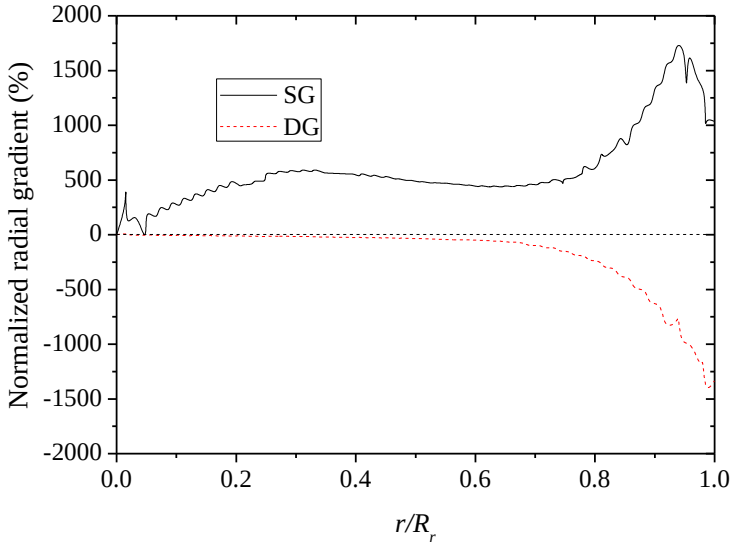

Figure 9.12: Magnetic field radial gradient normalized by its value at $r = 0$ mm as a function of the normalized radial position in SG (Tool #1) and DG (Tool #2) devices. $I = 5$ A. In DG case, $h_b = 1.6$ mm fulfilling that $CMF = 0$.

9.9.3 Normal forces acting on the upper plate

In the main text we discuss the shear force (torque) generated on the upper plate by field-induced particulate structures. However, the presence of a magnetic field itself also generates a normal force acting on the rotating plate despite the fact that the volume-averaged fields in the upper and bottom shear gaps are matched. In practice, this normal force must remain below a certain level, which in the particular case of the Anton Paar MCR 501 rheometer is 50 N. In Fig. 9.13 we demonstrate that this normal force remains below 50 N whatever the plate thickness and intensity current investigated.

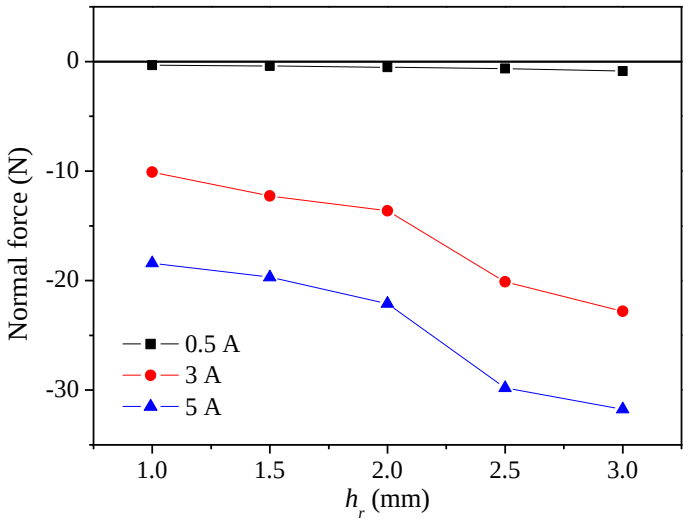

Figure 9.13: Normal force experienced by the soft iron rotor as a function of its thickness h_r for different applied currents. In all cases, vertical positions are $h_{b,x}$, that is, those fulfilling $CMF = 0$ (see Fig. 9.6a).

References

[1] Russel, W. B., Saville, D. A., and Schowalter, W. R. Colloidal dispersions (Cambridge University Press, Cambridge, 1991).

[2] Goncalves, F. D., Koo, J. H., and Ahmadian, M. (2006). A review of the state of the art in magnetorheological fluid technologies-Part I: MR fluid and MR fluid models. The Shock and Vibration Digest, 38(3), 203-220.

[3] Carlson, D. J. (2008). Magnetorheological Fluids. In: Schwartz, M. (Ed.) Smart Materials (CRC Press, Boca Raton).

[4] Vékás, L. (2008). Ferrofluids and magnetorheological fluids. Advances in Science and Technology, 54, 127-136.

[5] de Vicente, J., Klingenberg, D. J., and Hidalgo-Álvarez, R. (2011). Magnetorheological fluids: a review. Soft Matter, 7(8), 3701-3710.

[6] Wereley, N. (Ed.). Magnetorheology: advances and applications (Vol. 6) (Royal Society of Chemistry, Cambridge, 2013).

[7] Ashtiani, M., Hashemabadi, S. H., and Ghaffari, A. (2015). A review on the magnetorheological fluid preparation and stabilization. Journal of Magnetism and Magnetic Materials, 374, 716-730.

[8] Hajalilou, A., Mazlan, S. A., Lavvafi, H., and Shameli, K. Field responsive fluids as smart materials (Springer, Singapore, 2016).

[9] Ruiz-López, J. A., Hidalgo-Álvarez, R., and de Vicente, J. (2017). Towards a universal master curve in magnetorheology. Smart Materials and Structures, 26(5), 054001.

[10] Bossis, G., Volkova, O., Lacis, S., and Meunier, A. (2002). Magnetorheology: fluids, structures and rheology. In: Odenbach, S. (Ed.) Ferrofluids. Lecture Notes in Physics (Vol. 594) (Springer, Berlin).

[11] Laun, H. M., Kormann, C., and Willenbacher, N. (1996). Rheometry on magnetorheological (MR) fluids. Rheologica Acta, 35(5), 417-432.

[12] Ginder, J. M. (1998). Behavior of magnetorheological fluids. MRS Bulletin, 23(8), 26-29.

[13] Jolly, M. R., Bender, J. W., and Carlson, J. D. (1999). Properties and applications of commercial magnetorheological fluids. Journal of Intelligent Material Systems and Structures, 10(1), 5-13.

[14] Volkova, O., Cutillas, S., and Bossis, G. (1999). Shear banded flows and nematic-to-isotropic transition in ER and MR fluids. Physical Review Letters, 82(1), 233.

[15] Rankin, P. J., Horvath, A. T., and Klingenberg, D. J. (1999). Magnetorheology in viscoplastic media. Rheologica Acta, 38(5), 471-477.

[16] de Gans, B. J., Duin, N. J., Van den Ende, D., and Mellema, J. (2000). The influence of particle size on the magnetorheological properties of an inverse ferrofluid. The Journal of Chemical Physics, 113(5), 2032-2042.

[17] Wollny, K., Läuger, J., and Huck, S. (2002). Magneto sweep–A new method for characterizing the viscoelastic properties of magneto-rheological fluids. Applied Rheology, 12(1), 25-31.

[18] Laeuger, J., Wollny, K., Stettin, H., and Huck, S. (2005). A new device for the full rheological characterization of magneto-rheological fluids. International Journal of Modern Physics B, 19(07n09), 1353-1359.

[19] Laun, H. M., Gabriel, C., and Kieburg, C. (2011). Wall material and roughness effects on transmittable shear stresses of magnetorheological fluids in plate–plate magnetorheometry. Rheologica Acta, 50(2), 141-157.

[20] Jonkkari, I., Kostamo, E., Kostamo, J., Syrjala, S., and Pietola, M. (2012). Effect of the plate surface characteristics and gap height on yield stresses of a magnetorheological fluid. Smart Materials and Structures, 21(7), 075030.

[21] Ocalan, M., and McKinley, G. H. (2013). High-flux magnetorheology at elevated temperatures. Rheologica Acta, 52(7), 623-641.

[22] Ruiz-López, J. A., Fernández-Toledano, J. C., Klingenberg, D. J., Hidalgo-Álvarez, R., and de Vicente, J. (2016). Model magnetorheology: A direct comparative study between theories, particle-level simulations and experiments, in steady and dynamic oscillatory shear. Journal of Rheology, 60(1), 61-74.

[23] Laun, H. M., Gabriel, C., and Kieburg, C. (2010). Twin gap magnetorheometer using ferromagnetic steel plates—performance and validation. Journal of Rheology, 54(2), 327-354.

[24] Laun, H. M., Schmidt, G., Gabriel, C., and Kieburg, C. (2008). Reliable plate–plate MRF magnetorheometry based on validated radial magnetic flux density profile simulations. Rheologica Acta, 47(9), 1049-1059.

[25] de Vicente, J., Segovia-Gutiérrez, J. P., Andablo-Reyes, E., Vereda, F., and Hidalgo-Álvarez, R. (2009). Dynamic rheology of sphere-and rod-based magnetorheological fluids. The Journal of chemical physics, 131(19), 194902.

[26] Johnston, M. T., and Ewoldt, R. H. (2013). Precision rheometry: Surface tension effects on low-torque measurements in rotational rheometers. Journal of Rheology, 57(6), 1515-1532.

[27] M acosko, C. W. Rheology: Principles, Measurements, and Applications. (Wiley-VCH, New York, 1994).

[28] Morillas, J. R., Bombard, A. J., and de Vicente, J. (2018). Enhancing magnetorheological effect using bimodal suspensions in the single-multidomain limit. Smart Materials and Structures, 27(7), 07LT01.

Chapter 10. Rheological behavior of Magnetic Colloids in the Borderline between Ferrofluids and Magnetorheological Fluids

Keshvad Shahrivar, Jose R. Morillas, Yurena Luengo, Helena Gavilan, Puerto Morales, Claas Bierwisch and Juan de Vicente

This article is published in: Journal of Rheology, 63(4), 547-558 (2019).

DOI: https://doi.org/10.1122/1.5093628

Abstract

Magnetic colloids were formulated by dispersion of magnetic oxide spheres in water. Their rheological behavior was investigated for a wide range of particle diameters covering in detail the magnetic single-multidomain transition and therefore spanning the gap between ferrofluids (FFs) and conventional magnetorheological fluids (MRFs). The magnetoviscous effect (i.e. the ratio between the viscosity increment under field and the viscosity value in the absence of field) was found to reach a maximum for a critical particle size in the single-multidomain transition region. The observations were explained in terms of magnetization changes with particle size. The results obtained are applicable to any magnetic material (not only iron oxides) and therefore constitute a new route to enhance MR effect. For very small particle sizes (in the superparamagnetic region) thermal motion plays a crucial role and the dimensionless viscosity scales with the Peclet number as expected for Brownian Hard Spheres. For larger particle sizes and $\lambda > 1$ the dimensionless viscosity scales with the Mason number and closely follows the Structural Viscosity Model under the Mean Magnetization Approximation.

10.1 Introduction

Magnetic colloids constituted by dispersions of a solid magnetic phase in a non-magnetic liquid carrier are traditionally classified in two groups in view of their rheological characteristics: ferrofluids (FFs) and magnetorheological fluids (MRFs) (see Fig. 10.1). On the one hand, FFs are formed by nanosized superparamagnetic (SP) particles, typically ferrites. Because of their small size, these particles are subjected to Brownian (thermal) motion and do not aggregate in spite of the fact that they are constituted by a single magnetic domain and hence magnetically interact even in the absence of magnetic fields [1]. On the other hand, MRFs are constituted by micronsized ferromagnetic particles, typically carbonyl iron. Because of their large size, these particles are not significantly affected by Brownian motion and are constituted by magnetic multidomains [2]. The critical size delimiting the borderline between these two well differentiated rheological behaviors is typically defined in the literature through the so-called λ ratio or coupling constant. The λ ratio is a measure of the importance of magnetostatic energy ($\propto a^3\langle M_p\rangle^2$)

to the thermal energy ($\propto \kappa_B T$). Here, a is the particle radius, $\langle M_p \rangle$ is the mean magnetization of the particle, κ_B is the Boltzmann constant and T is the absolute temperature.

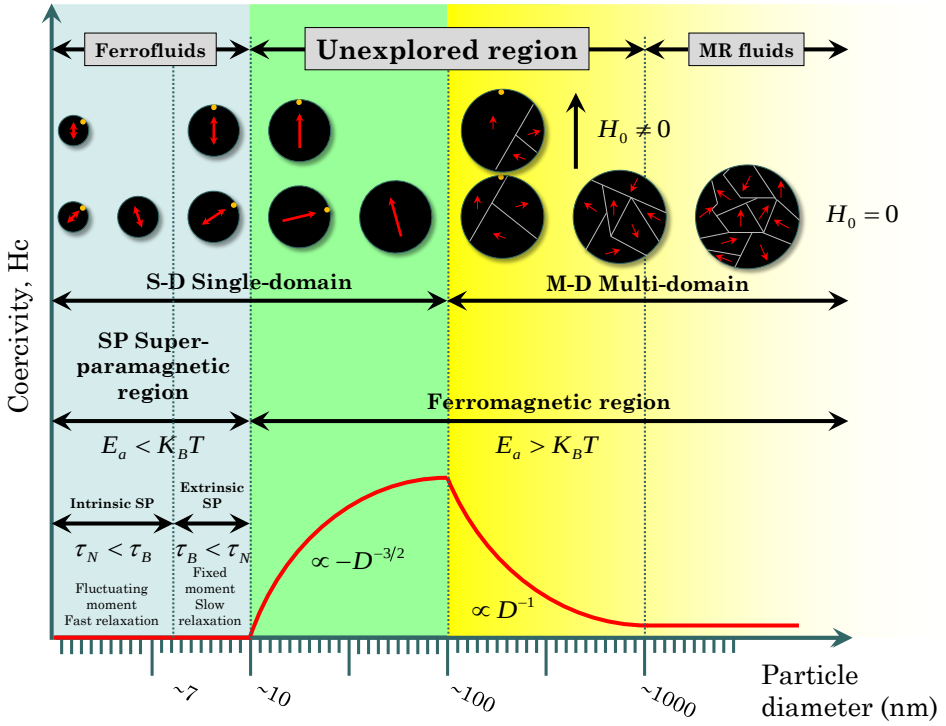

Figure 10.1: Schematics of the size region explored in this work bridging the gap between ferrofluids and magnetorheological fluids. Particle magnetization and variation of intrinsic coercivity with particle diameter. The particle size estimations correspond to magnetite. In the SP (ferromagnetic) region the anisotropy energy (E_a) is smaller (larger) than the thermal energy ($\kappa_B T$).

Recent work involving both kinds of materials, FFs and MRFs, demonstrates the need to better explore the frontier between these two limiting scenarios. On the one hand, FFs with larger particles are desired for a stronger magnetic response in biomedical applications [3-6]. On the other hand, MRFs with smaller particles are required to minimize sedimentation in mechanical engineering applications [7].

From a rheological perspective, the behavior of FFs seems to be well understood [1,8,9]. Most publications suggest that there is not a shear rate dependence unless for concentrated FFs. Two regions are identified within the SP regime depending on whether Néel relaxation time (τ_N) or Brownian relaxation time (τ_B) governs: intrinsic SP (if $\tau_N < \tau_B$) and extrinsic SP (if $\tau_B < \tau_N$). According to Ref. [10], the transition from intrinsic to extrinsic SP occurs for diameters of 14 nm. However, the particular value is strongly dependent on the material. For dilute FFs in the intrinsic SP regime the viscosity increase under field is negligible because of the thermal fluctuation of the magnetic moments within the particles. However, for dilute FFs in the extrinsic SP regime (so-called Brownian FFs), a slight viscosity increase occurs under fields perpendicular to the vorticity due to the hindrance of physical particle's rotation [11,12]. In concentrated ferrofluids there is typically a shear thinning behavior and in some cases the appearance of a yield stress. In this case, the formation of field-induced aggregates, involving the

largest particles in the size distribution are necessary to explain the magnetoviscous effect [13].

More recent work has mostly focused on MRFs with $\lambda \gg 1$. Under this premise, magnetostatic potential energy of interaction overcomes thermal energy promoting the formation of field-guided structures. In the case of shearing flows under uniaxial DC fields, models based on single-particle width gap-spanning chains predict a negligible particle size effect on the apparent yield stress. This is because the shear stress is proportional to the horizontal force required to separate two particles under affine motion ($\propto a^2$ in dipolar approximation) and to the number of chains per unit surface ($\propto a^{-2}$). However, contrary to the theoretical expectation, some experimental works demonstrate that the larger the particle size the larger the yield stress under fields for $\lambda \gg 1$ [14-17]. Up to now, there is not a commonly accepted explanation for this observation. In this manuscript we will give an explanation in terms of the mean magnetization increase with particle size.

To the best of our knowledge, the borderline between FF and MRF behavior (i.e. the region for $\lambda \approx 1$) has not been studied in the literature yet for dispersions of solid magnetic particles under a rheological perspective. In this manuscript we aim to explore the effect of particle size and magnetic field strength in this particular region. For this purpose we carefully prepare a wide range of highly monodisperse spherical magnetic particles having different diameters from 8 nm to 370 nm. This requires the use of different syntheses routes. These particles are then characterized in detail. Next, the particles are dispersed in water where the physicochemical conditions (and therefore the colloidal stability) can be easily controlled and finally the rheological properties of the suspensions are evaluated under magnetic fields. Results are then scaled using Peclet and Mason numbers for small and large particle sizes, respectively.

10.2 Experimental

10.2.1 Synthesis of the magnetic particles

Magnetic particles used in this work are based on magnetic iron oxides -either maghemite or magnetite (γ-Fe_2O_3 or Fe_3O_4)- because of two reasons. On the one hand, because they are more stable to oxidation if compared to pure metals (Fe, Co and Ni). On the other hand, because of the versatility of the synthesis procedures. In particular, those used in this work are based on precipitation in aqueous media which is very simple if compared to thermal decomposition or multistep synthesis. We followed three direct methods starting from different iron oxidation states (Fe(II)+Fe(III), Fe(II) and Fe(III)) for the preparation of magnetic particles kinetically stable in aqueous media with sizes from 8 nm to 370 nm.

The smallest nanoparticles (8 nm and 12 nm) used in this work were obtained following a modification of Massart's coprecipitation protocol [18]. Briefly, magnetite particles were synthesized by adding 425 mL of an aqueous solution of $FeCl_3 \cdot 6H_2O$ (0.09 M) and $FeCl_2 \cdot 4H_2O$ (0.054 M) to 75 mL of alkaline medium. The particle size can be tuned by the nature of the alkaline medium, the addition rate, and the aging time [19]. Thus, fast addition rates (40 mL/s) and NH_4OH (25 %) alkaline solutions were used to produce the 8 nm particles. Slow addition rates (0.2 mL/s) over NH_4OH (25 %) followed by a heating process at 90 ºC for 1 h were used to synthesize 12 nm particles (see Table 10.1). After every synthesis the magnetic particles were washed three times with distilled water and

collected with the help of a permanent magnet. Then, an optimized oxidizing (so-called acidic) treatment was carried out. This procedure is based on an oxidation-dispersion process previously reported in the literature [20,21]. Through a series of partial dissolution-recrystallization steps, we oxidized magnetite to maghemite (γ-Fe_2O_3). This step enhanced both the kinetic stability of the magnetic particles and their magnetic properties. It also reduced the size distribution to a polydispersity index (PDI) of around 0.2. Note that the PDI is defined as the ratio between the standard deviation (σ) and the mean particle diameter as obtained by TEM (D_{TEM}). Briefly, 300 mL of HNO_3 (2M) were added to 500 mL of the dispersion produced previously, and the mixture was stirred for 15 min. Then, the supernatant was removed by magnetic decantation and 75 mL of $Fe(NO_3)_3$ (1 M) and 130 mL of water were added to the magnetic particles. The mixture was heated to boiling temperature and stirred for 30 min. The particles were then cooled to room temperature and, by magnetic decantation, the supernatant was substituted by 300 mL of HNO_3 (2 M) and the solution stirred for 15 min. Finally, the magnetic particles were washed three times with acetone and redispersed in water. A rotary evaporator was used to remove any acetone waste as well as for concentrating the sample.

Size (nm)	Media	Iron salt nature	[Fe] (M)	Base salt nature	$[OH^-]$ (M)	$[OH^-]$ excess (M)	Oxidant reductant salt nature	$[NO_3^-]$ (M)
8	100% H_2O fast addition rate	$FeCl_2$/ $FeCl_3$	$[Fe^{3+}]$=0.054 $[Fe^{2+}]$=0.09	NH_4OH	0.25	—	—	—
12	100% H_2O slow addition rate	$FeCl_2$/ $FeCl_3$	$[Fe^{3+}]$=0.054 $[Fe^{2+}]$=0.09	NH_4OH	0.25	—	—	—
30	30% EtOH	$FeCl_2$	$[Fe^{2+}]$= 0.05	NaOH	0.121	0.02	$NaNO_3$	0.05
43	100% H_2O	$FeSO_4$	$[Fe^{2+}]$= 0.2	NaOH	0.422	0.02	$NaNO_3$	0.2
84	100% H_2O	$FeSO_4$	$[Fe^{2+}]$=0.032	NaOH	0.067	0.001	$NaNO_3$	0.1
116	Ethylene glycol	$FeCl_3$	$[Fe^{3+}]$=0.213	CH_3CO ONa	0.76	—	Ethylene glycol	—
370	25% EtOH	$FeSO_4$	$[Fe^{2+}]$= 0.2	KOH	0.361	-0.043	KNO_3	0.2

Table 10.1: Synthesis conditions for the fabrication of the iron oxide nanoparticles. All concentrations correspond to the final concentration.

To obtain particles with sizes from 30 to 370 nm we used a procedure consisting in the precipitation of an iron (II) salt ($FeCl_2$ or $FeSO_4$) in a basic media (NaOH or KOH) and in the presence of a mild oxidant ($NaNO_3$ or KNO_3) under stirring in an oxygen free atmosphere (glove box under nitrogen) giving rise to magnetite nanoparticles [22,23]. The reaction was carried out in a 500 ml double-walled reactor heated by means of a fluid set to 90 ºC using a thermostat recirculating bath. In a typical experiment, two solutions were prepared independently before the precipitation: (a) 200 ml of water containing OH^- and NO_3^- to obtain a final concentration of 0.2 M OH^- and 0.02 M OH^- excess. The hydroxyl ion excess concentration $[OH^-]_{excess}$ was calculated using $[OH^-]_{excess} = [OH^-] - 2[Fe^{2+}] - n[H^+]$ where n is 1 or 2 depending on the monoprotic or diprotic character of the acid used to dissolve the iron salt [24]. (b) 50 ml of Fe^{2+} in 10^{-2} M of acid solution (H_2SO_4, HCl depending on the iron salt) to obtain a final concentration value of 0.2 M. The dissolution of Fe^{2+} was carried out in acid medium immediately before its use to prevent uncontrolled hydrolysis. The iron salt concentration was selected on the basis of previous results [4,22,24] (see Table 10.1). The iron (II) solution (b) was quickly added to the basic solution (a) under stirring, obtaining a final volume of 250 ml. When the

addition was completed the green rust formed initially was mechanically stirred for 15 min. After this time, this reaction intermediate was aged at 90 ºC for 24 h without agitation to obtain magnetite nanocrystals. At the end of the synthesis the system was left to cool and the nanocrystals were separated by magnetic decantation followed by several washings with distilled water. The oxidation rate and, therefore, the average particle size, was controlled by changing the reaction conditions, such as the iron salt and base concentration (from 0.05 to 0.2 M and from 0.06 to 0.4 M, respectively), the nature of the iron, base and nitrate salt and the use of mixed solvents (water and different proportions of water/ethanol) (see Table 10.1). The stabilities of the different green rusts and the Fe(II) dehydration and oxidation processes are responsible for the differences in magnetite particles sizes [23].

The 116 nm sample was synthesized by a polyol method. In this process, a precursor compound is suspended in a liquid polyol. The suspension is stirred and heated to a given temperature that reaches the boiling point of the polyol. During this reaction, the iron salt becomes solubilized in the polyol, forms an intermediate, and is then reduced to form iron oxide nuclei that will then evolve to form the particles. Typically, 2.702 g of $FeCl_3$ and 0.75 g of trisodium citrate were first dissolved in ethylene glycol (47 mL), afterward 4.89 g of sodium acetate was added with magnetic stirring [25]. The mixture is stirred vigorously for 30 min and then sealed in a Teflon-lined aluminium autoclave (125 mL capacity) and maintained at 200 °C for 10 h. It is then allowed to cool down to room temperature and the black product was washed 3 times with distilled water by centrifugation.

10.2.2 Characterization of the magnetic particles

Particle size and shape were determined by transmission electron microscopy (TEM) using a 200 keV JEOL-2000 FXII microscope. TEM samples were prepared by placing one drop of a dilute water suspension of magnetic particles on a copper grid covered with a perforated carbon film and allowing the solvent to evaporate slowly at room temperature. The mean particle size and distribution were evaluated by measuring the largest internal dimension of at least 300 particles. Afterwards, data were fitted to a log normal or Gaussian distribution to obtain the mean size (D_{TEM}) and the standard deviation (σ) representative of the absolute error of the measurement.

The crystal structure of the samples was identified by X-ray powder diffraction. The test was performed in a Bruker D8 Advance powder diffractometer using Cu Kα radiation with an energy-discriminator (Sol-X) detector. The patterns were collected between 10° and 70° in 2θ. The XRD spectra were indexed to an inverse spinel structure. The average crystallite size was calculated by Scherrer's equation using the half width of the (311) X-ray diffraction peak using the utilities of the automatic powder diffraction computer program (APD) from Phillips. The error in the crystallite sizes obtained by use of the Scherrer's equation is ± 0.1 nm and is related to the instrumental line width of the diffractometer ($\Delta 2\theta = 0.11°$).

The magnetic characterization of the powders was carried out using a vibrating sample magnetometer (MagLabVSM, Oxford Instrument). Coercive field and saturation magnetization values were obtained from the hysteresis loops recorded at room temperature (290 K) after applying a magnetic field of ± 4000 kA/m. Saturation magnetization values were evaluated by extrapolation to infinite field the experimental results obtained in the high field range where the magnetization linearly decreases with

$1/H$. Samples were prepared by packing the powder into pellets. The remnant field of the VSM is around 1 kA/m.

10.2.3 Colloidal stability of the magnetic suspensions

The magnetic particles were thoroughly dispersed in milli-Q water using a centrifugal mixer at a particle concentration of $\phi = 0.011 \pm 0.001$ (1.1 vol%). We assumed a particle density of 5 g/cm^3. A careful mixing protocol was especially important in the case of particles having intermediate sizes.

The pH of the suspensions was measured using a Metrohm pH meter (model 713) and the electrokinetic properties of the suspensions were determined with a Zetasizer Nano ZS (Malvern instrument). In particular, we measured the conductivity, hydrodynamic diameter and electrophoretic mobility. The Zeta potential was calculated using the Smoluchowski formula. The turbidity of the suspensions was determined using a multiple light scattering technique (Turbiscan Classic MA 2000, Formulaction, France). In these experiments, the suspensions are placed inside a cylindrical plastic tube and scanned from the bottom to the top with a pulsed near-infrared light source. The light transmitted through the sample is measured using an optical sensor along the height of the cell during time.

10.2.4 Colloidal suspension rheometry

The rheological evaluation of the suspensions was carried out using parallel disks of diameter 20 mm and gap thickness of 300 μm in a MCR 501 stress-controlled Anton Paar rheometer with the MRD70/1T geometry. In this fixture, the magnetic field is applied perpendicular to the plates in the velocity gradient direction. External magnetic field strengths investigated ranged from 0.8 to 137 kA/m. All the tests reported in this manuscript were performed under isothermal conditions at room temperature. Shearing flow tests were carried out using the following procedure: (i) the sample was preconditioned at a constant shear rate of 100 s^{-1} for 20 s, (ii) the magnetic field was applied instantly and the suspension was left to structure for 20 s, (iii) the torque was logarithmically ramped at a rate of 5 points/decade from 10^{-4} to 10^{2} mN·m with a measuring time of 5 seconds per data point. The tests where stopped if the shear rate exceeded 1000 s^{-1}. All measurements reported in this work correspond to torques larger than 0.1 μN·m and shear rates above 0.2 s^{-1}.

10.3 Theory and simulations

10.3.1 Ferrofluid (FF) limit

As stated in Sec. 10.1, FFs are dispersions of SP particles in a liquid carrier. In the dilute case, FFs are essentially Newtonian and the shear viscosity does not depend much on the shear rate. From a rheological perspective, the effect of magnetic field strength is negligible if the particles are intrinsically SP. Only in the case of extrinsic SP particles the viscosity slightly increases with the field as described by the rotational viscosity model [12]. Independently on the field strength, the rheological behavior of FFs should be scaled using the Peclet number similarly to Hard Sphere systems [26]:

$$\mathrm{Pe} = \frac{\dot{\gamma}}{D_0/a_H^2} = \frac{6\pi\eta_c\dot{\gamma}a_H^3}{\kappa_B T} \tag{10.1}$$

Here, $\dot{\gamma}$ is the magnitude of the shear rate tensor, D_0 is the diffusion coefficient of an isolated particle, a_H is the hydrodynamic radius of the particles, η_c is the viscosity of the carrier fluid (water), κ_B is Boltzmann constant and T is the absolute temperature. In Eq. (10.1) only the translational diffusion is considered because it is expected to dominate over the rotational one. The Peclet number characterizes the importance of the shear rate compared to the natural relaxation time due to Brownian motion.

10.3.2 Magnetorheological (MR) limit

Under the Mean Magnetization Approximation, the rheological performance of conventional MRFs, constituted by magnetic particles in a non-magnetic liquid carrier, is governed by the so-called Mason number [27]:

$$\mathrm{Mn} = \frac{72\eta_c\dot{\gamma}}{\mu_0\mu_{cr}\langle M_p\rangle^2} \tag{10.2}$$

Here, μ_0 is the permeability of vacuum, μ_{cr} is the relative permeability of the liquid carrier ($\mu_{cr}\sim 1$ in the case of water) and $\langle M_p\rangle$ is the mean magnetization of the particles.

It is worth to remark that the Mason number Mn (Eq. (10.2)) is related to the Peclet number Pe (Eq. (10.1)) via $\mathrm{Mn}\lambda = 2\mathrm{Pe}/3$ with the λ ratio expressed as follows [27,28]:

$$\lambda = \frac{\pi\mu_0\mu_{cr}a^3\langle M_p\rangle^2}{18\kappa_B T} \tag{10.3}$$

Here, a is the radius of the magnetic core of the particle (typically $a \lesssim a_H$).

The rheological behavior of conventional MRFs in a shearing flow is well described by a Casson plastic equation [28]. This equation is a limiting case of the Structural Viscosity Model proposed by Ref. [29] for $\eta_0 \gg \eta_\infty$. In dimensionless form, the Casson equation can be written as follows:

$$\frac{\eta}{\eta_\infty} = 1 + \left(\frac{\mathrm{Mn}}{\mathrm{Mn}^*}\right)^{-1} + 2\left(\frac{\mathrm{Mn}}{\mathrm{Mn}^*}\right)^{-1/2} \tag{10.4}$$

Here, η is the shear viscosity, η_∞ is the high shear viscosity, and Mn^* is a critical Mason number that determines the transition from magnetostatic to hydrodynamic control of the suspension structure. Mn^* is related to the *apparent yield stress* τ_y as follows:

$$\mathrm{Mn}^* = \frac{72\tau_y}{\mu_0\mu_{cr}\langle M_p\rangle^2}\frac{\eta_c}{\eta_\infty} \tag{10.5}$$

For dilute suspensions and low magnetic field strengths, the Mean Magnetization Approximation becomes exact. In this case $\eta_\infty \approx \eta_c$ and a linear relationship exists between Mn^* and ϕ [27]: $\mathrm{Mn}^* = A\phi^B$ where A = 0.235 and B = 0.972 (note that $\langle M_p\rangle$ is a weak function of the volume fraction [27]). Using this expression for the particle concentration of interest in this work, ϕ = 0.011, we get Mn^* = 0.003.

10.3.3 Particle level simulations

Simulations were performed to ascertain the role of the particle and magnetic moment rotation in the suspension viscosity. Two sets of DEM simulations [30] were performed in SimPARTIX® software package (https://www.simpartix.com) by fixing or not the particle magnetic moment to the particle body. In addition, to decouple these results from

the effect of magnetization enhancement, in both sets of simulations, magnetic moment magnitude was constant $m = VM_S$ with $M_S = 497.76$ kA/m.

Firstly, as a control, the magnetic moment was supposed to be always aligned with the applied field and particle rotation was not considered. Therefore, only translational equations of motion for each particle are solved:

$$m_p \ddot{\boldsymbol{r}}_i = \boldsymbol{F}_i \tag{10.6}$$

Here m_p, $\ddot{\boldsymbol{r}}_i$ and $\boldsymbol{F}_i$ are ith-particle's mass, acceleration and total force acting on it respectively. In these simulations, particles interact with other particles, walls and carrier fluid through magnetic dipolar, Hertz repulsive and Stokes' drag forces:

$$\boldsymbol{f}_{ij}^{mag} = \frac{3\mu_0}{4\pi}\left[\frac{(\boldsymbol{m}_i \cdot \boldsymbol{m}_j)\boldsymbol{r}_{ij} + (\boldsymbol{m}_j \cdot \boldsymbol{r}_{ij})\boldsymbol{m}_i + (\boldsymbol{m}_i \cdot \boldsymbol{r}_{ij})\boldsymbol{m}_j}{r_{ij}^5} - 5\frac{(\boldsymbol{m}_i \cdot \boldsymbol{r}_{ij})(\boldsymbol{m}_j \cdot \boldsymbol{r}_{ij})\boldsymbol{r}_{ij}}{r_{ij}^7}\right] \tag{10.7a}$$

$$\boldsymbol{f}_{ij}^{rep} = \frac{2}{3}\frac{E}{1-\nu^2}\sqrt{\frac{a}{2}}h_{ij}^{3/2}\frac{\boldsymbol{r}_{ij}}{r_{ij}} \tag{10.7b}$$

$$\boldsymbol{f}_i^{drag} = -6\pi\eta_c a(\dot{\boldsymbol{r}}_i - \boldsymbol{u}(\boldsymbol{r})) \tag{10.7c}$$

where $\boldsymbol{m}_i = V\boldsymbol{M}_i$ is the ith-particle dipole moment, V its volume and $\boldsymbol{M}_i$ its magnetization. $\boldsymbol{r}_{ij} = \boldsymbol{r}_i - \boldsymbol{r}_j$ is the relative position of ith-particle respect to jth-particle, E is the Young's modulus, ν is the Poisson's ratio, $h_{ij} = 2a - r_{ij}$ is the interpenetration distance during a contact and $\boldsymbol{u}(\boldsymbol{r})$ is the background carrier fluid velocity.

Secondly, in another set of simulations coercivity was also taken into consideration by solving, together with previous equations, the rotational degrees of freedom:

$$\underline{I}\ddot{\boldsymbol{\theta}}_i = \boldsymbol{T}_i \tag{10.8}$$

Here $\underline{I}$ is the inertia tensor of the particles, $\ddot{\boldsymbol{\theta}}_i$ is the angular acceleration of the ith-particle and $\boldsymbol{T}_i = \boldsymbol{m}_i \times \boldsymbol{B}(\boldsymbol{r}_i)$ is the magnetic torque acting on it. Here $\boldsymbol{B}(\boldsymbol{r}_i)$ is the local magnetic induction [30] (the applied one plus contributions from surrounding particles dipoles) at the i-th particle position $\boldsymbol{r}_i$:

$$\boldsymbol{B}(\boldsymbol{r}_i) = \boldsymbol{B}_0 + \sum_j \frac{\mu_0}{4\pi}\left[3\frac{(\boldsymbol{m}_j \cdot \boldsymbol{r}_{ij})\boldsymbol{r}_{ij}}{r_{ij}^5} - \frac{\boldsymbol{m}_j}{r_{ij}^3}\right] \tag{10.9}$$

In this set of simulations, magnetic moment has the same magnitude than in the previous one but, in contrast, its direction is governed by the rotation of the particle.

Note that the purpose of these simulations is solely to investigate the difference between (i) a magnetic moment which is always aligned with the external field and (ii) a magnetic moment that is bound to an axis of the particle and, thus, causes a torque on the particle if not aligned with the external field. To focus on this property, the numerical model is otherwise chosen to be as simple as possible – only consisting of magnetic and repulsive interaction as well as fluid drag. Brownian motion is omitted and, thus, the simulations represent athermal suspensions in the limit of large λ ratios. In accordance to the neglect of Brownian motion the model particle size is chosen in the micron range.

Initially, N =1000 particles of radius a = 2.5 μm are randomly distributed (and also their magnetization randomly oriented if it applies) in a box of volume V = 127.5 × 235 × 235 μm^3 (volume fraction of 1 vol%). At time 0, a magnetic induction $\boldsymbol{B}_0$ of 67 kA/m $\cdot \mu_0$ in the x-direction (to generate anisotropic aggregates) and a simple shear flow $\boldsymbol{u}(\boldsymbol{r}) = \dot{\gamma} x \hat{\boldsymbol{z}}$ are applied. The magnetic induction corresponds to the second largest magnetic field strength used in the experiments. Equations of motions are numerically integrated using a velocity Verlet scheme.

The simulation box is bounded in the x-direction by two parallel walls also made of particles (same properties than the suspended ones) but without magnetic response and at a prescribed velocity to match fluid flow velocity $\boldsymbol{u}(\boldsymbol{r})$ at these boundaries. In the rest of box limits, periodic boundary conditions are applied. In Table 10.2, we summarize the rest of simulation parameters.

V	Simulation box volume	127.5 × 235 × 235 μm^3
N	Number of particles	1000
ϕ	Volume fraction	0.01
a	Particle's radius	2.5 μm
ρ	Particle's density	7800 kg/m^3
E	Young modulus	1 GPa
ν	Poisson's ratio	0.25
M_S	Particles' saturation magnetization	497.76 kA/m
B_0	Applied magnetic induction	67 kA/m $\cdot \mu_0$
r_{cut}	Cutoff distance for the magnetic force	$8a$ = 20 μm
η_c	Carrier fluid's viscosity	1 mPa·s
Δt	Time step (adaptively calculated)	~ 7 ns

Table 10.2: Simulation parameters. Only saturation magnetization is taken from magnetite. The remaining parameters are chosen, in a feasible range, to speed up simulations while preserving all relevant physical mechanisms.

Once the system has reached a stationary state, the resulting shear stress is computed as follows:

$$\tau = \eta_c \dot{\gamma} - \frac{1}{V} \sum_{i,j>i} (\boldsymbol{r}_{ij} \cdot \hat{\boldsymbol{x}}) \left[\left(\boldsymbol{f}_{ij}^{mag} + \boldsymbol{f}_{ij}^{rep} \right) \cdot \hat{\boldsymbol{z}} \right] \tag{10.10}$$

The first term in the RHS stands for viscous stress due to the background fluid while the second one comes from internal forces in the particles system (i index only runs over suspended, i.e. magnetic, particles).

10.4 Results and discussion

10.4.1 Morphological and structural characterization of the particles

A schematic of the experimental synthesis conditions used to obtain the particles is reported in Table 10.1. A dramatic change in particle size was observed depending on the synthesis method. The smallest nanoparticles were obtained by coprecipitation of Fe^{2+}/Fe^{3+} salts and the difference in the particle size was achieved by slowing the base addition rate. On the other hand, magnetic nanoparticles with increasing diameters from 30 nm up to 370 nm were synthesized by oxidative precipitation of a Fe^{2+} salt by controlling the iron salt concentration, which is related to the excess of Fe^{2+} or OH^- in the initial reaction media (Table 10.1, Fig. 10.2) [24]. Thus, larger spherical particles of 370 nm in diameter were obtained in Fe^{2+} excess. However, in excess of OH^-, the largest magnetic particles were obtained using $FeSO_4$, KOH and KNO_3 while the smallest ones using $FeCl_2$, NaOH and $NaNO_3$ showing the effect of the counter ions in the particle growth process [23]. Finally, samples with 116 nm particle size were prepared by a polyol method. In this case each particle consists on aggregates of smaller cores. In view of Fig. 10.2 particle shape also changes when changing the particle size. However, we do not expect any influence of the particle shape in the rheological behavior of the suspensions because the suspensions are very dilute (ϕ = 0.011 ± 0.001).

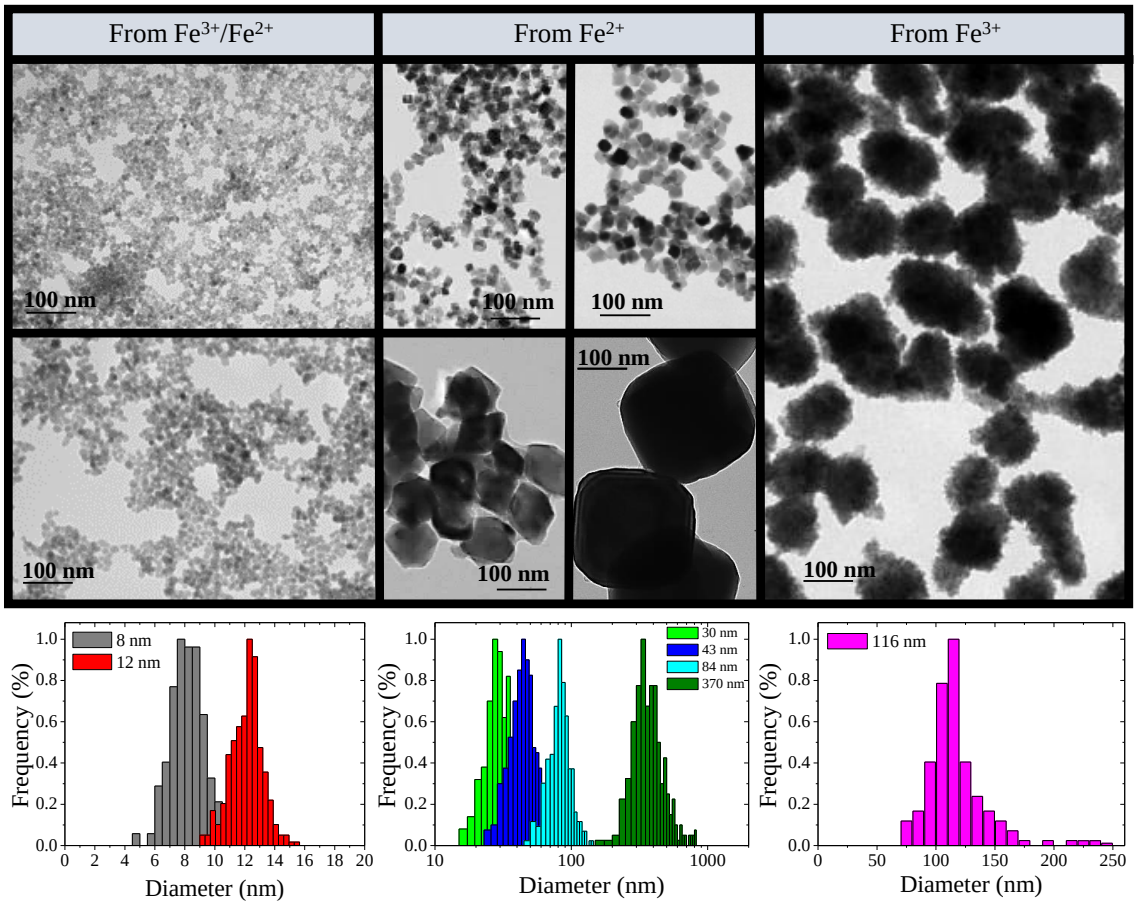

Figure 10.2: Micrographs and size histograms of the particles used in this work.

X-ray diffractograms for the samples prepared in water and water/ethanol media are shown in Fig. 10.3. Independently on the iron salt precursor, the formation of crystalline magnetite particles was confirmed by the X-ray analysis. All peaks were assigned to a

spinel structure similar to magnetite (JCPDS 890691). Crystal sizes calculated from the (311) peak broadening were similar to the particle sizes obtained by TEM except for 116 nm sample, revealing the formation mechanism of these particles by aggregation of much smaller subunits (Table 10.3). According to this, the diffraction peaks become broader as the particle size decreases except for 116 nm sample.

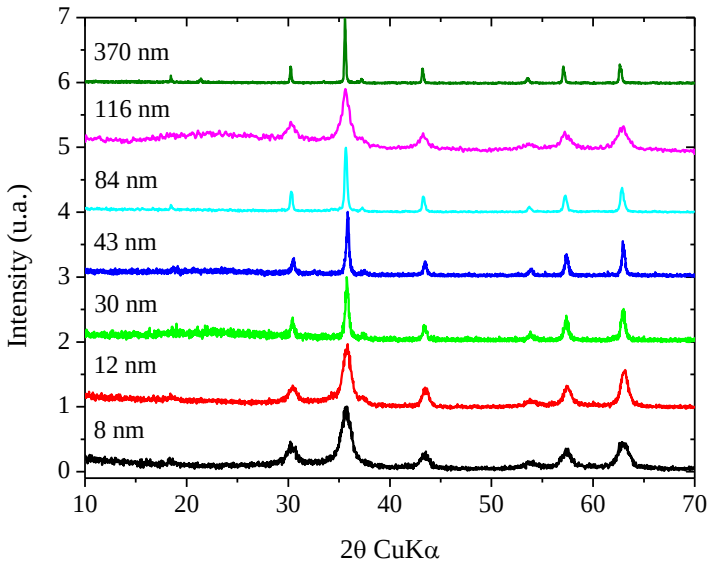

Figure 10.3: X-ray diffraction patterns for particles of different sizes.

10.4.2 Magnetic properties of the particles

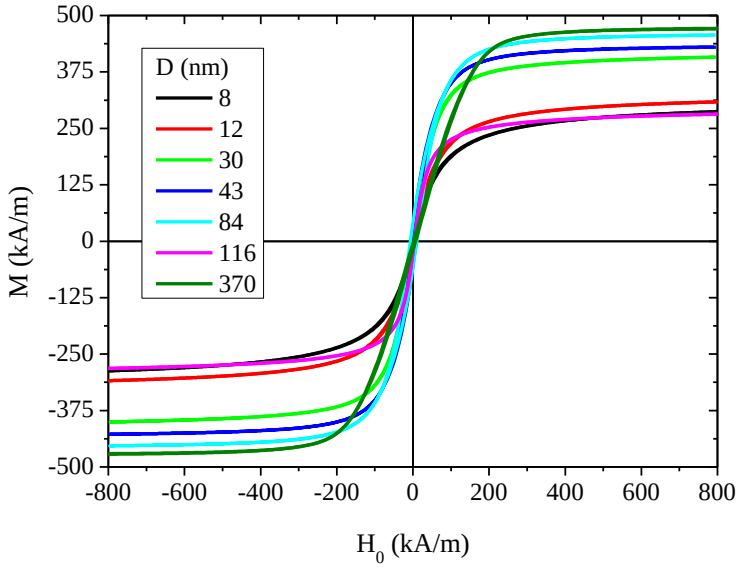

Figure 10.4: Magnetization curves at room temperature for different particle sizes.

Figure 10.4 contains magnetization curves at room temperature. Very different behaviors were observed depending on the particle size. Hysteretic parameters are summarized in Table 10.3 for magnetic particles with different sizes. In general, it can be observed that saturation magnetization (M_S) increases with increasing particle size from 308.1 to 496.6 kA/m for 370 nm particles, a value close to the one reported for bulk magnetite [31] (see Fig. 10.5a). Although saturation magnetization is described as an intrinsic magnetic property, a reduction with the nanoparticle size, as this observed in our samples, is

frequently showed and may explain why some experimental works exhibit a larger yield stress for larger particle sizes also for $\lambda \gg 1$ [14-17]. The reduction in M_S is significant for particles smaller than 20 nm and accounts for the increase in surface/volume ratio as the nanoparticle size decreases [21]. Surface effects reducing the M_S value are related to the presence of a disordered iron oxide surface layer around the particle, that seems to be the case here, or by the bonding of organic molecules when surfactants are present [32]. In the last case, M_S could increase or decrease as the particle size decreases.

Diameter (nm)	TEM size (nm)	XRD size (nm)	Saturation magnetization M_S (kA/m)	Coercive field H_C (kA/m)	Initial magnetic susceptibility χ_i
8	8.3 (0.21)	8	308.1	2.1	3.9
12	12.1 (0.19)	12	326.1	1.7	4.2
30	30.4 (0.22)	31	445.4	3.9	5.8
43	42.9 (0.17)	42	469.3	6.4	6.6
84	84.4 (0.15)	81	496.1	8.5	5.9
116	116.2 (0.21)	11	314.0	3.9	6.1
370	369.7 (0.23)	348	496.6	4.4	2.9

Table 10.3: Experimental results on mean particle diameters obtained by TEM and XRD and magnetic properties. Magnetic iron oxide density: 5 g/cm^3

Table 10.3 and Fig. 10.5a also shows the variation of the coercivity (H_C) as a function of the nanoparticle size. This extrinsic property depends on the size, shape and interactions between the particles [33]. As expected, a maximum in the coercive field is observed that determines the transition between single- to multidomain behavior. In the single-domain region the magnetization of the particle is reversed through *spin rotation*. However, in the multidomain region, the magnetization is reversed through *domain wall motion*. In the curve we can identify up to four different regions. These regions are schematically represented in Fig. 10.1.

1) The smallest nanoparticles (below 12 nm) showed a SP behavior with nearly zero coercivity and remanence. In this region the magnetic moment of the particles rotates continuously changing orientation because of the importance of thermal motion.
2) For larger particles (above 12 nm), coercivity increases as $\propto -a^{-3/2}$. In our particular case it goes from 1.7 kA/m (12 nm) up to 8.5 kA/m (84 nm). Similar observations have been reported in the literature for magnetite particles. An increase in coercivity, at room temperature, from 0 kA/m to 4 kA/m has been measured when the size is increased from 13 nm to 45 nm [34,35].
3) Then, the coercive field reaches a maximum for a particle size of approximately 84 nm diameter. This result is in good agreement with theoretical calculations by [36] that predicted an upper (76 nm) and lower (50 nm) critical size for the maximum in the coercivity. The theoretical critical size for single- to multidomain transition for magnetite is typically around 100 nm [37].

4) Finally, the coercive field decreases as $\propto a^{-1}$ to reach a value of 4.4 kA/m in the case of 370 nm particles. This low coercive field corresponds to a relatively small field energy to make the domains walls move.

As expected, the variation of the initial susceptibility χ_i with particle size is similar to the coercivity (see Table 10.3). We observe an increase from 3.9 for 8 nm up to 6.6 for 43 nm nanoparticles which can be due to the reduction in surface area when increasing the nanoparticle size. However, χ_i decreases for particles of 84 to 370 nm (χ_i = 5.9 and 2.9, respectively).

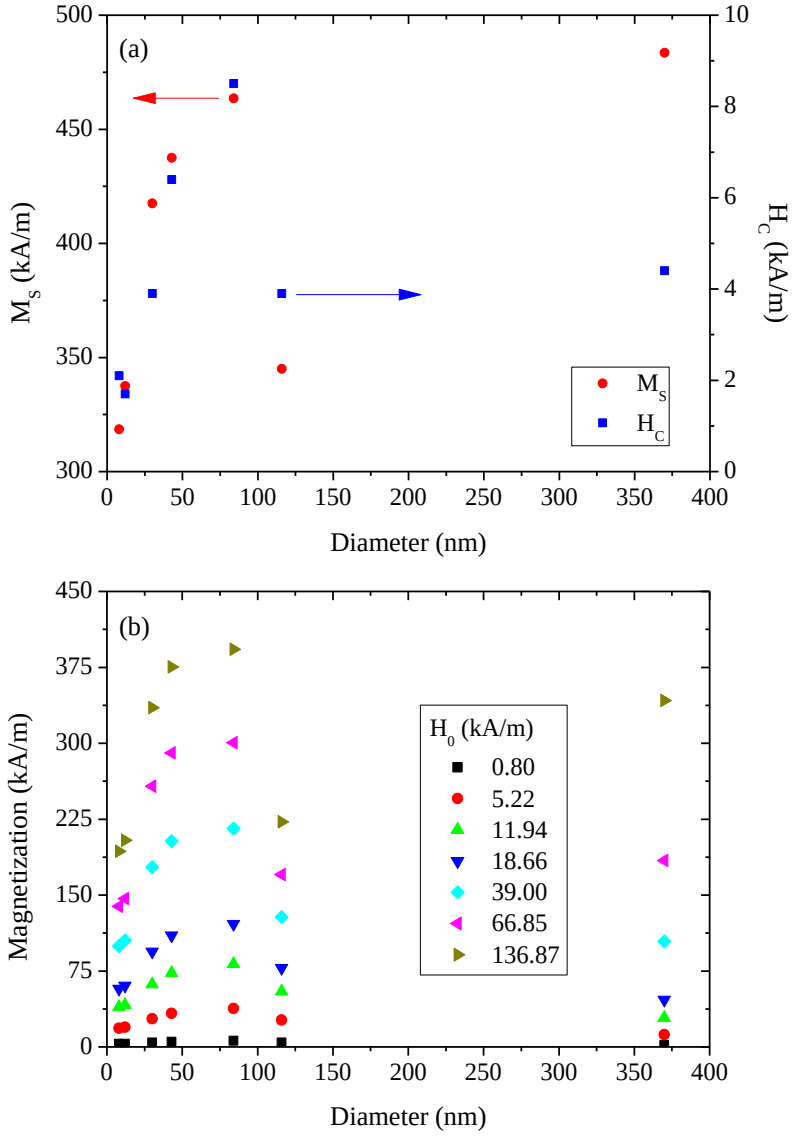

Figure 10.5: a) Saturation magnetization (M_S) and coercivity values (H_C) at room temperature for particles with different sizes. b) Particle magnetization as a function of the particle diameter at different magnetic field strengths.

More important than the initial susceptibility is the magnetization of the particles because it appears in the dimensionless numbers governing the rheological response (see Eqs. (10.2) and (10.3)) and because it incorporates a field dependence. As expected, the magnetization follows a similar trend to the coercivity. Experimental results are shown in Fig. 10.5b for different field strengths. Again, there is a critical particle size corresponding to the single- multidomain transition region. The smaller the particle size the lower the

magnetization as a result of the increasing importance of thermal motion. Above the critical size, particles contain magnetic domains and the net contribution is not zero under field. However, the magnetization is always smaller than the magnetization for particles below the critical size where a single domain exists. The point is that in multidomain particles the external field competes with the demagnetizing field and therefore the magnetization decreases. The observed maximum in the magnetization curve shown in Fig. 10.5b is closely related to the maximum in the coercive field. Importantly, these results are applicable whatever the material (being magnetically soft or hard).

10.4.3 Colloidal stability

Physico-chemical characteristics of the suspensions prepared are summarized in Table 10.4. The two smallest particles exhibited a positive charge while the rest where negatively charged. According to DLVO theory [38], data contained in Table 10.4 suggest that in all suspensions studied, the particles are highly charged (Zeta potential larger than 20 mV) and the suspensions should remain stable against flocculation. However, the hydrodynamic sizes of the particles in the transition between mono- and multidomain regions are clearly larger than the sizes observed in TEM. This is due to the formation of aggregates induced by remnant magnetostatic interactions that overcome electrostatic double layer repulsions.

Diameter (nm)	pH	Electrophoretic mobility (μm·cm/V·s)	Conductivity (mS/cm)	Zeta potential (mV)	Hydrodynamic/TEM diameter
8	1.3	3.7	9.5	47.0	6.3
12	1.5	3.1	3.5	39.5	5.3
30	10.3	-2.9	0.603	-36.7	30.8
43	9.7	-3.2	1.943	-41.3	19.1
84	8.4	-3.3	0.189	-42.3	11.3
116	4.1	-3.2	0.967	-40.7	1.5
370	5.8	-1.6	0.007	-20.2	3.4

Table 10.4: Physico-chemical properties of the magnetic colloids investigated in this work. The particle concentration was fixed at ϕ = 0.011. The last column stands for the ratio between the hydrodynamic diameter (measured with a Zetasizer Nano ZS) and the TEM diameter (second column in Table 10.3)

Turbidity data confirm that suspensions in the transition region are not kinetically stable. Results are shown in Fig. 10.6 in the form of sediment height (h/h_0) as a function of time. Here, h is the height of the sediment-supernatant interface and h_0 is the initial height of the suspension. The transmission level remains constant as a function of time for the smaller and larger particles. This implies that the suspensions are fully stable and particles do not appreciably aggregate nor sediment in the time range investigated. However, suspensions prepared with particles in the single- multidomain transition region (30 - 84 nm) were not stable and h/h_0 decreased with time. A more appropriate way to quantify how unstable the suspensions are is through the calculation of the migration rate of the particles at the initial stage of the sedimentation process. Results are included as an inset

in Fig. 10.6. They demonstrate that, as expected, sedimentation is clearly important in the transition region.

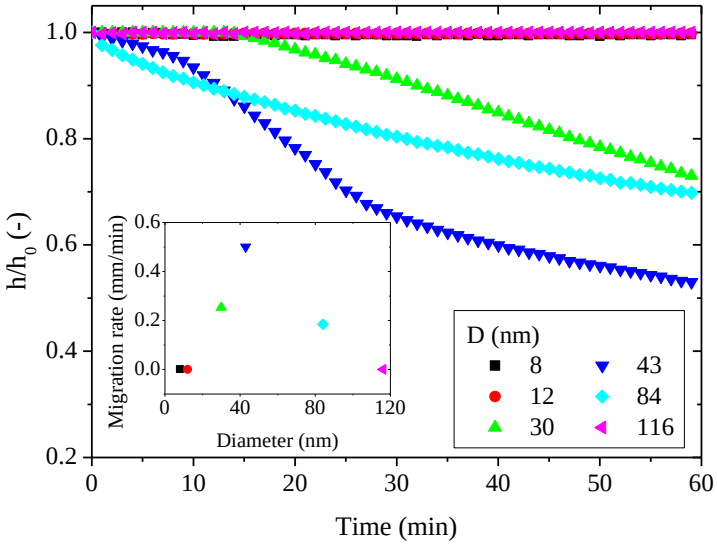

Figure 10.6: Sediment height (h/h_0) as a function of time for magnetic colloids in the single- multidomain transition region. Inset: migration rate as a function of particle size.

10.4.4 Rheological behavior

Field-induced gap-spanning structures are only expected when the λ ratio is sufficiently large. In Table 10.5 we show the calculated λ ratios for all the sizes explored at the different magnetic field strengths investigated. According to the $\lambda = 1$ criteria, only the largest particles under the presence of the largest fields result in the formation of field-induced structures (MRF limit). Other samples should form loose chain-like structures that do not connect the shearing plates and therefore a yield stress would not be observed (FF limit).

H (kA/m)	Diameter (nm)						
	8	12	30	43	84	116	370
0.8	3.03×10^{-5}	1.13×10^{-4}	3.35×10^{-3}	0.014	0.14	0.20	0.57
5.2	0.001	0.004	0.14	0.58	5.67	7.35	26.12
11.9	0.005	0.02	0.69	2.84	26.55	31.26	149.19
18.7	0.01	0.04	1.59	6.42	58.11	63.28	390.52
39.0	0.03	0.13	5.66	21.89	183.95	171.17	1955.29
66.9	0.07	0.25	11.92	44.66	356.65	301.36	6105.88
136.9	0.13	0.48	20.19	74.66	608.80	513.79	21074.12

Table 10.5: λ ratio for suspensions of magnetic particles having different sizes at different magnetic field strengths (H). The Mean Magnetization Approximation is used in the calculation of the λ ratio. The shaded region corresponds to $\lambda < 1$, while the white region corresponds to $\lambda > 1$.

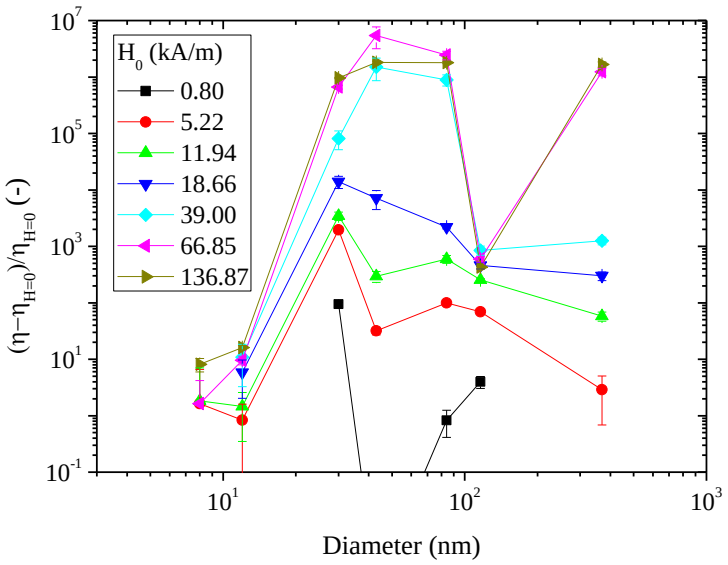

Figure 10.7: Magnetoviscous effect, $[\eta(H) - \eta(H = 0)]/\eta(H = 0)$, as a function of the particle diameter for a constant stress level (1.61 Pa) and for different magnetic field strengths.

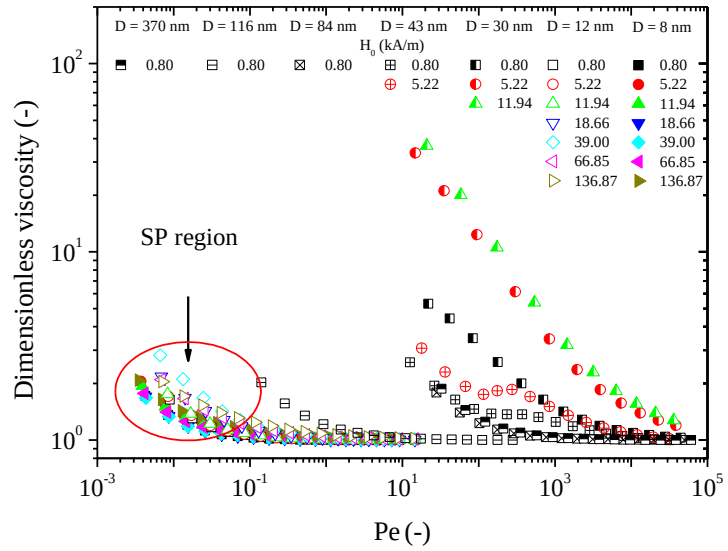

Figure 10.8: Dimensionless viscosity (η/η_∞) as a function of Peclet number (Pe) for different particle diameters and $\lambda < 1$. Data correspond to $\dot{\gamma} > 0.2$ s^{-1}. A scaling is only observed in the superparamagnetic (SP) region (i.e. FF limit).

The magnetoviscous effect is better quantified here using the relative viscosity as follows:

$$MVE = \frac{\eta(H \neq 0) - \eta(H = 0)}{\eta(H = 0)} \tag{10.11}$$

This number measures the influence of the magnetic field strength on the viscosity of magnetic colloids compared to the viscosity in the absence of a field. As observed in Fig. 10.7, the MVE experiences a maximum in a particle size that matches very well with the typical size where both the coercivity and the magnetization reaches a maximum (see Fig. 10.5). Obviously, a larger magnetization of the particles must result in a larger field-induced viscosity and therefore a larger MVE. This is an important result that

demonstrates another route for the enhancement of the MR effect; for a given magnetic field strength, the use of particle sizes in the transition from the single- to multidomain.

Another convenient way to plot viscosity curves is through the use of the Peclet number Pe and Mason number Mn [27]. In Fig. 10.8 we show dimensionless curves as a function of Pe for $\lambda < 1$. Dimensionless viscosity curves do not collapse for all particle sizes as expected because magnetostatic interparticle forces predominate over thermal motion at intermediate and large sizes. However, in suspensions formulated with SP particles (8 and 12 nm diameter, in the FF limit) the collapse is reasonably good. This was expected because in this size range these suspensions behave as nearly Brownian Hard Spheres.

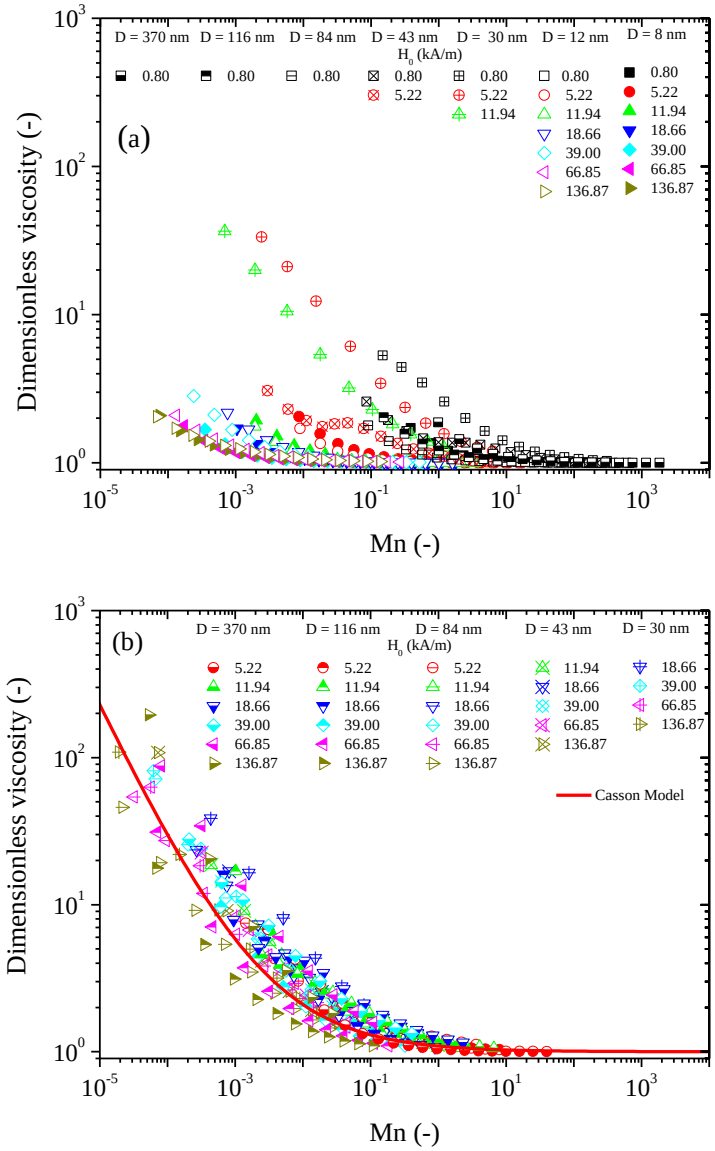

Figure 10.9: Dimensionless viscosity (η/η_∞) as a function of Mason number (Mn) for different particle diameters. a) $\lambda < 1$, b) $\lambda > 1$. Data correspond to $\dot{\gamma} > 0.2$ s^{-1}. In the calculation of Mn the first magnetization curves were used for particles of diameters 30 nm, 43 nm, 84 nm and 370 nm. In contrast, the Frohlich-Kennelly expression [31] was used for particles of diameters 8 nm, 12 nm and 116 nm.

In Fig. 10.9 we show the scaling of the dimensionless viscosity curves with the Mason number Mn. For the calculation of Mn the mean magnetization of the particles $\langle M_p \rangle$ was

taken from the magnetization of the powders (Fig. 10.4). As expected, the scaling is rather poor for $\lambda < 1$. However, for $\lambda > 1$ the collapse is rather good in agreement with the literature on dilute conventional MR fluids [27]. These results are also in good qualitative agreement with Ref. [39]. They suggested a scaling with $\mathrm{Mn} \propto \eta_c \dot{\gamma}/(\mu_0 \mu_{cr} M H_0)$ being M the magnetization of the ferrofluid (i.e. Langevin expression). This scaling is equivalent to Eq. (10.2) if we bear in mind that for dilute suspensions at reasonably small fields $M = \phi\langle M_p \rangle$ and $\langle M_p \rangle \approx 3\beta H_0$ (see Fig. 10.11 in Sec. 10.6).

Together with the experimental data, in Fig. 10.9b we also show the predictions according to the Casson model (Eq. (10.4)) with $\mathrm{Mn}^* = 0.003$. This critical Mason number Mn^* is the one corresponding to the particular solids concentration employed in this work. As observed, the theoretical prediction (red solid line) is in reasonably good agreement with experiments suggesting that the Mean Magnetization Approximation is valid.

To sum up, in the transition regime between FF and MRFs the scaling with Pe does not work. However the scaling with Mn is still reasonably good especially for the largest fields whenever $\lambda > 1$ independently of the particle size.

At this point it is important to stress that the collapse observed in Fig. 10.9b for $\lambda > 1$ also involves experimental data for particles in the borderline between FFs and MRFs. There are two important differences between these particles and those constituting FFs and MRFs: the magnetization of the particles is larger (see Fig. 10.5b) and the magnetic moment rotates together with the physical rotation of the particle (see Fig. 10.1). In view of Fig. 10.9b, it seems that the rheological behavior is dictated by the difference in the particle magnetization and that particle rotation does not play an important role. To demonstrate that indeed the particle rotation does not significantly contribute to the viscosity enhancement reported in Fig. 10.7, next we show simulation results for two systems where the magnetization is kept constant.

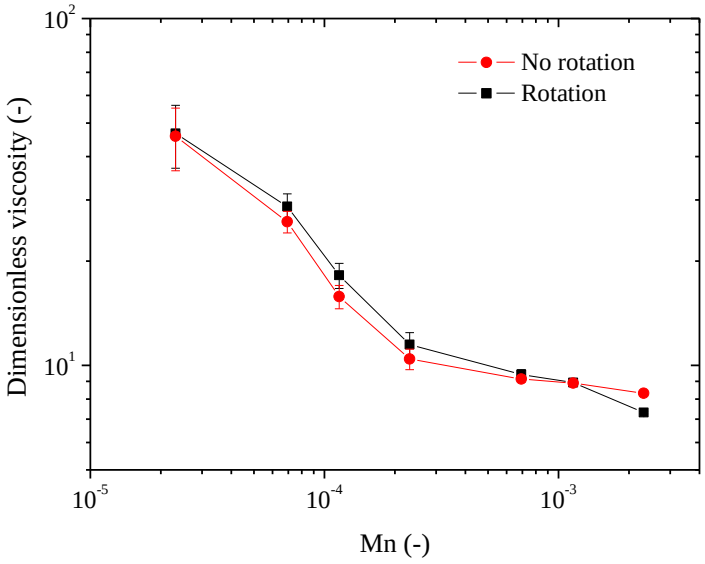

Figure 10.10: Simulated rheograms obtained using Eq. (10.10). Red circles symbols correspond to simulations where the magnetic moment is permanently aligned with the applied magnetic field (i.e. the particle does not rotate). Black squares correspond to simulations where the magnetic moment is fixed to the particle's body (i.e. the particle rotates).

Results are shown in Fig. 10.10 for different applied shear rates in the two simulated scenarios (without and with particle/moment rotation). No significant differences can be observed between both cases. This, together with the fact that experimental viscosity data already collapse in a master curve using the Mean Magnetization Approximation (Fig. 10.9b), would suggest that coercivity influences the magnetoviscous effect only by increasing the magnetization level but not by introducing a new stress transfer mechanism based on fixing magnetic dipoles to the particles body.

10.5 Conclusions

We report the influence of particle size in a wide range of λ ratios around the mono-multidomain transition region (i.e. $\lambda = 1$). The use of dilute suspensions (1.1 vol%) at low fields (below 140 kA/m) allows us to safely employ the Mean Magnetization Approximation.

For the largest magnetic fields the magnetization of the particles increases with the particle size. This finding may serve as an explanation for the repeatedly reported yield stress enhancement with the particle size at large λ ratio (where Brownian motion does not play a role).

For low magnetic fields, we demonstrate that depending on the particle size we can move from a FF dominated region to a MRF dominated region. A key point is the appearance of a maximum in the particle magnetization that is linked to the maximum in the coercive field. It is for the particle sizes corresponding to this maximum where the magnetoviscous effect also reaches a maximum. The physical reason for this is that single-domain particles in the transition region are easier to orient with the field than multidomain particles that need to be magnetized first and then oriented.

Finally, the viscosity curves can be scaled with the Peclet number Pe for suspensions in the FF limit, and with the Mason number Mn for any suspensions with $\lambda > 1$. Particle magnetization governs the rheological behavior and not the fact that the magnetic moment is fixed to the particles.

Acknowledgements

This work was supported by MINECO MAT 2016-78778-R and PCIN-2015-051 projects (Spain) and European Regional Development Fund (ERDF). J. R. Morillas acknowledges FPU14/01576 fellowship. C. Bierwisch acknowledges financial support by the Deutsche Forschungsgemeinschaft (DFG) under grant number BI 1859/1-1.

10.6 Supplementary material

According to the Mean Magnetization approximation, each particle in the magnetic colloid can be substituted by a point dipole placed at its center. The magnitude of this dipole is given by the particle volume times its magnetization level.

In the limit of low volume fractions (i.e. isolated particles) and small applied fields, the particle magnetization can be written as $M = 3\beta H_0$ where H_0 is the applied field, $\beta = \chi/(3+\chi)$ the contrast factor and χ the particle susceptibility.

The ratio between the particle magnetization and the saturation magnetization (i.e. $M/M_s = 3\beta H_0/M_s$) is plotted with lines in Fig. 10.11 for the different particles used through this work together with the results for conventional carbonyl iron particles (CIP). In the calculation of $3\beta H_0/M_s$ we used the experimental χ as obtained from the magnetization curves. It can be seen a linear dependence for all samples, at least for low fields, pointing out that χ is not a function of the applied field in this regime.

In Fig. 10.11 we also plot with solid symbols the experimental data directly taken from the magnetization curves. Although these points are shifted upwards with respect to the isolated case (magnetization measurement is not carried out over isolated particles but over powder samples) they still exhibit a linear relationship hence validating the definitions given for the Mason number in the main text.

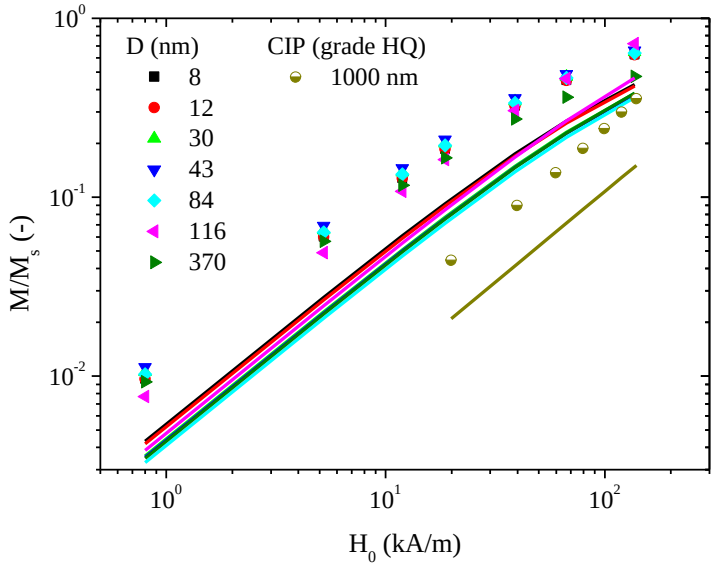

Figure 10.11: Mean magnetization of the particles scaled with the saturation magnetization of the particles as a function of the external magnetic field. As a reference, we also include data for carbonyl iron particles (HQ grade from BASF-SE) as obtained from the powder. Solid lines correspond to $3\beta H_0/M_S$.

References

[1] Rosensweig, R. E. Ferrohydrodynamics (Dover Publications, Mineola, 2014).

[2] Wereley, N. (Ed.). Magnetorheology: advances and applications (Vol. 6) (Royal Society of Chemistry, Cambridge, 2013).

[3] Salas, G., Casado, C., Teran, F. J., Miranda, R., Serna, C. J., and Morales, M. P. (2012). Controlled synthesis of uniform magnetite nanocrystals with high-quality properties for biomedical applications. Journal of Materials Chemistry, 22(39), 21065-21075.

[4] Marciello, M., Connord, V., Veintemillas-Verdaguer, S., Vergés, M. A., Carrey, J., Respaud, M., Serna, C. J., and Morales, M. P. (2013). Large scale production of biocompatible magnetite nanocrystals with high saturation magnetization values through green aqueous synthesis. Journal of Materials Chemistry B, 1(43), 5995-6004.

[5] Veintemillas-Verdaguer, S., Marciello, M., Morales, P., Serna, C. J., and Andres-Verges, M. (2014). Magnetic nanocrystals for biomedical applications. Progress in Crystal Growth and Characterization of Materials. 60, 80–86.

[6] Cotin, G., Piant, S., Mertz, D., Felder-Flesch, D., and Begin-Colin, S. (2018). Iron oxide nanoparticles for biomedical applications: Synthesis, functionalization, and application. In: Mahmoudi, M., and Laurent, S. (Eds.) Iron Oxide Nanoparticles for Biomedical Applications (Elsevier, Amsterdam).

[7] Bombard, A. J., Gonçalves, F. R., Morillas, J. R., and de Vicente, J. (2014). Magnetorheology of dimorphic magnetorheological fluids based on nanofibers. Smart Materials and Structures, 23(12), 125013.

[8] Odenbach, S., and Thurm, S. (2002). Magnetoviscous effects in ferrofluids. In: Odenbach, S. (Ed.) Ferrofluids. Lecture Notes in Physics (Vol. 594) (Springer, Berlin).

[9] Felicia, L. J., Vinod, S., and Philip, J. (2016). Recent advances in magnetorheology of ferrofluids (magnetic nanofluids)—a critical review. Journal of Nanofluids, 5(1), 1-22.

[10] Odenbach, S., and Raj, K. (2000). The influence of large particles and agglomerates on the magnetoviscous effect in ferrofluids. Magnetohydrodynamics, 36(4), 312-319.

[11] McTague, J. P. (1969). Magnetoviscosity of magnetic colloids. The Journal of Chemical Physics, 51(1), 133-136.

[12] Shliomis, M. I. (1971). Effective viscosity of magnetic suspensions. Zhurnal Eksperimentalnoi i Teoreticheskoi Fiziki, 61(2411), s1971d.

[13] Odenbach, S. (Ed.) Ferrofluids: magnetically controllable fluids and their applications. Lecture Notes in Physics (Vol. 594) (Springer, Berlin, 2008).

[14] Lemaire, E., Meunier, A., Bossis, G., Liu, J., Felt, D., Bashtovoi, P., and Matoussevitch, N. (1995). Influence of the particle size on the rheology of magnetorheological fluids. Journal of Rheology, 39(5), 1011-1020.

[15] Felt, D. W., Hagenbuchle, M., Liu, J., and Richard, J. (1996). Rheology of a magnetorheological fluid. Journal of Intelligent Material Systems and Structures, 7(5), 589-593.

[16] Rosenfeld, N., Wereley, N. M., Radakrishnan, R., and Sudarshan, T. S. (2002). Behavior of magnetorheological fluids utilizing nanopowder iron. International Journal of Modern Physics B, 16(17n18), 2392-2398.

[17] Trendler, A. M., and Böse, H. (2005). Influence of particle size on the rheological properties of magnetorheological suspensions. International Journal of Modern Physics B, 19(07n09), 1416-1422.

[18] Massart, R. (1981). Preparation of aqueous magnetic liquids in alkaline and acidic media. IEEE Transactions on Magnetics, 17(2), 1247-1248.

[19] de la Presa, P., Luengo, Y., Velasco, V., Morales, M. P., Iglesias, M., Veintemillas-Verdaguer, S., Crespo, P., and Hernando, A. (2015). Particle interactions in liquid magnetic colloids by zero field cooled measurements: Effects on heating efficiency. The Journal of Physical Chemistry C, 119(20), 11022-11030.

[20] van Ewijk, G. A., Vroege, G. J., and Philipse, A. P. (1999). Convenient preparation methods for magnetic colloids. Journal of Magnetism and Magnetic Materials, 201(1-3), 31-33.

[21] Costo, R., Bello, V., Robic, C., Port, M., Marco, J. F., Morales, P., and Veintemillas-Verdaguer, S. (2011). Ultrasmall iron oxide nanoparticles for

biomedical applications: improving the colloidal and magnetic properties. Langmuir, 28(1), 178-185.

[22] Vergés, M. A., Costo, R., Roca, A. G., Marco, J. F., Goya, G. F., Serna, C. J., and Morales, M. P. (2008). Uniform and water stable magnetite nanoparticles with diameters around the monodomain–multidomain limit. Journal of Physics D: Applied Physics, 41(13), 134003.

[23] Leong, S. A. N., Mazlan, S. A., Samin, P. M., Idris, A., and Ubaidillah. (2016). Performance of bidisperse magnetorheological fluids utilizing superparamagnetic maghemite nanoparticles. AIP Conference Proceedings, 1710, 030050.

[24] Sugimoto, T., and Matijević, E. (1980). Formation of uniform spherical magnetite particles by crystallization from ferrous hydroxide gels. Journal of Colloid and Interface Science, 74(1), 227-243.

[25] Liu, J., Sun, Z., Deng, Y., Zou, Y., Li, C., Guo, X., Xiong, L., Gao, Y., Li, F., and Zhao, D. (2009). Highly water-dispersible biocompatible magnetite particles with low cytotoxicity stabilized by citrate groups. Angewandte Chemie International Edition, 48(32), 5875-5879.

[26] Dhont, J. K. G. An introduction to dynamics of colloids (Vol. 2) (Elsevier, Amsterdam, 1996).

[27] Ruiz-López, J. A., Fernández-Toledano, J. C., Hidalgo-Álvarez, R., and de Vicente, J. (2016). Testing the mean magnetization approximation, dimensionless and scaling numbers in magnetorheology. Soft Matter, 12(5), 1468-1476.

[28] de Vicente, J., Klingenberg, D. J., and Hidalgo-Álvarez, R. (2011). Magnetorheological fluids: a review. Soft Matter, 7(8), 3701-3710.

[29] Berli, C. L., and de Vicente, J. (2012). A structural viscosity model for magnetorheology. Applied Physics Letters, 101(2), 021903.

[30] Lagger, H. G., Bierwisch, C., Korvink, J. G., and Moseler, M. (2014). Discrete element study of viscous flow in magnetorheological fluids. Rheologica Acta, 53(5-6), 417-443.

[31] Cullity, B. D., and Graham, C. D. Introduction to Magnetic Materials (John Wiley & Sons, Hoboken, 2009).

[32] Costo, R., Morales, M. P., and Veintemillas-Verdaguer, S. (2015). Improving magnetic properties of ultrasmall magnetic nanoparticles by biocompatible coatings. Journal of Applied Physics, 117(6), 064311.

[33] Bozorth, R. M. Ferromagnetism. (IEEE, Sewaren, 1993).

[34] Guardia, P., Pérez, N., Labarta, A., and Batlle, X. (2009). Controlled synthesis of iron oxide nanoparticles over a wide size range. Langmuir, 26(8), 5843-5847.

[35] Guardia, P., Pérez-Juste, J., Labarta, A., Batlle, X., and Liz-Marzán, L. M. (2010). Heating rate influence on the synthesis of iron oxide nanoparticles: the case of decanoic acid. Chemical Communications, 46(33), 6108-6110.

[36] Butler, R. F., and Banerjee, S. K. (1975). Theoretical single-domain grain size range in magnetite and titanomagnetite. Journal of Geophysical Research, 80(29), 4049-4058.

[37] Leslie-Pelecky, D. L., and Rieke, R. D. (1996). Magnetic properties of nanostructured materials. Chemistry of Materials, 8(8), 1770-1783.

[38] Russel, W. B., Saville, D. A., and Schowalter, W. R. Colloidal dispersions (Cambridge University Press, Cambridge, 1991).

[39] Rosensweig, R. E., Kaiser, R., and Miskolczy, G. (1969). Viscosity of magnetic fluid in a magnetic field. Journal of Colloid and Interface Science, 29(4), 680-686.

Chapter 11. Enhancing Magnetorheological Effect using Bimodal Suspensions in the Single-Multidomain Limit

Jose R. Morillas, Antonio J. F. Bombard and Juan de Vicente

This article is published in: Smart Materials and Structures, 27(7), 07LT01 (2018).

DOI: https://doi.org/10.1088/1361-665X/aac8ae

Abstract

We demonstrate a new route to enhance the magnetorheological (MR) effect using bimodal suspensions in the single- multidomain limit. Experimental results are satisfactorily compared to 3D Finite Element Method simulations. The physical reason behind this enhancement is the coating of the larger particles by the smaller ones due to the remnant magnetization of the latter.

11.1 Introduction

Bimodal suspensions are particle mixtures having two well-differentiated size distributions. In the following, we will call σ_L to the mean particle diameter of the Large size distribution and σ_S to the mean particle diameter of the Small size distribution.

At present, bimodal suspensions constitute a widely used approach to enhance MR effect or to minimize sedimentation. In general, for the MR effect to be sufficiently large, the largest particles in suspension must be in the range $\sigma_L \approx 10$ μm [1]; otherwise Brownian motion disrupts the field-induced structures. With this in mind, previous works in this field can be classified in two limiting cases; either $\sigma_L/\sigma_S \approx 10$ [2-11] or $\sigma_L/\sigma_S \approx 1000$ [12-17].

For $\sigma_L/\sigma_S \approx 10$, experimental and simulation works demonstrate an on-state yield stress enhancement if compared to monomodal suspensions composed of either the small or large particles. Contrary to the intuition, particle level simulations suggest that the reason for this enhancement is not associated with an increase in particle packing within the aggregates but to the changes bimodality causes in the microstructure [7,10]. These bimodal suspensions suffer from important sedimentation problems because of the large particle sizes.

For $\sigma_L/\sigma_S \approx 1000$, experiments demonstrate that sedimentation is strongly mitigated because of the thermal convection of the nanoparticles that delay the sedimentation of the bigger ones. The price to be paid is that the on-state yield stress is substantially reduced (when the concentration of the small particles exceeds approx. 10 wt%) presumably

because of chain growth inhibition or inferior magnetic properties of the nanoparticles if compared to the microparticles [15].

In this letter we demonstrate that bimodal suspensions in the frontier (i.e. $\sigma_L/\sigma_S \approx 100$) exhibit a significantly larger on-state yield stress if compared to their monomodal counterparts and at the same time sedimentation is significantly reduced. The explanation for this is that the smallest particles in the formulation have a size in the range between magnetic mono- and multidomains and therefore exhibit a remarkable remnant magnetization [18]. Because of this, the smallest particles surround the bigger ones increasing the on-state response and reducing the sedimentation. Finite Element Method calculations qualitatively explain the experimental observations.

11.2 Experimental

Both kinds of particles used in the formulation of the bimodal MR fluids were made of iron. The biggest ones ('Large particles') were a gift from BASF SE (EW grade, Germany). The smallest particles ('Small particles') were obtained from US Research Nanomaterials (Iron Nanopowder/Nanoparticles; Fe, 99.5 +%, 95-105 nm, metal basis). SEM observations were carried out to determine their morphological characteristics while Squid magnetometry was used to determine the magnetic characteristics of the particles (see Table 11.1). As observed, the magnetic properties are slightly superior for small particles at low fields (i.e. larger initial permeability); the contrary is true for large fields (i.e. smaller saturation magnetization).

	Particles	
	Large	Small
Number average diameter (nm)	1327.4	111.64
Weight average diameter (nm)	2642.8	206.99
Volume average diameter (nm)	1729.3	137.87
Polydispersity index (-)	1.991	1.854
Initial magnetic permeability (-)	7.42	9.66
Coercive field, H_C (kA/m)	0.7	11
Saturation magnetization, M_S (emu/g)	204	176
N (-)	446	286

Table 11.1: Iron powders used in the formulation of the bimodal MR fluids. 'Large' stands for the carbonyl iron microparticles and 'Small' stands for the iron nanoparticles. N stands for the number of particles counted to evaluate the particle size.

The particles were thoroughly dispersed at various mixing ratios in polyalphaolefin oil (PAO 2 cSt, dynamic viscosity 6.4 mPa·s, Synfluid, Chevron-Philips). To facilitate the processability of the MR fluids, a certain amount of 1-octanol was also added to the PAO (3.5 wt% in the total amount of PAO) [19].

Steady shear rheometry was carried out in a rotational rheometer (MCR501, Anton Paar). Magnetic fields were generated using a MRD70/1T magnetocell in parallel plate

configuration (20 mm diameter, 300 microns gap). Yield stresses were obtained using a carefully designed protocol. This protocol consisted in several stages: (Stage 1) a constant rim shear rate ($\dot{\gamma}$ = 100 s^{-1}) was applied during 20 seconds. (Stage 2) the upper plate was stopped and a uniaxial DC magnetic field (147 kA/m) was suddenly applied for 60 s to structure the MR fluid. (Stage 3) a stress log-ramp was imposed to evaluate the yielding point similarly to [20]. The interval time employed to get every data within the full rheogram was 5 seconds. At least three independent measurements with fresh new samples were taken. Error bars in the figures correspond to the standard deviation of the different repetitions.

To explore the sedimentation stability (in the absence of fields) a given volume of MR fluid was placed inside a cylindrical plastic tube and visually observed during time to determine the time evolution of sedimentation ratio $H(t)/H_0$ curves. Here $H(t)$ represents the height of the sediment/liquid interface (i.e. mudline) at a given time, t, and H_0 is the corresponding height value of the MR fluid at the beginning of the test $H_0 \equiv H(t=0)$.

Penetration and redispersibility tests were carried out using a four-blade vane tool attached to the MCR 501 rheometer head coupling. The test consisted in slowly displacing the tool (1 mm/s) towards a fully sedimented suspension (i.e. one week after preparation) while recording the axial (normal) force acting on the vane. Once the vane was well inside the sample, a continuous torque ramp was initiated to determine the flow curve (from 0.0001 mN·m to 0.5 mN·m).

11.3 Simulations

3D finite element method simulations were also carried out to compute the on-state yield stress in bimodal MR fluids. For this, the largest particles in the ensemble were arranged in a cubic network of infinite single particle-width chains aligned in the direction of the external magnetic field. Two possibilities were explored with regards to the spatial distribution of the smallest particles in the suspension under the presence of magnetic fields (see Fig. 11.1):

Case 1.- On the one hand, due to their non-negligible remnant magnetization, the smallest particles could stick around the larger ones covering them with a layer of thickness d_s (i.e. *core-shell* supraparticles). The magnetic properties of the *shell* are therefore dictated by the magnetic properties of the smallest particles.

Case 2.- On the other hand, due to their nanometric size, the smallest particles could remain properly dispersed within the carrier liquid, because of thermal/Brownian motion, hosting the largest particles. The magnetic properties of the *carrier fluid* are therefore given by the magnetic properties of the suspension of small particles (with volume concentration ϕ).

The magnetic field distribution was computed in the magnetostatic limit, without free currents, using COMSOL Multiphysics software. A reduced field formulation was employed to split the total magnetic field $\vec{H}$ into the external applied field $\vec{H}_{ext}$ and the perturbation due to the magnetic suspension $\vec{H}_p = -\overrightarrow{\nabla V_p}$. An important advantage of using the reduced field formulation is that it is not necessary to fix the magnetic field in any boundary of the computational domain and therefore the deformation of a unit cell is representative of the full lattice with periodic boundaries [21]. The dimensions of the unit

cell (B_h, B_w) are a function of the large particle diameter σ_L, and the concentration of small ϕ_S and/or large ϕ_L particles (see Fig. 11.1). Two scenarios were studied:

Case 1.- In the first case, it is supposed that all small particles stick to the larger ones. Therefore, the thickness of the shell is given by $d_S = \sigma_L\left(1/\sqrt[3]{8(1-\phi_r)} - 1/2\right)$ where $\phi_r \equiv \phi_S/\phi_T$ and $\phi_T \equiv \phi_S + \phi_L$. As a result, $B_h = \sigma_L + 2d_S$ and $B_w = \sqrt{\pi(\sigma_L + 2d_S)^2/6\phi_T}$ in order to fulfill the condition that the magnetic concentration inside the cell is ϕ_T.

Case 2.- In the second case, as the small particles are supposed to remain suspended within the continuum phase, cell dimensions only depend on ϕ_L and on the diameter of the bare large particles σ_L: $B_h = \sigma_L$, $B_w = \sqrt{\pi\sigma_L^2/6\phi_L}$.

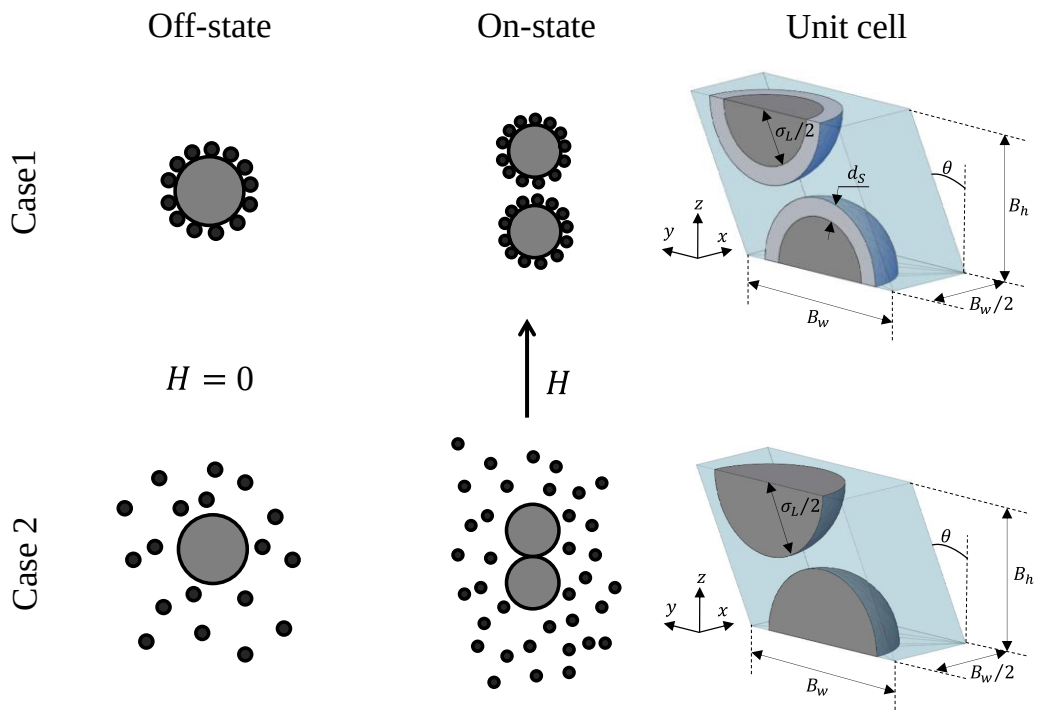

Figure 11.1: Two cases are considered for small iron particles. In the first one they are adhered to large iron particles due to their remnant magnetization. In the second case, small particles are well dispersed in suspension. Both cases were modeled in the on-state using FEM simulations. A schematics of the computational domain is also represented: a strain $\gamma = \tan\theta$ is applied in the y direction while the magnetic field is applied in the z direction. Periodic Boundary Conditions are fixed in all boundary faces except in those faces perpendicular to x direction, where Mirror Symmetry Boundary Conditions apply.

The non-linear magnetic behavior of both populations of particles was accounted for by means of Fröhlich-Kennelly equation using experimental fitting parameters from the powders; initial permeability and saturation magnetization [22]. The magnetic properties of the suspensions of small particles were calculated using Maxwell-Garnett theory [23]. Assuming that all small particles inside the unit cell constitute a suspension, the relationship between the small particles concentration ϕ_S and the suspension concentration ϕ is given by:

$$\phi = \frac{\phi_s B_h B_w^2}{B_h B_w^2 - \pi\sigma_L^3/6} = \frac{\phi_s}{1-\phi_L} \tag{11.1}$$

Once the magnetic field distribution is computed within the computational domain, the shear stress τ on the lower half of the lattice is calculated similarly to Refs. [21] and [24] by integrating the Maxwell stress tensor on the plane (normal to the external field direction) that halves the unit cell:

$$\tau = \frac{2}{B_w^2}\int B_y H_z dS \tag{11.2}$$

Finally, the static yield stress τ_y is given by the maximum shear stress achieved as the strain level is increased. It is worth to remark that the affine deformation experienced by the cubic lattice under a simple shear flow is simply modeled here by shearing its unit cell (see Fig. 11.1). Due to the symmetries of the sheared cubic lattice, the computational domain can be reduced to one half of the unit cell.

11.4 Results and discussion

Figure 11.2a shows the results for the on-state yield stress, at a fixed large particles concentration of $\phi_L = 0.30$, as a function of the concentration of small particles ϕ_S. As observed, the yield stress increases upon increasing the concentration of small particles. This was expected because the total iron concentration $\phi_T \equiv \phi_S + \phi_L$ is increasing. Interestingly, numerical simulations predict reasonably well the order of magnitude for the yield stress despite the simplifications in the model. Note that there are not free fitting parameters. Only in the case where the nanoparticles are coating the microparticles (Case 1), the yield stress increases with ϕ_S in good qualitative agreement with the experimental results. Numerical simulations for microparticles dispersed in suspensions of small particles give a yield stress that monotonically decreases with ϕ_S in good agreement with previous experimental data reported in the literature for $\sigma_L/\sigma_S \approx 1000$ [15]. The fact that the experimental yield stress increases faster than the numerical simulations for core-shell particles is expected because of the simplification in the microstructure. In practice the shell should be porous and asymmetric in the field direction (see Fig. 11.3).

In Fig. 11.2b we show the on-state yield stress as a function of the relative concentration of small particles ϕ_S/ϕ_T for a constant total concentration $\phi_T = 0.45$. In this case the addition of small particles results in a significant increase in the yield stress: approximately, a twofold increase is obtained when 5% of the large size particles are replaced by smaller ones (cf. second experimental data point in Fig. 11.2b; $\phi_S/\phi_T = 11\%$). The reason of this enhancement is presumably again the formation of a shell of small particles surrounding the larger ones (see below). This hypothesis is supported by simulation results although the increasing rate is clearly smaller than in the experimental case. Figure 11.2b also demonstrates that the hypothesis that nanoparticles remain well-dispersed within the carrier fluid is not realistic; in this case the simulated yield stress decreases with ϕ_S in contrast to experiments.

To get a better understanding of the internal structure of the aggregates we also performed microscopy observations. In Fig. 11.3 we show Scanning Electron Microscopy pictures of the micro and nanoparticles within a resin after gelation under DC magnetic fields (750 mT). As observed, the larger particles are clearly surrounded by a shell of nanoparticles in good agreement with our hypothesis.

A useful way to visualize the importance of adding a second population of nanoparticles to the suspension of large particles is through the so-called effective enhancement, that is defined as follows:

$$\frac{\tau_{yb}(\phi_S + \phi_L = 0.45) - \tau_{ym}(\phi_L = 0.45)}{\tau_{ym}(\phi_L = 0.45)} \tag{11.3}$$

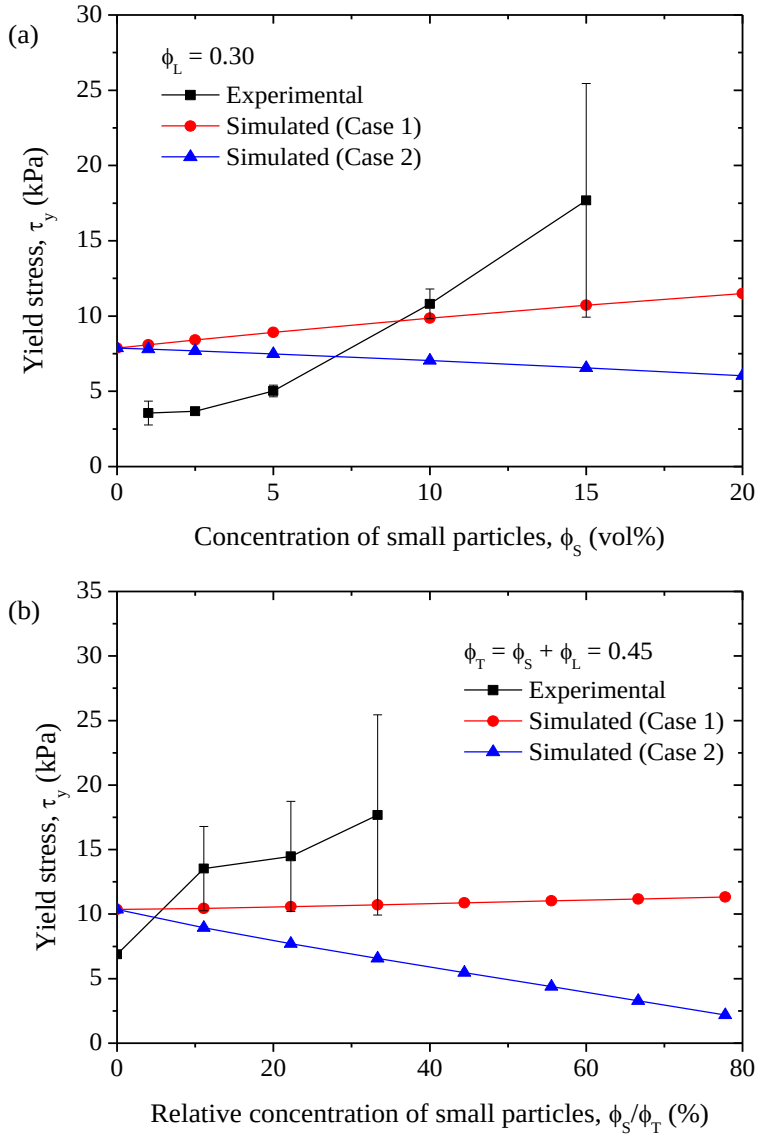

Figure 11.2: On-state yield stress of bimodal MR fluids as a function of: a) concentration of small particles ϕ_S for a constant volume fraction of large iron particles of 30 vol% ($\phi_L = 0.30$); b) fraction of small particles ϕ_S/ϕ_T for a constant total volume fraction of solids of 45 vol% ($\phi_T = 0.45$). The external magnetic field strength is 147 kA/m.

The effective enhancement directly compares the performance of bimodal suspensions τ_{yb} to monomodal ones τ_{ym} having the same total concentration $\phi_T \equiv \phi_S + \phi_L = 0.45$. Results are contained in Fig. 11.4. Here we clearly observe a remarkable increase in the effective enhancement for bimodal MR fluids containing small particles in striking contrast to monomodal MR fluids only containing large particles. Simulations considering core-shell supraparticles also show an enhancement of the yield stress

although its increase is not so significant. Again, the fact that the order of magnitude is well captured by numerical simulations suggests that major (interparticle) interactions involved are essentially magnetostatics. These are indeed the only interactions simulated in this work. However, other colloidal forces may influence the experimental data and are not considered in the simulations (e.g. van der Waals, friction, surface charges...). Also, the calculations shown here ground on very strong assumptions; the numerical calculations assume a perfect cubic lattice formed by the larger particles and that the shell of nanoparticles is a continuum of uniform thickness. However, a cubic lattice is never observed at these (large) concentrations and lateral/secondary connections between aggregates appear [25]. Furthermore, a magnetic field gradient is established upon the application of the field around the larger particles and therefore the nanoparticles concentration should be larger in the proximity of the polar regions of the larger particles.

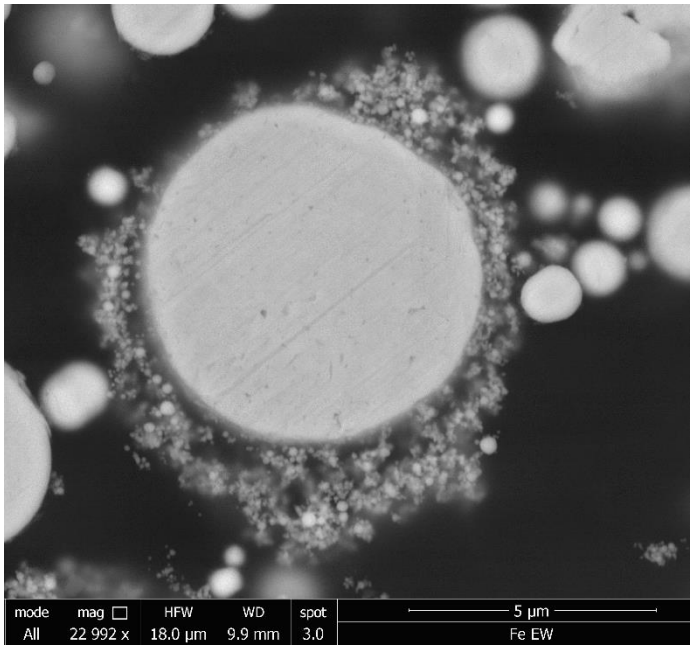

Figure 11.3: Scanning Electron Microscopy picture of the bimodal suspensions in a resin. The detail shows a large carbonyl iron microparticle surrounded by iron nanoparticles. Magnetic field density 750 mT.

In view of Fig. 11.4, it is worth to note that the effective enhancement increases as a result of the fact that the nanoparticles, within the shell structure, have superior magnetic properties than bare microparticles at the magnetic fields investigated (see Table 11.1). Unrealistic results are found again if nanoparticles are well dispersed in the carrier fluid instead of covering the large particles. In this case, as the small size particles concentration increases, the magnetic field within the gap between larger particles is screened due to the increase in the magnetic permeability of the suspension of small particles. In addition, increasing small particles concentration, that is ϕ_S, implies the reduction of ϕ_L, and consequently, the contribution of surrounding large particles is diminished.

The next step was to explore the sedimentation characteristics of the bimodal suspensions compared to the monomodal ones. Results are shown in Fig. 11.5 for three suspensions: (i) large particles at a 30 vol% concentration, (ii) large particles at a 35 vol% concentration and (iii) binary mixtures (30 vol% large L + 5 vol% small S). As observed, the sedimentation rate is significantly reduced when microparticles are replaced with

nanoparticles. The most tightly packed sediments are always those corresponding to monomodal MR fluids (see Table 11.2). As observed, bimodal suspensions give place to a higher sediment. Such a high sediment is the result of the formation of a not well compacted sediment. This is coherent with the fact that small and large particles are magnetically interacting and do not behave as non-Brownian hard spheres because in this case a particle mixture would give a more efficient packing. The observed slower sedimentation rate is coherent with the presence of more aggregates in suspension [16].

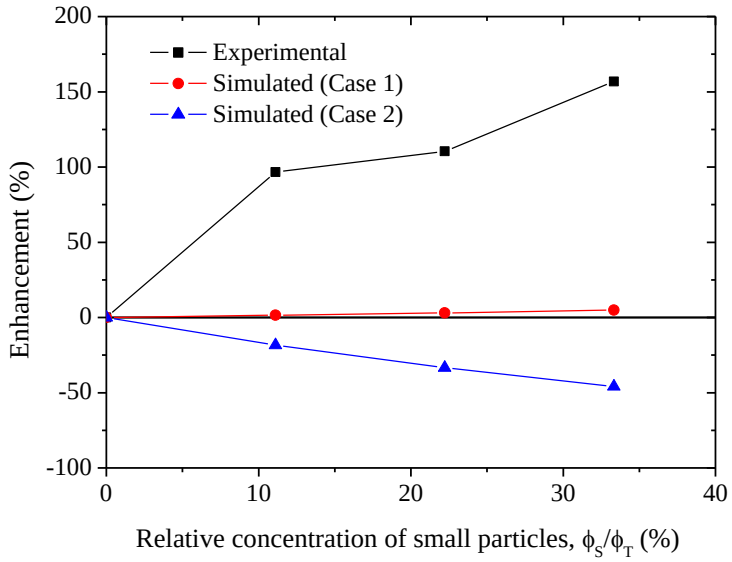

Figure 11.4: Effective enhancement (%) as a function of the relative concentration of small particles ϕ_S/ϕ_T for a constant total volume fraction of solids of 45 vol% ($\phi_T = 0.45$). The external magnetic field strength is 147 kA/m.

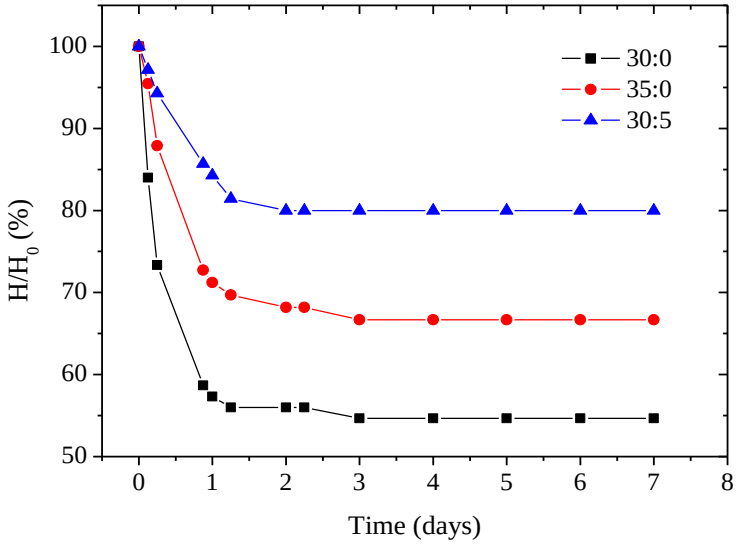

Figure 11.5: Time evolution of the sedimentation ratio (H/H_0) for conventional MR fluids (30 vol% and 35 vol% large particles) and bimodal MR fluids (30 vol% large + 5 vol% small).

Finally, penetration tests demonstrate that sediments formed in bimodal mixtures are also easier to redisperse than monomodal ones. In bimodal suspensions, the mechanical work, for a penetration distance of 40 mm, was of only 1.83 mJ while the torque required for

redispersion (at 0.001 rpm) was of only 30 ± 2 μN·m. It is worth to note that the monomodal suspensions formed a very compacted cake that could not be penetrated with our rheometer.

MR fluid composition (L:S)	Maximum packing fraction (vol%)
30:0	54.9
35:0	52.5
30:5	43.8

Table 11.2: Sedimentation characteristics of the bimodal MR fluids (Large:Small mixtures in vol%).

Overall, bimodal MR fluids in the single- multidomain limit exhibit a significantly large MR effect (i.e. increase in the on-state yield stress) similar to bimodal suspensions in the range $\sigma_L/\sigma_S \approx 10$ and good stability properties (i.e. reduced settling rate) similar to bimodal suspensions in the range $\sigma_L/\sigma_S \approx 1000$. The key point is the coexistence of two particle populations having an induced and permanent magnetic moment, respectively.

Finite element method simulations results suggest that a crucial point is the superior magnetic characteristics of the nanoparticles if compared to the microparticles. Hence, it can be speculated that the partial substitution of carbonyl iron microparticles by a small amount of very strong magnetic particles (e.g. iron alloys) in the single- multidomain region would provide an even stronger enhancement in the MR response.

Acknowledgements

This work was supported by MAT 2016-78778-R and PCIN 2015-051 projects (FEDER FUNDS and MINECO, Spain). A. J. F. Bombard is grateful to FAPEMIG grants: APQ-01824-17, PEE-00081-16, RED-00144-16, ETC-00043-15, PEP-00231-15, APQ-00463-11 and RDP-00164-10. J. R. Morillas acknowledges FPU14/01576 fellowship.

References

[1] Foister, R. T. (1997). U.S. Patent No. 5667715. Washington, DC: U.S. Patent and Trademark Office.

[2] Weiss, K. D., Carlson, J. D., and Nixon, D. A. (2000). U.S. Patent No. 6027664. Washington, DC: U.S. Patent and Trademark Office.

[3] See, H., Kawai, A., and Ikazaki, F. (2002). The effect of mixing particles of different size on the electrorheological response under steady shear flow. Rheologica Acta, 41(1-2), 55-60.

[4] Trendler, A. M., and Böse, H. (2005). Influence of particle size on the rheological properties of magnetorheological suspensions. International Journal of Modern Physics B, 19(07n09), 1416-1422.

[5] Ulicny, J. C., Smith, A. L., Golden, M. A., McDermott, B. L., and Chapaton, T. J. (2004). U.S. Patent No. 6824701. Washington, DC: U.S. Patent and Trademark Office.

[6] Bombard, A. J., Joekes, I., Alcantara, M. R., and Knobel, M. (2003). Magnetic susceptibility and saturation magnetization of some carbonyl iron powders used in magnetorheological fluids. Materials Science Forum, 416-418, 753-758.

[7] Kittipoomwong, D., Klingenberg, D. J., and Ulicny, J. C. (2005). Dynamic yield stress enhancement in bidisperse magnetorheological fluids. Journal of Rheology, 49(6), 1521-1538.

[8] Goncalves, F. D., Koo, J. H., and Ahmadian, M. (2006). A review of the state of the art in magnetorheological fluid technologies-Part I: MR fluid and MR fluid models. The Shock and Vibration Digest, 38(3), 203-220.

[9] Dodbiba, G., Park, H. S., Okaya, K., and Fujita, T. (2008). Investigating magnetorheological properties of a mixture of two types of carbonyl iron powders suspended in an ionic liquid. Journal of Magnetism and Magnetic Materials, 320(7), 1322-1327.

[10] Ekwebelam, C., and See, H. (2009). Microstructural investigations of the yielding behaviour of bidisperse magnetorheological fluids. Rheologica Acta, 48(1), 19-32.

[11] Li, W. H., and Zhang, X. Z. (2010). A study of the magnetorheological effect of bimodal particle based magnetorheological elastomers. Smart Materials and Structures, 19(3), 035002.

[12] Rosenfeld, N., Wereley, N. M., Radakrishnan, R., and Sudarshan, T. S. (2002). Behavior of magnetorheological fluids utilizing nanopowder iron. International Journal of Modern Physics B, 16(17n18), 2392-2398.

[13] Chaudhuri, A., Wang, G., Wereley, N. M., Tasovksi, V., and Radhakrishnan, R. (2005). Substitution of micron by nanometer scale powders in magnetorheological fluids. International Journal of Modern Physics B, 19(07n09), 1374-1380.

[14] López-López, M. T., de Vicente, J., Bossis, G., González-Caballero, F., and Durán, J. D. G. (2005). Preparation of stable magnetorheological fluids based on extremely bimodal iron–magnetite suspensions. Journal of Materials Research, 20(4), 874-881.

[15] Wereley, N. M., Chaudhuri, A., Yoo, J. H., John, S., Kotha, S., Suggs, A., Radhakrishnan, R., Love, B. J., and Sudarshan, T. S. (2006). Bidisperse magnetorheological fluids using Fe particles at nanometer and micron scale. Journal of Intelligent Material Systems and Structures, 17(5), 393-401.

[16] Jönkkäri, I., Isakov, M., and Syrjälä, S. (2015). Sedimentation stability and rheological properties of ionic liquid–based bidisperse magnetorheological fluids. Journal of Intelligent Material Systems and Structures, 26(16), 2256-2265.

[17] Leong, S. A. N., Mazlan, S. A., Samin, P. M., Idris, A., and Ubaidillah. (2016). Performance of bidisperse magnetorheological fluids utilizing superparamagnetic maghemite nanoparticles. AIP Conference Proceedings, 1710, 030050.

[18] Cullity, B. D., and Graham, C. D. Introduction to Magnetic Materials (John Wiley & Sons, Hoboken, 2009).

[19] Morillas, J. R., Bombard, A. J., and de Vicente, J. (2015). Preparation and characterization of magnetorheological fluids by dispersion of carbonyl iron microparticles in PAO/1-octanol. Smart Materials and Structures, 25(1), 015023.

[20] Bombard, A. J., Gonçalves, F. R., Morillas, J. R., and de Vicente, J. (2014). Magnetorheology of dimorphic magnetorheological fluids based on nanofibers. Smart Materials and Structures, 23(12), 125013.

[21] Morillas, J. R., and de Vicente, J. (2019). On the yield stress in magnetorheological fluids: a direct comparison between 3D simulations and experiments. Composites Part B: Engineering, 160, 626-631.

[22] Jiles, D. Introduction to magnetism and magnetic materials (CRC Press, Boca Raton, 2015).

[23] Garnett, J. M. (1904). Colours in metal glasses and in metallic films. Philosophical Transactions of the Royal Society of London. Series A, Containing Papers of a Mathematical or Physical Character, 203, 385-420.

[24] Ginder, J. M., Davis, L. C., and Elie, L. D. (1996). Rheology of magnetorheological fluids: Models and measurements. International Journal of Modern Physics B, 10(23n24), 3293-3303.

[25] de Vicente, J. (2013). Magnetorheology: A review. The Ibero-American Journal of Rheology, 1, 1-18.

Chapter 12. Magnetorheology of Bimodal Fluids in the Single-Multidomain Limit

Jose R. Morillas, Antonio J. F. Bombard and Juan de Vicente

This article is published in: Industrial & Engineering Chemistry Research, 57(40), 13427-13436 (2018).

DOI: https://doi.org/10.1021/acs.iecr.8b03438

Abstract

In this manuscript we investigate the shear rheology, sedimentation stability and redispersibility characteristics of bimodal MR fluids with a Large-to-Small size ratio $\sigma_L/\sigma_S \approx 100$ where the small-size population of particles is in the single- multidomain limit ($\sigma_S \approx 100$ nm) to promote the formation of core-shell supraparticles (i.e. large particles surrounded by the smaller ones). We focus on the effect of mixing the two kinds of particles in different proportions while keeping either the large particles volume fraction or the total volume fraction constant. Five different nanoparticles, having different chemical composition and shape, are investigated in this work: barium ferrite, magnetite, iron, chromium dioxide and goethite. Results demonstrate that nanoparticles fill the voids between microparticles and this locally enhances the magnetic field. The on-state yield stress and effective enhancement may increase or decrease depending on the magnetization of the nanoparticles as compared to that of the microparticles. An enhanced MR effect is experimentally observed, and also simulated with Finite Element Methods, when the magnetization of the nanoparticles is larger than that of the microparticles. Bimodal MR fluids exhibit better penetration and redispersability response than the monomodal counterparts and dimorphic magnetorheological fluids based on nanofibers.

12.1 Introduction

Conventional magnetorheological (MR) fluids are suspensions of magnetizable particles in a non-magnetic liquid carrier. Under appropriate conditions (sufficiently large fields and concentrations) they exhibit a field-dependent apparent yield stress, $\tau_y = \tau_y(H)$, as a result of the formation of field-induced structures [1-8].

Undoubtedly, the main characteristic of any MR fluid is the so-called MR effect (or *turn-up ratio*). It can be described by a 'relative' yield stress, RYS, that measures the increase in the yield stress as the ratio between the yield stress increment under field and the yield stress value in the absence of the field:

$$RYS = \frac{\tau_y(H \neq 0) - \tau_y(H = 0)}{\tau_y(H = 0)} \tag{12.1}$$

In view of Eq. (12.1), the off-state yield stress, i.e. the yield stress with no magnetic field applied $\tau_y(H = 0)$, and the on-state yield stress, i.e. the yield stress with the magnetic field applied $\tau_y(H \neq 0)$, are both important in the MR performance. Most attempts reported in the literature to increase the on-state yield stress also result in an increase in the off-state yield stress carrying a penalty in the RYS [9]. However, there exists a very simple way to decouple the off-state yield stress and the on-state yield stress. It consists in the use of bimodal suspensions.

The idea behind the use of bimodal suspensions comes from classical studies on non-Brownian conventional (i.e. non field-responsive) particle suspensions. In that particular case, the rheology is dictated by the hydrodynamics once the carrier fluid viscosity and particle volume fraction are known [10,11]. Interestingly, incorporating multimodal particles reduces the viscosity of the suspensions, because of particle packing arguments, while keeping the same total volume fraction. In the particular case of bimodal (Large/Small) suspensions, the viscosity is a function of the carrier fluid viscosity, total particle volume fraction ϕ_T, relative fraction of small particles by volume ϕ_S/ϕ_T, and the size ratio σ_L/σ_S (diameter of the large particles divided by the diameter of small particles). This viscosity reduction is more significant for large ϕ_T and large σ_L/σ_S (within the non-Brownian regime). For a given ϕ_T and σ_L/σ_S, the lowest viscosities are typically obtained for $\phi_S/\phi_T \approx 0.3$ [12]. Note that in this manuscript ϕ_S is defined as $\phi_S = V_S/V_{sus}$ where V_S is the volume of small particles and V_{sus} is the total volume of the suspension, that is, the volume of small particles plus the volume of large particles plus the volume of the carrier liquid.

12.2 Background

A seminal work on the use of a bimodal distribution in magnetorheology is that of Foister [13]. In that patent, two highly polydisperse non-Brownian carbonyl iron powders ($\sigma_L =$ 7.9 µm, $\sigma_S = 1.25$ µm, $\sigma_L/\sigma_S \approx 6.3$) were mixed in different proportions $\phi_S/\phi_T \in [0, 1]$. The goal was to reduce the off-state viscosity of the MR fluid and hence to increase the RYS. It was thought that the magnetic characteristics of the suspensions would, *a priori*, solely depend on the particle volume fraction, and not on the particle size distribution. As expected, for a given total concentration ($\phi_T = 0.55$) the off-state viscosity was monotonically reduced in nearly one order of magnitude adding small particles to the formulation. However, in contrast to the initial expectations, for a given ϕ_T, the on-state yield stress was found to reach a maximum for $\phi_S/\phi_T \approx 0.1 - 0.25$, in disagreement with a weighted average mixing rule, hence suggesting that structural particle arrangements play a key role. In summary, compared to the monomodal counterparts, the RYS in bimodal MR fluids could be significantly increased because both the off-state yield stress decreased and the on-state yield stress increased.

12.2.1 Bimodal MR fluids with $\sigma_L/\sigma_S \approx 10$

In magnetorheology, magnetostatic forces between particles must overcome thermal forces coming from Brownian motion. This provides a lower limit for the typical size of the largest particles σ_L. Also, a higher limit exists because of sedimentation issues. Overall, a preferred particle size is $\sigma_L \approx 10$ µm. In view of the work by Foister [13], most of the following literature in this field concerned non-Brownian suspensions with $\sigma_S \approx$ 1 µm and therefore $\sigma_L/\sigma_S \approx 10$. Most of these works provided similar observations to Foister [13] with bimodal suspensions giving place to larger yield stresses than

monomodal suspensions composed of either the small or large particles [14-23]. Although the observed off-state viscosity reduction is well understood in terms of particle packing characteristics, the on-state yield stress enhancement is still not well understood. Bearing in mind that the effect of relative particle sizes on the magnetostatic force magnitude cannot explain the enhancement in the on-state yield stress in bimodal suspensions [18], one may think that the use of bimodal suspensions would result in more efficiently packed aggregates which are therefore stronger and promote a larger yield stress (e. g. Ref. [20]). However, particle level simulations conclusively demonstrate that the enhanced on-state yield stress in bimodal suspensions is a result of the tendency of the smaller particles to induce the larger particles to form more chainlike structures. In summary, the enhancement is not associated with an increase in particle packing within the aggregates but to the changes polydispersity causes in the microstructure [18,21]. A common issue in non-Brownian bimodal suspensions with $\sigma_L/\sigma_S \approx 10$ is that they suffer from important sedimentation because of the large particle size of the two populations.

12.2.2 Bimodal MR fluids with $\sigma_L/\sigma_S \approx 1000$

Apart from the interest in enhancing the MR effect, a drawback of MR fluids is that they tend to settle rapidly because of the density mismatch between the particles and the carrier. In an attempt to improve the kinetic stability of the MR fluids, some researchers explored in the past the use of bimodal suspensions with $\sigma_S \approx 10$ nm and therefore $\sigma_L/\sigma_S \approx 1000$ [24-33]. An important observation is that in this case, a portion of the particle population is Brownian and therefore the off-state viscosity reduction is not guaranteed despite the large size ratio. Investigations on the off-state properties of these bimodal MR fluids are scarce in the literature. Also, the theoretical description of these suspensions becomes strongly complicated because particle level simulations are precluded (involving two extraordinarily different length scales). Anyway, a generalized observation is that the settling problem becomes strongly mitigated presumably because of the thermal convection of nanoparticles that delays the sedimentation of the bigger ones [27,29,31]. However, after a slight initial increase (presumably due to the smaller particles filling the voids between microparticles which locally enhance the magnetic field [29,34]), the on-state yield stress is substantially reduced, ($\phi_S/\phi_T \approx 5$ wt% when the total particle loading is 45 wt% [26], $\phi_S/\phi_T \approx 7.5$ wt% when the total particle loading is 60 wt% [28]), maybe because of chain-growth inhibition [18], despite the fact that the nanoparticles were observed to fill in the interparticle spaces between the larger particles in the chain-like structures locally rising the magnetic permeability and resulting in a higher magnetic flux density [29] or because of the inferior magnetic properties of the nanoparticles if compared to the microparticles [31,35].

12.2.3 Bimodal MR fluids with $\sigma_L/\sigma_S \approx 100$

As reviewed above, bimodal MR fluids have been traditionally studied in two clearly differentiated regimes depending on whether the RYS is enhanced ($\sigma_L/\sigma_S \approx 10$) or the sedimentation is mitigated ($\sigma_L/\sigma_S \approx 1000$). Currently, to the best of our knowledge, there is only one work dealing with bimodal suspensions in the intermediate region ($\sigma_L/\sigma_S \approx 100$) [34]. According to this publication, bimodal suspensions in this size range exhibit a large MR effect at the same time the sedimentation is reduced if compared to bimodal suspensions with $\sigma_L/\sigma_S \approx 10$ or $\sigma_L/\sigma_S \approx 1000$, respectively. The explanation for this is that nanoparticles in the single-multidomain limit exhibit a magnetic remanence (i.e. a permanent non-zero magnetic moment) that promotes their adsorption onto the bigger magnetic multidomain microparticles. When these nanoparticles exhibit superior

magnetic properties than the microparticles, the resulting core-shell particles interact stronger than bare microparticles. Concomitantly, the sedimentation is reduced because of the presence of a cloud of nanoparticles surrounding the big ones.

In this manuscript we aim to get deeper in the previous publication by Morillas *et al.* [34] in order to better understand the gap between the two classical regimes: $\sigma_L/\sigma_S \approx 10$ and $\sigma_L/\sigma_S \approx 1000$. With this aim, in this manuscript we study mixtures with different magnetic characteristics. In particular we employ three kinds of nanospheres: barium ferrite, magnetite and iron. The first material is a hard magnetic material while the last two ones are soft magnetic materials with different saturation magnetization. Results are also compared with previous work where micronsized particles are partially substituted by (magnetic and non-magnetic) nanofibers [35]. Two nanofibers are discussed: goethite and chromium dioxide; the last one exhibiting a very similar magnetic behavior to magnetite to decouple the influence of particle shape (see Fig. 12.1).

12.3 Materials and methods

12.3.1 Particulate materials

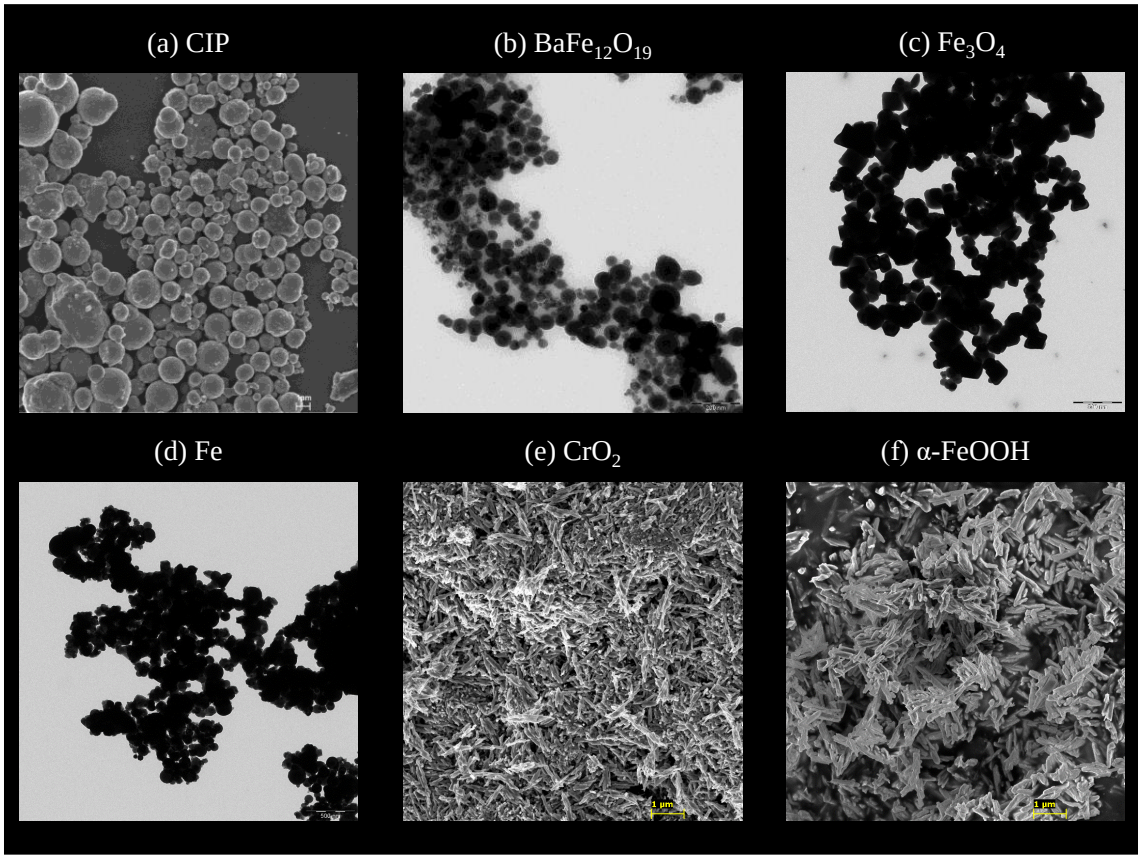

Figure 12.1: EM micrographs of the particulate materials employed. a) CIP, b) $BaFe_{12}O_{19}$, c) Fe_3O_4 ,d) Fe, e) CrO_2 and f) α-FeOOH.

The micron-sized magnetic powder used in this work is a carbonyl iron powder (CIP) EW grade from BASF SE (Germany). This is a particularly fine grade that has been exhaustively investigated in the recent literature. Using larger CIPs does not affect the conclusions of this work as soon as the nanoparticles are in the single- multidomain limit.

Nano-sized magnetic powders were made of barium ferrite -$BaFe_{12}O_{19}$- (Sigma-Aldrich), magnetite -Fe_3O_4- (Sigma-Aldrich) and iron -Fe- (US Research Nanomaterials). For comparative purposes, we also used nanofibers of magnetic and non-magnetic character; chromium dioxide -CrO_2- and goethite -α-FeO(OH)-, respectively (Sigma-Aldrich).

SEM was used to determine the morphological characteristics of CIP. On the other hand, TEM was used to obtain the particle size distribution of the nanoparticles ($BaFe_{12}O_{19}$, Fe_3O_4 and Fe). Typical EM pictures of the dry nanoparticles are included in Fig. 12.1. These pictures clearly demonstrate the submicron size of the particles.

The magnetic properties of the dry powders were measured with a vibrating sample magnetometer (MLVSM9 MagLab 9 T, Oxford Instruments) at room temperature. The results are shown Fig. 12.2. As observed, the particles exhibit a very different magnetization level in the range of magnetic field strengths investigated. In particular, the coercivity of CIP, $BaFe_{12}O_{19}$, Fe_3O_4, Fe, CrO_2 and α-FeOOH was measured to be 0.7 kA/m, 1.1 kA/m, 5.6 kA/m, 11 kA/m, 50 kA/m and 0.02 kA/m, respectively. In Table 12.1 we provide a detailed morphological and magnetic characterization of the particles used in this work. For the fields of interest here (147 kA/m in steady shear), the magnetization level decreased in the following order: Fe > CIP > Fe_3O_4 ≈ CrO_2 > $BaFe_{12}O_{19}$ >> α-FeOOH.

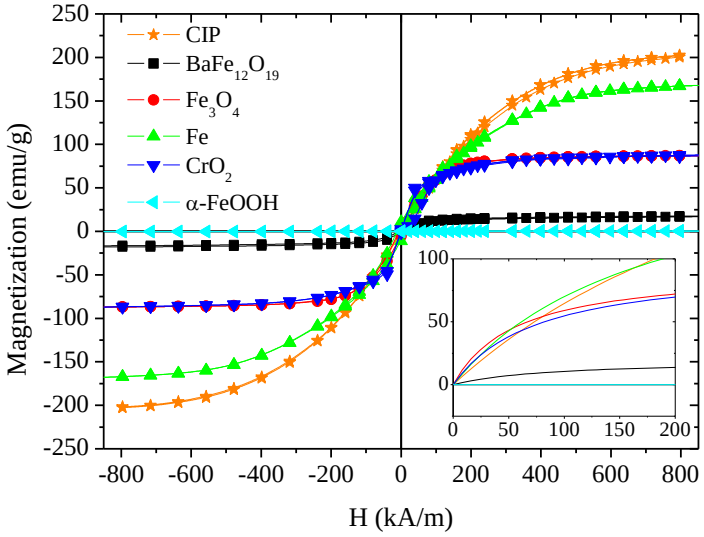

Figure 12.2: Magnetic hysteresis curves of the powders at room temperature. The inset represents the magnetization curves according to the Fröhlich-Kennelly model as fitted to the experimental ones.

12.3.2 Preparation of the MR fluids

First, several powder mixtures were prepared at various mixing ratios in polyethylene containers. These mixtures consisted in large carbonyl iron microparticles (CIP) and small nanoparticles from Table 12.1. Then, polyalphaolefin oil (PAO 2 cSt, Synfluid, Chevron-Philips) was added to the particles. In order to facilitate the processability of the MR fluids, a certain amount of 1-octanol was added to the PAO (3.5 wt% in the total amount of PAO). It has been previously reported that the addition of 1-octanol in the MR fluid formulation has a negligible effect on the on-state yield stress. However, it significantly improves the dispersability of the solids [36]. In this work we operate in the

widest solids concentration range possible. Higher concentration compositions do not mix properly due to the high surface area of the nanopowders.

	Microparticles	Nanoparticles				
Material	CIP - Carbonyl iron spheres	$BaFe_{12}O_{19}$ - Barium ferrite	Fe_3O_4 - Magnetite	Fe - Nano iron	CrO_2 - Chromium dioxide	α-FeOOH Goethite
Shape	Spheres	Spheres	Irregular	Irregular	Fibers	Fibers
Number average diameter (nm)	1327.4	54.50	156.54	111.64	*	*
Weight average diameter (nm)	2642.8	80.47	206.75	206.99	*	*
Volume average diameter (nm)	1729.3	62.76	173.73	137.87	*	*
PDI	1.991	1.477	1.321	1.854	*	*
Initial susceptibility χ_i	6.42	1.25	8.30	8.66	6.20	0.00**
Saturation magnetization (emu/g)	204	21	89	176	93	1.3
Coercive field (kA/m)	0.7	1.1	5.6	11	50	0.02
N	446	343	298	286	*	*

Table 12.1: Morphological and magnetic characteristics of the micro- and nanoparticles employed in this manuscript to investigate the effect of mixing ratio in the on-state yield stress. The initial susceptibility (χ_i) is taken from the best fitting to the Frohlich-Kenelly equation (see Fig. 12.2). PDI stands for the polydispersity index. In the calculations we considered a number of particles N > 200. *Particles are clumped and overlap in electron microscopy pictures. Therefore they cannot be measured. **Goethite particles are non-magnetic (see Ref. [35]).

12.3.3 Shear rheometry

A stress controlled magnetorheometer (MCR501, Anton Paar) was used for the rheological characterization of the MR fluids. All tests were run at 25 ºC.

Two kinds of simple shear experiments were conducted:

(i) Steady shear flow tests were performed with a MRD70/1T magnetocell in plate-plate configuration (20 mm diameter, 300 microns gap) to ascertain the apparent yield stress of the MR fluids. Yield stresses were obtained using a carefully designed protocol. This protocol consists in several stages: (Stage 1) A constant rim shear rate ($\dot{\gamma}$ = 100 s^{-1}) is applied during 20 seconds. (Stage 2) The upper plate is stopped and a uniaxial DC magnetic field (147 kA/m) is suddenly applied for 60 s to promote the structuration of the MR fluid. (Stage 3) A stress log-ramp is applied to evaluate the yielding point similarly

to Bombard *et al.* [35]. The interval time employed to get every data within the full rheogram was 5 seconds. At least three independent measurements with fresh new samples were taken. Error bars in the figures correspond to the standard deviation of the different repetitions.

(ii) Small amplitude dynamic oscillatory tests were carried out using a Twin gap magnetocell from Anton Paar (15.867 mm diameter, 0.339 mm gap). This magnetocell allows us to achieve very strong magnetic fields (very close to the magnetic saturation) at the same time it minimizes wall slip. In these tests the magnetic field strength is logarithmically increased from 0 to 830 kA/m (external field in the measuring gap without sample) under the presence of a small-amplitude oscillatory shear deformation (strain amplitude 0.01%, frequency 10 rad/s). Similarly to Bombard *et al.* [35], the experimental protocol was as follows: (Stage 1) Precondition at a constant shear rate $\dot{\gamma} = 100$ s^{-1} for 30 s. (Stage 2) The suspension is left to equilibrate for 25 s at rest with the magnetic field off. (Stage 3) Constant dynamic-mechanical shear conditions are preset (both amplitude and frequency remain constant) and the external magnetic field was logarithmically increased. Again, experiments were repeated three times with fresh new samples.

12.3.4 Sedimentation and redispersibility tests

To explore the sedimentation stability (in the absence of fields) a given volume of MR fluid was placed inside a cylindrical plastic tube and visually observed during time to determine the time evolution of sedimentation ratio $h(t)/h_0$ curves. Here $h(t)$ represents the height of the sediment/liquid interface (i.e. mudline) at a given time, t, and h_0 is the corresponding height value of the MR fluid at the beginning of the test $h_0 = h(t = 0)$.

Penetration and redispersibility tests were carried out using a four-blade vane tool attached to a MCR 501 rheometer head coupling. The test consisted in slowly displacing the tool (1 mm/s) towards the sample while recording the normal force acting on the vane. Once the vane was well inside the sample, a continuous torque ramp was initiated to determine the flow curve (from 0.0001 mN·m to 0.5 mN·m). Tests were carried out when the MR fluid was completely sedimented (exactly one week after the preparation of the suspension).

12.4 Results and discussion

12.4.1 Effect of the addition of small particles to MR fluids with $\phi_L = 0.30$

First, experiments were carried out at a fixed large particles (CIP) concentration of $\phi_L = 0.30$ and the total particle concentration ϕ_T $(= \phi_L + \phi_S)$ was changed by varying the small particles concentration ϕ_S. Results are summarized in Fig. 12.3.

For small particles having quasi-spherical shape (i.e. $BaFe_{12}O_{19}$, Fe_3O_4 and Fe) the off-state yield stress remained essentially constant at a low level (approximately 0.1-1 Pa) when ϕ_S < 5 vol% (see Fig. 12.3a). Above this particular concentration value, the off-state yield stress increased sharply as a result of the formation of a percolating particle network. In the absence of magnetic fields the rheological behavior of these bimodal MR fluids was very similar, independently of the particular material employed, for a given ϕ_S. This suggests that the percolating structure is not driven by magnetostatic interparticle forces despite the fact that it may be expected a difference due to the coercive field.

In contrast to the trend exhibited by the off-state yield stress, the on-state yield stress exhibits an initial increase with small particles concentration up to $\phi_S = 5$ vol% (see Fig. 12.3b). This increase is quantitatively similar whatever the chemical composition of the particles. Above this concentration level, the yield stress increased with ϕ_S at a higher rate for Fe. The rate of increase of the yield stress above this concentration threshold was strongly dependent on the particular material employed and correlated very well with the magnetization level of the nanoparticles at the external magnetic field applied (Fe > Fe_3O_4 > $BaFe_{12}O_{19}$).

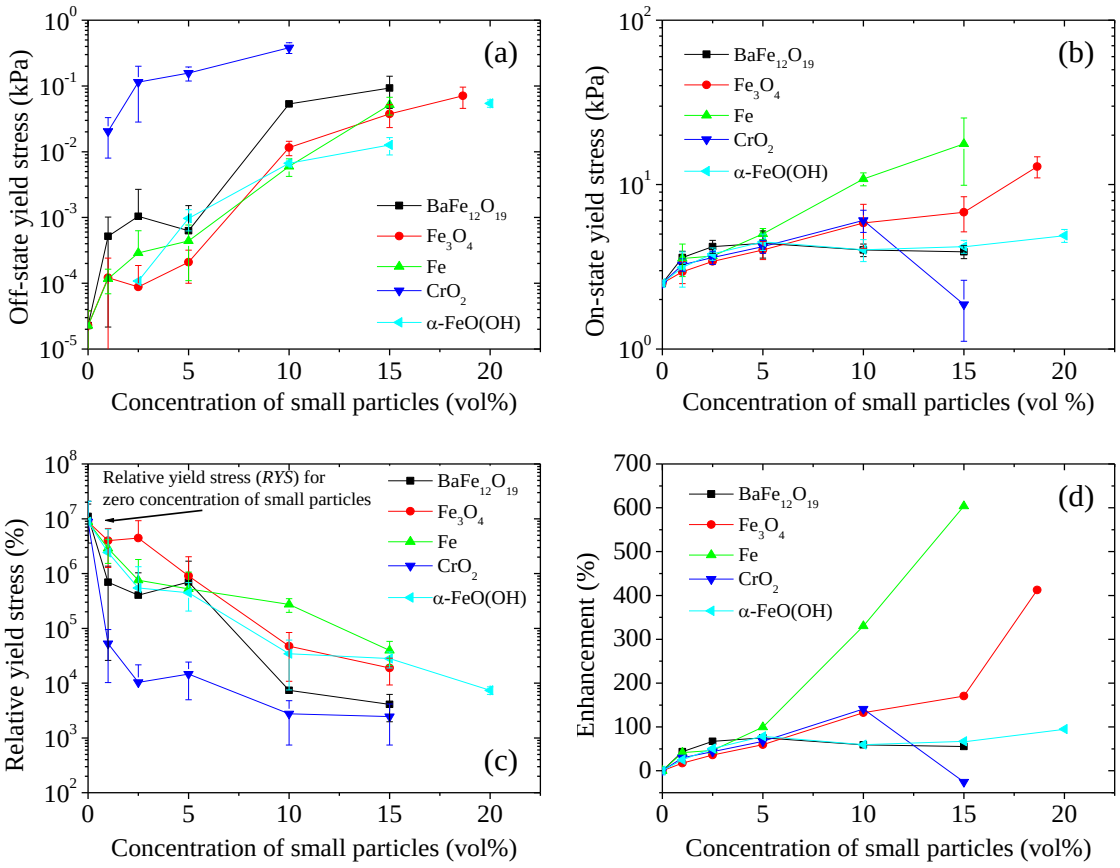

Figure 12.3: Magnetorheology of bimodal MR fluids as a function of the concentration of small particles for a constant CIP volume fraction $\phi_L = 30$ vol%. a) Yield stress as a function of the concentration of small particles ϕ_S in the off-state. b) Yield stress as a function of the concentration of small particles ϕ_S in the on-state (147 kA/m). c) Relative yield stress as a function of the concentration of small particles ϕ_S. d) Enhancement (%) as a function of the concentration of small particles ϕ_S.

A more convenient way to quantify the MR effect is to use the relative yield stress RYS (see Fig. 12.3c). The RYS remained at a very high level (approx. 10^6 %) for low ϕ_S concentrations. However, for ϕ_S > 5 vol% the RYS decreased in good agreement with the fact that the off-state yield stress increased at this concentration (see Fig. 12.3b). The arrow in Fig. 12.3c represents the RYS for monomodal MR fluids (without nanoparticles). The fact that RYS for monomodal MR fluids is slightly above the RYS for bimodal MR fluids demonstrates that for the smallest concentration of nanoparticles studied in this work (1 vol%) the off-state yield stress of the bimodal MR fluids is already significantly larger than that of the monomodal suspensions (see Fig. 12.3a). This is coherent with the fact that the yield stress in monomodal MR fluids was below the torque resolution of the rheometer thanks to the addition of 1-octanol.

Finally, in Fig. 12.3d we also plot the yield stress 'enhancement' as a function of the small particles concentration. The enhancement represented in Fig. 12.3d was calculated as follows:

$$\frac{\tau_{yb}(\phi_S + \phi_L) - \tau_{ym}(\phi_L = 0.3)}{\tau_{ym}(\phi_L = 0.3)} \tag{12.2}$$

where $\tau_{yb}(\phi_S + \phi_L)$ corresponds to the yield stress of the bimodal suspension and $\tau_{ym}(\phi_L = 0.3)$ stands for the yield stress of the monomodal suspension. As expected, the enhancement is larger the more magnetic are the small particles. Note, however, that this kind of representation is not appropriate when the nanoparticles are magnetic (see below).

12.4.2 Influence of the relative fraction of small particles in MR fluids with $\phi_T = 0.45$

In a second part of this study we explored the influence of the relative fraction of small particles by volume at a fixed total volume fraction $\phi_T = 45$ vol%.

In striking contrast to what happens in non-Brownian suspensions, the addition of small particles to the MR fluid formulation results in a significant increase in the off-state yield stress (see Fig. 12.4a). This increase is the result of interparticle colloidal interactions between small and large particles. Again, the fact that the curves are very similar whatever the material constituting the small particles suggests that these interactions are not of magnetic origin. Above $\phi_S/\phi_T \approx 0.20$ the off-state yield stress levels off; it is worth to note that we cannot achieve $\phi_S/\phi_T = 1$ because of the presence of very strong interparticle interactions that result in a flocculated gap-spanning structure.

As expected, the on-state yield stress strongly depends on the material employed (see Fig. 12.4b). While $BaFe_{12}O_{19}$ contributes to a decrease of the yield stress with ϕ_S/ϕ_T, Fe contributes increasing the on-state yield stress. On the other hand, for Fe_3O_4, the on-state yield stress remains essentially constant. There are two important contributions to the on-state yield stress that explain these different trends: On the one hand, the small particles tend to fill the empty spaces between the large particles forming chain-like structures and locally increasing the magnetic permeability. On the other hand, the superior/inferior magnetic response of the nanoparticles compared to the microparticles at the particular field investigated also plays a role [31]. While $BaFe_{12}O_{19}$ nanoparticles have inferior magnetic properties than CIP microparticles, Fe nanoparticles have superior magnetic properties than CIP microparticles. This explains their different behavior. In the case of Fe_3O_4, it seems that the two contributions almost perfectly balance and therefore the yield stress remains essentially constant. In any case, the change in the on-state yield stress is quite modest whatever the particular material and as a result, the relative yield stress continuously decreases when adding nanoparticles (see Fig. 12.4c).

In this case, a useful way to visualize the importance of adding a second population of nanoparticles to the suspension of large particles is through the so-called yield stress 'effective enhancement', that is defined as follows:

$$\frac{\tau_{yb}(\phi_S + \phi_L = 0.45) - \tau_{ym}(\phi_L = 0.45)}{\tau_{ym}(\phi_L = 0.45)} \tag{12.3}$$

The effective enhancement directly compares the performance of bimodal suspensions to monomodal ones of the same total concentration $\phi_T = \phi_S + \phi_L = 0.45$. Results are contained in Fig. 12.4d. Here we clearly observe a remarkable increase in the effective

enhancement for bimodal MR fluids containing Fe nanoparticles in striking contrast to monomodal MR fluids only containing CIP.

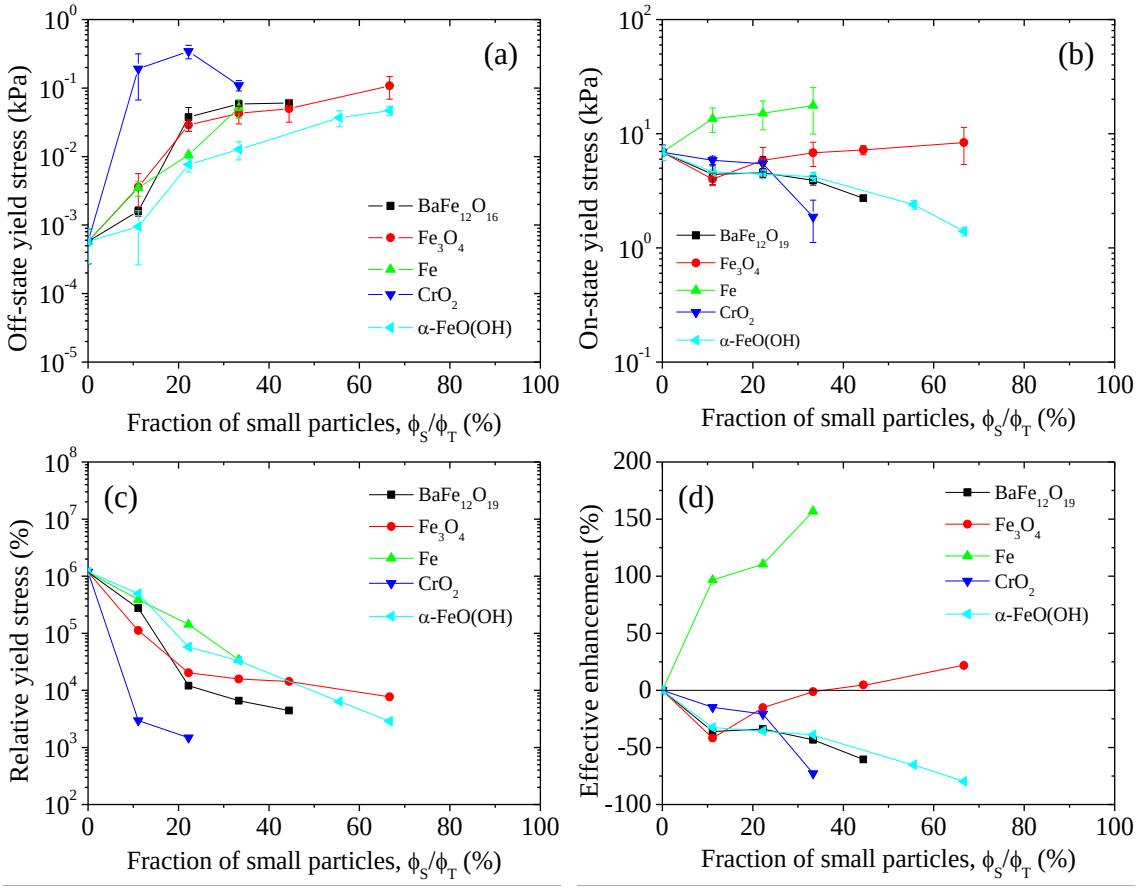

Figure 12.4: Magnetorheology of bimodal MR fluids as a function of the fraction of small particles for a constant total volume fraction of solids of $\phi_T = 45$ vol%. a) Off-state yield stress as a function of the fraction of small particles (ϕ_S/ϕ_T). b) On-state yield stress as a function of ϕ_S/ϕ_T for an external magnetic field of 147 kA/m. c) Relative yield stress as a function of ϕ_S/ϕ_T. d) Effective enhancement (%) as a function of ϕ_S/ϕ_T.

12.4.3 Study of 30 vol% large particles + 5 vol% small particles composites

We now pay attention to 30 vol% CIP + 5 vol% nanoparticles composite MR fluids. These are chosen because they still exhibit a reasonably large MR effect (cf. Fig. 12.3c on the relative yield stress) before the off-state yield stress begins to increase (cf. Fig. 12.3a). These results will be compared with monomodal MR fluids having the same total volume fraction $\phi_T = 0.35$.

12.4.3.1 *Magnetosweep tests under dynamic oscillatory shear*

Magnetosweep tests were carried out to investigate the influence of magnetic field strength in the linear viscoelastic properties of bimodal MR fluids. These results are shown in Fig. 12.5. A log-log representation is used in Fig. 12.5a to show the low field response while a lin-lin representation is used in Fig. 12.5b to better appreciate the high field response.

As a general trend, bimodal MR fluids exhibit a larger low field storage modulus than their monomodal counterparts. This suggests the formation of a percolating structure at

rest. This low field plateau is expected to be related to off-state yield stress measurements and sedimentation tests.

Regarding the high field region it is worth to remark the significantly larger storage modulus for bimodal MR fluids using iron when compared to monomodal ones at the same carbonyl iron concentration ($\phi_T = 0.35$).

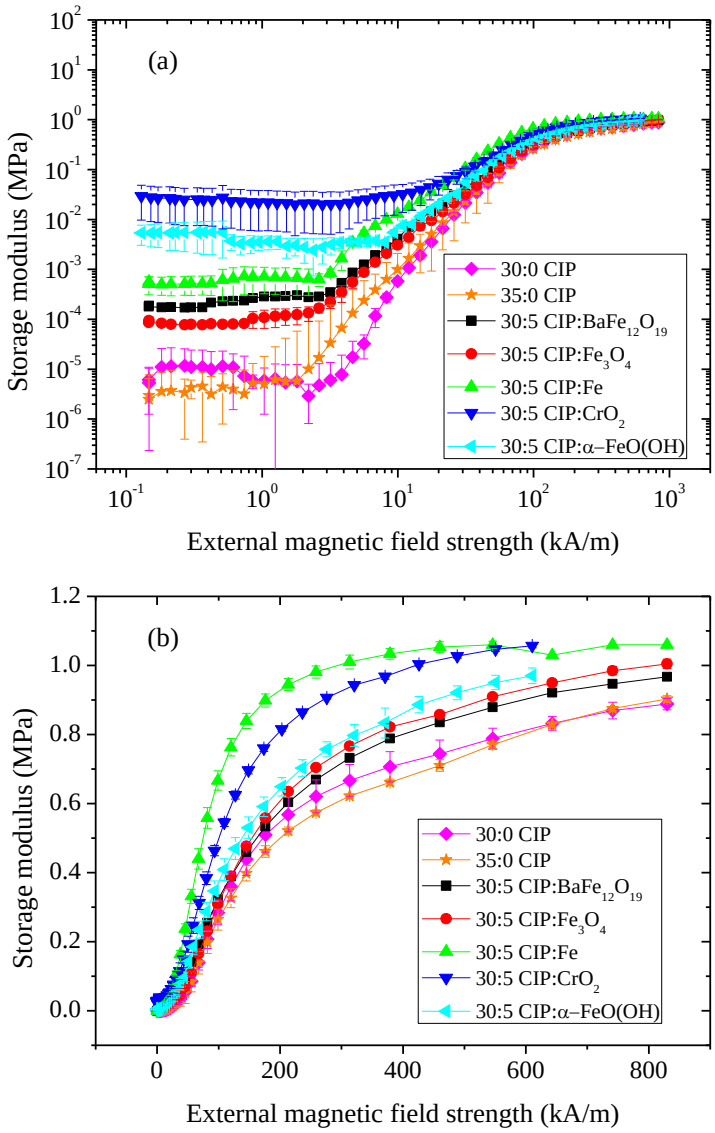

Figure 12.5: Storage modulus versus magnetic field strength dependence for MR fluids. Strain amplitude 0.01%. Excitation frequency 10 rad/s. a) Log-log representation to visualize the low field region. b) Lin-lin representation to visualize the high field region.

12.4.3.2 *Sedimentation stability*

Figure 12.6 contains sedimentation data for the bimodal MR fluids (30:5) and other monomodal ones (30:0 and 35:0) for comparison. As expected, the MR fluids do not have long shelf lives; all MR fluids sediment in the course of a few days. However, it is clear that bimodal MR fluids exhibit a delayed sedimentation.

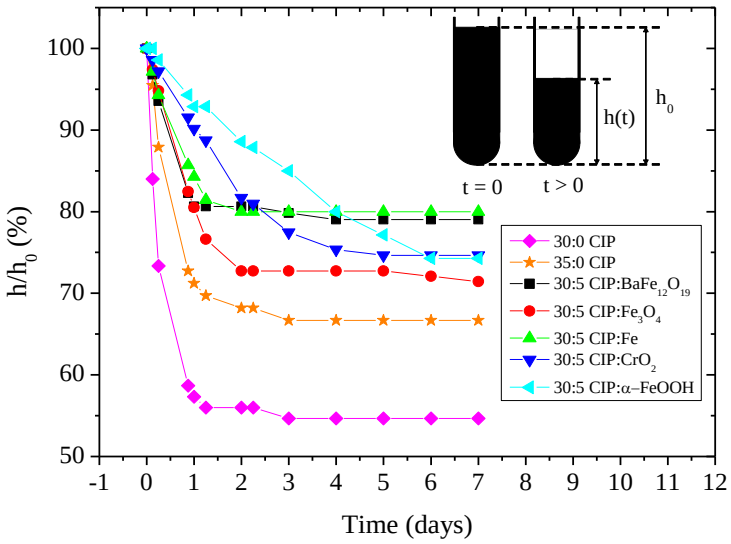

Figure 12.6: Time evolution of the sedimentation ratio (h/h_0) for conventional MR fluids (30 vol% and 35 vol% carbonyl iron) and bimodal MR fluids (30 vol% carbonyl iron + 5 vol% nanoparticles).

MR fluid	Maximum packing fraction	Maximum force peak (N) after penetrating a given distance (40 mm)	Work (mJ) for a penetration distance of 40 mm	Torque (μNm) at 0.001 rpm
30:0 CIP	0.549	*	*	*
35:0 CIP	0.525	*	*	*
30:5 $BaFe_{12}O_{19}$	0.443	0.137	4.15	32.2
30:5 Fe_3O_4	0.490	0.094	2.51	34.7
30:5 Fe	0.438	0.072	1.83	32.2
30:5 CrO_2	0.469	0.130	3.14	66.3
30:5 α-FeOOH	0.471	0.116	2.65	49.6

Table 12.2: Sedimentation, penetration and redispersibility characteristics of the bimodal MR fluids. *The sediments formed were so compact that they could not be penetrated to a distance of 40 mm.

In view of Fig. 12.6 we have to distinguish between the behavior at short and long times. With regards to short times, the sedimentation rate is significantly reduced when microparticles are replaced with nanoparticles. This is explained by the fact that small particles adhere onto the larger ones, forming an halo, and preventing the latter from close approach. On the other hand, the long time behavior is well described by the packing density of the sediment that in its turn gives valuable information on the dispersion quality. These results are included in Table 12.2. The most tightly packed sediments are always those corresponding to monomodal MR fluids. On the contrary, bimodal

suspensions give place to a higher sediment. Such a high sediment is the result of the formation of a loose sediment at the bottom of the tube. This is coherent with the fact that small and large particles are interacting and do not behave as non-Brownian hard spheres because in this case a particle mixture would give a more efficient packing. A slower sedimentation is also coherent with the presence of more aggregates in suspension [31].

Overall, the sedimentation stability of these bimodal MR fluids is similar to classical bimodal suspensions with $\sigma_L/\sigma_S \approx 1000$. In the latter, the reduced settling is claimed to result from the effect of thermodynamic forces coming from nanoparticles and frictional forces between both populations. However, in our bimodal MR fluids where $\sigma_L/\sigma_S \approx 100$, thermodynamic forces are expected to be negligible and therefore the reduced settling is explained by the formation of clusters of big particles surrounded by small ones that possess a large single-domain magnetic moment and remanence [34].

12.4.3.3 *Penetration and redispersibility*

Generally speaking, a porous (ill compacted) sediment is expected to be easy to penetrate and redisperse. However, the existence of strong interparticle interactions in the bimodal MR fluids obliges us to perform the tests.

The penetration and redispersibility characteristics of the MR fluids are summarized in Table 12.2. The monomodal suspensions could not be penetrated with the rheometer; they were too stiff. On the other hand, all bimodal suspensions were penetrated. In particular, the easiest to penetrate was that of Fe. In good agreement with penetration tests, bimodal suspensions based on Fe also exhibited the smaller torque level for full redispersion. Other mixtures exhibited an intermediate behavior between monomodal CIP suspensions and CIP-Fe bimodal suspensions.

12.4.4 Electron microscopy observations of structured bimodal MR fluids

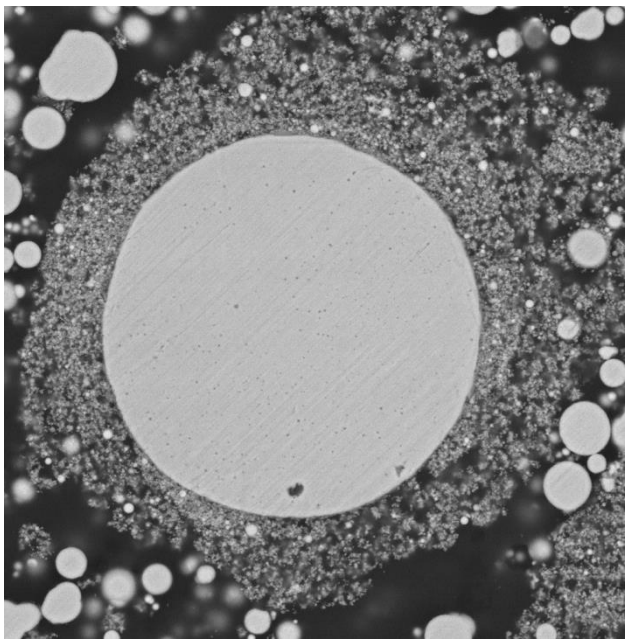

Figure 12.7: Scanning electron microscopy image corresponding to a big carbonyl iron microparticle surrounded by iron nanoparticles.

Particle mixtures were structured in a resin under magnetic fields in order to get a deeper understanding on the microstructures formed. Then, the resin was cut and observed under

an Environmental Scanning Electron Microscope. Results for iron particles mixures are shown in Fig. 12.7. This picture demonstrates that big carbonyl iron microparticles are surrounded by a cloud of iron nanoparticles. This suggests that the cloud formation is driven by strong magnetostatic interparticle interactions between micro- and nanoparticles. The fact that the small size particles are in the single-multidomain region results in the existence of a remnant magnetization in the particles that drives their adsorption onto the bigger particles.

12.4.5 Finite Element Method simulations

In this section we aim to elucidate the contribution of magnetostatics to the yield stress (i.e. neglecting colloidal forces) using a Finite Element Methodology (FEM).

First, we need to define the computational domain. For this, we consider a collection of core-shell supraparticles preassembled in single-particle width structures (i.e. a tetragonal lattice). In these simulations, the core mimics the CIP microparticles while the shell mimics the nanoparticles that surround each microparticle. Numerical simulations are performed on the lattice unit cell by imposing periodic boundary conditions in the magnetic field.

The magnetic field is simulated for a range of strain levels by numerically solving Maxwell's equations in COMSOL Multiphysics. A reduced field formulation is employed. According to this, the total magnetic field comes from two contributions: a homogeneous one (i.e. the applied external field, 147 kA/m) and a perturbation one due to the presence of the lattice. The magnetic constitutive equation of the different domains in the computational domain (core and shell) corresponds to the Fröhlich-Kennelly model as fitted to the experimental magnetization curves shown in Fig. 12.2.

Once the magnetic field distribution is calculated in the unit cell, internal stresses in the lattice are computed using the Maxwell's stress tensor. Finally, the yield stress is identified as the maximum shear stress when it is plotted as a function of the strain. For more details see Ref. [34].

Figure 12.8 contains the simulation results. On the one hand, in Figs. 12.8a and 12.8b we show the on-state yield stress and enhancement dependence on small particles concentration when CIP (large particles) concentration is fixed to $\phi_L = 30$ vol%. On the other hand, in Figs. 12.8c and 12.8d we show the on-state yield stress and effective enhancement dependence on small particles concentration when the total solids concentration is fixed to $\phi_T = 45$ vol%. Comparing Fig. 12.8 with Figs. 12.3 and 12.4 we conclude that the simulations provide the right order of magnitude for the (on-state) yield stress. In agreement with the experiment, simulations demonstrate that the more magnetic the nanoparticles the larger the yield stress of the bimodal MR fluids for a given concentration. Both the yield stress and enhancement increase with small particles concentration if the nanoparticles are 'sufficiently' magnetic (i.e. their magnetization is larger than that of CIP at the prescribed field strength).

This behavior is understood taking into consideration that for small applied fields, interparticles forces are dominated by multipolar terms, which are strongly enhanced for short distances between particles. As the small particles concentration increases the shell of the supraparticles gets thicker and consequently, the magnetic properties of the shell will play the major role in the magnetic interparticle interaction. Depending on magnetic properties of the shell (in relation to the core), the yield stress could be enhanced (shell magnetization larger than the core) or reduced (shell magnetization smaller than the core).

The previous discussion also points out that, in addition to magnetostatics, in the experiments, other colloidal forces play a role. Furthermore, for so highly concentrated suspensions, lateral interconnections between aggregates may also contribute making our simplified model a too bold one.

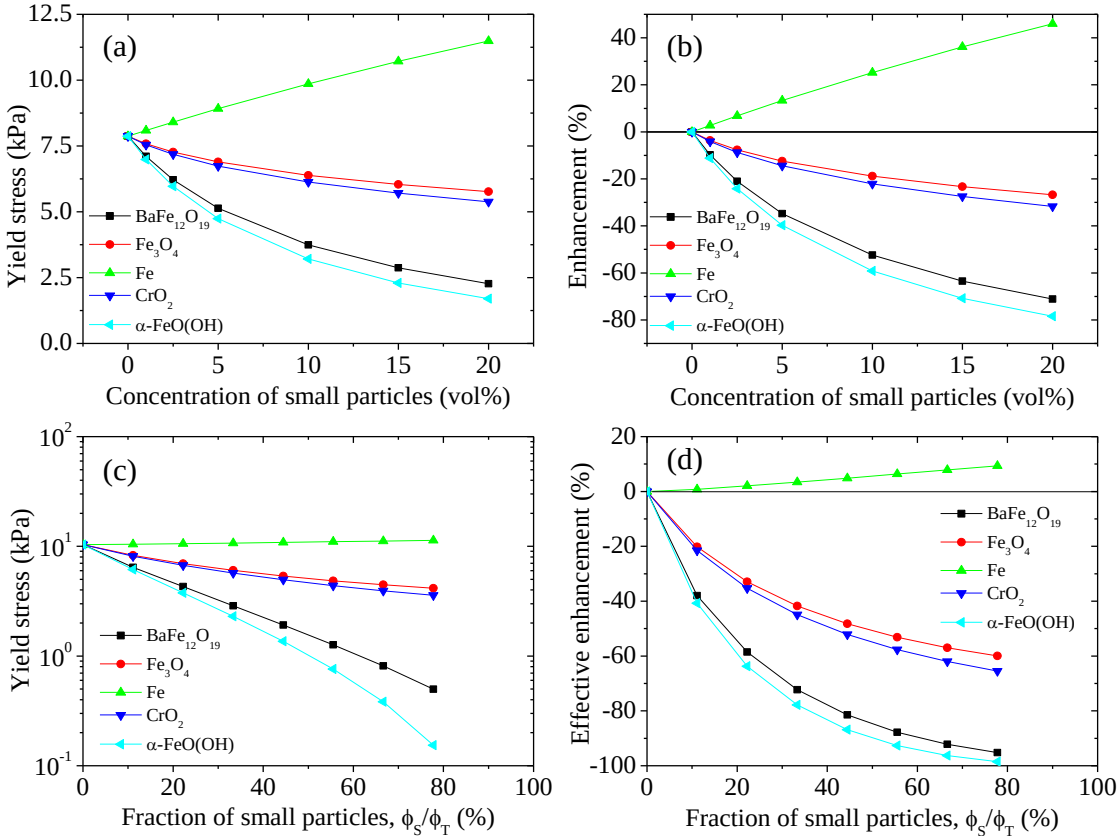

Figure 12.8: Finite element simulations of model structures for a constant CIP volume fraction $\phi_L = 30$ vol% (a and b) and for a constant total volume fraction of solids of $\phi_T = 45$ vol% (c and d). a) and c) represent the on-state yield stress while b) and d) represent the effective enhancement (%).

12.4.6 Comparison with bimodal MR fluids based on nanofibers

For completeness, in Figs. 12.3 and 12.4 we also include experimental data from Bombard *et al.* [35] for bimodal MR fluids prepared with nanofibers. Two kinds of nanofibers are studied: non-magnetic (α-FeO(OH)) and magnetic ones (CrO_2).

Figure 12.3a demonstrates that the addition of non-magnetic nanofibers (α-FeO(OH)) to 30 vol% CIP suspensions gives a similar off-state yield stress than using spherical nanoparticles, hence discarding the importance of the shape anisotropy of the nanoparticles. Note, however, that the off-state yield stress always remains below 20 Pa. In agreement with the previous discussion in Secs. 12.4.1 and 12.4.2, this observation again suggests that the off-state yield stress increase with the concentration of small particles is dominated by colloidal forces (i.e. dominated by the size of the nanoparticles and not their shape). In the case of magnetic nanofibers, the off-state yield stress is clearly above the results obtained for the other samples. This is something expected in view of the fact that these nanofibers exhibit an extraordinarily large coercive field (see Table 12.1). In view of Fig. 12.3b, the on-state yield stress of the suspensions is very similar for the nanofibers and for the weakest magnetic nanoparticles, again suggesting that the

nanoparticle shape does not play an important role. This suggests that both nanofibers and nanoparticles form reasonably well-compacted shells surrounding the CIP microparticles.

Special attention must be paid to the comparison between bimodal suspensions containing Fe_3O_4 and CrO_2. The difference between these two nanomaterials is basically their shape anisotropy and coercivity. While Fe_3O_4 is roughly spherical in shape, CrO_2 has an acicular shape. Also, Fe_3O_4 is significantly magnetically softer than CrO_2. As observed in Fig. 12.3a, CrO_2 gives a larger off-state yield stress presumably because of the magnetically hard character (i.e. remnant magnetization) of the nanofibers. On the other hand, the observation of Fig. 12.3b demonstrates that the on-state yield stress is very similar for both bimodal suspensions for a small particles concentration below 15 vol%. This suggests that colloidal forces dominate this low concentration regime. However, the deviation observed for a concentration of 15 vol% suggests that CrO_2 nanofibers interfere with the chain-like structure formed by CIP's more strongly than their spherical Fe_3O_4 counterparts.

Both the relative and enhancement in the yield stress depicted in Figs. 12.3c and 12.3d can be interpreted as a consequence of the previous discussion; the relative yield stress of the magnetic nanofibers remains below the rest of the curves because of the large off-state yield stress exhibited whatever the small particles concentration. On the other hand, the enhancement in the yield stress remains at a similar level than weakly magnetic spherical nanoparticles. Results for a constant total volume fraction of solids of $\phi_T = 45$ vol% are in qualitative agreement with the previous discussion for $\phi_L = 30$ vol% (see Fig. 12.4); again, a similar trend is observed if compared to weakly magnetic spherical nanoparticles.

Undoubtedly, the most remarkable difference between the use of nanofibers and nanospheres concerns the off-state behavior and, in particular, the sedimentation stability of the bimodal suspensions. A storage modulus above 1 kPa in the absence of fields is a clear indication of the formation of a gelled structure that percolates the available volume (cf. Fig. 12.5a). This is coherent with the slow sedimentation rate at the initial times observed in Fig. 12.6. However, for very long settling times the nanofibers clearly form stronger cakes than their spherical counterparts.

12.5 Conclusions

We demonstrate a new route to enhance magnetorheology. It consists in the use of bimodal suspensions, containing micro- and nanoparticles, where the smaller particles in dispersion have a typical size in the frontier from magnetic mono- to multidomains. In this particular size scale, the nanoparticles exhibit a sufficiently large coercive field for them to adhere onto the surface of the larger ones.

In this manuscript we first demonstrate the importance of the magnetic characteristics of the nanoparticles. A remarkable enhancement is found when the nanoparticles have superior magnetic properties than the microparticles. This experimental observation is supported by Finite Element Method simulations. On the other hand, the enhancement is modest or even negligible when the nanoparticles are weakly magnetic (as compared to the CIPs). The sedimentation stability, penetration and redispersability characteristics of these bimodal suspensions also improve with respect to the monomodal counterparts; the suspensions settle more slowly, penetration is easier and redispersibility occurs at lower torque levels. Overall, the performance of these bimodal suspensions is still better than

that of dimorphic MR fluids based on nanofibers, independently of whether the nanofibers are magnetic or not.

Finally, it is worth to note that in the experiments we have kept constant the 1-octanol concentration at the same time the concentration of small particles has been changed. Of course, this may have an effect because of the difference in surface area and therefore colloidal interparticle interactions. This aspect is worth to be studied in detail in a future investigation.

Acknowledgements

This work was supported by MINECO MAT 2016-78778-R and PCIN-2015-051 projects (Spain), European Regional Development Fund (ERDF) and by Junta de Andalucía P11-FQM-7074 project (Spain). J. R. Morillas acknowledges FPU14/01576 fellowship. A. J. F. Bombard is grateful to FAPEMIG grants: ETC-00043-15, PEE-00081-16, APQ-01824-17; and CNPq grant 200278/2018-5 (Brasil).

References

[1] Ginder, J. M. (1998). Behavior of magnetorheological fluids. MRS Bulletin, 23(8), 26-29.

[2] Bossis, G., Volkova, O., Lacis, S., and Meunier, A. (2002). Magnetorheology: fluids, structures and rheology. In: Odenbach, S. (Ed.) Ferrofluids. Lecture Notes in Physics (Vol. 594) (Springer, Berlin).

[3] Park, B. J., Fang, F. F., and Choi, H. J. (2010). Magnetorheology: materials and application. Soft Matter, 6(21), 5246-5253.

[4] de Vicente, J., Klingenberg, D. J., and Hidalgo-Álvarez, R. (2011). Magnetorheological fluids: a review. Soft Matter, 7(8), 3701-3710.

[5] de Vicente, J. (2013). Magnetorheology: A review. The Ibero-American Journal of Rheology, 1, 1-18.

[6] Wereley, N. (Ed.). Magnetorheology: advances and applications (Vol. 6) (Royal Society of Chemistry, Cambridge, 2013).

[7] Bica, I., Liu, Y. D., and Choi, H. J. (2013). Physical characteristics of magnetorheological suspensions and their applications. Journal of Industrial and Engineering Chemistry, 19(2), 394-406.

[8] Ashtiani, M., Hashemabadi, S. H., and Ghaffari, A. (2015). A review on the magnetorheological fluid preparation and stabilization. Journal of Magnetism and Magnetic Materials, 374, 716-730.

[9] Shahrivar, K., and de Vicente, J. (2013). Thermoresponsive polymer-based magneto-rheological (MR) composites as a bridge between MR fluids and MR elastomers. Soft Matter, 9(48), 11451-11456.

[10] Russel, W. B., Saville, D. A., and Schowalter, W. R. Colloidal dispersions (Cambridge University Press, Cambridge, 1991).

[11] Larson, R. G. The structure and rheology of complex fluids (Vol. 150) (Oxford University Press, New York, 1999).

[12] Chong, J. S., Christiansen, E. B., and Baer, A. D. (1971). Rheology of concentrated suspensions. Journal of Applied Polymer Science, 15(8), 2007-2021.

[13] Foister, R. T. (1997). U.S. Patent No. 5667715. Washington, DC: U.S. Patent and Trademark Office.

[14] Weiss, K. D., Carlson, J. D., and Nixon, D. A. (2000). U.S. Patent No. 6027664. Washington, DC: U.S. Patent and Trademark Office.

[15] See, H., Kawai, A., and Ikazaki, F. (2002). The effect of mixing particles of different size on the electrorheological response under steady shear flow. Rheologica Acta, 41(1-2), 55-60.

[16] Ulicny, J. C., Smith, A. L., Golden, M. A., McDermott, B. L., and Chapaton, T. J. (2004). U.S. Patent No. 6824701. Washington, DC: U.S. Patent and Trademark Office.

[17] Trendler, A. M., and Böse, H. (2005). Influence of particle size on the rheological properties of magnetorheological suspensions. International Journal of Modern Physics B, 19(07n09), 1416-1422.

[18] Kittipoomwong, D., Klingenberg, D. J., and Ulicny, J. C. (2005). Dynamic yield stress enhancement in bidisperse magnetorheological fluids. Journal of Rheology, 49(6), 1521-1538.

[19] Goncalves, F. D., Koo, J. H., and Ahmadian, M. (2006). A review of the state of the art in magnetorheological fluid technologies-Part I: MR fluid and MR fluid models. The Shock and Vibration Digest, 38(3), 203-220.

[20] Dodbiba, G., Park, H. S., Okaya, K., and Fujita, T. (2008). Investigating magnetorheological properties of a mixture of two types of carbonyl iron powders suspended in an ionic liquid. Journal of Magnetism and Magnetic Materials, 320(7), 1322-1327.

[21] Ekwebelam, C., and See, H. (2009). Microstructural investigations of the yielding behaviour of bidisperse magnetorheological fluids. Rheologica Acta, 48(1), 19-32.

[22] Li, W. H., and Zhang, X. Z. (2010). A study of the magnetorheological effect of bimodal particle based magnetorheological elastomers. Smart Materials and Structures, 19(3), 035002.

[23] Machovský, M., Mrlík, M., Plachý, T., Kuřitka, I., Pavlínek, V., Kožáková, Z., and Kitano, T. (2015). The enhanced magnetorheological performance of carbonyl iron suspensions using magnetic Fe 3 O 4/ZHS hybrid composite sheets. RSC Advances, 5(25), 19213-19219.

[24] Ginder, J. M., Elie, L. D., and Davis, L. C. (1996). U.S. Patent No. 5549837. Washington, DC: U.S. Patent and Trademark Office.

[25] Rosenfeld, N., Wereley, N. M., Radakrishnan, R., and Sudarshan, T. S. (2002). Behavior of magnetorheological fluids utilizing nanopowder iron. International Journal of Modern Physics B, 16(17n18), 2392-2398.

[26] Chaudhuri, A., Wang, G., Wereley, N. M., Tasovksi, V., and Radhakrishnan, R. (2005). Substitution of micron by nanometer scale powders in magnetorheological fluids. International Journal of Modern Physics B, 19(07n09), 1374-1380.

[27] López-López, M. T., de Vicente, J., Bossis, G., González-Caballero, F., and Durán, J. D. G. (2005). Preparation of stable magnetorheological fluids based on extremely bimodal iron–magnetite suspensions. Journal of Materials Research, 20(4), 874-881.

[28] Wereley, N. M., Chaudhuri, A., Yoo, J. H., John, S., Kotha, S., Suggs, A., Radhakrishnan, R., Love, B. J., and Sudarshan, T. S. (2006). Bidisperse

magnetorheological fluids using Fe particles at nanometer and micron scale. Journal of Intelligent Material Systems and Structures, 17(5), 393-401.

[29] Ngatu, G. T., and Wereley, N. M. (2007). Viscometric and sedimentation characterization of bidisperse magnetorheological fluids. IEEE Transactions on Magnetics, 43(6), 2474-2476.

[30] Song, K. H., Park, B. J., and Choi, H. J. (2009). Effect of magnetic nanoparticle additive on characteristics of magnetorheological fluid. IEEE Transactions on Magnetics, 45(10), 4045-4048.

[31] Jönkkäri, I., Isakov, M., and Syrjälä, S. (2015). Sedimentation stability and rheological properties of ionic liquid–based bidisperse magnetorheological fluids. Journal of Intelligent Material Systems and Structures, 26(16), 2256-2265.

[32] Leong, S. A. N., Mazlan, S. A., Samin, P. M., Idris, A., and Ubaidillah. (2016). Performance of bidisperse magnetorheological fluids utilizing superparamagnetic maghemite nanoparticles. AIP Conference Proceedings, 1710, 030050.

[33] Susan-Resiga, D., and Vékás, L. (2017). Ferrofluid based composite fluids: Magnetorheological properties correlated by Mason and Casson numbers. Journal of Rheology, 61(3), 401-408.

[34] Morillas, J. R., Bombard, A. J., and de Vicente, J. (2018). Enhancing magnetorheological effect using bimodal suspensions in the single-multidomain limit. Smart Materials and Structures, 27(7), 07LT01.

[35] Bombard, A. J., Gonçalves, F. R., Morillas, J. R., and de Vicente, J. (2014). Magnetorheology of dimorphic magnetorheological fluids based on nanofibers. Smart Materials and Structures, 23(12), 125013.

[36] Morillas, J. R., Bombard, A. J., and de Vicente, J. (2015). Preparation and characterization of magnetorheological fluids by dispersion of carbonyl iron microparticles in PAO/1-octanol. Smart Materials and Structures, 25(1), 015023.

Conclusions

Through this dissertation a model, based on the finite element method, has been proposed to compute the static yield stress in magnetorheology. In addition, the model has been experimentally validated using a novel magnetorheological device and extended to novel bimodal MRFs. The major conclusions read as follows:

- Classic axisymmetric finite element methods do not properly simulate a true affine deformation under simple shear. Instead, they underestimate the yield stress for highly concentrated MRFs.
- A new model is proposed for the prediction of the static yield stress. The model captures multipoles and non-linear effects (as it solves Maxwell's equations without any approximations) as well as multibody effects (as it is based on periodic boundary conditions and a reduced field formulation) regardless of the external field strength and particle concentration.
- Under the assumption of affine deformation, the model is capable to be used on any periodic structure and under any applied strain.
- Independent of the field strength, a body-centered basis in a tetragonal/monoclinic lattice is energetically more favorable than a simple basis case. Nevertheless, differences in the yield stress between both bases only appear at particle concentrations well above 30 vol%.
- Multibody effects start to play a role for concentrations around 10 vol% (when interactions between neighboring chains are no longer negligible). This leads to a reduction of the yield stress (it does not linearly increase with concentration any more) and eventually, at large concentrations (approx. 45 vol%), can be responsible for a maximum in the yield stress.
- In the linear regime (small external field strengths), due to the relevance of multipoles and their short-range nature, the static yield stress is strongly dependent on the interactions between close particles. As a consequence:
    - Even small interparticle gaps in the field-induced chains dramatically decrease the static yield stress, especially if particles have a large relative permeability.
    - Classic models based on elongation + rotation of the chains offer an acceptable approximation to affine shear motion of diluted simple basis lattices.
- In the saturated regime (high external fields), due to the presence of only long-ranged dipolar interactions, the static yield stress shows a significant dependence on neighboring chain interactions:
    - Interparticle gaps along the field-induced chains only slightly reduce the static yield stress.
    - Classic models based on elongation + rotation of the chains completely fail in approximating the shearing motion and, thus, in the computation of the yield stress.
    - Analytical computations show that the conventional techniques imposing cutoff distances to the dipolar interaction do not necessarily capture multibody effects, in particular, when simulating unbounded particle arrangements.

    - Proposed analytical computation is in perfect agreement with the model as it also takes into consideration multibody effects of long range origin. It is more efficient from a computational point of view although limited to the saturated regime.

- Bearing in mind that the proposed model does not contain any free parameters and supposes structures with strong symmetries, the multipole, non-linear and multibody effects seems to be responsible for the good agreement between experiments and simulations (even in the post-yield regime where symmetric structures are clearly absent).
- Conventional single gap geometries used in magnetorheometry can introduce errors in the yield stress measurements. Particularly, the onset of the yield stress plateau is underestimated at both a lower saturation stress and external field strength. Interestingly, a double gap magnetorheological setup is capable of performing measurements under homogeneous magnetic fields, also in the saturating regime, and recovering the theoretically predicted trends in the yield stress.
- Yield stress measurements in the saturating regime demonstrate that the sudden application of a magnetic field would favor the sample structuration in a simple basis tetragonal lattice. However, normal stress measurements do not offer clear results highlighting their strong dependence on the finite sample size and internal structure defects.
- MRFs based on permanently magnetized magnetic particles, with mid-range size between single and multidomain regimes, exhibit an enhanced MR response compared to classic FFs and CMRFs because of their superior magnetization. Their rheological behavior can be collapsed by the Mason number similarly to CMRFs.
- Bimodal MRFs based on microparticles (primary population) and mid-range sized particles between the single and the multidomain regime (secondary population) show an enhanced yield stress, storage modulus and colloidal stability (lower sedimentation rate, easy to be redispersed and penetrated) in contrast to classic monomodal and bimodal MRFs. Both experiments and simulations demonstrate that the yield stress enhancement is a consequence of a secondary population with superior magnetic characteristics than the primary population.

Conclusiones

En esta tesis se ha propuesto un modelo, basado en el método de elementos finito, para calcular el esfuerzo umbral estático en magnetorreología. Además, el modelo se ha validado experimentalmente usando una nueva celda magnetorreológica y se ha extendido a nuevos FMR bimodales. Las principales conclusiones se resumen como sigue:

- Los modelos clásicos de elementos finitos basados en simetría axial no simulan correctamente la deformación afín. En su lugar, subestiman el esfuerzo umbral en FMR altamente concentrados.
- Se ha propuesto un nuevo modelo para calcular el esfuerzo umbral. Captura los efectos multipolares y no lineales (dado que resuelve las ecuaciones de Maxwell sin ninguna aproximación) así como los efectos multicuerpo (pues está basado en condiciones de contorno periódicas y una formulación de campo reducida) independientemente de la intensidad de campo externo o la concentración de partículas.
- Si se admite deformación afín, el modelo puede aplicarse en cualquier estructura periódica bajo cualquier grado de deformación.
- Independientemente del campo aplicado, las redes tetragonales/monoclínicas con base centrada en el cuerpo son energéticamente más favorables que aquellas con base simple. De cualquier modo, las diferencias entre ambas bases solo aparecen a concentraciones de partículas muy por encima del 30 vol%.
- Los efectos multicuerpo se han de tener en cuenta para concentraciones en torno al 10 vol% (cuando las interacciones entre cadenas vecinas no son despreciables). Dichos efectos producen une reducción en el esfuerzo umbral (que deja de ser proporcional a la concentración) y finalmente, a concentraciones altas (aproximadamente del 45 vol%), pueden ser responsables de la aparición de un máximo en el esfuerzo umbral.
- En el régimen lineal (campos externos pequeños), debido a la importancia de los multipolos y su naturaleza de corto alcance, el esfuerzo umbral estático depende fuertemente de las interacciones entre partículas cercanas. Como consecuencia:
    - Incluso pequeños espacios entre las partículas que forman las cadenas inducidas por el campo aplicado originan caídas dramáticas en el esfuerzo umbral estático, especialmente si las partículas tienen una permeabilidad magnética relativa elevada.
    - Los modelos clásicos basados en la aproximación de elongación + rotación simulan aceptablemente la deformación afín en redes de base simple poco concentradas.
- En el régimen de saturación (campos externos elevados), debido a la presencia de interacciones dipolares de largo alcance, el esfuerzo umbral estático muestra una marcada dependencia con las interacciones entre cadenas:
    - Los pequeños espacios entre partículas a lo largo de las cadenas reducen levemente el esfuerzo umbral.
    - Los modelos clásicos basados en la aproximación de elongación + rotación fallan completamente en simular la deformación de cizalla y, por tanto, en calcular el esfuerzo umbral.

    - Se ha demostrado analíticamente que las técnicas de cálculo convencionales consistentes en aplicar una distancia de corte a la interacción dipolar no capturan necesariamente los efectos multicuerpo, en concreto, cuando se simulan redes infinitas de partículas.
    - El cálculo analítico propuesto está en perfecto acuerdo con el modelo de elementos finitos puesto que tiene en cuenta efectos multicuerpo de largo alcance. Desde un punto de vista computacional es más eficiente aunque limitado al régimen de saturación.
- Teniendo en cuenta que el modelo propuesto no tiene ningún parámetro libre y supone estructuras muy simétricas, se deduce que los efectos multipolares, multicuerpo y no lineales son los principales responsables del buen acuerdo entre experimentos y simulaciones (incluso cuando el sistema fluye y claramente no hay estructuras periódicas presentes en el FMR).
- Las celdas magnetorreológicas convencionales de un solo gap pueden introducir errores en la medida del esfuerzo umbral. En particular, comparado con las predicciones teóricas, se obtienen esfuerzos umbrales en saturación más bajos y a campos aplicados menores. Es interesante señalar que, sin embargo, el uso de una celda magnetorreológica de gap doble permite medir el esfuerzo umbral bajo campos muy homogéneos, incluso en saturación, recobrando así la tendencia teóricamente predicha.
- Las medidas de esfuerzo umbral en saturación demuestran que la aplicación súbita del campo magnético favorecería la formación de redes tetragonales con base simple. Por el contrario, las medidas de esfuerzos normales no son concluyentes remarcando la fuerte dependencia de estos con el tamaño finito de la muestra y los defectos de su estructura interna.
- Los FMR basados partículas permanentemente magnetizadas, con tamaños en la frontera entre los regímenes mono- y multidominio magnético, exhiben una respuesta MR mejorada en comparación con FF y CMRF clásicos debido al mayor nivel de magnetización de sus partículas. Su comportamiento reológico puede describirse en función del número de Mason tal y como ocurre con los CMRF.
- Los FMR bimodales basados en micropartículas (población primaria) y partículas con tamaños en el límite entre los regímenes mono- y multidominio magnético (secundaria) muestran mejores esfuerzos umbrales, módulos de almacenamiento y estabilidad coloidal (sedimentan más lentamente y son más fáciles de redispersar) que los FMR monomodales y bimodales clásicos. Tanto medidas experimentales como resultados de simulación demuestran que la mejora en el esfuerzo umbral es consecuencia de las propiedades magnéticas superiores de la población secundaria en comparación con la primaria.